Modeling, Analysis, and Control of a Hypersonic Vehicle With Significant Aero-Thermo-Elastic-Propulsion Interactions, and Propulsive Uncertainty

by

Akshay Shashikumar Korad

A Thesis Presented in Partial Fulfillment
of the Requirements for the Degree
Master of Science

ARIZONA STATE UNIVERSITY

May 2010

Modeling, Analysis, and Control of a Hypersonic Vehicle With Significant Aero-Thermo-Elastic-Propulsion Interactions, and Propulsive Uncertainty

by

Akshay Shashikumar Korad

has been approved

April 2010

Graduate Supervisory Committee:

Armando A. Rodriguez, Chair
Konstantinos S. Tsakalis
Valana L. Wells

ACCEPTED BY THE GRADUATE COLLEGE

ABSTRACT

This thesis examines the modeling, analysis, and control system design issues for scramjet powered hypersonic vehicles. A nonlinear three degrees of freedom longitudinal model which includes aero-propulsion-elasticity effects was used for all analysis. This model is based upon classical compressible flow and Euler-Bernouli structural concepts. Higher fidelity computational fluid dynamics and finite element methods are needed for more precise intermediate and final evaluations. The methods presented within this thesis were shown to be useful for guiding initial control relevant design. The model was used to examine the vehicles static and dynamic characteristics over the vehicles trimmable region. The vehicle has significant longitudinal coupling between the fuel equivalency ratio (FER) and the flight path angle (FPA). For control system design, a two-input two-output plant (FER - elevator to speed-FPA) with 11 states (including 3 flexible modes) was used. Velocity, FPA, and pitch were assumed to be available for feedback.

Propulsion system design issues were given special consideration. The impact of engine characteristics (design) and plume model on control system design were addressed. Various engine designs were considered for comparison purpose. With accurate plume modeling, effective coupling from the FER to the FPA was increased, which made the peak frequency-dependent (singular value) conditioning of the two-input two-output plant (FER-elevator to speed-FPA) worse. This forced the control designer to trade off desirable (performance/robustness) properties between the plant input and output. For the vehicle under consideration (with a very aggressive engine and significant coupling), it has been observed that a large FPA settling time is needed in order to obtain reasonable (performance/robustness) properties at the plant input. Ideas for alleviating this fundamental tradeoff were presented. Plume modeling was also found to be particularly significant. Controllers based on plants with insufficient plume fidelity did not work well with the higher fidelity plants. Given the above, the thesis makes significant contributions to control-relevant hypersonic vehicle modeling, analysis, and design.

To my Family, Friends and Teachers

ACKNOWLEDGEMENTS

I am very grateful for the cooperation and support of my advisor Dr. A. A. Rodriguez, who has shown a great deal of patience and confidence in my work.

Besides my advisor, I would like to thank the rest of my thesis committee: Drs. K. Tsakalis, and V. Wells.

There are several other faculty members who have widened my horizons considerably through their courses and guidance. In particular, I would like to thank Dr. Montgomery and Dr. Mittelmann.

I would like to acknowledge the tremendous support and computing resources offered by the Ira A. Fulton School of Engineering High Performance Computing Initiative.

I would also like to acknowledge the help and guidance of Jeffrey J. Dickeson and Srikanth Sridharan.

This work has been supported by NASA grant NNX07AC42A. .

TABLE OF CONTENTS

CHAPTER Page

LIST OF TABLES

LIST OF FIGURES

1. INTRODUCTION

1.1 Motivation

With the historic 2004 scramjet-powered Mach 7 and 10 flights of the X-43A [15–18] , hypersonics research has seen a resurgence. This is attributable to the fact that air-breathing hypersonic propulsion is viewed as the next critical step towards achieving (1) reliable affordable access to space, (2) global reach vehicles. Both of these objectives have commercial as well as military applications. While rocket-based (combined cycle) propulsion systems [19] are needed to reach orbital speeds, they are much more expensive to operate because they must carry oxygen. This is particularly expensive when travelling at lower altitudes through the troposphere (i.e. below 36,152 ft). Current rocket-based systems also do not exhibit the desired levels of reliability and flexibility (e.g. airplane like takeoff and landing options). For this reason, much emphasis has been placed on two-stage-to-orbit (TSTO) designs which involve a turbo-ram-scramjet combined cycle in the first stage and a rocket-scramjet in the second stage. In this thesis, we focus on modeling and control challenges associated with scramjet-powered hypersonic vehicles. Such vehicles are characterized by significant aero-thermo-elastic-propulsion interactions and uncertainty [1, 3, 5, 15–32].

1.2 Related Work and Literature Survey

1.2.1 Overview of Hypersonics Research

The 2004 scramjet-powered X-43A flights ushered in the era of air-breathing hypersonic flight. Hypersonic vehicles that have received considerable attention include the National AeroSpace Plane (NASP, X-30) [33–36], X-33 [25, 37, 38], X-34 [39, 40], X-43 [15, 17, 18, 41], X-51 [42], and Falcon (Force Application from CONUS) [37, 43–45]. A summary of hypersonics research programs prior to the X-43A flights is provided within [46]. Some of this, and more recent, work is now described.

- *General Research on Scramjet Propulsion.* NASA has pursued scramjet propulsion research for over 40 years [46, 47]. During the mid 1960's, NASA built and tested a hydrogen-fueled and cooled scramjet engine that verified scramjet efficiency, structural integrity, and first generation design tools. During the early 1970's, NASA designed and demonstrated a fixed-geometry, airframe-integrated scramjet "flowpath" (capable of propelling a hypersonic vehicle from Mach 4 to 7) in wind tunnel tests.
- *NASP.* The NASP X-30 (1984-1996, $\$3B^{+}$) was a single-stage-to-orbit (SSTO) shovel-shaped (waverider) hydrogen fueled vehicle development effort involving DOD and NASA. At its peak, over 500 engineers and scientists were involved in the project [46, 48]. Despite the fact that no flights took place, much aero-thermo-elastic-propulsion research was accomplished through this effort [17, 33, 46, 49–52]. The program was unquestionably too ambitious [16] given the (very challenging) manned requirement as well as the state of materials, thermal protection, propulsion, computer-aided-design technology readiness levels (TRLs) and integration readiness levels (IRLs). Within [53], relevant cutting-edge structural strength/thermal protection issues are addressed; e.g. high specific strength (strength/density) that ceramic matrix composites (CMCs) offer for air-breathing hypersonic vehicles experiencing $2000^{\circ} - 3000^{\circ} F$ temperatures.
- *SSTO Technology Demonstrators.* The X-33 and X-34 would follow NASP.
  - The X-33 (Mach 15, 250 kft) [25, 37, 38] was a Lockheed Martin Skunk Works unmanned sub-scale (triangularly shaped) lifting body (linear aerospike) rocket-engine powered technology demonstrator for their proposed VentureStar SSTO reusable launch vehicle (RLV).
  - The X-34 (Mach 8, 250 kft) [39, 40], much smaller than the X-33, was an unmanned sub-scale (shuttle shaped) Orbital Sciences (Fastrac) rocket-engine powered technology demonstrator intended to operate like the space shuttle.

- *HyShot Flight Program.* Supersonic combustion of a scramjet in flight was first demonstrated July 30, 2002 (designated HyShot II) by the University of Queensland Center for Hypersonics (HyShot program) [54, 55]. Another flight demonstration took place on March 25, 2006 (HyShot III). During each flight, a two-stage Terrier-Orion Mk70 rocket was used to boost the payload (engine) to an apogee of 330 km. Engine measurements took place at altitudes between 23 km and 35 km when the payload carrying re-entry Orion reached Mach 7.6. Gaseous hydrogen was used to fuel the scramjet. Flight results were correlated with the University of Queensland's T4 shock tunnel. Thus far, the center has been involved with five flights - the last on June 15, 2007 (HyCAUSE) [56].

- *Hyper-X.* In 1996, the Hyper-X Program was initiated to advance hypersonic air-breathing propulsion [47]. The goal of the program was to (1) demonstrate an advanced, airframe-integrated, air-breathing hypersonic propulsion system in flight and (2) validate the supporting tools and technologies [15–18, 41]. The Hyper-X program culminated with the (March 27, November 16) 2004 Mach 7, 10 (actually 6.83, 9.8) X-43A scramjet-powered flights [16–18]. Prior to these flights, the SR-71 Blackbird held the turbojet record of just above Mach 3.2 while missiles exploiting ramjets had reached about Mach 5 [48].

  - *Flight 1.* The first X-43A flight was attempted on June 2, 2001. After being dropped from the B-52, the X-43A stack (Orbital Sciences Pegasus rocket booster plus X-43A) lost control. A "mishap investigation team" concluded that the (Pegasus) control system design was deficient for the trajectory selected due to inaccurate models [16, 57]. The trajectory was selected on the basis of X-43A stack weight limits on the B-52. The mishap report [57] (5/8/2003) said the (Pegasus) control system could not maintain stack stability during transonic flight. Stack instability was observed as a roll oscillation. This caused the rud-

der to stall. This resulted in the loss of the stack. Return to flight activities are summarized in [58].

– *Flight 2.* Results from Flight 2 (Mach 7, 95 kft, 1000 psf) are described within [20, 22, 59, 60]. The X-43A (Hyper-X research vehicle) was powered by an airframe-integrated hydrogen-fueled, dual mode scramjet. The fueled portion of the scramjet test lasted approximately 10 sec. The vehicle possessed 4 electromechanically actuated aerodynamic control surfaces: two (symmetrically moving) rudders for yaw control and two (symmetrically and differentially moving) all moving wings (AMWs) for pitch and roll control.

  Onboard flight measurements included [20] 1) three axis translation accelerations, 2) three axis rotational accelerations, 3) control surface deflections, 4) three space inertial velocities, 5) geometric altitude, 6) Euler angles (i.e. roll, pitch, and heading angles), and 7) wind estimates, 8) flush air data systems (FADS), amongst others (e.g. over 200 surface pressure measurements, over 100 thermocouples, GPS, weather balloon atmospheric measurements) [17, 61]. Body axis velocities, AOA, and sideslip angle [20] were estimated using (4) and (6).

  Control system design was based on sequential loop closure root locus methods [60]. Gains were scheduled on Mach and angle-of-attack (AOA) with dynamic pressure compensation. Gain and phase margins of 6 dB and 45° were designed into each loop for most flight conditions. Smaller margins were accepted for portions of the descent. Control system operated at 100 Hz, while guidance commands were issued at 25 Hz.

  Scramjet engine performance was within 3% of preflight predictions. During powered flight, AOA was kept at $2.5^\circ \pm 0.2^\circ$. Pre-flight aero-propulsive database development for Flight 2 (based on CFD and available ground-test data) is dis-

cussed within [62]. Relevant X-43A pre-flight descent aero data, including experimental uncertainty, is discussed within [23]. The data suggests vehicle static stability (in all three axes) along the descent trajectory. Moreover, longitudinal stability and rudder effectiveness are diminished for AOA's above 8°.

– *Flight 3.* Flight 3 (Mach 10, 110 kft, 1000 psf) results are described within [63]. Scramjet development tests exploiting the NASA/HyPulse Shock Tunnel in support of Flight 3 are described within [64]. The X-43A was a very heavy, short, very rigid (3000 lb, 12 ft, 5 ft wide, 2 ft high, 42 Hz lowest structural frequency [65]) lifting body and hence thermo-elastic considerations were not significant.

  Aerodynamic parameter identification results obtained from Flight 3 descent data at Mach 8, 7, 6, 5, 4, 3, based on multiple orthogonal phase-optimized sweep inputs applied to the control surfaces, are described within [66]. A linear aero model was used for fitting purposes. The fitting method (which led to the best results) was an equation-error frequency domain method. In short, estimated data agreed well with preflight data based on wind tunnel testing and computational fluid dynamics (CFD).

It is instructive to compare the operational envelops of several modern hypersonic vehicles. This is done in [39]. Approximate altitude and Mach extremes for some vehicles are as follows:

X-30: 250 kft, Mach 25;

X-33: 250 kft, Mach 15;

X-34: 250 kft, Mach 8;

X-43A: 110 kft, Mach 10.

The associated envelop scale back is, no doubt, a direct consequence of the aggressive goals of NASP - goals, in part, motivated by the politics of gaining congressional and

presidential approval [16]. More fundamentally, this scale back reflects the need for carefully planned demonstrations and flight tests.

- *HiFIRE.* The Hypersonic International Flight Research Experimentation (HiFIRE) is an ongoing collaboration between NASA, AFRL, Australian Defence Science and Technology Organization (DSTO), Boeing Phantom Works, and the University of Queensland [67]. It will involve 10 flights over 5 years. HiFIRE flights will focus on the goal of understanding fundamental hypersonic phenomena.

- *X-51A Scramjet Demonstrator Waverider.* The Boeing X-51A is an expendable hydrocarbon fueled scramjet engine demonstrator waverider vehicle (16 ft long, 1000 lb.) that is being developed by AFRL, Boeing, and Pratt & Whitney [42]. Multiple flight tests are scheduled for 2009. An X-51-booster stack will be carried via B-52 to a drop altitude. The Army tactical missile system solid rocket booster will then propel the vehicle to Mach 4.5. At that point, the scramjet will take over and the vehicle will accelerate to Mach 7.

- *Falcon.* Aspects of the Falcon waverider project are described within [37, 43–45, 68, 69] . The project began in 2003 with the goal of developing a series of incremental hypersonic technology vehicle (HTV) demonstrators. It involves the United States Air Force (USAF) and DARPA. Initially, ground demonstrations (HTV-1) were conducted. HTV-3X will involve a reusable launch vehicle with a hydrocarbon-fueled turbine-based combined-cycle (TBCC) propulsion system that takes off like an airplane, accelerates to Mach 6, and makes a turbojet powered landing. These demonstrations are designed to develop technologies for a future reusable hypersonic cruise vehicle (HCV) designed for prompt global reach missions.

- *Aero-Thermo-Elastic-Propulsion CFD-FE Tools.* The design of subsonic, transonic, and supersonic vehicles have benefited from extensive ground testing. Such testing

is much more difficult for hypersonic vehicles. As such, the use of state-of-the-art CFD-FE-based aero-thermo-elasticity-propulsion modeling tools is particularly crucial for the development of hypersonic vehicles. While much has been done at the component level (e.g. wings, surfaces), relatively little has been done that addresses the entire vehicle (at least in the published literature). This, of course, is due to the fact that accurate CFD studies often require the nation's most advanced supercomputing resources. Relevant work in this area is described within the following and the associated references [37, 48, 70, 71]. A major contribution of the 2004 X-43A flights was the validation of design tools [15, 16]. It should be noted that CFD is often applied in conjunction with or after applying classic engineering methods (e.g. panel methods) as described within [21, 27, 72]. Widely used programs that support such methods include (amongst many others) HABP (Hypersonic Arbitrary Body Program), APAS (Aerodynamic Preliminary Analysis System), and CBAERO (Configuration Based Aerodynamics prediction code) [21, 27, 36, 72]. Given the above, it is useful to know what was used for the X-43A. The primary CFD tool used for preflight performance analysis of the X-43A is GASP [62] - a multiblock, structured grid, upwind-based, Navier-Stokes flow solver which addresses (1) mixtures of thermally perfect gases via polynomial thermodynamic curve fits, (2) frozen, equilibrium, or finite-rate chemistry, (3) turbulent flow via Baldwin-Lomax algebraic turbulence model with Goldberg backflow correction. The SRGULL (developed by NASA's Zane Pinckney) and SHIP (supersonic hydrogen injection program) codes were used to predict scramjet performance for the X-43A [17, 61, 62]. SRGULL uses a 2D axis-symmetric Euler flow solver (SEAGULL). This was used [62] to address the forebody, inlet, and external nozzle regions of the X-43A lower surface flowpath. SRGULL also includes a 1D chemical equilibrium analysis code (SCRAM) which was used to approximate the combustor flowfield. X-43A CFD flow field solutions

may be visualized in [17]. Extensive databases exist for designing engines which exhibit good performance in the range Mach 4-7 [17].

1.2.2 Controls-Relevant Hypersonic Vehicle Modeling

The following describes control-relevant hypersonic vehicle models addressing aero-thermo-elastic-propulsion effects.

- In support of NASP research, the work within [36] describes a 6DOF model for a 300,00 lb, 200 ft, horizontal-takeoff winged-cone SSTO hypersonic vehicle. The model was generated using a (1) subsonic/supersonic panel code (APAS [72]), (2) hypersonic local surface inclination code (HABP [72]), (3) 2D forebody, inlet, nozzle code, and a (4) 1D combustor code. This model/vehicle has been used to guide the work of many controls researchers [73–80]. A significant short coming of the above model is that it cannot be used for control-relevant vehicle configuration design studies (at least not without repeating all of the work that went into generating the model); e.g. examining stability and coupling as vehicle geometry is varied. Efforts to address this are described below.

- Within [81] the authors describe the development of one of the first control-relevant first principles 3-DOF models for a generic hypersonic vehicle. Aerodynamic forces and moments are approximated using classical 2D Newtonian impact theory [21] . A simple static scramjet model is used. The flow is assumed to be quasi-one-dimensional and quasi-steady. Scramjet components include an isentropic diffuser, a combustor modeled via Rayleigh flow (1D compressible flow with heat addition) [82], and an isentropic internal nozzle. The aft portion of the fuselage serves as the upper half of an external nozzle. The associated free-stream shear layer forms the lower half of the external nozzle. This layer is formed by the equilibration of the static pressure of the exhaust plume and that of the free-stream flow. A simplifying

aft nozzle-plume-shear layer assumption is made that smoothly transitions the aft body/nozzle pressure from an exit pressure value p_e to the downstream free-stream value p_∞. Implicit in the assumption is the idea that Mach and AOA perturbations do not change the location of the shear layer and that aft pressure changes are determined solely by exit pressure changes and elastic motion [81, pg. 1315]. Controls include an elevator, increase in total temperature across the combustor, and diffuser area ratio. A single body bending mode was included based on a NASTRAN derived mode shape and frequency for a vehicle with a similar geometry. This model is a big step toward permitting control-relevant vehicle configuration design studies.

- The following significant body of work (2005-2007) [2, 3, 11, 14] examines aero-thermo-elastic-propulsion modeling and control issues using a first principles non-linear 3-DOF longitudinal dynamical model which exploits inviscid compressible oblique shock-expansion theory to determine aerodynamic forces and moments, a 1D Rayleigh flow scramjet propulsion model with a variable geometry inlet, and an Euler-Bernoulli beam based flexible model. The model developed in this work will be used as the basis for this thesis - one which describes important control system design issues; e.g. importance of FER margin as it relates to the control of scramjet powered vehicles.

- Within [83] the authors describe the development of a nonlinear 3-DOF longitudinal model using oblique shock-expansion theory and a Rayleigh scramjet (as above) for the winged-cone vehicle described within [36]. Euler-based (inviscid) computational fluid dynamics (CFD) is used to validate the model. A related line of work has been pursued in [84]. Within [73], wind-tunnel-CFD based nonlinear and linear longitudinal and lateral models are obtained for the above winged-cone vehicle.

- X-43A related 6-DOF Monte-Carlo robustness work is described within [15]. Results obtained from conducting closed loop simulations in the presence of uncertainty are

presented (as permitted). Limited comparisons between flight data and simulation data are made in an effort to highlight modeling shortfalls.

The above demonstrates the need for (mathematically tractable) parameterized control system design models that can be used for configuration design studies as well as higher fidelity control system evaluation models.

1.2.3 Modeling and Control Issues/Challenges

Lifting Body and Waverider Phenomena/Dynamics. Much attention has been given in the literature to integrated-airframe air-breathing propulsion [19] lifting body designs; e.g. X-30 [33–35], X-33 [25, 37, 38], X-34 [39, 40], X-43 [15, 17, 18, 41], X-51 [42]. Waverider designs [21, 85–88] - a special subclass of lifting body designs - have received particular attention; e.g. X-30, X-51 [42], Falcon [43–45, 68, 69, 89] . Relevant phenomena/dynamics are now discussed.

Why Waveriders? Generally, lift-to-drag (L/D) decreases with increasing Mach and is particularly poor for hypersonic vehicles (flat plate: $(L/D)_{max} = 6.5$; Boeing 707: $(L/D)_{max} = 20$ cruising near Mach 1) [21, page 251]. Conventional hypersonic vehicles typically have a detached shock wave along the leading edge and a reduced $(L/D)_{max}$. This is particularly true for blunt lifting body designs. In contrast, waveriders are hypersonic vehicles that (if properly designed and controlled) have an attached shock wave along the leading (somewhat sharp) edge [21, pp. 251-252] and "*appear to ride the bow shock wave*." Moreover, the high pressure flowfield underneath the vehicle remains somewhat contained with little leakage over the top in contrast to conventional hypersonic vehicles. As such, waveriders can exhibit larger L/D ratios, a larger lift for a given angle-of-attack (AOA), and can be flown at lower AOAs. A maximum L/D is desirable to maximize range [21]. It follows, therefore, that *waveriders are ideal for global reach cruise applications*.

A major design advantage associated with waveriders is that their associated flow fields are generally (relatively speaking) easy to compute [21]. This can be particularly useful during the initial design phase where it is critical to explore the vehicle parameter design space in order to address the inherent multidisciplinary optimization [89, 90].

Aero-Thermo. Drag can be reduced by making the body more slender (increased fineness) [91]. While this can reduce drag, it increases structural heating [21]; e.g. nose (stagnation point) heating, is inversely proportional to the nose radius. For this reason, *most hypersonic vehicles possess blunt noses*; e.g. Space Shuttle [21, page 200]. The needle-nosed coned-wing studied in [76, 79] and other studies may generate excessive heat for the first stage of a TSTO solution. Despite this, the authors strongly recommend that the reader examine the work described within [76, 79]. The point here is that fundamentally, hypersonic vehicle design is heat-driven, not drag-driven. This is because within the hypersonic regime *heating varies cubicly with speed, while drag varies quadratically* [21, pp. 347-348].

Scramjet Propulsion. The *entire underbelly of a waverider is part of the scramjet propulsion system*. Waveriders rely on bow shock and forebody design to provide significant *compression lift*, while the aftbody acts as the upper half of an expansion nozzle. Hypersonic vehicles generally possess long forebody compression surfaces to make the effective free-stream capture area as large as possible relative to the engine inlet area [19, pp. 40-41]. Generally, multiple compression ramps are used to achieve the desired conditions at the inlet. The X-43A, for example, used three compression ramps.

In contrast to rockets, air-breathing propulsion systems need not carry an oxidizer. This significantly reduces take-off-gross-weight (TOGW) [92]. Roughly, for a given payload weight $W_{payload}$, $\frac{W_{rocket}}{W_{payload}} \approx 25$ while $\frac{W_{airplane}}{W_{payload}} \approx 6.5$ [19, page 16]. Moreover, air-breathing systems offer increased safety, flexibility, robustness, and reduced operating costs [47, 93].

Scramjet propulsion specifically offers the potential for significantly increased specific impulse I_{sp} in comparison to rocket propulsion - hence lower cost-per-pound-to-orbit [58] (I_{sp} for hydrogen is much greater than that for hydrocarbon fuels). Scramjet operation is roughly Mach 5-16 [19], while air-breathing propulsion operation is roughly below 200kft [19, page 44]. In contrast to regular jets which have a compressor, scramjets (which rely on forebody compression) have no moving parts. When fuelled with hydrogen, they can (in theory) operate over a large range of Mach numbers (Mach 5-24) [94]. Scramjets are typically optimized at a selected design Mach number (e.g. Mach 7) to satisfy a shock-on-lip condition. At off-design speeds, a cowl door can be used to minimize air mass flow spillage. Cowl doors are generally scheduled open-loop [94]. For a very flexible vehicle, however, feedback may be required in order to reduce sensitivity to modeling errors.

Trajectories. Likely vehicle trajectories will lie within the so-called air-breathing corridor corresponding to dynamic pressures in the range $\overline{q} \in [500, 2000]$ psf - lower bound dictated by lifting area limit, upper bound dictated by structural limits. At Mach 16, the lower $\overline{q} = 500$ bound will require flight below 150kft [19, page 39]. Generally speaking, scramjet-powered vehicles will fly at the highest allowable (structure permitting) dynamic pressure in order to maximize free-stream mass airflow per unit area to the engine. It should be noted, however, that accelerating vehicles would have to increase dynamic pressure in order to maintain mass flow per unit area to the engine [19, page 41]. For this reason, we may wish to fly the vehicle being considered at $\doteq 1500-1750$ psf (see Figure 1) so that it has room to increase dynamic pressure by moving toward larger Mach numbers while avoiding thermal choking at the lower Mach numbers (e.g. Mach 5). Within [19, page 39], we see that the air-breathing corridor is about 30 kft wide vertically (see Figure 1). Assuming that the vehicle is flying along the center of the corridor, a simple calculation shows that if the flight path angle (FPA) deviates by about 2.86° ($\gamma \geq \sin^{-1}\left(\frac{\Delta h/\Delta t}{v}\right) \approx \sin^{-1}\left(\frac{15000/30}{10(1000)}\right)$)

for 30 sec at Mach 10, then the vehicle will leave the corridor. (This simple calculation, of course, does not capture the potential impact of dynamics.) This unacceptable scenario illustrates the need for FPA control - particularly in the presence of uncertain flexible modes.

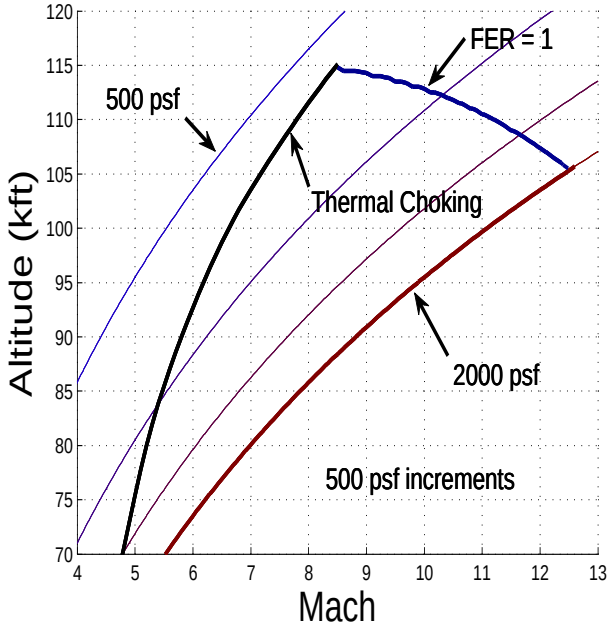

Figure 1: Air-Breathing Corridor Illustrating Constant Dynamic Pressure (Altitude vs Mach) Profiles, Thermal Choking Constraint, and FER Constraint; Notes: (1) Hypersonic vehicle considered in this thesis cannot be trimmed above the thermal choking line; (2) An FER ≤ 1 constraint is enforced to stay within validity of model; (3) Constraints in figure were obtained using viscous-unsteady model for level flight [1–14]

Figure 1 shows the constant dynamic pressure "trajectories" (or profiles) of altitude versus Mach. (It should be noted that the term trajectory is used loosely here since time is not shown in the figure.) With that said, Figure 1 demonstrates the permissible "air-breathing flight corridor" or "flight envelope" for air-breathing hypersonic vehicles. In addition to the dynamic pressure constraints discussed above, the figure also indicates a constraint associated with thermal choking and one due to unity stoichiometrically normalized fuel equivalency ratio (FER=1). Additional air-breathing corridor constraints are discussed within

[95].

Aero-Propulsion Coupling. In contrast to sub- and supersonic vehicles, hypersonic vehicles are uniquely characterized by *unprecedented aero-propulsion coupling*; i.e. the components providing lift, propulsion, and volume are strongly coupled [21, pp. 11-12]. More specifically, *aero performance cannot be decoupled from engine performance* because external forebody and nozzle surfaces are part of the engine flowpath [96]. For this reason, the integrated airframe-engine is sometimes referred to as an "engineframe." More specifically, vehicle aerodynamic properties impact the bow shock - detached for blunt leading edges, attached for sharp leading edges. This influences the engine inlet conditions which, in turn, influences thrust, lift, drag, external nozzle conditions, and pitching moment. More specifically, while forebody compression results in lift and a nose-up pitching moment aftbody expansion results in lift and a nose-down pitching moment. With the engine thrust situated below the c.g., this produces a nose-up pitching moment that must be countered by some control effector. Finally, it must be noted that scramjet air mass capture area, spillage, engine performance, as well as overall vehicle stability and control properties depend upon Mach, angle-of-attack (AOA), side-slip-angle (SSA), and engine power setting.

Hypersonic Flow Phenomena. Hypersonic flow is characterized by certain physical variables becoming progressively important as Mach is increased [21, 27, 29]. The boundary layer (BL), for example, grows as $\frac{M_\infty^2}{\sqrt{Re_{local}}}$. This causes the body to appear thicker than it really is. Viscous interactions refers to BL mixing with the inviscid far field. This impacts pressure distribution, lift, drag, stability, skin friction, and heat transfer. Shock layer variability is observed to start at around Mach 3 [21, page 13].

Aero-Thermo-Elastic-Propulsion. Hypersonic vehicles are generally unstable (long fore-

body, rearward engine, cg aft of ac) [3, 81]. As such, such vehicles generally require a *minimum control bandwidth (BW) for stabilization* [3, 97, 98]. The achievable BW, however, can be limited by flexible (structural) dynamics, actuator dynamics, right half plane zeros, other high frequency uncertain dynamics, and variable limits (e.g. control saturation level) [98]. High Mach numbers can induce significant heating and flexing (reduction of flexible mode frequencies) [33, 37, 99]. Carbon-Carbon leading edge temperatures on the X-43A Mach 10 flight, for example, reached nearly $2000^{\circ}F$ [17]. During the Pegasus boost (100 sec), surface temperatures reached nearly $1500^{\circ}F$ [17].

Heat induced forebody flexing can result in bow shock wave and engine inlet oscillations. This can impact the available thrust, stability, and achievable performance $-$ a major control issue if the vehicle is too flexible (light) and open loop unstable. A thermal protection system (TPS) is important to reduce heat-induced flexing; i.e. *prevent lowering of structural mode frequencies* [5, 9, 53, 59]. Designers must generally tradeoff vehicle lightness (permissible payload size) for increased thermal protection and vice versa. Type IV shock-shock interactions (e.g. bow shock interaction with cowl shock, results in supersonic jet impinging on cowl) - can cause excessive heating [21, page 226] that leads to structural damage. Within [53], relevant cutting-edge structural strength/thermal protection issues are addressed; e.g. high specific strength (strength/density) that ceramic matrix composites (CMCs) offer for air-breathing hypersonic vehicles experiencing $2000^{\circ} - 3000^{\circ}F$ temperatures. Materials for leading edges, aeroshells, and control surfaces are also discussed.

Non-minimum Phase Dynamics. Tail controlled vehicles are characterized by a non-minimum phase (right half plane, RHP) zero which is associated with the elevator to flight path angle (FPA) map [14]. This *RHP zero limits the achievable elevator-FPA BW* [97, 98, 100].

High Temperature Gas Effects. Relevant high temperature gas effects include [21] caloric imperfection (temperature dependent specific heats and specific heat ratio), vibrational excitation, O_2 dissociation, N_2 dissociation, plasma/ionization, radiation, rarefied gas effects [19, 21]. A more detailed description of these effects (and the conditions at which they are manifested) is provided in this thesis (see section 2.1, page 22).

The above hypersonic phenomena are accurately modeled by suitable partial differential equations (PDEs); e.g. Navier-Stokes, Euler, Euler-Bernoulli, Timoshenko, and heat transfer PDEs. This, together with the above interactions and associated uncertainty [1, 3, 5, 15–22, 24–32], highlights the relevant modeling and control challenges.

Model Limitations. The limitations of the model used in this thesis are listed here by functional section

1. **Aero.** the inviscid flow does not properly feed the viscid flow. In this model the Inviscid flow is computed over the skin of the vehicle and the viscous effects are added into the drag and lift forces. In reality the inviscid flow is dependent on the viscid flow over the body. Boundary Layer/Shock interactions are not captured in the model, as well as Shock/Shock interactions
2. **Propulsion.** The scramjet engine is modeled as having 1-Dimensional Rayliegh flow, this gives algebraic equations for the temperature inside the engine, rather that ODE's which would account for the finite chemistry rate that is actually taking place.
3. **Elastics.** the model uses 2 beams pinned at the center of gravity to model the vibrations. This is not an accurate depiction as this leads to no deflection at the center of gravity.
4. **Atmosphere.** There is no heating equation for the vehicle, a temperature profile is assumed. This assumed temperature profile is then used to calculate the viscous

effects.

This motivates the following control-relevant questions:

- When do each of the above become significant for controls?
- How can each of the above phenomena be modeled with a desired level of user-specified fidelity in an effort to capture control needs?

1.3 Contributions

This thesis addresses a myriad of issues that are of concern to both vehicle and control system designers, and represents a step toward answering the following critical control-relevant vehicle design questions:

1. How do accurate vehicle plume calculation impact a vehicle's static and dynamic properties?
2. How do these impact control system design?
3. How should a hypersonic vehicle be designed to permit/facilitate the development of an adequately robust control system?
4. What fundamental tradeoffs exist between vehicle control objectives?

A nonlinear 3DOF (degree of freedom) longitudinal model which includes aero-propulsion-elasticity effects is used for all analysis. The model is used to examine the vehicle's static and dynamic characteristics over the vehicle's trimmable region. The vehicle is characterized by unstable non-minimum phase dynamics with significant (approximately lower triangular) longitudinal coupling between fuel equivalency ratio (FER) or fuel flow and flight path angle (FPA). For control system design purposes, the plant is a two-input two-output plant (FER-elevator to speed-FPA) 11 state system (including 3 flexible modes). Speed, FPA, and pitch are assumed to be available for feedback. it is shown that the peak frequency-dependent (singular value) conditioning of the two-input two-output plant (FER-elevator to speed-FPA) worsens. This forces the control designer to trade off desirable (per-

formance/robustness) properties between the plant input and output. For the vehicle under consideration (with a very aggressive engine and significant coupling), it is shown that a large FPA settling time is needed in order to obtain reasonable (performance/robustness) properties at the plant input.

Plume modeling is also shown to be particularly significant. It is specifically shown that the fidelity of the plume (shear-layer) model is critical for adequately predicting vehicle static properties, dynamic properties, and assessing the overall difficulty of the control system design. Accurate plume calculation requires higher computational time. To address this issue procedure for suitable plume approximation is developed. This new approximation shown to be valid for whole trimmable region. It is also shown that this approximation is well suitable for control system design

1.4 Outline

The rest of this thesis is organized as follows. Chapter 2 describes the mathematical models of the HSV aircraft for the longitudinal dynamics. Chapter 3 describes how the properties of the nominal nonlinear HSV change as a function of flight condition, when trimmed at a zero flight path angle (FPA). Chapter 4 describes the linearization process and investigates in detail how the linear dynamics of the trimmed HSV model change as a function of flight condition. In Chapter 5, accurate vehicle plume plume calculations are presented. Effect of more accurate plume calculation over static and dynamic properties of vehicle are also discussed. Chapter 6 presents a simple control architecture, and the changes in the controller for different vehicle configurations is presented. Finally, Chapter 7 summarizes the results of this thesis, and suggests possible directions for future research.

1.5 Table of Definitions

The following is a list of variables with units which are used throughout the thesis.

v	Speed	(k ft/sec)
α	Angle of Attack	(deg)
q	Pitch Rate	(deg/sec)
Θ	Pitch Angle	(deg)
h	Altitude	(ft)
η_1	First Flexible Mode	(rad)
$\dot{\eta_1}$	First Flexible Mode Rate	(rad/s)
η_2	Second Flexible Mode	(rad)
$\dot{\eta_2}$	Second Flexible Mode Rate	(rad/s)
η_3	Third Flexible Mode	(rad)
$\dot{\eta_3}$	Third Flexible Mode Rate	(rad/s)
δ_e	Elevator Deflection	(deg)
FER	Fuel Equivalence Ratio	(-)
N_i	i^{th} Generalized Modal Force	(rad/s^2)
Φ_i	i^{th} mode shape	(-)
$\bar{q}$	Dynamic Pressure	(lbs/ft^2)
M_∞	Speed of freestream flow	(Mach)
V_∞	Speed of freestream flow	(ft/s)
p_∞	Freestream pressure	(lbs/ft^2)
T_∞	Freestream temperature	($^\circ R$)
p_f	Pressure acting on the lower forebody	(lbs/ft^2)
$F_{x,f}$	Lower body forces in the x direction	(lbs)
$F_{z,f}$	Lower body forces in the z direction	(lbs)
M_f	Moment acting on the lower forebody	(lbs-ft)

p_u	Pressure acting on the upper forebody	(lbs/ft^2)
$F_{x,u}$	Upper body forces in the x direction	(lbs)
$F_{z,u}$	Upper body forces in the z direction	(lbs)
M_u	Moment acting on the upper forebody	(lbs-ft)
p_b	Pressure acting on the bottom of the engine	(lbs/ft^2)
$F_{z,b}$	Forces on the bottom of the engine in the z direction	(lbs)
M_b	Moment acting on the bottom of the engine	(lbs-ft)
M_1	Speed of flow in the engine inlet, behind the shock	(Mach)
V_1	Speed of flow in the engine inlet, behind the shock	(ft/s)
p_1	Pressure at the engine inlet, behind the shock	(lbs/ft^2)
T_1	Temperature at the engine inlet, behind the shock	($^\circ R$)
$F_{x,inlet}$	forces at the engine inlet in the x direction	(lbs)
$F_{z,inlet}$	forces at the engine inlet in the z direction	(lbs)
M_2	Speed of flow in the engine diffuser	(Mach)
p_2	Pressure at the engine diffuser	(lbs/ft^2)
T_2	Temperature at the engine combustor entrance	($^\circ R$)
M_3	speed of flow in the engine combustor	(Mach)
p_3	pressure at the engine combustor	(lbs/ft^2)
T_3	temperature at the engine combustor exit	($^\circ R$)
ΔT_c	change in total temperature in the combustor	($^\circ R$)
H_f	specific heat of LH2	(-)
$\dot{m}_f$	Massflow of fuel	(slugs/s)
M_e	Speed of flow in the engine exit	(Mach)
V_e	Speed of flow in the engine exit	(ft/s)
p_e	Pressure at the engine exit	(lbs/ft^2)
T_e	Temperature at the engine exit	($^\circ R$)

$F_{x,e}$	exhaust forces on the aftbody in the x direction	(lbs)
$F_{z,e}$	exhaust forces on the aftbody in the z direction	(lbs)
$Lift_{viscous}$	Lift due to viscous effects	(-)
$Drag_{viscous}$	Drag due to viscous effects	(-)
$Normal_{viscous}$	Normal force due to viscous effects	(lbs)
$Tangent_{viscous}$	Tangent force due to viscous effects	(lbs)
$M_{viscous}$	Moment due to viscous effects	(-)
$F_{x,cs}$	elevator force in the x direction	(lbs)
$F_{x,cs}$	elevator force in the z direction	(lbs)
$F_{x,unsteady}$	forces due to unsteady pressure distribution in the x direction	(lbs)
$F_{z,unsteady}$	forces due to unsteady pressure distribution in the z direction	(lbs)
$M_{unsteady}$	Moment due to unsteady pressure distribution	(lbs-ft)
F_x	sum of the forces in the x direction	(lbs)
F_z	sum of the forces in the z direction	(lbs)
h_i	Engine Inlet Hieght	(ft)
A_d	Diffuser Area Ratio	(-)
A_n	exit nozzle area ratio	(-)

2. OVERVIEW OF HYPERSONIC VEHICLE MODEL

2.1 Overview

In this chapter, we consider a first principles nonlinear 3-DOF dynamical model for the longitudinal dynamics of a generic scramjet-powered hypersonic vehicle developed by Bolender et. al. [1–13]. The vehicle is 100 ft long with weight 6,154 lb per foot of depth and has a bending mode at about 21 rad/sec. The controls include: elevator, stoichiometrically normalized fuel equivalency ratio (FER), diffuser area ratio (not considered in our work), and a canard (not considered in our work). The vehicle may be visualized as shown in Figure 2 [1]. Nominal model parameter values for the vehicle are given in Table 2.4 (page 32).

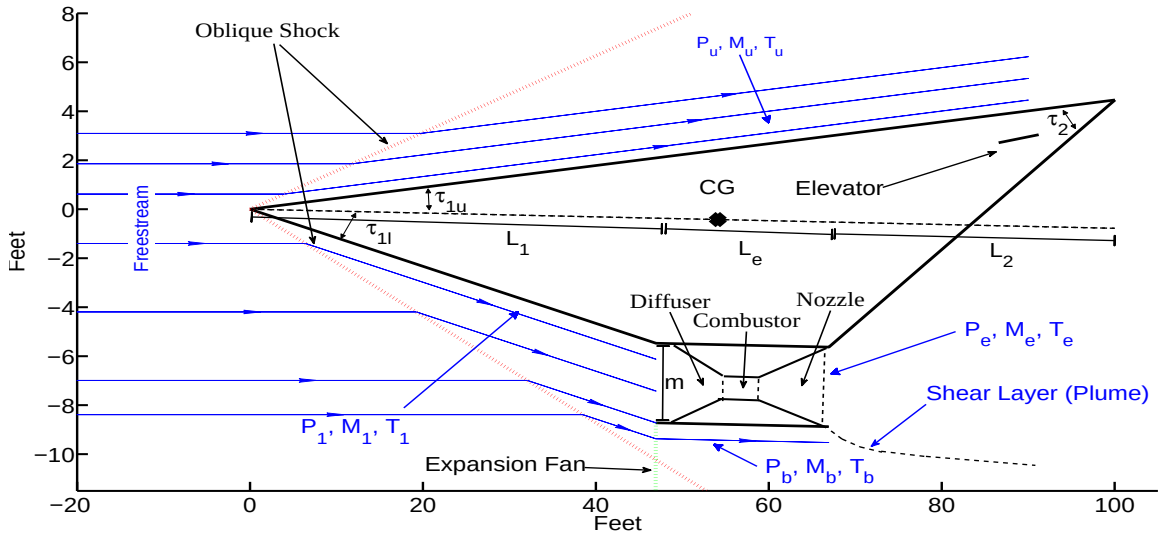

Figure 2: Schematic of Hypersonic Scramjet Vehicle

Modeling Approach. The following summarizes the modeling approach that has been used. Details are given in sections 2.3, 2.4, 2.7, 2.8.

- *Aerodynamics.* Pressure distributions are computed using inviscid compressible oblique-shock and Prandtl-Meyer expansion theory [13, 21, 27, 82]. Air is assumed to be

calorically perfect; i.e. constant specific heats and specific heat ratio $\gamma \stackrel{\text{def}}{=} \frac{c_p}{c_v} = 1.4$ [21, 82]. A standard atmosphere model is used (see section 2.4.1, page 32).

Viscous drag effects (i.e. an analytical skin friction model) are captured using Eckerts temperature reference method [1, 21]. This relies on using the incompressible turbulent skin friction coefficient formula for a flat plate at a reference temperature (see section 2.4.2, page 35). Of central importance to this method is the so-called wall temperature used. The model assumes a steady state wall temperature of $2500°R$ after 1800 seconds of flight [1, page 12]. This will be examined further in [101].

Unsteady effects (e.g. due to rotation and flexing) are captured using linear piston theory [1, 102]). The idea here is that flow velocities induce pressures just as the pressure exerted by a piston on a fluid induces a velocity (see section 2.4.3, page 37, or [103]).

- *Propulsion.* A single (long) forebody compression ramp provides conditions to the rear-shifted scramjet inlet. The inlet is a variable geometry inlet (variable geometry is not exploited in our work).

  The model assumes the presence of an (infinitely fast) cowl door which uses AOA to achieve shock-on-lip conditions (assuming no forebody flexing - i.e. FTA is precisely known). Forebody flexing, however, results in air mass flow spillage [13]. At the design cruise condition, the bow shock impinges on the engine inlet (assuming no flexing). At speeds below the design-flight condition and/or larger flow turning angles, the shock angle is large and the cowl moves forward to capture the shock. At larger speeds and/or smaller flow turning angles, the shock angle is small and the bow shock is swallowed by the engine. In either case, there is a shock reflected from the cowl or within the inlet (i.e. we have a bow shock reflection - Figure 6, page 46). This reflected shock further slows down the flow and steers it into the engine.

It should be noted that shock-shock interactions are not modeled. For example, at larger speeds and smaller flow turning angles there is a shock off of the inlet lip. This shock interacts with the bow shock. This interaction is not captured in the model. Such interactions are discussed in [21, page 225].

The model uses liquid hydrogen (LH2) as the fuel. It is assumed that fuel mass flow is negligible compared to the air mass flow. Thrust is linearly related to FER for all expected FER values. For large FER values, the thrust levels off. In practice, when FER > 1, the result is decreased thrust. This phenomena [13] is not captured in the model. As such, control designs based on this nonlinear model (or derived linear models) should try to maintain FER below unity (see section 2.7.5, page 48). The model also captures thermal choking (i.e. unity combustor exit Mach - see section 2.7.5, page 48, or [104]). In what follows, we show how to compute the FER required to induce thermal choking as well as the so-called *thermal choking FER margin*. The above will lead to a useful FER margin definition - one that is useful for the design of control systems for scramjet-powered hypersonic vehicles.

Finally, it should be noted that the model offers the capability for addressing linear fuel depletion that can be exploited for nonlinear simulations.

- *Structural.* A single free-free Euler-Bernoulli beam partial differential equation (infinite dimensional pde) model is used to capture vehicle longitudinal elasticity. As such, out-of-plane loading, torsion, and Timoshenko effects are neglected. The assumed modes method (based on a global basis) is used to obtain natural frequencies, mode shapes, and finite-dimensional approximants. This results in a model whereby the rigid body dynamics influence the flexible dynamics through the generalized forces [9, page 18]. This is in contrast to the model described within [13] which uses fore and aft cantilever beams (clamped at the center of gravity) and leads to the rigid body modes being inertially coupled to the flexible modes (i.e. rigid body

modes directly excite flexible modes). Within the current model, the forebody deflection (a function of the generalized forces N_i - see section 2.8, page 59) influences the rigid body dynamics via the bow shock which influences engine inlet conditions, thrust, lift, drag, and moment [9]. Aftbody deflections influence the AOA seen by the elevator. As such, the flexible modes influence the rigid body dynamics as well.

The beam model associated with the vehicle is assumed to be made of titanium. It is 100 ft long, 9.6 inches high, and 1 ft wide (deep), resulting in the nominal modal frequencies $\omega_1 = 21.02$ rad/sec, $\omega_2 = 50.87$ rad/sec, $\omega_3 = 101$ rad/sec [5, page 18, Table 2].

- *Actuator Dynamics.* Simple first order actuator models (contained within the original model) were used in each of the control channels: elevator - $\frac{20}{s+20}$, FER - $\frac{10}{s+10}$, canard - $\frac{20}{s+20}$ (Note: canard not used in our study). These dynamics did not prove to be critical in our study. An elevator saturation of $\pm 30^\circ$ was used [7, 105]. It should be noted, however, that these limits were never reached in our studies [104, 106–108]. A (state dependent) saturation level - associated with FER (e.g. thermal choking and unity FER) - was also directly addressed [104]. This (velocity bandwidth limiting) nonlinearity is discussed in this chapter (section 2.7.5, page 48).

Generally speaking, the vehicle exhibits unstable non-minimum phase dynamics with nonlinear aero-elastic-propulsion coupling and critical (state dependent) FER constraints. The model contains 11 states: 5 rigid body states (speed, pitch, pitch rate, AOA, altitude) and 6 flexible states.

Unmodeled Phenomena/Effects. All models possess fundamental limitations. Realizing model limitations is crucial in order to avoid model misuse. Given this, we now provide a (somewhat lengthy) list of phenomena/effects that are not captured within the above nonlinear model. (For reference purposes, flow physics effects and modeling requirements for

the X-43A are summarized within [62].)

- *Dynamics.* The above model does not capture longitudinal-lateral coupling and dynamics [109] and the associated 6DOF effects.

- *Aerodynamics.* Aerodynamic phenomena/effects not captured in the model include the following: boundary layer growth, displacement thickness, viscous interaction, entropy and vorticity effects, laminar versus turbulent flow, flow separation, high temperature and real gas effects (e.g. caloric imperfection, electronic excitation, thermal imperfection, chemical reactions such as 0_2 dissociation) [21], non-standard atmosphere (e.g. troposphere, stratosphere), unsteady atmospheric effects [20], 3D effects, aerodynamic load limits.

  Figure 3 shows the shuttle trajectory during re-entry. The angle-of-attack was fairly constant, ranging from 41 degrees at entry to 38 degrees at 10kft/s [110, page 3]. As can be seen, the vehicle passes through regions where the vibrational excitation and chemical reactions are significant. The 10% and 90% markers denote the approximate regions where particular effects start/are completed. Some of the relevant high temperature gas effects include (see figure 3)[21]

  1. Caloric imperfection (temperature dependent specific heats and specific heat ratio $\gamma \stackrel{\text{def}}{=} \frac{c_p}{c_v}$) begins at about 800K or about Mach 3.5 [21, page 18]
  2. Vibrational excitation is observed around Mach 3 and fully excited around Mach 7.5 [21, page 460]
  3. O_2 dissociation occurs at around 2000K and is observed at about Mach 7.5-8.5. It is complete at around 4000K or about Mach 15-17.[21], pp. 460-461

  For the scramjet Mach ranges under consideration (5-15), the following phenomena are likely not to be relevant: N_2 dissociation, plasma/ionization, radiation, rarefied gas effects [19, 21]. It should be noted that onset temperatures for molecular vibra-

tional excitation, dissociation, and ionization decrease when pressure is increased.

- *Propulsion.* Propulsion phenomena/effects not captured in the model include the following: cowl door dynamics, multiple forebody compression ramps (e.g. three on X-43A [111, 112]), forebody boundary layer transition and turbulent flow to inlet [111, 112], diffuser losses, shock interactions, internal shock effects, diffuser-combustor interactions, fuel injection and mixing, flame holding, engine ignition via pyrophoric silane [17] (requires finite-rate chemistry; cannot be predicted via equilibrium methods [89]), finite-rate chemistry and the associated thrust-AOA-Mach-FER sensitivity effects [113], internal and external nozzle losses, thermal choking induced phenomena (2D and 3D) and unstart, exhaust plume characteristics, combined cycle issues [19].

  Within [113], a higher fidelity propulsion model is presented which addresses internal shock effects, diffuser-combustor interaction, finite-rate chemistry and the associated thrust-AOA-Mach-FER sensitivity effects. While the nominal Rayleigh-based model (considered here) exhibits increasing thrust-AOA sensitivity with increasing AOA, the more complex model in [113] exhibits reduced thrust-AOA sensitivity with increasing AOA - a behavior attributed to finite-chemistry effects.

- *Structures.* Structural phenomena/effects not captured in the model include the following: out of plane and torsional effects, internal structural layout, unsteady thermo-elastic heating effects, aerodynamic heating due to shock impingement, distinct material properties [53], and aero-servo-elasticity [114, 115].

  - *Heating-Flexibility Issues.* Finally, it should be noted that Bolender and Doman have addressed a variety of effects in their publications. For example, within [5, 9] the authors address the impact of heating on (longitudinal) structural mode

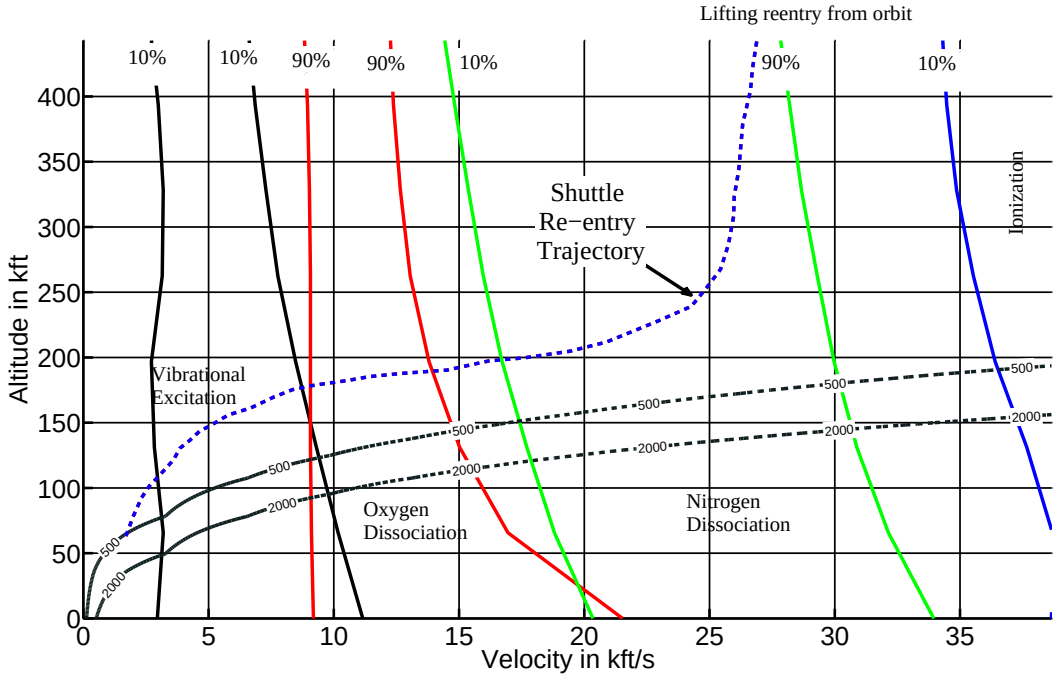

Figure 3: Visualization of High Temperature Gas Effects Due - Normal Shock, Re-Entry Vehicle (page 460, Anderson, 2006; Tauber-Menees, 1986) Approx: 1 Mach $\approx$ 1 kft/s

frequencies and mode shapes.

Within [5], the authors consider a sustained two hour straight and level cruise at Mach 8, 85 kft. It is assumed that no fuel is consumed (i.e. neglecting the impact of mass variations, in order to focus on the impact of heat addition). The presence of a thermal protection system (TPS) consisting of a PM2000 honeycomb outer skin followed by a layer of silicon dioxide (SiO_2) insulation is assumed. The vehicle - modeled by a titanium beam - is assumed to be insulated from the cryogenic fuel. The heat rate is computed via classic heat transfer equations that depend on speed (Mach), altitude (density), and the thermal properties of the TPS materials as well as air - convection and radiation at the air-PM2000 surface, conduction within the three TPS materials [5]. The initial temperature of all three TPS materials was set to $559.67°R = 100°F$) [5, page 11]. The maximum heat rate (achieved at the flight's inception) was

approximately $12\frac{BTU}{ft^2 sec}$ (1 foot aft of the nose) [101]. By the end of the two hour level flight, the average temperature within the titanium increased by $125^\circ R$ and it was observed that the vehicle's (longitudinal) structural frequencies did not change appreciably ($< 2\%$) [5, Table 2, page 18].

When one assumes a constant $15\frac{BTU}{ft^2 sec}$ heat rate at the air-PM2000 surface (same initial TPS temperature of $559.67^\circ R = 100^\circ F$), then after two hours of level flight the average temperature within the titanium increased by $205^\circ R$ [5, page 12]. In such a case, it can be shown that the vehicle's (longitudinal) structural frequencies do not change appreciably ($< 3\%$ [5, page 14]). This high heat rate scenario gives one an idea by how much the flexible mode frequencies can change by. Such information is critical in order to suitably adapt/schedule the flight control system.

- *Actuator Dynamics.* Future work will examine the impact of actuators that are rate limited; e.g. elevator, fuel pump.

It should be emphasized that the above list is only a partial list. If one needs fidelity at high Mach numbers, then many other phenomena become important.

2.2 Vehicle Layout

In [9, page 9, Figure 2], the authors provide a notional layout for the internal volume of the model. In section 2.8 (page 59), the assumed modes method, based on Lagrange's equations (see section 2.8, page 59 or [9, page 9]) is used to calculate the natural frequencies and mode shapes for the flexible structure. The potential and kinetic energy calculations require the mass distribution for the vehicle. Below, we present the mass distributions used for the model considered in this thesis. The load of a subsystem is assumed to be uniformly distributed over the interval specified in the column 'Range'.

It should be noted that the model can account for fuel depletion. The fraction of oxygen and hydrogen consumed is used to recalculate the mass of left within the tanks. It is assumed

Table 2.1: Mass Distribution for HSV Model

Subsystem	Mass (lbs)	Range (ft)
Beam	75000	[0 100]
Fore system	5000	[8 12]
Fore H_2 tank	114000	[30 50]
O_2 tank	155000	[48 62]
Payload	2500	[50 60]
Propulsion system	10000	[53 67]
Aft H_2 system	86000	[67.5 82.5]
Aft system	7500	[88 92]
Structure	50000	[40 70]

that the fraction of fuel depleted in the fore and aft hydrogen tanks is the same.

2.3 Equations of Motion

Longitudinal Dynamics. The equations of motion for the 3DOF flexible vehicle are given as follows:

$$\dot{v} = \left[\frac{T\cos\alpha - D}{m}\right] - g\sin\gamma \tag{2.1}$$

$$\dot{\alpha} = -\left[\frac{L + T\sin\alpha}{mv}\right] + q + \left[\frac{g}{v} - \frac{v}{R_E + h}\right]\cos\gamma \tag{2.2}$$

$$\dot{q} = \frac{\mathcal{M}}{I_{yy}} \tag{2.3}$$

$$\dot{h} = v\sin\gamma \tag{2.4}$$

$$\dot{\theta} = q \tag{2.5}$$

$$\ddot{\eta}_i = -2\zeta\omega_i\dot{\eta}_i - \omega_i^2\eta_i + N_i \qquad i = 1, 2, 3 \tag{2.6}$$

$$\gamma \stackrel{\text{def}}{=} \theta - \alpha \tag{2.7}$$

$$g = g_0\left[\frac{R_E}{R_E + h}\right]^2 \tag{2.8}$$

where L denotes lift, T denotes engine thrust, D denotes drag, $\mathcal{M}$ is the pitching moment, N_i denotes generalized forces, ζ demotes flexible mode damping factor, ω_i denotes flexible mode undamped natural frequencies, m denotes the vehicle's total mass, I_{yy} is the pitch

axis moment of inertia, g_0 is the acceleration due to gravity at sea level, and R_E is the radius of the Earth.

- *States.* The states consist of five classical rigid body states and six flexible modes states: the rigid states are velocity v, FPA γ, altitude h, pitch rate q, pitch angle θ, and the flexible body states $\eta_1, \dot{\eta}_1, \eta_2, \dot{\eta}_2, \eta_3, \dot{\eta}_3$. These eleven (11) states are summarized in Table 2.2.

Table 2.2: States for Hypersonic Vehicle Model

♯	**Symbol**	**Description**	**Units**
1	v	speed	kft/sec
2	γ	flight path angle	deg
3	α	angle-of-attack (AOA)	deg
4	q	pitch rate	deg/sec
5	h	altitude	ft
6	η_1	1^{st} flex mode	-
7	$\dot{\eta}_1$	1^{st} flex mode rate	sec^{-1}
8	η_2	2^{nd} flex mode	-
9	$\dot{\eta}_2$	2^{nd} flex mode rate	sec^{-1}
10	η_3	3^{rd} flex mode	-
11	$\dot{\eta}_3$	3^{rd} flex mode rate	sec^{-1}

- *Controls.* The vehicle has three (3) control inputs: a rearward situated elevator δ_e, a forward situated canard δ_c (not considered), and stoichiometrically normalized fuel equivalence ratio (FER). These control inputs are summarized in Table 2.3. In this research, we will only consider elevator and FER; i.e. the canard has been removed.

Table 2.3: Controls for Hypersonic Vehicle Model

♯	**Symbol**	**Description**	**Units**
1	FER	stoichiometrically normalized fuel equivalence ratio	-
2	δ_e	elevator deflection	deg
3	δ_c	canard deflection	deg

Nominal model parameter values for the vehicle under consideration are given in Table 2.4. Additional details about the model may be found in sections 2.4, 2.3, 2.7, 2.8, and within

the following references [1–13].

Table 2.4: Vehicle Nominal Parameter Values

Parameter	Nominal Value	Parameter	Nominal Value
Total Length (L)	**100 ft**	Lower forebody angle (τ_{1L})	6.2^o
Forebody Length (L_1)	47 ft	Tail angle (τ_2)	14.342^o
Aftbody Length (L_2)	33 ft	Mass per unit width	$191.3024\frac{slugs}{ft}$
Engine Length	20 ft	Weight per unit width	**6,154.1 lbs/ft**
Engine inlet height h_i	3.25 ft	Mean Elasticity Modulus	8.6482×10^7 psi
Upper forebody angle (τ_{1U})	3^o	Moment of Inertia I_{yy}	$86{,}723\frac{slugs ft^2}{ft}$
Elevator position	(-85,-3.5) ft	Center of gravity	(-55,0) ft
Diffuser exit/inlet area ratio	1	Elevator Area	17 ft^2
Titanium Thickness	9.6 in	Nozzle exit/inlet area ratio	6.35
First Flex. Mode (ω_{n_1})	**21.02 rad/s**	Second Flex. Mode (ω_{n_2})	**50.87 rad/s**
Third Flex. Mode (ω_{n_3})	**101.00 rad/s**	Flex. Mode Damping (ζ)	**0.02**

2.4 Aerodynamic Modeling

The U.S. Standard Atmosphere (1976) is a commonly used atmospheric model that extends previous models (1962, 1966) from 5 up to 1000 km [116]. Above 100 kilometers, solar and geomagnetic activity cause significant variations in temperature and density [117].

2.4.1 U.S. Standard Atmosphere (1976)

Key assumptions associated with the model are as follows:

1. Sea level pressure is $2116.2\ \mathrm{lb/ft^2}$ ($14.6958\ \mathrm{lb/in^2}$, 29.92” Hg)
2. Sea level temperature is 59° F
3. Acceleration due to gravity at sea level is $g = 32.17\ \mathrm{ft/s^2}$

   - decreasing with increasing altitude as inverse of (distance from earth’s center)^2
4. Molecular composition is sea level composition
5. Air is dry and motionless
6. Air obeys ideal gas law

7. Temperature decreases linearly with increasing altitude within troposphere ($-3.566°$F/1000 ft)

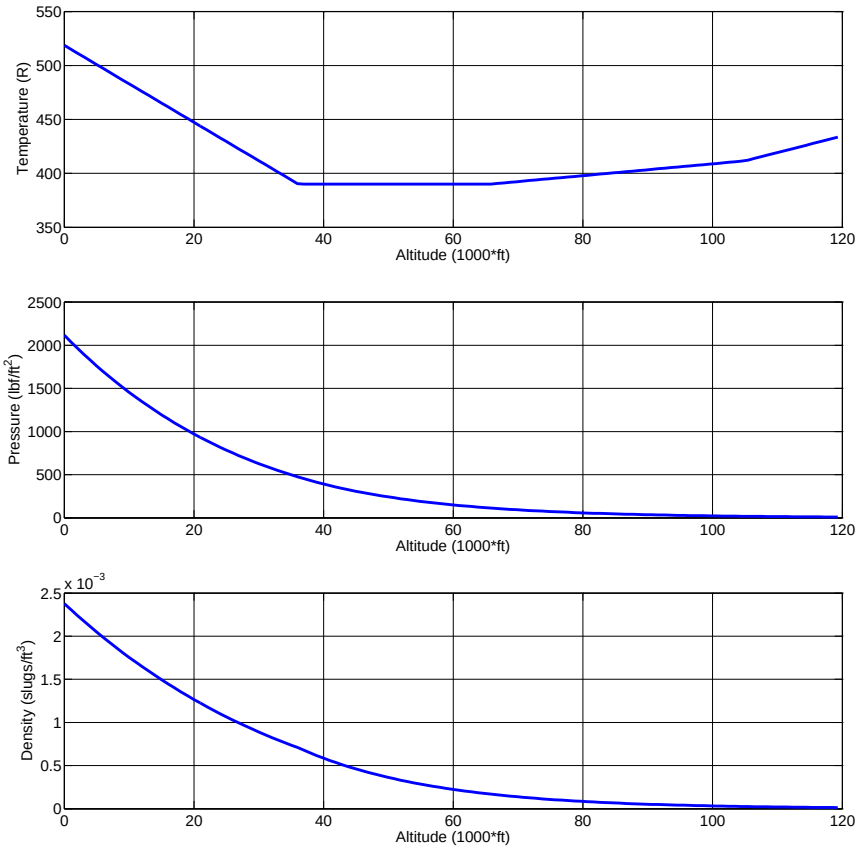

Figure 4: Atmospheric Properties vs. Altitude

- $0 \leq h < 36,089$ ft (6.835 miles)

$$t_r = 518.67 - .0036h \tag{2.9}$$

$$p = 2116 \left[\frac{t_r}{518.6}\right]^{-5.256} \tag{2.10}$$

$$\rho = 0.0024 \left[\frac{t_r}{518.6}\right]^{-4.256} \tag{2.11}$$

- $36,089 \text{ ft} \leq h < 65,617 \text{ ft}$ (6.835 to 12.427 miles)

$$t_r = 389.97 \tag{2.12}$$

$$p = 472.68e^{-0.000048(h-36,069)} \tag{2.13}$$

$$\rho = \frac{p}{1416} \tag{2.14}$$

- $65,617 \text{ ft} \leq h < 104,987 \text{ ft}$ (12.427-19.884 miles)

$$t_r = 389.97 + .000549(h - 65,617) \tag{2.15}$$

$$p = 114.34 \left[\frac{t_r}{389.97}\right]^{-34.16} \tag{2.16}$$

$$\rho = .0001708 \left[\frac{t_r}{389.97}\right]^{-35.16} \tag{2.17}$$

- $104,987 \text{ ft} \leq h < 154,199 \text{ ft}$ (19.884-29.204 miles)

$$t_r = 411.57 + .0015(h - 104,987) \tag{2.18}$$

$$p = 18.128 \left[\frac{t_r}{411.57}\right]^{-12.2} \tag{2.19}$$

$$\rho = .0000257 \left[\frac{t_r}{411.57}\right]^{-13.2} \tag{2.20}$$

t_r - temperature (°Rankine) h - altitude above sea level (ft)

p - pressure (lbs/ft^2) ρ - density (slug/ft^3)

Limitations of 1976 U.S. Standard Atmosphere Model.

The atmosphere model does not capture fact that

- Air properties depend on latitude and are impacted by moisture,
- Air is not motionless (e.g. North-South, East-West, and vertical winds - the X-43A

team assumed min-max limits at

- 80 kft: $[-30.94, 24.46]$, $[-76.32, 70.40]$, 10 ft/sec

- 120 kft: $[-64.34, 83.94]$, $[-78.24, 258.6]$, 10 ft/sec

2.4.2 Viscous Effects

The viscous effects [118] add a substantial amount of drag to the vehicle through the skin friction of the fluid moving around the vehicle. In this model, Eckert's Reference Temperature Method [1] is used to compute the viscous skin friction.

1. The method starts with the computation of the reference temperature which is a function of the Mach number (M_e) and temperature (T_e) at the edge of the boundary layer as well as the wall (skin) temperature T_w.

$$T^* = T_e \left[1 + M_e^2 + 0.58 \left(\frac{T_w}{T_e} - 1 \right) \right] \tag{2.21}$$

   where the wall temperature was given in ref [1] to be $2500^\circ R$. For simplicity we assume a constant wall temperature for all surfaces (see Table 2.5 for the surfaces for which viscous interaction are considered).

2. Using the perfect gas law, the density at the reference temperature ρ^* can be found from the following equation:

$$\rho^* = \frac{p}{RT^*} \tag{2.22}$$

   where p is the static pressure of the fluid.

3. The viscosity at the reference temperature μ^* can then be computed using Sutherland's Formula, which is known to be valid up to $3500^\circ R$.

$$\mu^* = 2.27 * 10^{-8} \frac{(T^*)^{3/2}}{T^* + 198.6} \tag{2.23}$$

4. Once the viscosity μ^* and the pressure are computed the Reynolds number at the reference temperature can be computed using:

$$Re^* = \frac{\rho^* V L}{\mu^*} \tag{2.24}$$

where V and L are the fluid velocity and the length, respectively.

5. Once the Reynolds number (Re) is calculated at the reference temperature, the skin friction coefficient for turbulent, supersonic flow over a flat plate can be computed as follows:

$$c_f = \frac{0.0592}{(Re^*)^{1/5}} \tag{2.25}$$

6. Now the shear stress at the wall τ_w can be computed by the following equation:

$$\tau_w = c_f((1/2)\rho_\infty V_\infty^2) \tag{2.26}$$

where Equation 2.26 gives the local skin friction.

7. Once τ_w is computed, integration over each surface is done to calculate the skin friction drag for each surface on the vehicle. This yields

$$F_{viscous} = \frac{5}{4}\tau_w L_s \tag{2.27}$$

When the local skin coefficient (c_f)is found for each surface of the vehicle, the normal and tangential forces are computed for each surface. The normal and tangential forces are obtained as follows:

$$Normal_{viscous} = F_{viscous}\sin(\beta) \tag{2.28}$$

$$Tangential_{viscous} = F_{viscous}\cos(\beta) \tag{2.29}$$

Table 2.5: Viscous Interaction Surfaces

Surface	Inclination to body axis (β)
Upper forebody	τ_{1u}
Lower forebody	$-\tau_{1l}$
Engine base	0
Aftbody	τ_{1U}+τ_2
Elevator (upper surface)	$-\delta_e$
Elevator (lower surface)	$-\delta_e$

where $F_{viscous}$ is calculated as above, and β is the surface inclination to the body axis (refer Table 2.5, page 37)

The lift and drag contribution of the viscous effects are computed using these normal and tangential forces, and are given as:

$$Lift_{viscous} = Normal_{viscous}\cos(\alpha) - Tangential_{viscous}\sin(\alpha) \quad (2.30)$$

$$Drag_{viscous} = Normal_{viscous}\sin(\alpha) - Tangential_{viscous}\cos(\alpha) \quad (2.31)$$

2.4.3 Unsteady Effects

The unsteady effects are calculated using linear piston theory [1, 4, 102]. This unsteady pressure distribution is a direct result of the interactions between the flow and the structure, as well as the unsteady, rigid body motion of the vehicle. The pressure acting on the face of a piston moving in a (supersonic) perfect gas is:

$$\frac{P}{P_i} = \left(1 + \frac{V_{n,i}}{5a_i}\right)^7 \quad (2.32)$$

where P_i is the local static pressure behind the bow shock, P is the pressure on the piston face, $V_{n,i}$ is the velocity of the surface normal to the flow, and a_i ($= \sqrt{\gamma RT}$)is the local

speed of sound. Using first order binomial expansion of equation 2.32:

$$\frac{P}{P_i} = 1 + \frac{7V_{n,i}}{5a_i} \tag{2.33}$$

$$P = P_i + \rho_i a_i V_{n,i} \tag{2.34}$$

The infinitesimal force acting on the face of the piston is given by:

$$d\mathbf{F}_i = (PdA)\,\mathbf{n}_i \tag{2.35}$$

$$\implies d\mathbf{F}_i = \left[-\left(P_i + \rho_i a_i V_{n,i}\right) dA\right] \mathbf{n}_i \tag{2.36}$$

The unsteady effects are computed by integrating 2.36 over each surface of the vehicle.

2.5 Properties Across a Shock

Properties Across Bow Shock. Let (M_∞, T_∞, p_∞) denote the free-stream Mach, temperature, and pressure. Let $\gamma \stackrel{\text{def}}{=} \frac{c_p}{c_v} = 1.4$ denote the specific heat ratio for air - assumed constant in the model; i.e. air is calorically perfect [21]. The shock wave angle $\theta_s = \theta_s(M_\infty, \delta_s, \gamma)$ can be found as the middle root (weak shock solution) of the following shock angle polynomial [13, 82]:

$$sin^6\theta_s + bsin^4\theta_s + csin^2\theta_s + d = 0 \tag{2.37}$$

where

$$\begin{aligned} b &= -\frac{M_\infty^2 + 2}{M_\infty^2} - \gamma sin^2\delta_s \\ c &= \frac{2M_\infty^2 + 1}{M_\infty^4} + \left[\frac{(\gamma+1)^2}{4} + \frac{\gamma - 1}{M_\infty^2}\right] sin^2\delta_s \\ d &= -\frac{cos^2\delta_s}{M_\infty^4} \end{aligned}$$

The above can be addressed by solving the associated cubic in $sin^2\theta_s$. A direct solution is possible if Emanuel's 2001 method is used [82]:

$$\tan\theta_s = \frac{M_\infty^2 - 1 + 2\lambda\cos\left[\frac{1}{3}(4\pi\delta + \cos^{-1}\chi)\right]}{3\left(1+\frac{\gamma-1}{2}M_\infty^2\right)\tan\delta_s} \quad (2.38)$$

$$\lambda = \left[(M_\infty^2-1)^2 - 3\left(1+\frac{\gamma-1}{2}M_\infty^2\right)\left(1+\frac{\gamma+1}{2}M_\infty^2\right)\tan^2\delta_s\right]^{\frac{1}{2}} \quad (2.39)$$

$$\chi = \frac{(M_\infty^2-1)^3 - 9\left(1+\frac{\gamma-1}{2}M_\infty^2\right)\left(1+\frac{\gamma-1}{2}M_\infty^2+\frac{\gamma+1}{4}M_\infty^4\right)\tan^2\delta_s}{\lambda^3} \quad (2.40)$$

where $\delta = 1$ corresponds to desired weak shock solution; $\delta = 0$ yields strong solution. After determining the shock wave angle θ_s, one can determine properties across the bow shock using classic relations from compressible flow [82]; i.e. M_s, T_s, p_s - functions of $(M_\infty, \delta_s, \gamma)$:

$$\frac{T_s}{T_\infty} = \frac{(2\gamma M_\infty^2\sin^2\theta_s + 1 - \gamma)((\gamma-1)M_\infty^2\sin^2\theta_s + 2)}{(\gamma+1)^2 M_\infty^2\sin^2\theta_s} \quad (2.41)$$

$$\frac{p_s}{p_\infty} = 1 + \frac{2\gamma}{\gamma+1}\left(M_\infty^2\sin^2\theta_s - 1\right) \quad (2.42)$$

$$M_s^2 sin^2(\theta_s - \delta_s) = \frac{M_\infty^2\sin^2\theta_s(\gamma-1)+2}{2\gamma M_\infty^2\sin^2\theta_s - (\gamma-1)} \quad (2.43)$$

It should be noted that for large M_∞, the computed temperature T_s across the shock will be larger than it should be because our assumption that air is calorically perfect (i.e. constant specific heats) does not capture other forms of energy absorption; e.g. electronic excitation and chemical reactions [21, page 459].

Properties Across Prandtl-Meyer Expansion. An expansion fan occurs when there is a flow over a convex corner; i.e. flow turns away from itself. More specifically to the bow, if $\delta_s < 0$ a Prandtl-Meyer expansion will occur. To determine the properties across the expansion, let (M_∞, T_∞, p_∞) denote the free-stream (supersonic) Mach, temperature, and

pressure, respectively. If we let $\delta = -\delta_s > 0$ denote the expansion ramp angle (in radians), the properties across the expansion fan (M_e, T_e, p_e) can be calculated as follows[13, 82]:

$$\nu_1 = \sqrt{\frac{\gamma+1}{\gamma-1}}\tan^{-1}\left(\sqrt{\frac{\gamma-1}{\gamma+1}(M_\infty^2-1)}\right) - \tan^{-1}\left(\sqrt{M_\infty^2-1}\right) \quad (2.44)$$

$$\nu_2 = \nu_1 + \delta \quad (2.45)$$

$$\nu_2 = \sqrt{\frac{\gamma+1}{\gamma-1}}\tan^{-1}\left(\sqrt{\frac{\gamma-1}{\gamma+1}(M_e^2-1)}\right) - \tan^{-1}\left(\sqrt{M_e^2-1}\right) \quad (2.46)$$

$$\frac{p_e}{p_\infty} = \left[\frac{1+\frac{\gamma-1}{2}M_\infty^2}{1+\frac{\gamma-1}{2}M_e^2}\right]^{\frac{\gamma}{\gamma-1}} \quad (2.47)$$

$$\frac{T_e}{T_\infty} = \left[\frac{1+\frac{\gamma-1}{2}M_\infty^2}{1+\frac{\gamma-1}{2}M_e^2}\right] \quad (2.48)$$

ν_1 is the angle for which a Mach 1 flow must be expanded to attain the free stream Mach.

2.6 Force and Moment Summations

While the above equations of motion (equations 2.1-2.6) apply to any 3-DOF aircraft, the force and moment summations (Lift, Drag, Thrust, Moment, N_i) which are summed below are specific to the scramjet powered HSV. These forces and moments are comprised of the breakdown of pressures in the body x and z directions. Some of these forces are shown in Figure 5.

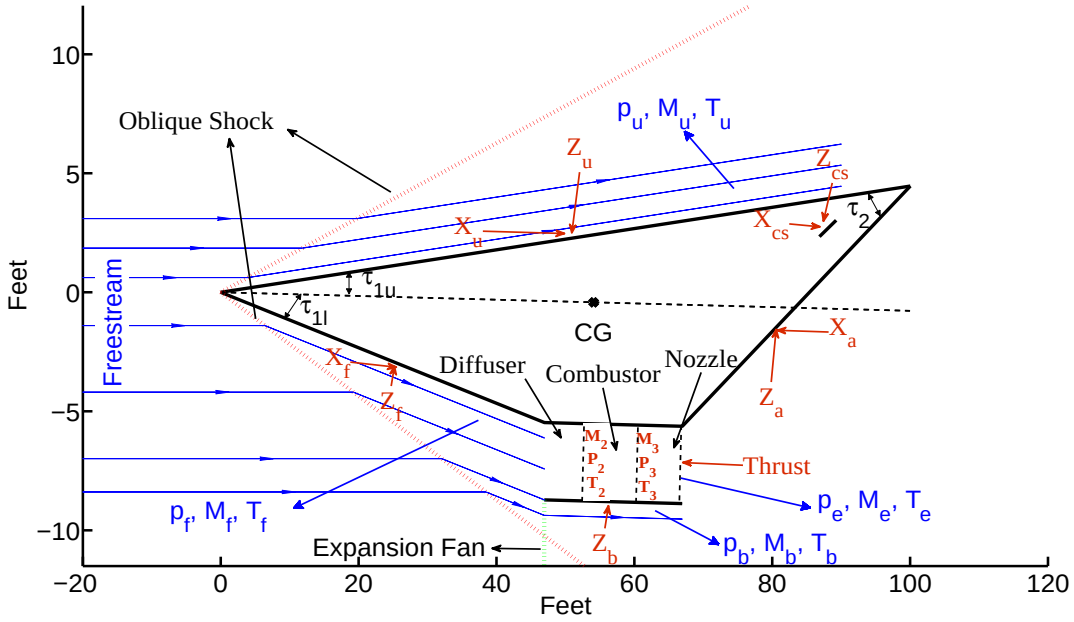

Figure 5: Free Body Diagram for the Bolender model

The equations for these forces and moments were given in [13]:

$$Lift = F_x \sin(\alpha) - F_z \cos(\alpha) + Lift_{viscous} \tag{2.49}$$

$$Drag = -(F_x \cos(\alpha) - F_z \sin(\alpha)) + Drag_{viscous} \tag{2.50}$$

$$Thrust = \dot{m}_a(V_e - V_\infty) + (p_e - p_\infty)A_e \tag{2.51}$$

$$\begin{aligned} Moment &= M_f + M_e + M_{inlet} + M_{cs} + M_u + M_b + M_{unsteady} \\ &\quad + (L_1 \tan(\tau_{1l})\frac{h_i}{2} - cg_z)Thrust + M_{viscous} \end{aligned} \tag{2.52}$$

$$N_i = \int p(x,t)\Phi_i(x)dx + \Sigma_j F_j(t)\Phi_i(x_j) \tag{2.53}$$

where n_i is the i^{th} modal coordinate of the flexible dynamics, $\Phi_i(x)$ is the i^{th} mode shape, V_e is the speed of flow exiting the engine, V_∞ is the freestream speed, p_e is the pressure at the exit of the internal nozzle, p_∞ is freestream pressure, $\dot{m}_a$ is the mass airflow into the engine, A_e is engine exit area per unit span, F_x and F_z are the sum of forces in the x and z direction respectively, and α is the angle of attack of the vehicle. The forces and moments

are summarized in Table 2.6.

Body Forces. The sum of the forces in the x and z directions (excluding viscosity, thrust) are given as

$$F_x = F_{x,f} + F_{x,u} + F_{x,e} + F_{x,inlet} + F_{x,cs} + F_{x,unsteady} \quad (2.54)$$

$$F_z = F_{z,f} + F_{z,u} + F_{z,b} + F_{z,e} + F_{z,inlet} + F_{z,cs} + F_{z,unsteady} \quad (2.55)$$

Table 2.6: HSV - Forces and Moments

Symbol	**Description**
N_i	i^{th} generalized force
$F_j(t)$	j^{th} point load acting at point x_j on the vehicle
F_x, F_z	sum of forces in x and z direction
$Lift_{viscous}$	lift due to viscous effects
$Drag_{viscous}$	drag due to viscous effects
$F_{x,f}, F_{z,f}$	lower forebody forces, x and z direction
$F_{x,u}, F_{z,u}$	upper forebody forces, x and z direction
$F_{x,inlet}, F_{z,inlet}$	forces in the engine inlet, x and z direction
$F_{x,e}, F_{z,e}$	exhaust forces on aftbody, x and z direction
$F_{x,cs}, F_{z,cs}$	elevator forces, x and z direction
$F_{x,unsteady}, F_{z,unsteady}$	unsteady forces, x and z direction
$F_{z,b}$	pressure on bottom of vehicle, z direction
$M_{unsteady}$	moment due to unsteady pressure distribution
$M_{viscous}$	moment due viscous effects
M_f	moment due to lower forebody forces
M_u	moment due to upper forebody forces
M_{inlet}	moment due to turning force at engine inlet
M_{cs}	moment due to control surface (elevator) forces
M_b	moment due to engine base forces

Forebody Forces and Moments. The forces acting on the upper and lower forebody are computed using the pressures acting on the upper and lower forebody (p_u, p_f). These pressures are computed using one of two methods depending on the angle of the shock wave created by the nose of the vehicle. These methods are now summarized.

- If the flow over the forebody is flowing over a concave corner, use oblique shock

theory

- If the flow over the forebody is flowing over a convex corner, use Prandtl-Meyer theory

Once the Mach, pressure and temperature after the shock have been calculated the pressures on the forebody are divided up into the upper forebody, the lower forebody and the x and z directions of each. The resulting moment acting on the lower forebody and upper forebody is also calculated.

The forces and moment acting on the lower forebody are given as:

$$F_{x,f} = -p_f L_f \tan \tau_{1l} \tag{2.56}$$

$$F_{z,f} = -p_f L_f \tag{2.57}$$

$$M_f = z_f F_{x,f} - x_f F_{z,f} \tag{2.58}$$

where (x_f, z_f) is the location of the lower forebody mid point w.r.t. the cg (L_f is the length of the lower forebody - see figure 2).

The pressures and moment acting on the upper forebody are given as:

$$F_{x,u} = -p_u L_u \tan \tau_{1u} \tag{2.59}$$

$$F_{x,u} = -p_u L_f \tag{2.60}$$

$$M_u = z_u F_{x,u} - x_u F_{z,u} \tag{2.61}$$

where (x_u, z_u) is the location of the upper forebody mid point w.r.t. the cg (L_u is the length of the upper forebody - see figure 2).

Engine Inlet Forces. The flow is parallel to the forebody after the shock at the nose. It must turn parallel to the body axis at the engine. This is achieved by an oblique shock with flow turn angle of $\tau_1 L$. The conditions behind the oblique shock gives the inlet conditions

for the engine. The forces and moments imparted on the aircraft are given by:

$$F_{x,inlet} = \gamma M_f^2 p_f \left(1 - \cos\left(\tau_{1l} + \alpha\right)\right) \frac{A_e}{b} \frac{1}{A_d A_n} \quad (2.62)$$

$$F_{z,inlet} = \gamma M_f^2 p_f \sin\left(\tau_{1l} + \alpha\right) \frac{A_e}{b} \frac{1}{A_d A_n} \quad (2.63)$$

$$M_{inlet} = z_{inlet} F_{x,inlet} - x_{inlet} F_{z,inlet} \quad (2.64)$$

where (M_f, p_f) are the Mach and pressure after the lower forebody shock, and (x_{inlet}, z_{inlet}) is the location of the engine inlet w.r.t. the cg.

Engine Base Forces. Depending on spillage at the engine inlet, the pressure on the lower forebody is calculated:

- Spillage - Expansion fan (shock angle = τ_l, upstream conditions - lower forebody stream)
- No spillage - Oblique shock (shock angle = α, upstream conditions - freestream)

The forces and moment due to the base are:

$$F_{z,b} = -p_b L_e \quad (2.65)$$

$$M_b = -F_{z,b} x_b \quad (2.66)$$

where $F_{z,b}$ is the force on the engine base, x_b is the location of the center of the engine base w.r.t. the cg (L_e is the length of the engine base - see figure 2).

Aftbody Forces. Due to the physical configuration of this vehicle the exhaust from the scramjet engine creates pressure acting on the aftbody (we use the plume assumption in calculating this pressure - see section 2.7.7). The upper section of the exit nozzle makes up the lower aftbody, consequently the external expansion of the exhaust from the scramjet

engine results in an aftbody pressure. The lower section of the exit nozzle in comprised of the resulting shear layer from the interaction of the exhaust with the freestream flow under the vehicle. The position of this shear layer dictates the pressure along the aftbody of the vehicle.

The pressure at any point on the aftbody is given by [81] as follows:

$$p_a = \frac{p_e}{1 + \frac{s_a}{L_a}(p_e/p_\infty - 1)} \tag{2.67}$$

where s_a is the location of the point along the aftbody (varies from 0 at the internal nozzle exit to L_a at the tip of the aftbody).

The contribution of the aftbody pressure in the z direction results in additional lift, and an offset to the drag in the x direction.

$$F_{x,e} = p_\infty L_a \frac{p_e}{p_\infty} \left[\frac{ln\frac{p_e}{p_\infty}}{\frac{p_e}{p_\infty} - 1} \right] \tan(\tau_2 + \tau_{1,u}) \tag{2.68}$$

$$F_{z,e} = -p_\infty L_a \frac{p_e}{p_\infty} \left[\frac{ln\frac{p_e}{p_\infty}}{\frac{p_e}{p_\infty} - 1} \right] \tag{2.69}$$

The aftbody pressure also creates a pitching moment centered around the point where the mean value of the pressure distribution occurs, with x_{exit}, and z_{exit} are the x and z coordinates of the effective aftbody pressure point w.r.t the cg respectively.

$$M_e = z_{exit} F_{x,e} - x_{exit} F_{z,e} \tag{2.70}$$

Control Surfaces. The elevator control surface is modeled here as flat plates, therefore to determine the pressures generated Prandtl-Meyer flow will be used on one side of the control surface and by oblique shock theory on the other. These pressures are centered around the mid-chord of the control surface. The elevator forces in the x and z direction

and moment are given by equations 2.71-2.73

$$F_{x,cs} = -(p_{cs,l} - p_{cs,u}) \sin \delta_{cs} S_{cs} \quad (2.71)$$

$$F_{z,cs} = -(p_{cs,l} - p_{cs,u}) \cos \delta_{cs} S_{cs} \quad (2.72)$$

$$M_{cs} = z_{cs} F_{x,cs} - x_{cs} F_{z,cs} \quad (2.73)$$

where δ_{cs} is the deflection in the elevator, S_{cs} is the surface area of the elevator, x_{cs} and z_{cs} refer to the x and z location of the elevator w.r.t the cg (S_{cs} is the area of the elevator).

2.7 Propulsion Modeling

Scramjet Model. The scramjet engine model is that used in [13, 81]. It consists of an inlet, an isentropic diffuser, a 1D Rayleigh flow combustor (frictionless duct with heat addition [82]), and an isentropic internal nozzle. A single (long) forebody compression ramp provides conditions to the rear-shifted scramjet inlet. Although the model supports a variable geometry inlet, we will not be exploiting variable geometry in this research; i.e. diffuser area ratio $A_d \stackrel{\text{def}}{=} \frac{A_2}{A_1}$ will be fixed (see Figure 6.)

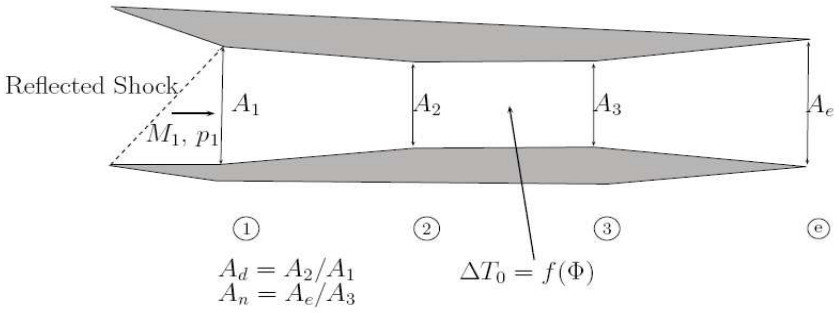

Figure 6: Schematic of Scramjet Engine

2.7.1 Shock Conditions.

A bow shock will occur provided that the flow deflection angle δ_s is positive; i.e.

$$\delta_s \stackrel{\text{def}}{=} \text{AOA} + \text{forebody flexing angle} + \tau_{1l} > 0^\circ \tag{2.74}$$

where $\tau_{1l} = 6.2^\circ$ is the lower forebody wedge angle (see Figure 2). An expansion fan occurs when there is a flow over a convex corner; i.e. flow turns away from itself. More specifically to the bow, if $\delta_s < 0$ a Prandtl-Meyer expansion will occur.

2.7.2 Translating Cowl Door.

The model assumes the presence of an (infinitely fast) translating cowl door which uses AOA to achieve shock-on-lip conditions (assuming no forebody flexing). Forebody flexing, however, results in an oscillatory bow shock and air mass flow spillage [13]. A bow shock reflection (off of the cowl or inside the inlet) further slows down the flow and steers it into the engine. Shock-shock interactions are not modeled.

Impact of Having No Cowl Door. Associated with a translating cowl door are potentially very severe heating issues. For our vehicle, the translating cowl door can extend a great deal. For example, at Mach 5.5, 70kft, the trim FTA is 1.8° and the cowl door extends 14.1 ft. Of particular concern, due to practical cowl door heating/structural issues, is what happens when the cowl door is over extended through the bow shock. This occurs, for example, when structural flexing results in a smaller FTA (and hence a smaller bow shock angle) than assumed by the rigid-body shock-on-lip cowl door extension calculation.

2.7.3 Inlet Properties.

The bow reflection turns the flow parallel into the scramjet engine [13]. The oblique shock relations are implemented again, using M_s as the free-stream input, $\delta_1 = \tau_{1l}$ as the flow deflection angle to obtain the shock angle $\theta_1 = \theta_1(M_s, \delta_1, \gamma)$ and the inlet (or diffuser entrance) properties: M_1, T_1, p_1 - functions of (M_s, θ_1, γ).

2.7.4 Diffuser Exit-Combustor Entrance Properties.

The diffuser is assumed to be isentropic. The combustor entrance properties are therefore found using the formulae in [13, 82] - $M_2 = M_2(M_1, A_d, \gamma)$, $T_2 = T_2(M_1, M_2, \gamma)$, $p_2 = p_2(M_1, M_2, \gamma)$:

$$\frac{\left[1 + \frac{\gamma-1}{2} M_2^2\right]^{\frac{\gamma+1}{\gamma-1}}}{M_2^2} = A_d^2 \frac{\left[1 + \frac{\gamma-1}{2} M_1^2\right]^{\frac{\gamma+1}{\gamma-1}}}{M_1^2} \tag{2.75}$$

$$T_2 = T_1 \left[\frac{1 + \frac{1}{2}(\gamma-1)M_1^2}{1 + \frac{1}{2}(\gamma-1)M_2^2}\right] \tag{2.76}$$

$$p_2 = p_1 \left[\frac{1 + \frac{1}{2}(\gamma-1)M_1^2}{1 + \frac{1}{2}(\gamma-1)M_2^2}\right]^{\frac{\gamma}{\gamma-1}} \tag{2.77}$$

where $A_d \stackrel{\text{def}}{=} \frac{A_2}{A_1}$ is the diffuser area ratio. Also, one can determine the total temperature $T_{t_2} = T_{t_2}(T_2, M_2, \gamma)$ at the combustor entrance can be found using [82]:

$$T_{t2} = \left[1 + \frac{\gamma-1}{2} M_2^2\right] T_2. \tag{2.78}$$

Since $A_d = 1$ in the model, it follows that $M_2 = M_1$, $T_2 = T_1$, $p_2 = p_1$, and $T_{t2} = \left[1 + \frac{\gamma-1}{2} M_1^2\right] T_1 = T_{t_1}$.

2.7.5 Combustor Exit Properties.

The model uses liquid hydrogen (LH2) as the fuel. If f denotes fuel-to-air ratio and f_{st} denotes stoichiometric fuel-to-air ratio, then the stoichiometrically normalized fuel equivalency ratio is given by $FER \stackrel{\text{def}}{=} \frac{f}{f_{st}}$ [13, 19]. FER is the engine control. While FER is primarily associated with the vehicle velocity, its impact on FPA is significant (since the engine is situated below vehicle cg). This coupling will receive further examination in what follows.

In this model, we have a constant area combustor where the combustion process is captured via heat addition. To determine the combustor exit properties, one first determines the change in total temperature across the combustor [13]:

$$\Delta T_c = \Delta T_c(T_{t_2}, FER, H_f, \eta_c, c_p, f_{st}) = \left[\frac{f_{st} FER}{1 + f_{st} FER}\right]\left(\frac{H_f \eta_c}{c_p} - T_{t_2}\right) \tag{2.79}$$

where $H_f = 51,500$ BTU/lbm is the heat of reaction for liquid hydrogen (LH2), $\eta_c = 0.9$ is the combustion efficiency, $c_p = 0.24\ \mathrm{BTU/lbm^{\circ}R}$ is the specific heat of air at constant pressure, and $f_{st} = 0.0291$ is the stoichiometric fuel-to-air ratio for LH2 [19]. Given the above, the Mach M_3, temperature T_3, and pressure p_3 at the combustor exit are determined by the following classic 1D Rayleigh flow relationships [13, 82]:

$$\frac{M_3^2\left[1 + \frac{1}{2}(\gamma - 1)M_3^2\right]}{(\gamma M_3^2 + 1)^2} = \frac{M_2^2\left[1 + \frac{1}{2}(\gamma - 1)M_2^2\right]}{(\gamma M_2^2 + 1)^2} + \left[\frac{M_2^2}{(\gamma M_2^2 + 1)^2}\right]\frac{\Delta T_c}{T_2} \tag{2.80}$$

$$T_3 = T_2\left[\frac{1 + \gamma M_2^2}{1 + \gamma M_3^2}\right]^2\left(\frac{M_3}{M_2}\right)^2 \tag{2.81}$$

$$p_3 = p_2\left[\frac{1 + \gamma M_2^2}{1 + \gamma M_3^2}\right]. \tag{2.82}$$

Given the above, one can then try to solve equation (2.80) for $M_3 = M_3\left(M_2, \frac{\Delta T_c}{T_2}, \gamma\right)$. This will have a solution provided that M_2 is not too small, ΔT_c is not too large (i.e. FER is not too large or T_2 is not too small).

Thermal Choking FER ($M_3 = 1$). Once the change in total temperature ΔT_c = ΔT_c(T_{t_2} , FER, H_f , η_c , c_p , f_{st}) across the combustor has been computed, it can be substituted into equation (2.80) and one can "try" to solve for M_3. Since the left hand side of equation (2.80) lies between 0 (for $M_3 = 0$) and 0.2083 (for $M_3 = 1$), it follows that if the right hand side of equation (2.80) is above 0.2083 then no solution for M_3 exists. Since the first term on the right hand side of equation (2.80) also lies between 0 and 0.2083, it follows that this occurs

when ΔT_c is too large; i.e. too much heat is added into the combustor or too high an FER. In short, a solution M_3 will exist provided that FER is not too large, T_2 is not too small (i.e. altitude not too high), and the combustor entrance Mach M_2 is not too small (i.e. FTA not too large). When $M_3 = 1$, a condition referred to as *thermal choking* [19, 82] is said to exist. The FER that produces this we call the *thermal choking FER* - denoted FER_{TC}. In general, FER_{TC} will be a function of the following: M_∞, T_∞, and FTA.

Physically, the addition of heat to a supersonic flow causes it to slow down. If the thermal choking FER (FER_{TC}) is applied, then we will have $M_3 = 1$ (i.e. sonic combustor exit). When thermal choking occurs, it is not possible to increase the air mass flow through the engine. Propulsion engineers want to operate near thermal choking for engine efficiency reasons [19]. However, if additional heat is added, the upstream conditions can be altered and it is possible that this may lead to engine unstart [19]. This is highly undesirable. For this reason, operating near thermal choking has been described by some propulsion engineers as "operating near the edge of a cliff."

When Does Thermal Choking Occur? Within Figure 8, the combustor exit Mach M_3 is plotted versus the free-stream Mach M_∞ for level-flight with zero FTA at 85 kft. It should be noted from Figure 11 that at 85 kft, the vehicle can be trimmed between the shown thermal choking and dynamic pressure barriers for $\sim$Mach 5.5-8 (where Mach 8, 85 kft corresponds to 2076 psf - slightly more than the "standard" structural constraint of 2000 psf). For $M_\infty = 8.5$, the thermal choking FER is unity. As M_∞ decreases, the thermal choking FER is reduced. When $M_\infty = 1.54$ (well below trimmable Mach at 85kft), $M_2 = 1$, and the thermal choking FER reduces to zero. In general, thermal choking will occur if FER is too high, M_∞ is too low, altitude is too high (T_∞ too low), FTA is too high. We now examine the above engine relations as they relate to thermal choking.

M_3 **versus** M_2**.** Figure 7 shows the relationship between the speed of the flow at the combustor exit Mach M_3 versus that at the combustor entrance M_2 for different values of FER

(at 85 kft, level-flight, zero flow turning angle). The figure shows the following:

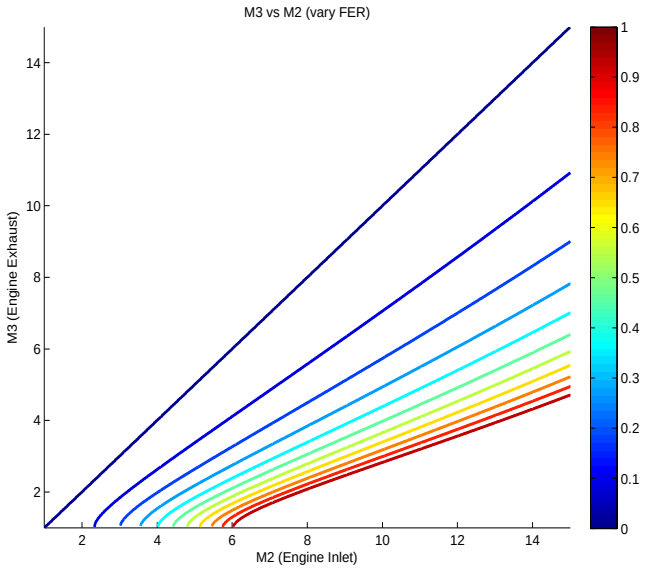

Figure 7: Combustor Exit Mach M_3 vs. Combustor Entrance Mach M_2 (85 kft, level-flight, zero FTA)

$M_2 = 7$	$FER = 1$	$M_3 = 2.06$
$M_2 = 6$	$FER = 1$	$M_3 = 1.27$
$M_2 = 5.85$	$FER = 1$	$M_3 = 1$
$M_2 = 5$	$FER_{TC} = 0.62$	$M_3 = 1$
$M_2 = 4$	$FER_{TC} = 0.33$	$M_3 = 1$
$M_2 = 3$	$FER_{TC} = 0.14$	$M_3 = 1$
$M_2 = 2$	$FER_{TC} < 0.1$	$M_3 = 1$
$M_2 = 1$	$FER_{TC} = 0$	$M_3 = 1$

For $M_2 = 6$ and $FER = 1$, we get $M_3 = 1.27$; i.e. we are nearly choking and the thermal choking FER is greater than unity. For $M_2 = 5.85$, the thermal choking FER becomes unity. As M_2 is reduced further, the thermal choking FER decreases. It decreases to zero as M_2 is reduced toward unity.

M_3 versus M_∞. Now consider Figure 8. In this figure, the combustor exit Mach M_3 is plotted versus the free-stream Mach M_∞ (at 85 kft, level-flight, zero flow turning angle). It should be noted from Figure 11 that at 85 kft, the vehicle can be trimmed within the shown thermal choking and dynamic pressure constraints for ∼Mach 5.5-8 (where Mach 8, 85 kft corresponds to slightly more than the "standard" structural constraint 2000 psf). The figure shows the following:

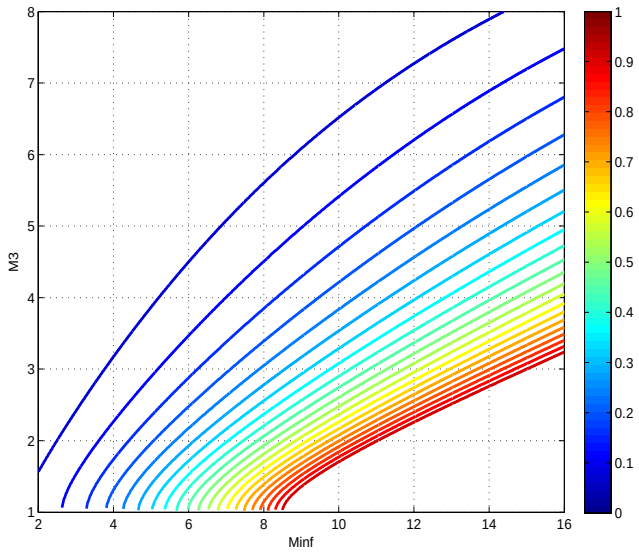

Figure 8: Combustor Exit Mach M_3 vs. Free-Stream Mach M_∞ (85 kft, zero FTA)

$M_\infty = 10$	$FER = 1$	$M_3 = 1.71$
$M_\infty = 8.5$	$FER = 1$	$M_3 = 1$
$M_\infty = 8$	$FER_{TC} = 0.88$	$M_3 = 1$
$M_\infty = 7$	$FER_{TC} = 0.64$	$M_3 = 1$
$M_\infty = 6$	$FER_{TC} = 0.45$	$M_3 = 1$
$M_\infty = 4$	$FER_{TC} = 0.17$	$M_3 = 1$
$M_\infty = 3.28$	$FER_{TC} = 0.1$	$M_3 = 1$
$M_\infty = 1.54$	$FER_{TC} = 0$	$M_3 = 1$

For $M_\infty = 8.5$ the thermal choking FER is unity. As M_∞ is reduced, the thermal choking

FER is reduced. When $M_\infty = 1.54$ (well below trimmable Mach numbers at 85 kft, see Figure 11), $M_2 = 1$, and the thermal choking FER is reduced to zero.

The analysis will be used to define an FER margin that will be useful for control system design.

Thermal Choking FER Properties. Figure 9 demonstrates FER margin properties that are characteristic of hypersonic vehicles. Figure 9 shows FER_{TC} for $FTA \in [-5^\circ, 5^\circ]$ (red curves). The solid red curve corresponds to a zero FTA. The lower (upper) dashed red curve corresponds to FTA of 5° (-5°). Consequently, FER_{TC} depends on the FTA. To summarize, FER_{TC} is (nearly) independent of altitude (for constant FTA, not shown in figure), decreases with decreasing Mach (for constant FTA), decreases (increases) with increasing (decreasing) FTA (for constant Mach).

Thermal Choking and Unity FER Margins. Next, we define FER margins that are useful for control system design. While the patterns revealed are based on the simple 1D Rayleigh flow model discussed above, the FER margin framework introduced is useful for designing control systems that suitably tradeoff scramjet authority and efficiency.

Thermal Choking FER Margin. The *thermal choking margin* at an instant in time is defined as follows:

$$FERM_{TC} \stackrel{\text{def}}{=} FER_{TC} - FER. \tag{2.83}$$

Since FER_{TC} depends upon altitude (free-stream temperature), free-stream Mach, and the FTA (hence vehicle state), so does $FERM_{TC}$. $FERM_{TC}$ measures FER control authority (or saturation margin) at a given time instant. It also measures the scramjet's ability to accelerate the vehicle. While an accurate FTA measurement may not be available, the $FERM_{TC}$ concept - when combined with measurements, models, and uncertainty bounds -

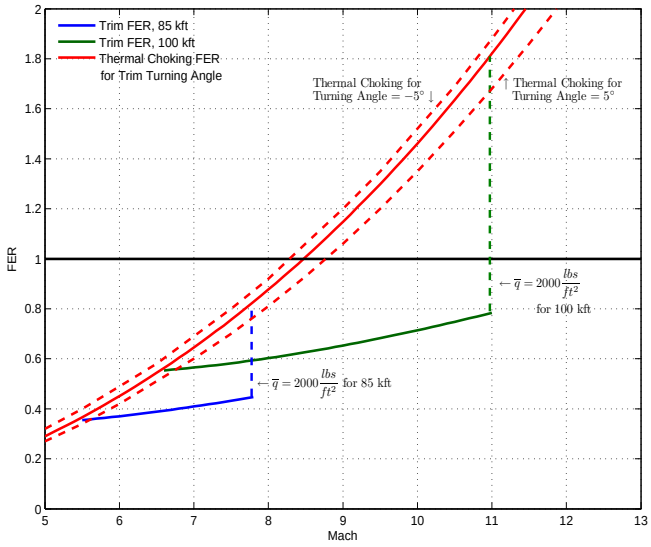

Figure 9: Visualization of FER Margins, Trim FER vs Mach for different altitudes, FER_{TC} vs Mach for different flow turning angles (FTAs)

could be very useful for controlling how close the scramjet gets to thermal choking; i.e. "to the edge of the cliff."

Trim FERM Properties. For a fixed FER, $FERM_{TC}$ exhibits behavior similar to the FER_{TC} (see above). Now suppose that FER is maintained at some trim FER and that the FTA is nearly constant; e.g. constant AOA and little flexing. For a nearly constant FTA and trim FER, $FERM^{FTA}_{TC_{trim\ fer}}$ decreases with decreasing Mach (altitude fixed), decreases with increasing altitude (Mach fixed), decreases with decreasing altitude and Mach along a constant $\bar{q}$ profile. Why is this? $FERM^{FTA}_{TC_{trim\ fer}}$ decreases with decreasing Mach because as Mach decreases, the FER_{TC} decreases faster than the trim FER; both decrease quadratically, but FER_{TC} decreases faster (Figure 9). It decreases with increasing altitude because as altitude increases, FER_{TC} remains constant while the trim FER increases. It decreases with decreasing altitude and Mach along a constant dynamic pressure profile because the trim FER decreases more slowly than FER_{TC} along such profiles. If one uses trim values, then one obtains $trim\ FERM_{TC} = \text{trim FER}_{\text{TC}} - \text{trim FER}$. Its dependence on the

flight condition is more difficult to analyze since the trim FTA changes with the flight condition.

Unity FER Margin. Within the model, thrust is linearly related to FER for all expected FER values - leveling off at (unrealistically) large FER values. In practice, when $FER > 1$, the result is decreased thrust. This phenomena is not captured in the model [3]. As such, control designs based on this model (or derived linear models) should try to maintain FER below unity. This motivates the instantaneous FER unity margin:

$$FERM_{unity} \stackrel{\text{def}}{=} 1 - \text{ FER}. \tag{2.84}$$

Figure 11 shows that if FER is set to a trim FER, then $FERM_{unity}^{trim\ fer}$ decreases with increasing Mach or increasing altitude because trim FER increases with Mach and altitude.

FER Margin ($FERM$). Given the above, it is reasonable to define the *instantaneous FER margin* $FERM$ as follows:

$$FERM \stackrel{\text{def}}{=} \min \{ FERM_{TC}, FERM_{unity} \}. \tag{2.85}$$

Alternatively, $FERM \stackrel{\text{def}}{=} \min \{ FER_{TC}, 1 \} - FER$. It should be emphasized that at any time instant the FERM depends on the system state (i.e. M_∞, altitude via T_∞, FTA). The trim FERM also depends on p_∞. The static nonlinear FERM map has been determined for our simple Rayleigh-based model. This "saturation" map is used when applying control laws to the nonlinear model to ensure that $FER > FER_{TC}$ is never applied. This is important because the simulation "crashes" if too large an FER is issued; i.e. hypersonic vehicles have low thrust margins [119].

Limitations of Analysis. The above is based on the simple 1D Rayleigh scramjet model being used. Thermal choking, strictly speaking, is not a 1D phenomena. Given this, the impact of 2D effects and finite-rate chemistry on estimating FERM will be examined in future work.

2.7.6 Internal Nozzle.

The exit properties $M_e = M_e(M_3, A_n, \gamma)$, $T_e = T_e(M_3, M_e, \gamma)$, $p_e = p_e(M_3, M_e, \gamma)$ of the scramjet's isentropic internal nozzle are founds as follows:

$$\frac{\left[1 + \frac{\gamma-1}{2} M_e^2\right]^{\frac{\gamma+1}{\gamma-1}}}{M_e^2} = A_n^2 \frac{\left[1 + \frac{\gamma-1}{2} M_3^2\right]^{\frac{\gamma+1}{\gamma-1}}}{M_3^2} \tag{2.86}$$

$$T_e = T_3 \left[\frac{1 + \frac{1}{2}(\gamma-1)M_3^2}{1 + \frac{1}{2}(\gamma-1)M_e^2}\right] \tag{2.87}$$

$$p_e = p_3 \left[\frac{1 + \frac{1}{2}(\gamma-1)M_3^2}{1 + \frac{1}{2}(\gamma-1)M_e^2}\right]^{\frac{\gamma}{\gamma-1}} \tag{2.88}$$

where $A_n \stackrel{\text{def}}{=} \frac{A_e}{A_3}$ is the internal nozzle area ratio (see Figure 6). $A_n = 6.35$ is used in the model.

Thrust due to Internal Nozzle. The purpose of the expanding internal nozzle is to recover most of the potential energy associated with the compressed (high pressure) supersonic flow. The thrust produced by the scramjet's internal nozzle is given by [82]

$$\text{Thrust}_{\text{internal}} = \dot{m}_a(v_e - v_\infty) + (p_e - p_\infty)A_e \tag{2.89}$$

where $\dot{m}_a$ is the air mass flow through the engine, v_e is the exit flow velocity, v_∞ is the free-stream flow velocity. p_e is the pressure at the engine exit plane, A_1 is the engine inlet area, A_e is the engine exit area, $v_e = M_e sos_e$, $v_\infty = M_\infty sos_\infty$, $sos_e = \sqrt{\gamma R T_e}$, $sos_\infty = \sqrt{\gamma R T_\infty}$, and R is the gas constant for air. Because we assume that the internal

nozzle to be symmetric, this internal thrust is always directed along the vehicle's body axis. The mass air flow into the inlet is given as follows:

$$\dot{m}_a = \begin{cases} p_\infty M_\infty \sqrt{\frac{\gamma}{RT_\infty}} \left[L_1 \frac{sin(\tau_{1l}-\alpha)}{tan(\tau_{1l})} + h_i cos(\alpha) \right] & \text{Oblique bow shock (swallowed by engine)} \\ p_\infty M_\infty \sqrt{\frac{\gamma}{RT_\infty}} h_i \left[\frac{sin(\theta_s) cos(\tau_{1l})}{sin(\theta_s - \alpha - \tau_{1l})} \right] & \text{Oblique bow shock - shock on lip} \\ p_\infty M_\infty \sqrt{\frac{\gamma}{RT_\infty}} h_i cos(\tau_{1l}) & \text{Lower forebody expansion fan} \end{cases} \tag{2.90}$$

2.7.7 External Nozzle.

The purpose of the expanding external nozzle is recover the rest of the potential energy associated with the compressed supersonic flow. A nozzle that is too short would not be long enough to recover the stored potential energy. In such a case, the nozzle's exit pressure would be larger than the free stream pressure and we say that it is under-expanded [82]. The result is reduced thrust. A nozzle that is too long would result in the nozzle's exit pressure being smaller than the free stream pressure and we say that it is over-expanded [82]. The result, again, is reduced thrust. When the nozzle length is "properly selected," the exit pressure is equal to the free stream pressure and maximum thrust is produced.

Plume Assumption. The engine's exhaust is bounded above by the aft body/nozzle and below by the shear layer between the gas and the free stream atmosphere. The two boundaries define the shape of the external nozzle, and the pressure distribution along the aftbody (Equation 2.67, page 45). Within [3, 81], a critical assumption is made regarding the shape of the external nozzle-and-plume in order to facilitate (i.e. speed up) the calculation of the aft body pressure distribution. The so-called "plume assumption" implies that the external nozzle-and-plume shape does not change with respect to the vehicle's body axes. This implies that the plume shape is independent of the flight condition. Our (limited) stud-

ies to date show that this assumption is suitable for preliminary trade studies but a higher fidelity aft body pressure distribution calculation is needed to understand how properties change over the trimmable region. This assumption is considered in more detail in [120]. In short, our fairly limited studies suggest that the plume assumption impacts static properties significantly while dynamic properties are only mildly impacted. The contribution of the external nozzle to the forces and moments acting on the vehicle have been discussed in section 2.4. In figure 10, we see how the actual pressure distribution along the aftbody compares to the plume approximation (vehicle trimmed at Mach 8, 85kft)

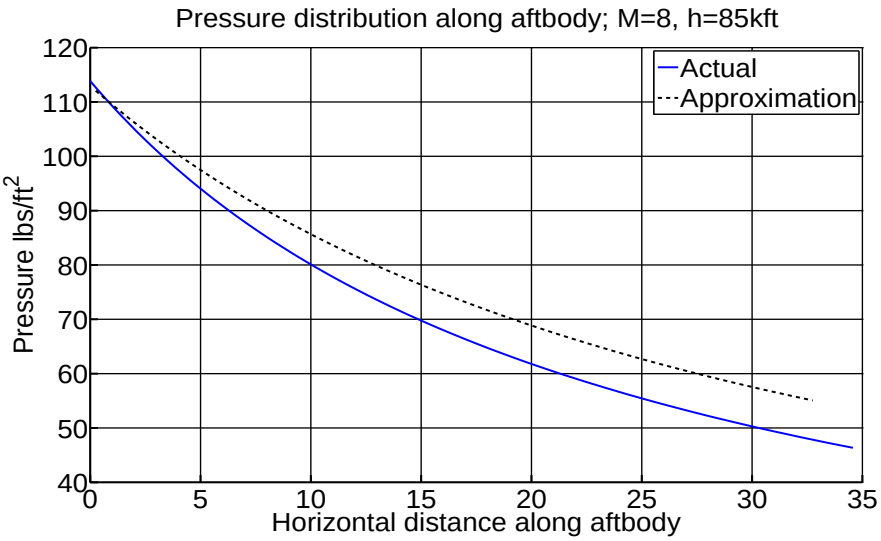

Figure 10: Aftbody pressure distribution: Plume vs. Actual

Within [121, 122] the authors say that the optimum nozzle length is about 7 throat heights. This includes the internal as well as the external nozzle. For our vehicle, the internal nozzle has no assigned length. This becomes an issue when internal losses are addressed. For the Bolender, et. al. model, the external nozzle length is 10.15 throat heights (with throat height $h_i = 3.25$ ft). For the new engine design presented later on in this research, the external nozzle length is 7.33 throat heights (with throat height $h_i = 4.5$ ft). The external nozzle contributes a force on the upper aft body. This force can be resolved into 2 components - the component along the fuselage water line is said to contribute to the

total thrust. This component is given by the expression:

$$\text{Thrust}_{\text{external}} = p_\infty L_a \left(\frac{p_e}{p_\infty}\right) \left[\frac{\ln\left(\frac{p_e}{p_\infty}\right)}{\frac{p_e}{p_\infty} - 1}\right] \tan(\tau_2 + \tau_{1U}). \tag{2.91}$$

Total Thrust. The total thrust is obtained by adding the thrust due to the internal and external nozzles.

2.8 Structure Modeling

Flexible Body Dynamics The natural frequencies and modes shapes for the flexible structure are computed using the assumed modes method. The assumed modes utilizes basis functions ω_i for the modes shapes of the vehicle that correspond to the analytical solution to the transverse vibration of a uniform free-free beam [1]. The assumed modes method is based on the following Lagrange equation

$$\frac{d}{dt}\left(\frac{\partial}{\partial \dot{q}_i}\right) - \frac{\partial T}{\partial q_i} = f_i, i = 1, \ldots, n \tag{2.92}$$

where T is the total kinetic energy of the system and V is the potential energy. Displacement along the structure is given by the following expansion

$$w(x,t) = \sum_{i=1}^{n} \Phi_i(x)\eta_i(t) \tag{2.93}$$

where $\eta_i(t)$ is the generalized modal coordinate.

The kinetic energy is given by

$$T = \frac{1}{2}\, \dot{\mathbf{w}}^T M \dot{\mathbf{w}} \tag{2.94}$$

where $\mathbf{w} = [w_1 \dots w_n]^T$ and

$$M = \begin{bmatrix} m_{11} & \dots & m_{1n} \\ \vdots & \ddots & \\ m_{n1} & & m_{nn} \end{bmatrix} \tag{2.95}$$

with

$$m_{ij} = \int_0^L \rho A(x) \Phi_i(x) \Phi_j(x) dx \tag{2.96}$$

where $\rho A(x)$ denotes the mass per unit length of the structure.

$$V = \frac{1}{2} \int_0^L EI(x) \left(\frac{\partial^2 w}{\partial x^2} \right)^2 dx \tag{2.97}$$

gives the matrix-vector expression

$$V = \frac{1}{2} \mathbf{w}^T K \mathbf{w} \tag{2.98}$$

where

$$K = \begin{bmatrix} k_{11} & \dots & k_{1n} \\ \vdots & \ddots & \\ k_{n1} & & k_{nn} \end{bmatrix} \tag{2.99}$$

with

$$k_{ij} = \int_0^L EI(x) \frac{\partial^2 \Phi_i(x)}{\partial x^2} \frac{\partial^2 \Phi_j(x)}{\partial x^2} dx \tag{2.100}$$

$$f_i(t) = \int_0^L p(x,t) \Phi_i(x) dx + \sum_{j=1}^{m} u_j(x_{sj}, t) \Phi_j(x_{sj}) \tag{2.101}$$

Forming the generalized force vector $\mathbf{f} = [f_1 \dots f_n]^T$, the n Langrange's Equations

result in

$$M\ddot{\mathbf{w}} + K\mathbf{w} = \mathbf{f} \tag{2.102}$$

The natural frequencies and mode shapes of the structure are obtained by setting $\mathbf{f} = \mathbf{0}$ and $\ddot{u} = -w^2 u$. The resulting eigenvalue problem is given as

$$\left(w^2 I - M^{-1}K\right)\mathbf{w} = \mathbf{0} \tag{2.103}$$

the square roots of the eigenvalues of $M^{-1}K$ are the resulting natural frequencies of the structure, while the corresponding mode shapes are just linear combinations of the assumed modes (Φ) with the coefficients given by the eigenvectors of $M^{-1}K$.

2.9 Summary and Conclusion

In this chapter, we considered a first principles nonlinear 3-DOF dynamical model for the longitudinal dynamics of a generic scramjet-powered hypersonic vehicle. The model attempted to capture interactions between the aerodynamics, the propulsion system and the flexible dynamics.

Simplifying assumptions (such as neglecting high-temperature gas dynamics, infinitely fast cowl door, out-of-plane loading, torsion, Timoshenko effects etc.) were made. The limitations of the model were discussed.

In subsequent chapters we shall consider trimming (section 3.2, page 63) and linearization (section 4.2, page 63) of the vehicle to analyze the static and dynamic properties of this model. A redesign of the engine will also be considered in order to improve performance and address geometric feasibility issues.

3. Static Properties of Vehicle

3.1 Overview

This chapter provides a trimming overview for the HSV, as well as an analysis on the static properties of the HSV over a range of flight conditions. Specifically what is shown is the equilibrium values required to trim the vehicle as Mach and altitude are varied throughout the air-breathing corridor.

Fundamental questions.

- Over what range of flight conditions can vehicle be trimmed? i.e. What is vehicles trimmable region?
- How do static trim properties vary over trimmable region?

Observations.

- Trimmable region limited by 3 effects:
  - Structural loading due to high dynamic pressure q = 2000 psf.
  - Thermal choking within engine (section 2.7.5, page 48, or [104]).
  - FER = 1 (section 2.7.5, page 48, or [104]).
- Many static properties are constant (or fairly constant) along lines of constant dynamic pressure (section 3.4, page 67).

Equilibrium of a general nonlinear system.

For a general nonlinear system, we have the following state space representation:

$$\dot{x}(t) \quad = \quad f(x(t), u(t)) \qquad\qquad x(0) = x_o \tag{3.1}$$

where

- $f \; = \; [\; f_1(x_1, \ldots, x_n, u_1, \ldots, u_m), \ldots, f_n(x_1, \ldots, x_n, u_1, \ldots, u_m) \;]^T \; \in \; \mathcal{R}^n$ - vector of n functions

- $u = [\ u_1, \ldots, u_m\ ]^T \in \mathcal{R}^m$ - vector of m input variables
- $x = [\ x_1, \ldots, x_n\ ]^T \in \mathcal{R}^n$ - vector of n state variables
- $x_o = [\ x_{1_o}, \ldots, x_{n_o}\ ]^T \in \mathcal{R}^n$ - vector of n initial conditions

(x_e, u_e) is an *equilibrium* or *trim* of the nonlinear system at t = 0 if

$$f(x, u) = 0 \qquad \text{for all } t \geq 0 \tag{3.2}$$

Trimming refers to finding system equilibria; i.e. state-control vector pairs (x_e, u_e) st $f(x_e, u_e) = 0$

3.2 Trimming

1. Choose Mach and altitude (within trimmable region).
2. Set pitch rate, flexible state derivatives to zero.
3. Set $\theta = \alpha$ (level flight or $\gamma = \theta - \alpha = 0^\circ$).
4. Solve for AOA, flexible states, controls (elevator, FER).

Trim Existence and Uniqueness Issues

- 2 controls, Rigid: given existence, trim solution is unique.
- 2 controls, Flexible: given existence, trim solution need not be unique.

Optimization-Based Approach

$$\min\ \dot{\mathbf{x}}^T\mathbf{Q}\dot{\mathbf{x}} + \mathbf{u}^T\mathbf{R}\mathbf{u} + \mathbf{F}^T\mathbf{Z}\mathbf{F} \tag{3.3}$$

where $\dot{x}$ is the derivatives of the state (we want them to be small at trim), u are the controls and F are the resultant forces in the x and z directions.

1. Entries within Q and Z control trim accuracy.
2. Entries within R used to control size of u.

3. Selection of (Q,R,Z) and initial guess (x, u) impacts convergence.

[Numerical Issues - (1) convergence, (2) solution steering under non-uniqueness]

Terminology

fmincon is a MATLAB routine used to solve nonlinear minimization problem in Equation (3.3) The routine employs a Trust Region Reflective Algorithm that uses finite differences to calculate search gradients/Hessians.

- Function Evaluation

  each time right hand side of Equation (3.3) is called

  - Requires one evaluation of nonlinear model.
  - Takes approx 0.005 seconds on 3 GHz Intel processor.

- Iteration

  process during which routine moves minimizer from x_n to x_{n+1}

  - Requires between 10 to 20 function evaluations per iteration.
  - Takes average of 0.1 seconds per iteration on a 3 GHz Intel processor.

3.2.1 Trim - Steps and Issues

Pros:

- Does not require analytic knowledge of gradient/Hessians
- Rapid convergence to solution (typically less than 30 iterations)
- Coded to handle multi-processor systems for increased computational speed
  - Gridding flight corridor every 0.1 Mach and 500 ft in altitude (10^4 points) requires $\sim$8 CPU hours.
  - Gridding flight corridor while studying 100 point parametric variation (10^6 points) requires $\sim$800 CPU hours.

  - Easily handled by Arizona State University High-Performance Computing Cluster (400 processors).

Cons:

- Many function evaluations are necessary to calculate gradient/Hessian for each iteration
  - Not a problem so long as nonlinear model is computationally "cheap" to evaluate
    - Suitable for control-relevant models based on algebraic equations and look-up tables.
    - Not suitable for models containing iterative methods (ODE/PDE solvers, CFD).
- Even initial guess that is close to minimizer does not guarantee convergence!
  - General problem with nonlinear minimization.
  - Easily handled by terminating routine after more than 50 iterations; then perturbing initial guess.
- Numerical Accuracy:
  - Increasing numerical accuracy by an order of magnitude increases number of function evaluations/iterations.
  - Relationship between numerical accuracy and total evaluations is still being investigated.
  - All previously listed specifications allow for an accuracy smaller than 10^{-3} for state derivatives.

3.3 Static Analysis: Trimmable Region

Within this work trim refers to a non-accelerating state; i.e. no translational or rotational acceleration. Moreover, all trim analysis has focused on level flight. Figure 11 shows the

level-flight trimmable region for the nominal vehicle being considered [2, 3, 11, 104, 107] (using the original nominal engine parameters). We are interested in how the static and dynamic properties of the vehicle vary across this region. Static properties of interest include: trim controls (FER and elevator), internal engine variables (e.g. temperature and pressure), thrust, thrust margin, AOA, L/D. Dynamic properties of interest include: vehicle instability and RHP transmission zero associated with FPA. Understanding how these properties vary over the trimmable region is critical for designing a robust nonlinear (gain-scheduled/adaptive) control system that will enable flexible operation. For example, consider a TSTO flight. The mated vehicles might fly up along $\overline{q} = 2000$ psf to a desired altitude, then conduct a pull-up maneuver to reach a suitable staging altitude [108].

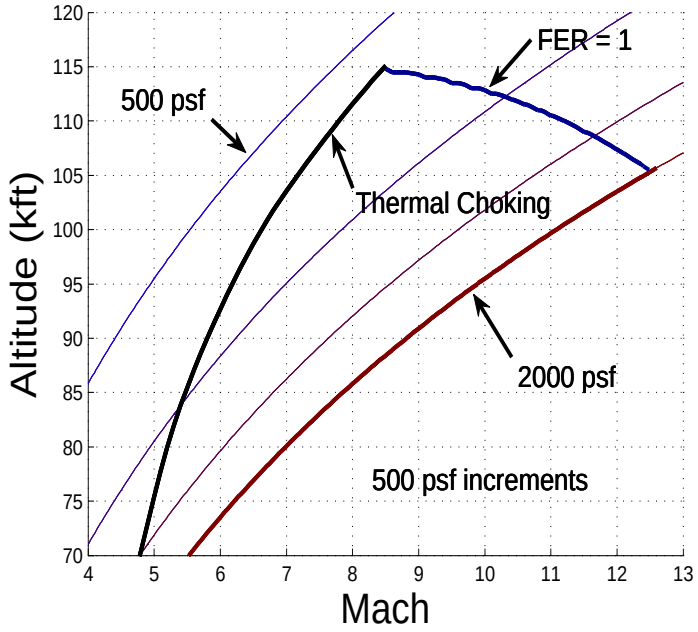

Figure 11: Visualization of Trimmable Region: Level-Flight, Unsteady-Viscous Flow, Flexible Vehicle

3.4 Static Analysis: Nominal Properties

3.4.1 Static Analysis: Trim FER

The following figures show the variations in the trim FER across the flight envelope, and for different Mach and altitudes.

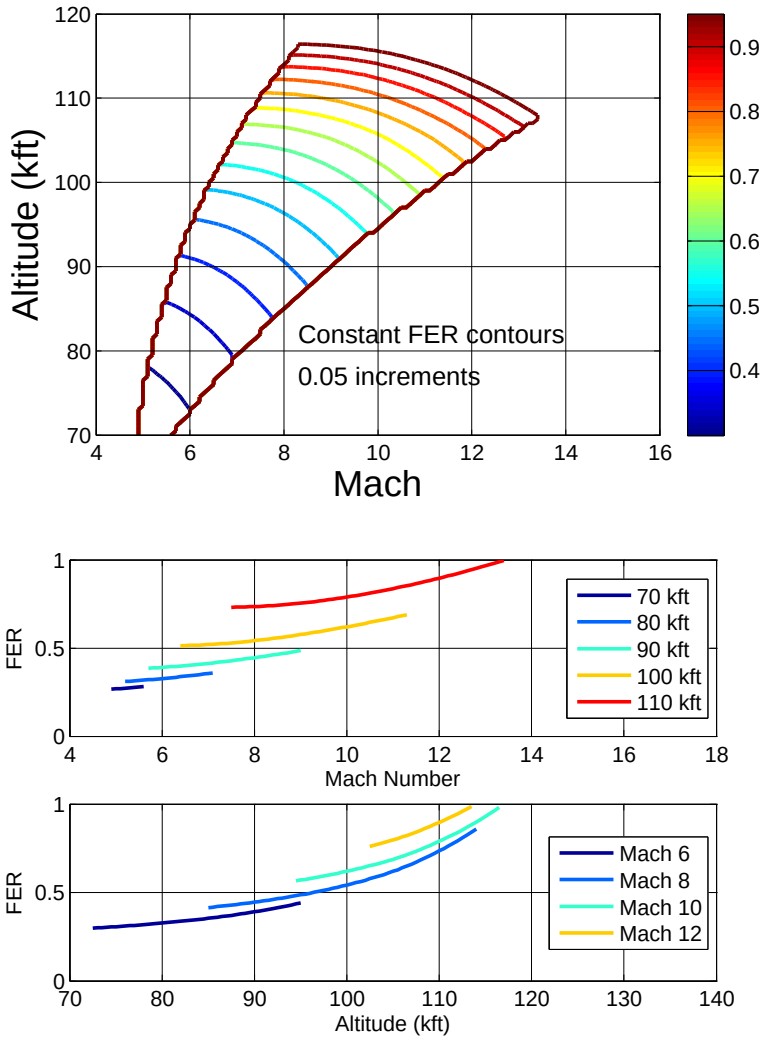

Figure 12: Trim FER: Level Flight, Unsteady-Viscous Flow, Flexible Vehicle

- FER increases monotonically with increasing mach/altitude

3.4.2 Static Analysis: Trim Elevator

The following figures show the variations in the trim elevator across the flight envelope, and for different Mach and altitudes.

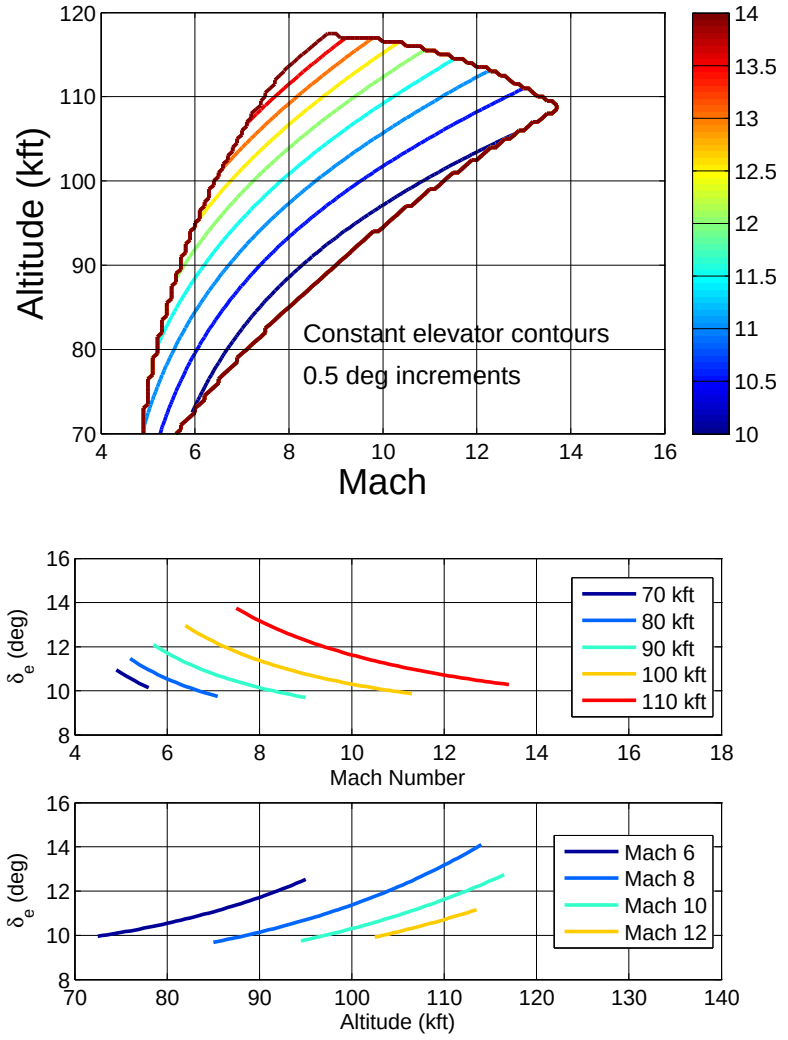

Figure 13: Trim Elevator: Level Flight, Unsteady-Viscous Flow, Flexible Vehicle

- Elevator deflection is fairly constant for constant dynamic pressures
- Elevator deflection decreases monotonically with increasing mach
- Elevator deflection increases monotonically with increasing altitude

3.4.3 Static Analysis: Trim Angle-of-Attack

The following figures show the variations in the trim angle-of-attack across the flight envelope, and for different Mach and altitudes.

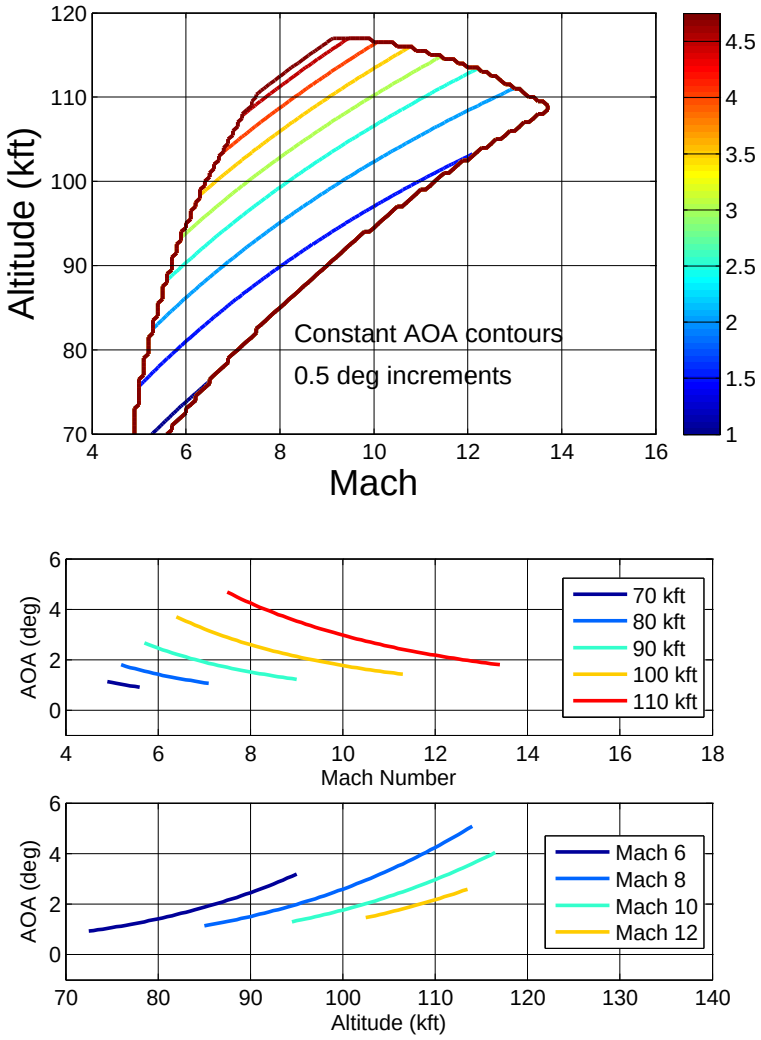

Figure 14: Trim AOA: Level Flight, Unsteady-Viscous Flow, Flexible Vehicle

- AOA is fairly constant for constant dynamic pressures
- AOA decreases monotonically with increasing mach
- AOA increases monotonically with increasing altitude

3.4.4 Static Analysis: Trim Forebody Deflection

The following figures show the variations in the trim forebody deflection across the flight envelope, and for different Mach and altitudes.

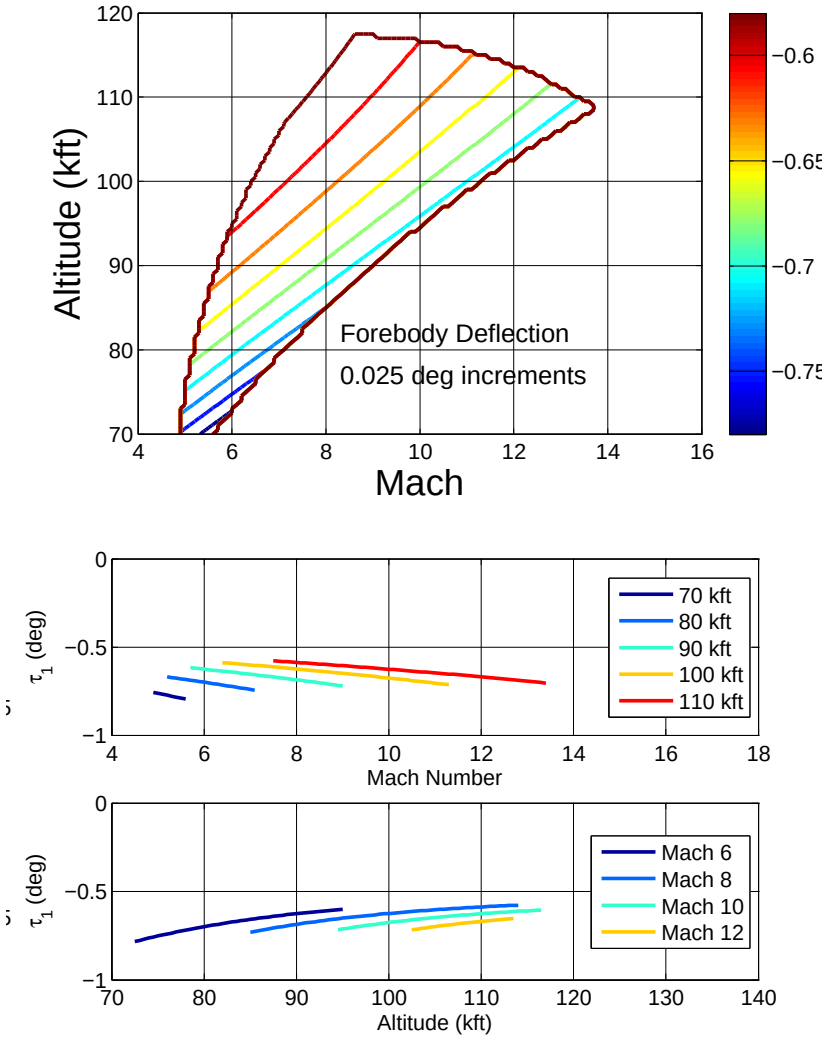

Figure 15: Trim Forebody Deflections: Level Flight, Unsteady-Viscous Flow, Flexible Vehicle

- Forebody deflections $< 1^\circ$ across the flight envelope
- Forebody deflections increase with increasing mach/decreasing altitude

3.4.5 Static Analysis: Trim Aftbody Deflection

The following figures show the variations in the trim aftbody deflection across the flight envelope, and for different Mach and altitudes.

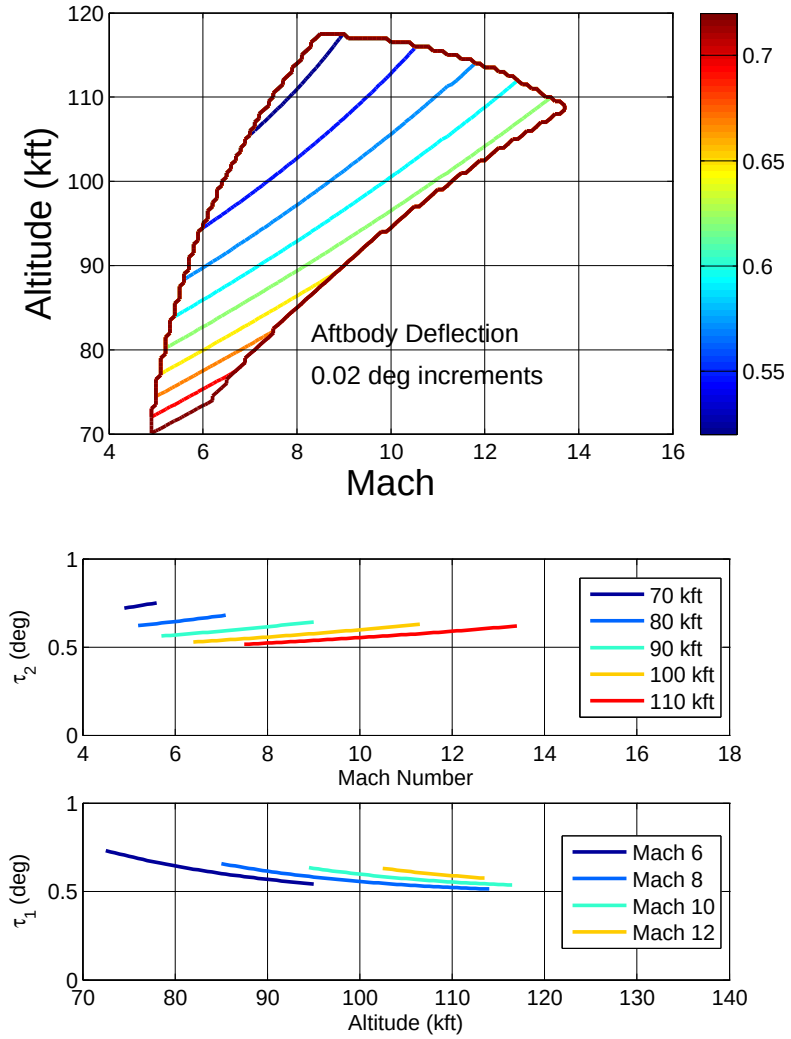

Figure 16: Trim Aftbody Deflections: Level Flight, Unsteady-Viscous Flow, Flexible Vehicle

- Aftbody deflections $< 1^{\circ}$ across the flight envelope
- Aftbody deflections increase with increasing mach/decreasing altitude

3.4.6 Static Analysis: Trim Drag

The following figures show the variations in the trim drag across the flight envelope, and for different Mach and altitudes.

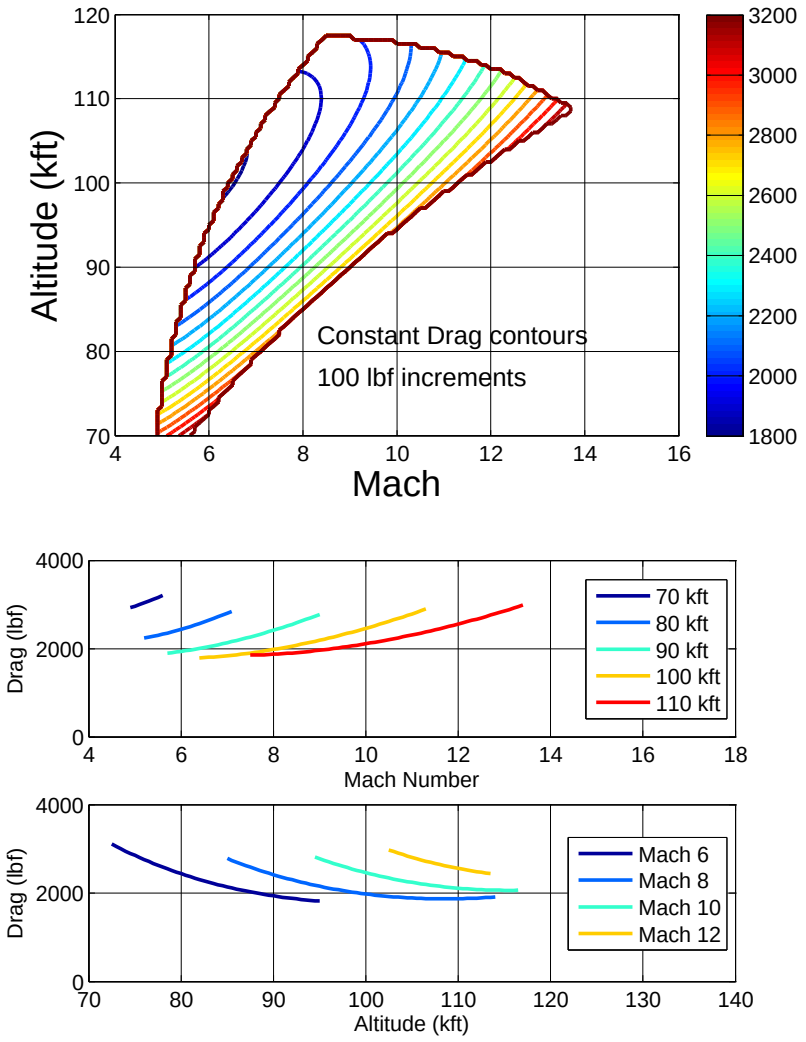

Figure 17: Trim Drag: Level Flight, Unsteady-Viscous Flow, Flexible Vehicle

- Drag increases with increasing mach
- Drag decreases with increasing altitude

3.4.7 Static Analysis: Trim Drag (Inviscid)

The following figures show the variations in the trim inviscid drag across the flight envelope, and for different Mach and altitudes.

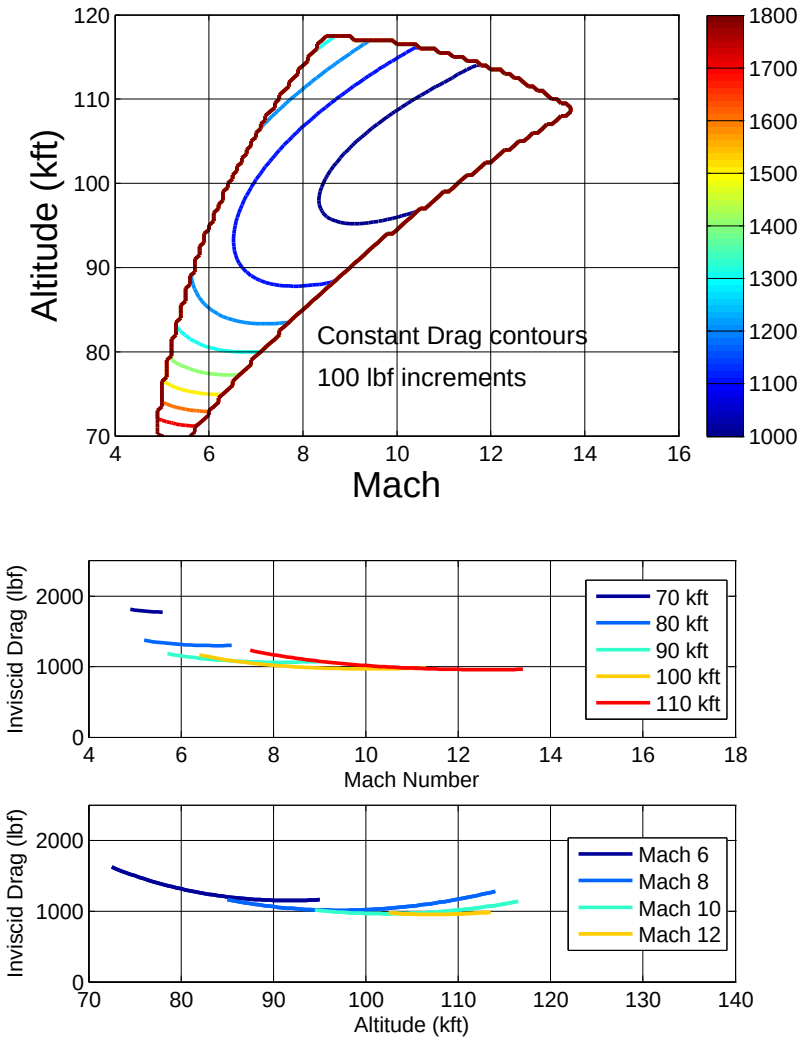

Figure 18: Trim Drag (Inviscid): Level Flight, Unsteady-Viscous Flow, Flexible Vehicle

- Inviscid drag decreases with increasing mach (due to decreasing AOA)
- Inviscid drag behaves nonlinearly with increasing altitude

3.4.8 Static Analysis: Trim Drag (Viscous)

The following figures show the variations in the trim viscous drag across the flight envelope, and for different Mach and altitudes.

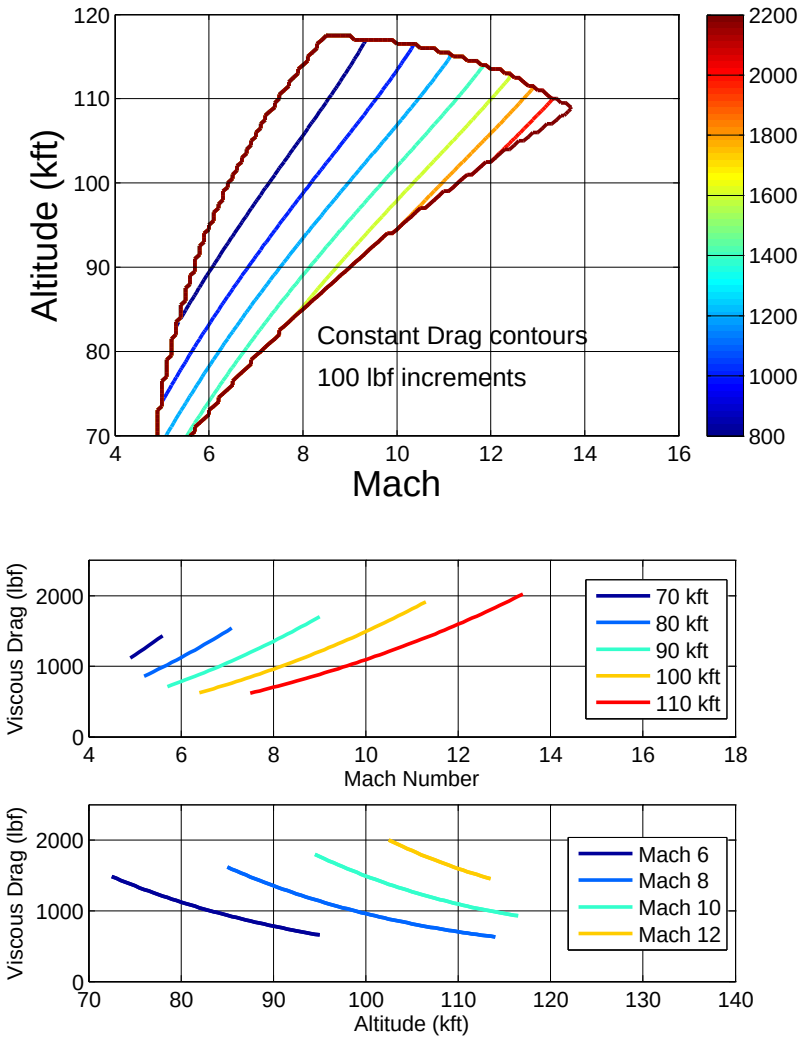

Figure 19: Trim Drag (Viscous): Level Flight, Unsteady-Viscous Flow, Flexible Vehicle

- Viscous drag increases with increasing mach
- Viscous drag decreases with increasing altitude

3.4.9 Static Analysis: Trim Drag Ratio (Viscous/Total)

The following figures show the variations in the ratio of the viscous drag to total drag across the flight envelope (at trim), and for different Mach and altitudes.

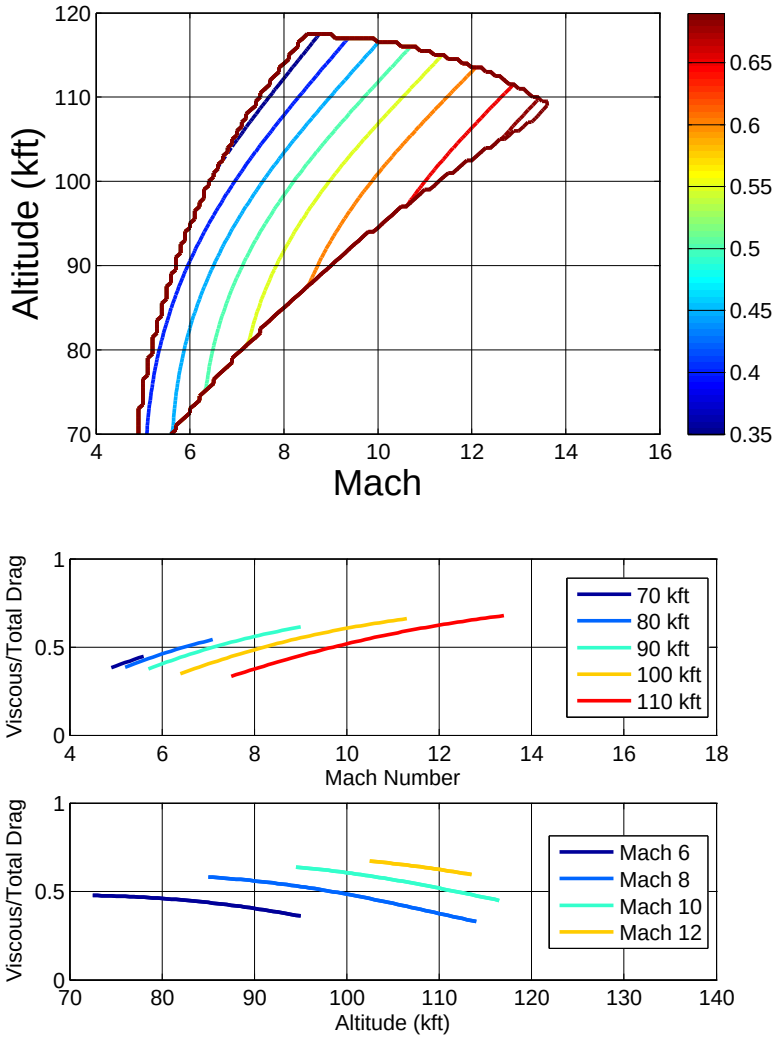

Figure 20: Trim Drag Ratio (Viscous/Total): Level Flight, Unsteady-Viscous Flow, Flexible Vehicle

- Drag ratio increases with increasing mach
- Drag ratio decreases with increasing altitude

3.4.10 Static Analysis: Trim L/D Ratio

The following figures show the variations in the trim lift-to-drag ratio across the flight envelope, and for different Mach and altitudes.

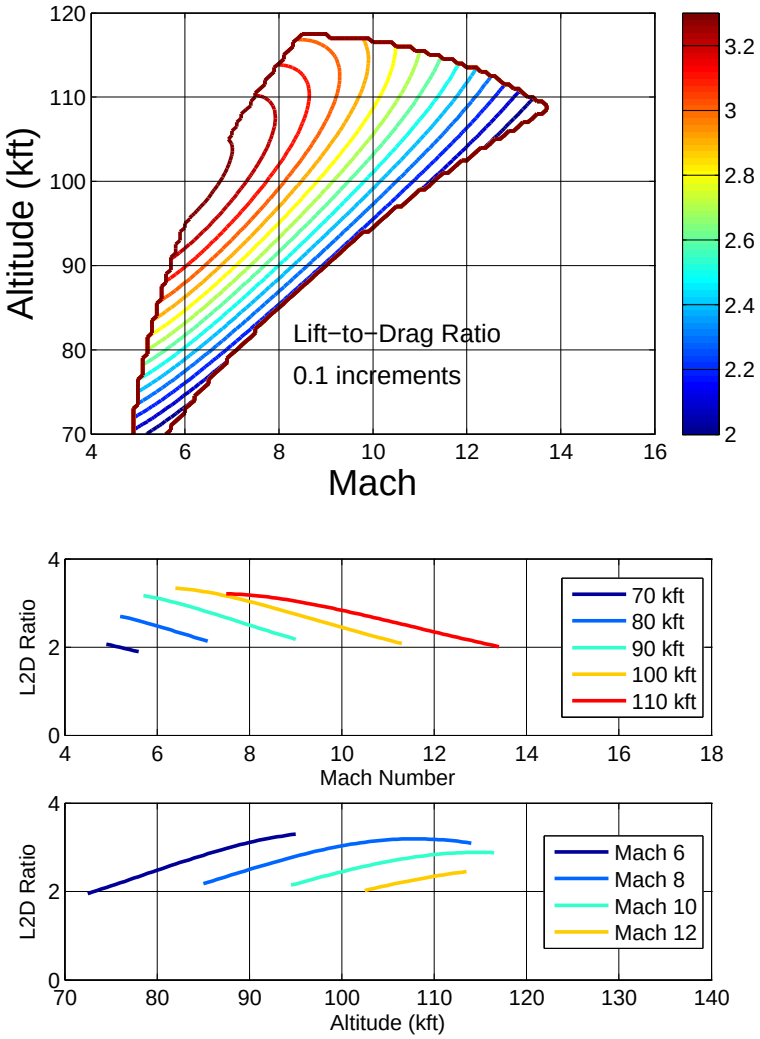

Figure 21: Trim L/D Ratio: Level Flight, Unsteady-Viscous Flow, Flexible Vehicle

- Lift-to-Drag decreases with increasing mach
- Lift-to-Drag generally increases with increasing altitude
- Lift-to-Drag is maximized at Mach 6.4, 100 kft

3.4.11 Static Analysis: Trim Elevator Force

The following figures show the variations in the trim force on the elevator across the flight envelope, and for different Mach and altitudes.

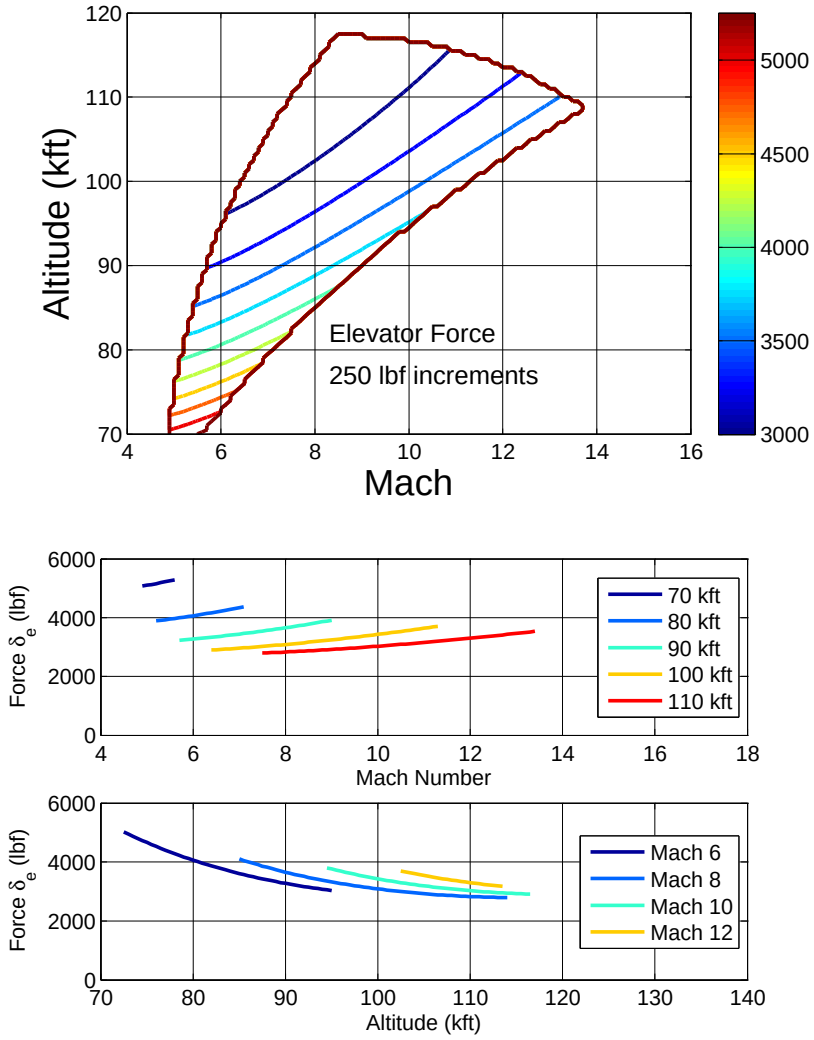

Figure 22: Trim Elevator Force: Level Flight, Unsteady-Viscous Flow, Flexible Vehicle

- Elevator resultant force increases linearly with increasing mach
- Elevator resultant force decreases with increasing altitude

3.4.12 Static Analysis: Trim Combustor Mach

The following figures show the variations in the trim Mach at the combustor exit across the flight envelope, and for different Mach and altitudes.

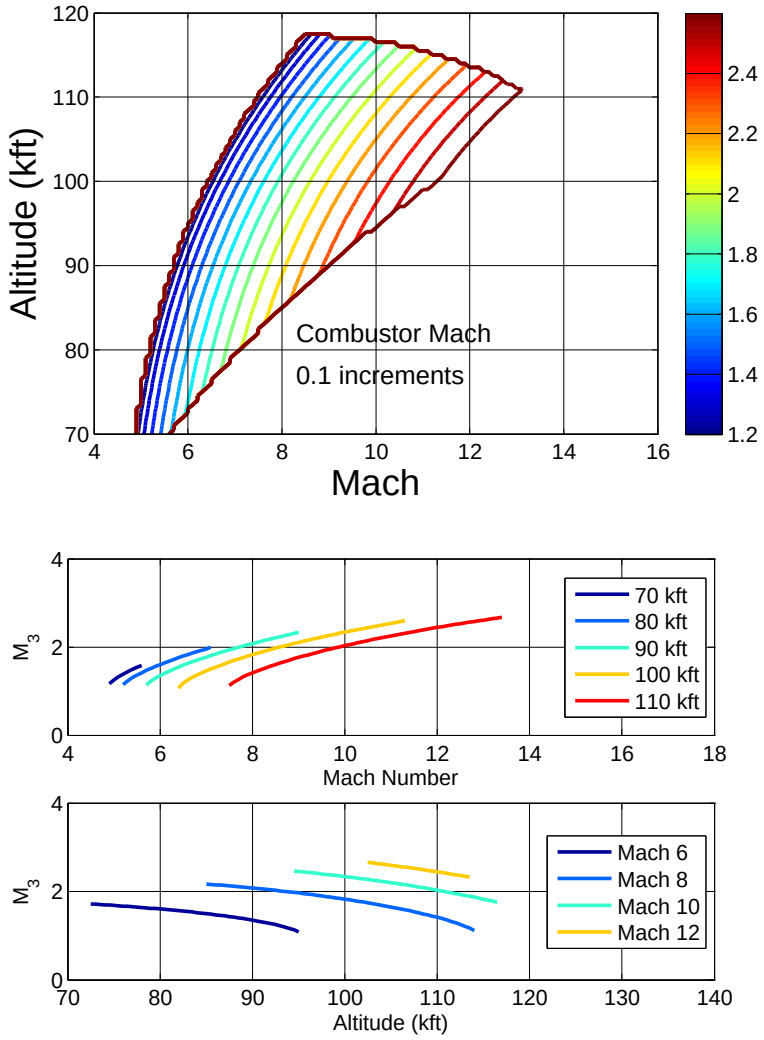

Figure 23: Trim Combustor Mach: Level Flight, Unsteady-Viscous Flow, Flexible Vehicle

- M_3 never goes below 1
- M_3 increases with increasing Mach
- M_3 decreases with increasing altitude

3.4.13 Static Analysis: Trim Combustor Temp.

The following figures show the variations in the trim temperature at the combustor exit (after fuel addition) across the flight envelope, and for different Mach and altitudes.

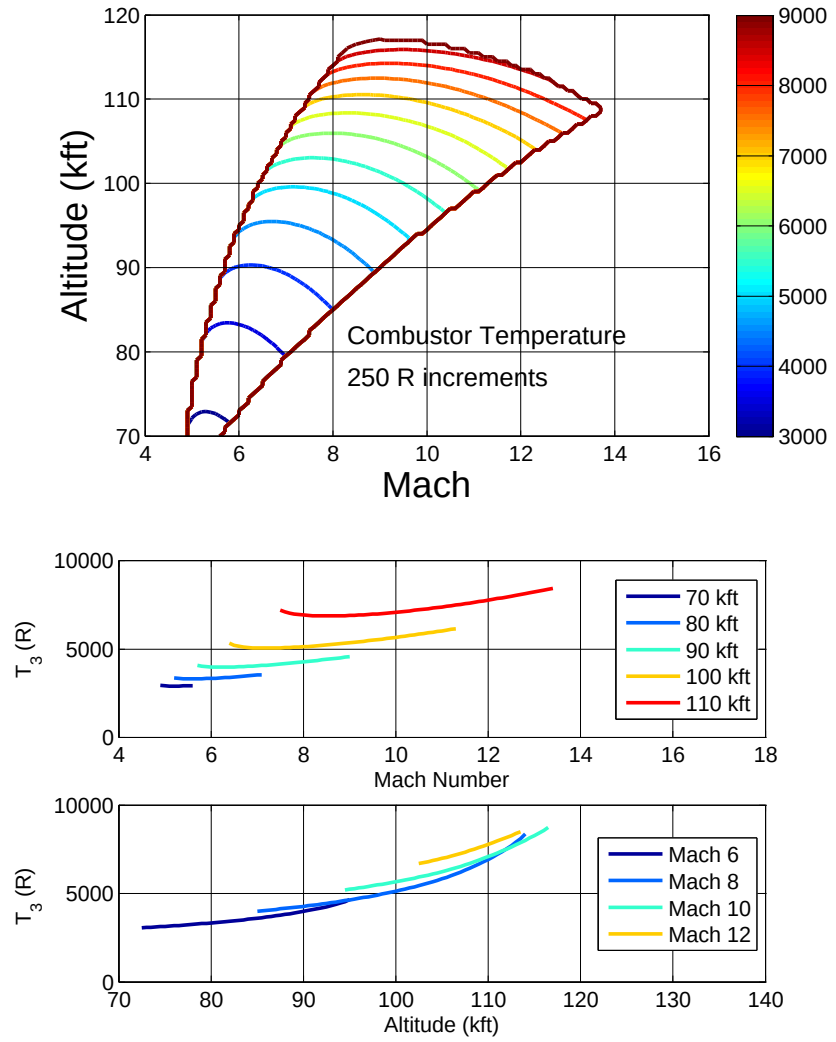

Figure 24: Trim Combustor Temp.: Level Flight, Unsteady-Viscous Flow, Flexible Vehicle

- T_3 displays similar behavior to the FER
- T_3 decreases slightly, then increases with increasing Mach
- T_3 increases with increasing altitude

3.4.14 Static Analysis: Trim Fuel Mass Flow

The following figures show the variations in the trim fuel mass flow across the flight envelope, and for different Mach and altitudes.

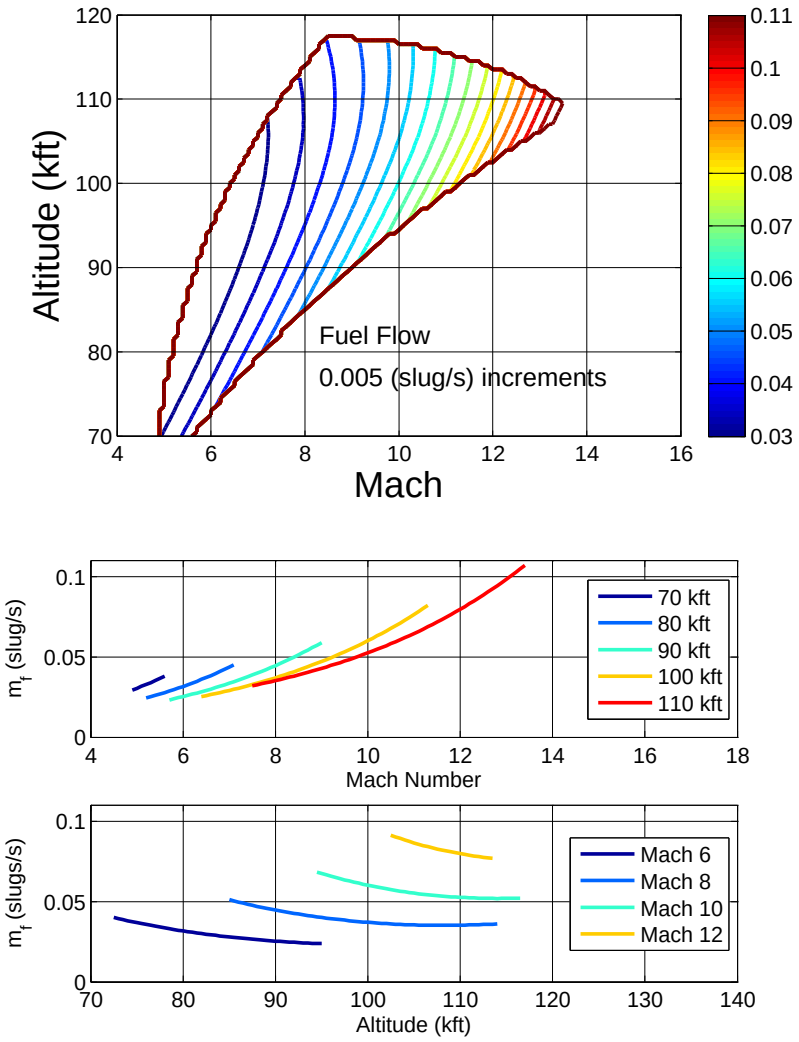

Figure 25: Trim Fuel Mass Flow: Level Flight, Unsteady-Viscous Flow, Flexible Vehicle

- $\dot{m}_f$ increases with increasing Mach
- $\dot{m}_f$ generally decreases with increasing altitude

3.4.15 Static Analysis: Trim Internal Nozzle Mach

The following figures show the variations in the trim Mach at the internal nozzle exit across the flight envelope, and for different Mach and altitudes.

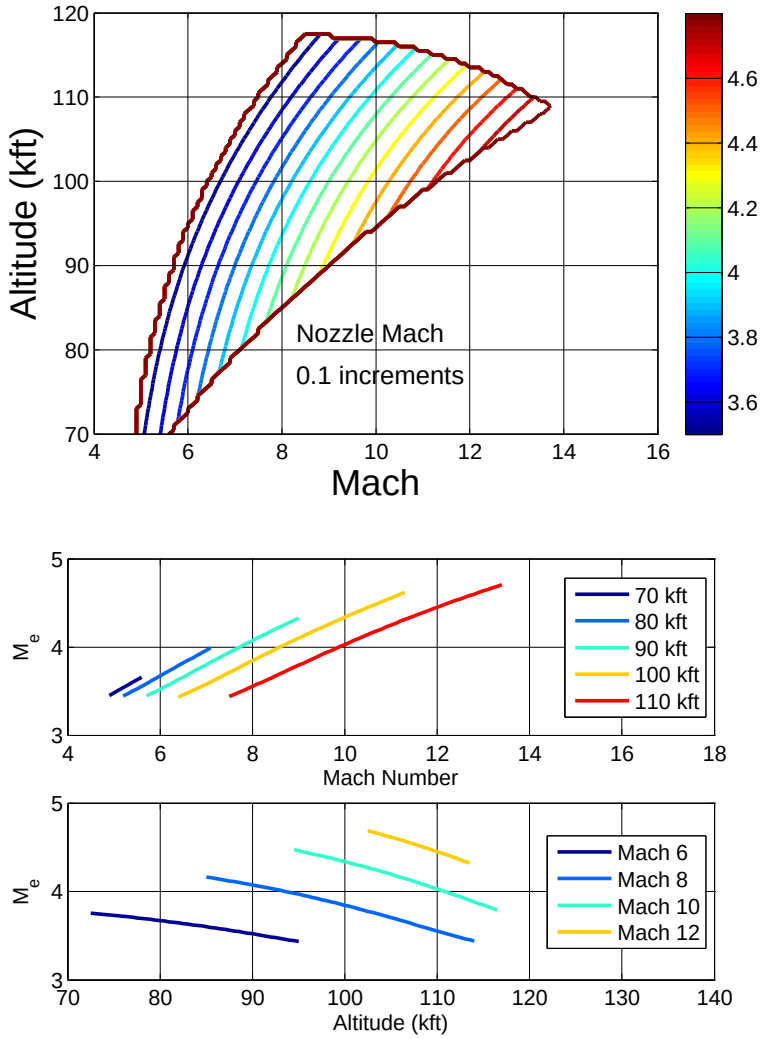

Figure 26: Trim Internal Nozzle Mach: Level Flight, Unsteady-Viscous Flow, Flexible Vehicle

- M_e increases fairly linearly with increasing Mach
- M_e decreases with increasing altitude

3.4.16 Static Analysis: Trim Internal Nozzle Temp.

The following figures show the variations in the trim temperature at the internal nozzle exit across the flight envelope, and for different Mach and altitudes.

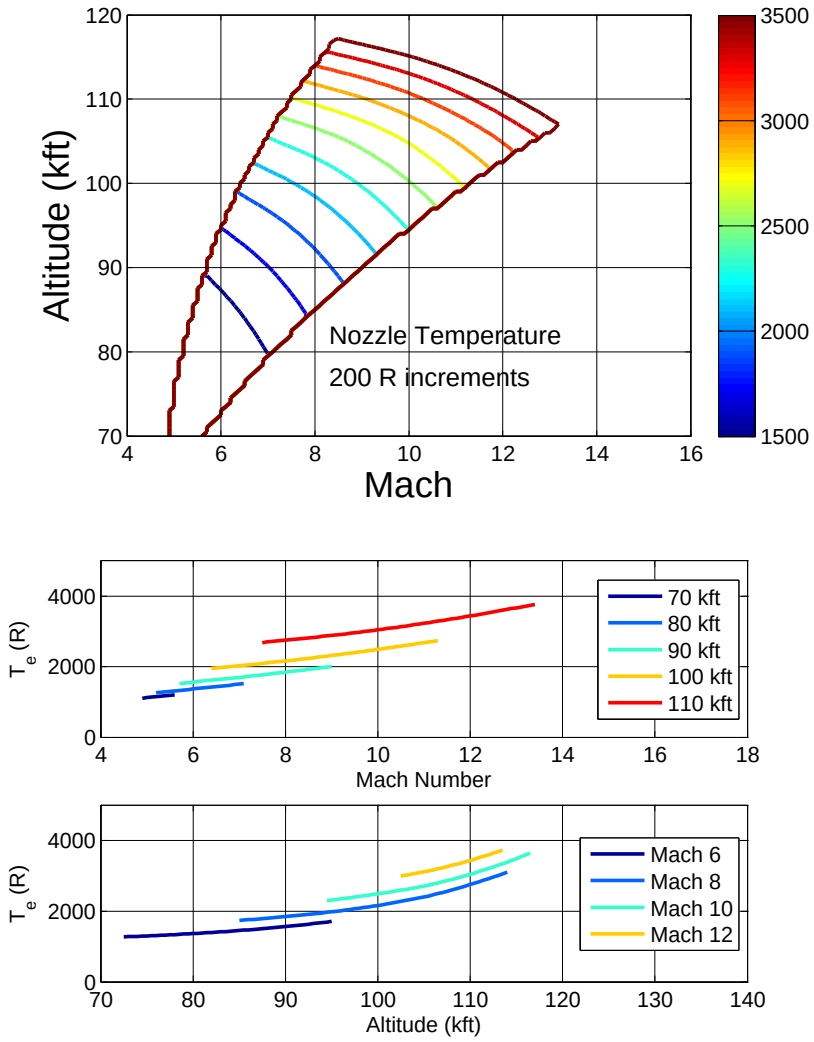

Figure 27: Trim Internal Nozzle Temp.: Level Flight, Unsteady-Viscous Flow, Flexible Vehicle

- T_e increases slightly with increasing Mach
- T_e increases with increasing altitude

3.4.17 Static Analysis: Trim Reynolds Number

The following figures show the variations in the trim Reynolds number across the flight envelope, and for different Mach and altitudes.

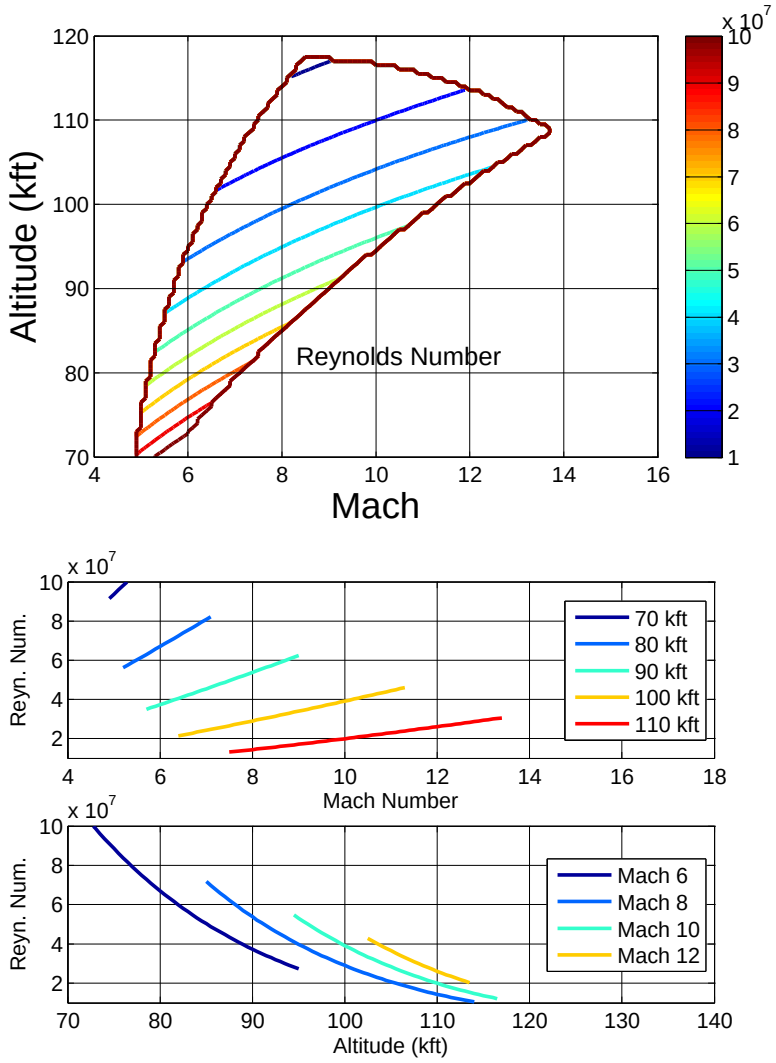

Figure 28: Trim Reynolds Number: Level Flight, Unsteady-Viscous Flow, Flexible Vehicle

- Reynolds Number increases linearly with increasing Mach
- Reynolds Number decreases with increasing altitude

3.4.18 Static Analysis: Trim Absolute Viscosity

The following figures show the variations in the trim absolute viscosity across the flight envelope, and for different Mach and altitudes.

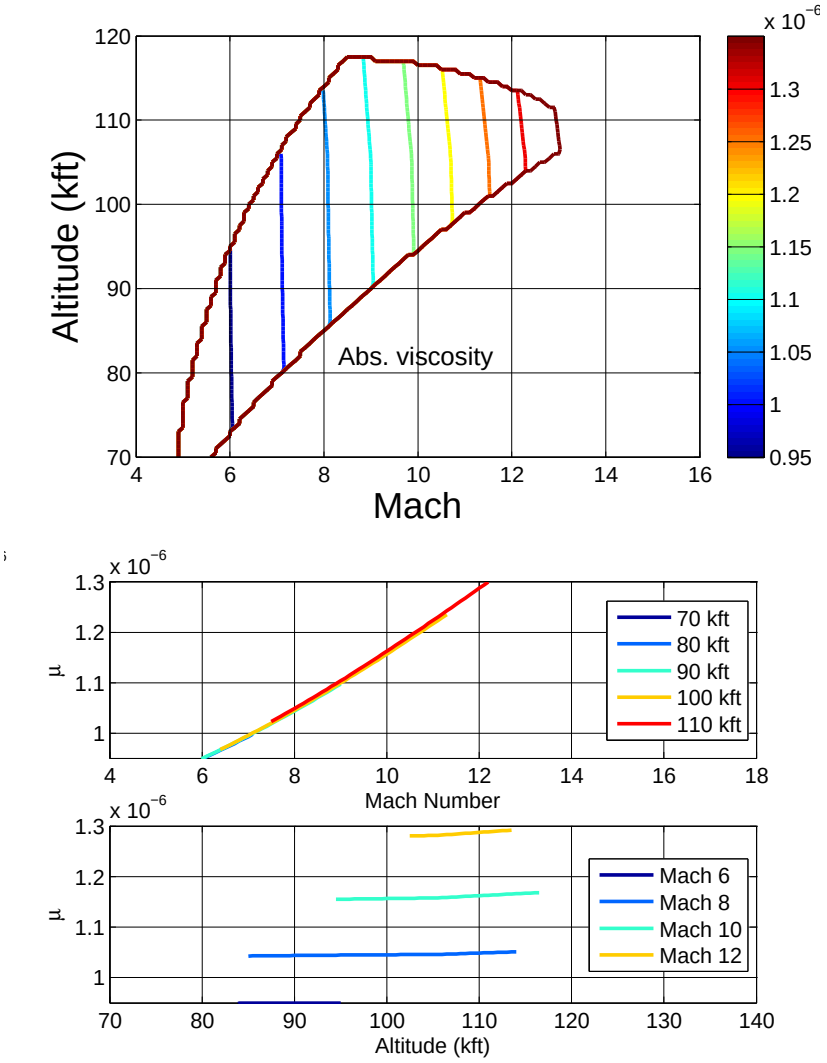

Figure 29: Trim Absolute Viscosity: Level Flight, Unsteady-Viscous Flow, Flexible Vehicle

- Absolute viscosity increases with increasing Mach
- Absolute viscosity is fairly constant w.r.t. increasing altitude

3.4.19 Static Analysis: Trim Kinematic Viscosity

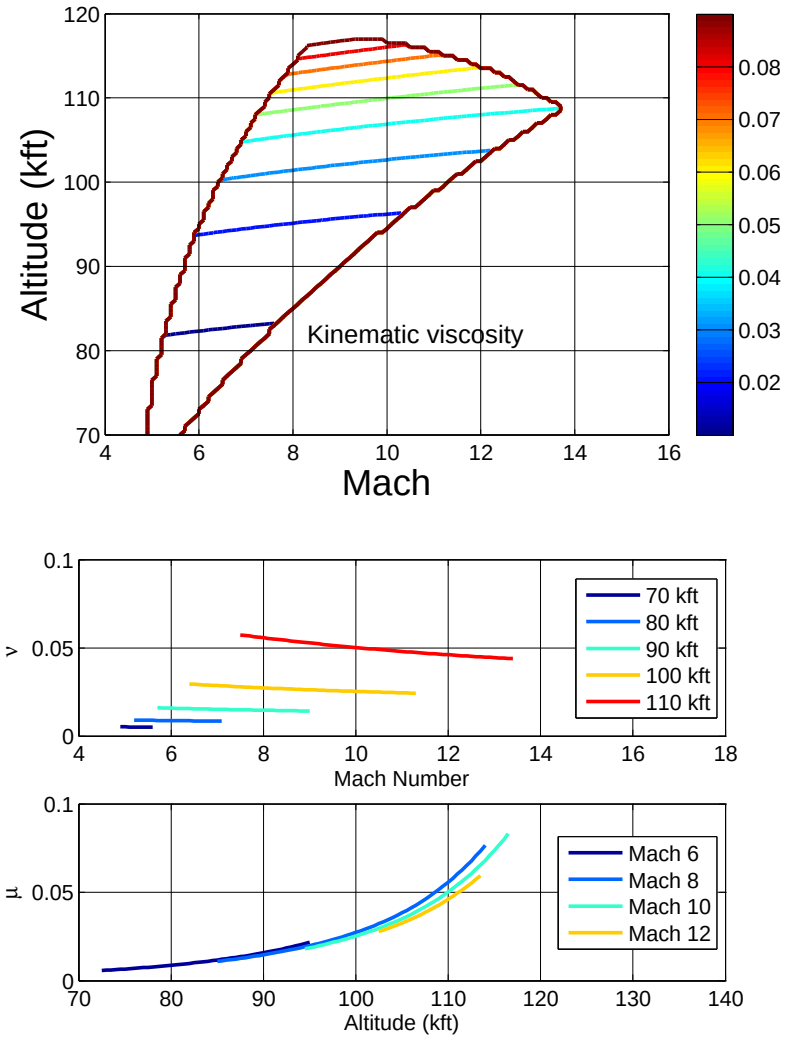

Figure 30: Trim Kinematic Viscosity: Level Flight, Unsteady-Viscous Flow, Flexible Vehicle

- Kinematic viscosity is fairly constant with increasing Mach (slight decrease at higher altitudes)
- Kinematic viscosity increases exponentially with increasing altitude

3.5 Summary and Conclusion

In this chapter the trimming algorithm was presented (a constrained optimization was used), and implementation of the algorithm (and its limitations) were discussed. Additionally the range of flight conditions over which the nominal vehicle can be trimmed was presented, and the variation in the trim properties in the region were presented.

The trimming algorithm will subsequently be used for performing trade studies in later chapters, and for vehicle optimization. The robustness of the algorithm is hence of importance, as it must be able to handle a variety of vehicle configurations and flight conditions.

Once the vehicle is trimmed at a given flight condition, lineaization at the equilibrium provides a model that can be used for linear system control design. The next chapter considers the linearization algorithm and the various dynamic properties of the system at different operating points.

4. Dynamic Properties

4.1 Overview

In this chapter, the linearization procedure for the HSV model is presented. Variations in the dynamic properties over the envelope are then examined. The following properties are examined:

- RHP Pole, RHP Zero, RHP Zero/Pole ratio variations
- Bode magnitude, phase responses
- Modal analysis
- Singular value decompositions

Fundamental questions.

- How do dynamic properties of vehicle vary over trimmable region?

Observations.

- Both instability and RHP zero tend to be constant along lines of constant dynamic pressure.

Linearization of a general dynamic system.

For a general nonlinear system, we have the following state space representation:

$$\dot{x}(t) = f(x(t), u(t)) \qquad x(0) = x_o \tag{4.1}$$

$$y(t) = g(x(t), u(t)) \tag{4.2}$$

where

- $f = [\ f_1(x_1, \ldots, x_n, u_1, \ldots, u_m), \ldots, f_n(x_1, \ldots, x_n, u_1, \ldots, u_m)\ ]^T \in \mathcal{R}^n$ - vector of n functions
- $g = [\ g_1(x_1, \ldots, x_n, u_1, \ldots, u_m), \ldots, g_p(x_1, \ldots, x_n, u_1, \ldots, u_m)\ ]^T \in \mathcal{R}^p$ - vector of p functions

- $u = [\ u_1, \ldots, u_m\ ]^T \in \mathcal{R}^m$ - vector of m input variables
- $x = [\ x_1, \ldots, x_n\ ]^T \in \mathcal{R}^n$ - vector of n state variables
- $x_o = [\ x_{1_o}, \ldots, x_{n_o}\ ]^T \in \mathcal{R}^n$ - vector of n initial conditions.
- $y = [\ y_1, \ldots, y_n\ ]^T \in \mathcal{R}^p$ - vector of p outputs

(x_e, u_e) is an *equilibrium* or *trim* of the nonlinear system at t = 0 if

$$f(x_e, u_e) = 0 \qquad \forall\ t \geq 0 \tag{4.3}$$

Trimming refers to finding system equilibria; i.e. state-control vector pairs (x_e, u_e) st $\dot{x}_e = f(x_e, u_e) = 0$

A linear state space representation (ssr) which approximates the nonlinear system near (x_e, u_e) is obtained:

$$\delta\dot{x}(t) = A\delta x(t) + B\delta u(t) \qquad \delta x(0) = \delta x_o \tag{4.4}$$

$$\delta y(t) = C\delta x(t) + D\delta u(t) \tag{4.5}$$

where

$$A = \left[\begin{array}{ccc} \frac{\partial f_1}{\partial x_1} & \cdots & \frac{\partial f_1}{\partial x_n} \\ \vdots & \vdots & \vdots \\ \frac{\partial f_n}{\partial x_1} & \cdots & \frac{\partial f_n}{\partial x_n} \end{array}\right]_{(x_e,u_e)} \qquad B = \left[\begin{array}{ccc} \frac{\partial f_1}{\partial u_1} & \cdots & \frac{\partial f_1}{\partial u_m} \\ \vdots & \vdots & \vdots \\ \frac{\partial f_n}{\partial u_1} & \cdots & \frac{\partial f_n}{\partial u_m} \end{array}\right]_{(x_e,u_e)} \tag{4.6}$$

$$C = \left[\begin{array}{ccc} \frac{\partial g_1}{\partial x_1} & \cdots & \frac{\partial g_1}{\partial x_n} \\ \vdots & \vdots & \vdots \\ \frac{\partial g_p}{\partial x_1} & \cdots & \frac{\partial g_p}{\partial x_n} \end{array}\right]_{(x_e,u_e)} \qquad D = \left[\begin{array}{ccc} \frac{\partial g_1}{\partial u_1} & \cdots & \frac{\partial g_1}{\partial u_m} \\ \vdots & \vdots & \vdots \\ \frac{\partial g_p}{\partial u_1} & \cdots & \frac{\partial g_p}{\partial u_m} \end{array}\right]_{(x_e,u_e)} \tag{4.7}$$

$$\delta u(t) \stackrel{\text{def}}{=} u(t) - u_e \qquad \delta x(t) \stackrel{\text{def}}{=} x(t) - x_e \qquad \delta x_o \stackrel{\text{def}}{=} x_o - x_e$$

$$\delta y(t) \stackrel{\text{def}}{=} y(t) - y_e \qquad y_e \stackrel{\text{def}}{=} g(x_e, u_e)$$

4.2 Linearization - Steps and Issues

Since analytic expressions for the partial derivatives listed in equation 4.1 are not available, they must be approximated numerically using finite differences.

The standard centralized finite difference has been implemented:

$$\frac{df}{dx} = \frac{f(x + \Delta x) - f(x - \Delta x)}{2\Delta x} \tag{4.8}$$

Consider the simple example where

$$f = sin(x) \tag{4.9}$$

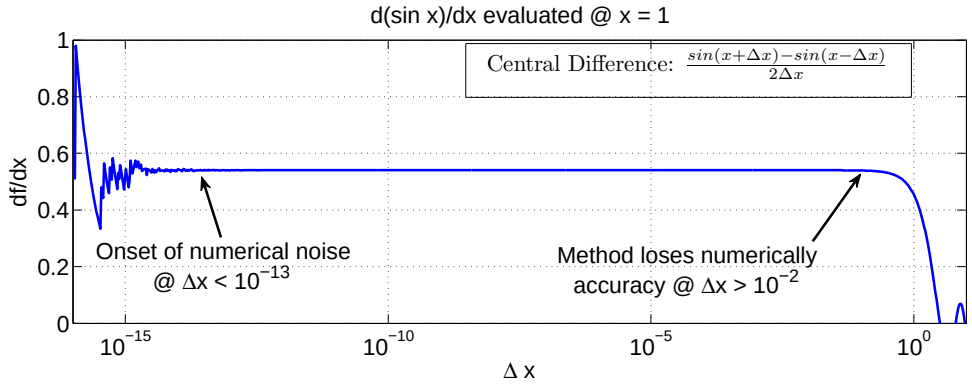

Figure 31: Simple Linearization Example

- For the simple example, step size bounds must be between $[10^{-13}\ 10^{-2}]$
- In general, for the complex nonlinear model the bounds are small: $[10^{-5}\ 10^{-3}]$

- Bounds may vary for each element of equation 4.1.
- Bounds may vary based on operating point.
- Blind implementation of MATLAB *linmod* command will not take this into account.

Based on the equations of motion (2.1-2.6), we define the following accelerations:

$$X = \frac{T\cos(\alpha) - D}{m} \tag{4.10}$$

$$Z = -\frac{T\sin(\alpha) + L}{m} \tag{4.11}$$

$$\mathscr{M} = \frac{M}{I_{yy}} \tag{4.12}$$

where L is the lift, D is the drag, T is the thrust, M is the moment, α is the angle of attack, m is the mass of the vehicle and I_{yy} is the moment of inertia.

We construct a model with the following states and controls

- $\mathbf{x} = [V_t \;\; \alpha \;\; Q \;\; h \;\; \theta \;\; \eta \;\; \dot{\eta} \;\; \cdots]^T$ (we may extend the vector x to include as many flexible modes as required. Below we use three flexible states and their derivatives)
- $\mathbf{u} = [\delta_e \;\; \delta_\phi]^T$ (we are considering a two control model with only the elevator and the FER as inputs)

Below, we provide a ssr for the linearized model [9]

$$\mathbf{A} = \begin{bmatrix}
X_v & X_\alpha & 0 & X_h & -g & X_{\eta_1} & 0 & \dots & X_{\eta_3} & 0 \\
\frac{Z_v}{V_{T_0}} & \frac{Z_\alpha}{V_{T_0}} & 1-\frac{Z_Q}{V_{T_0}} & \frac{Z_h}{V_{T_0}} & 0 & \frac{Z_{\eta_1}}{V_{T_0}} & 0 & \dots & \frac{Z_{\eta_3}}{V_{T_0}} & 0 \\
\mathscr{M}_v & \mathscr{M}_\alpha & \mathscr{M}_Q & \mathscr{M}_h & 0 & \mathscr{M}_{\eta\, h} & 0 & \dots & \mathscr{M}_{\eta\, h} & 0 \\
0 & -V_0 & 0 & 0 & V_0 & 0 & 0 & \dots & 0 & 0 \\
0 & 0 & 1 & 0 & 0 & 0 & 0 & \dots & 0 & 0 \\
0 & 0 & 0 & 0 & 0 & 0 & 1 & \dots & 0 & 0 \\
N_{1,v} & N_{1,\alpha} & 0 & N_{1,h} & 0 & -\omega_1^2+N_{1,\eta_1} & -2\zeta\omega_1+N_{1,\dot{\eta_1}} & \dots & N_{1,\eta_3} & 0 \\
0 & 0 & 0 & 0 & 0 & 0 & 0 & \dots & 0 & 0 \\
N_{2,v} & N_{2,\alpha} & 0 & N_{2,h} & 0 & N_{2,\eta_1} & 0 & \dots & N_{1,\eta_3} & 0 \\
0 & 0 & 0 & 0 & 0 & 0 & 0 & \dots & 0 & 1 \\
N_{3,v} & N_{3,\alpha} & 0 & N_{3,h} & 0 & N_{3,\eta_1} & 0 & \dots & -\omega_3^2+N_{3,\eta_3} & -2\zeta\omega_3+N_{3,\dot{\eta_3}}
\end{bmatrix} \tag{4.13}$$

$$\mathbf{B} = \begin{bmatrix} X_{\delta_e} & X_{\delta_\phi} \\ \frac{Z_{\delta_e}}{V_{T_0}} & \frac{Z_{\delta_\phi}}{V_{T_0}} \\ \mathscr{M}_{\delta_e} & \mathscr{M}_{\delta_\phi} \\ 0 & 0 \\ 0 & 0 \\ 0 & 0 \\ N_{1,\delta_e} & N_{1,\delta_\phi} \\ 0 & 0 \\ N_{2,\delta_e} & N_{2,\delta_\phi} \\ 0 & 0 \\ N_{3,\delta_e} & N_{3,\delta_\phi} \end{bmatrix} \tag{4.14}$$

For completeness, the dimensional derivatives equations for the rigid body modes are given below.

$$X_v = \frac{1}{m}\left(\frac{\partial T}{\partial V_T}\cos(\alpha_0) + \frac{\partial D}{\partial V_T}\right) \tag{4.15}$$

$$X_\alpha = \frac{1}{m}\left(\frac{\partial T}{\partial \alpha}\cos(\alpha_0) + \frac{\partial D}{\partial \alpha} + L_0\right) \tag{4.16}$$

$$X_h = \frac{1}{m}\left(\frac{\partial T}{\partial h}\cos(\alpha_0) + \frac{\partial D}{\partial h}\right) \tag{4.17}$$

$$Z_v = -\frac{1}{m}\left(\frac{\partial T}{\partial V_T}\sin(\alpha_0) + \frac{\partial L}{\partial V_T}\right) \tag{4.18}$$

$$Z_\alpha = -\frac{1}{m}\left(\frac{\partial T}{\partial \alpha}\sin(\alpha_0) + \frac{\partial L}{\partial \alpha} + D_0\right) \tag{4.19}$$

$$Z_Q = -\frac{1}{m}\left(\frac{\partial T}{\partial h}\sin(\alpha_0) + \frac{\partial L}{\partial h}\right) \tag{4.20}$$

$$Z_h = -\frac{1}{m}\left(\frac{\partial T}{\partial h}\sin(\alpha_0) + \frac{\partial L}{\partial h}\right) \tag{4.21}$$

$$\mathscr{M}_{V_T} = \frac{1}{I_{yy}}\frac{\partial M}{\partial V_T} \tag{4.22}$$

$$\mathscr{M}_\alpha = \frac{1}{I_{yy}}\frac{\partial M}{\partial \alpha} \tag{4.23}$$

$$\mathscr{M}_Q = \frac{1}{I_{yy}}\frac{\partial M}{\partial Q} \tag{4.24}$$

$$\mathscr{M}_h = \frac{1}{I_{yy}}\frac{\partial M}{\partial h} \tag{4.25}$$

$$X_{\delta_e} = \frac{1}{m}\left(\frac{\partial T}{\partial \delta_e}\cos(\alpha_0) + \frac{\partial D}{\partial \delta_e}\right) \tag{4.26}$$

$$Z_{\delta_e} = -\frac{1}{m}\left(\frac{\partial T}{\partial \delta_e}\sin(\alpha_0) + \frac{\partial L}{\partial \delta_e}\right) \tag{4.27}$$

$$\mathscr{M}_{\delta_e} = \frac{1}{I_{yy}}\frac{\partial M}{\partial \delta_e} \tag{4.28}$$

$$X_{\delta_\phi} = \frac{1}{m}\left(\frac{\partial T}{\partial \delta_\phi}\cos(\alpha_0) + \frac{\partial D}{\partial \delta_\phi}\right) \tag{4.29}$$

$$Z_{\delta_\phi} = -\frac{1}{m}\left(\frac{\partial T}{\partial \delta_\phi}\sin(\alpha_0) + \frac{\partial L}{\partial \delta_\phi}\right) \tag{4.30}$$

$$\mathscr{M}_{\delta_\phi} = \frac{1}{I_{yy}}\frac{\partial M}{\partial \delta_\phi} \tag{4.31}$$

4.3 Dynamic Analysis: Nominal Properties - Mach 8, 85kft

In this section, we consider the nominal plant's dynamic properties (linearized at Mach 8, 85kft). Below, we have the pole-zero map for the HSV model.

4.3.1 Nominal Pole-Zero Plot

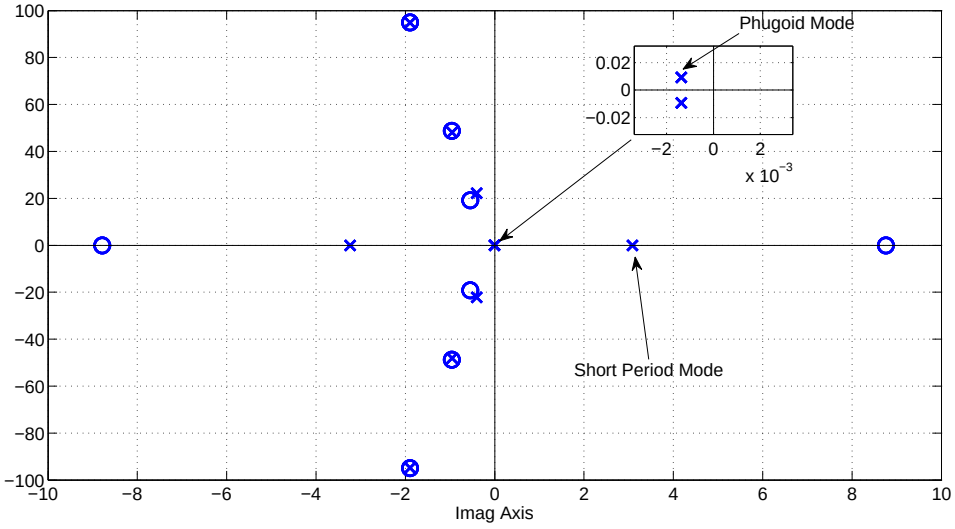

Figure 32: Pole Zero Map at Mach 8, 85kft: Level Flight, Flexible Vehicle

We note that the short period mode comprises of a stable and an unstable pole. The long lower forebody of typical hypersonic waveriders combined with a rearward shifted center-of-gravity (CG), results in a pitch-up instability. Hence, we need a minimum bandwidth

for stabilization [97]. Also, the flexible modes are lightly damped, and limit the maximum bandwidth [106–108].

Table 4.1: Poles at Mach 8, 85kft: Level Flight, Flexible Vehicle

Pole	**Damping**	**Freq. (rad/s**	**Mode Name**
3.21	-1	3.21	Unstable Short Period
-3.28	1	3.28	Stable Short Period
$-1.10 \cdot 10^{-3} \pm j5.75 \cdot 10^{-3}$	1.88	$5.85 \cdot 10^{-3}$	Phugoid Mode
$-0.41 \pm j22.1$	$2 \cdot 10^{-2}$	22.1	1^{st} Flex
$-0.96 \pm j48.1$	$2 \cdot 10^{-2}$	48.1	2^{nd} Flex
$-1.9 \pm j94.8$	$2 \cdot 10^{-2}$	94.8	3^{rd} Flex

Table 4.2 lists the zeros of the linearized model. We notice that the plant is non-minimum phase. This is a common characteristic for tail-controlled aircrafts, unless a canard is used [123, 124]. It is understood, of course, that any canard approach would face severe heating, structural, and reliability issues.

Table 4.2: Zeros at Mach 8, 85kft: Level Flight, Flexible Vehicle

Pole	**Damping**	**Freq. (rad/s**
8.54	-1	8.54
-8.55	1	-8.55
$-0.39 \pm j19.1$	$2 \cdot 10^{-2}$	19.1
$-0.96 \pm j48.7$	$1.96 \cdot 10^{-2}$	48.7
$-1.9 \pm j94.9$	$2.04 \cdot 10^{-2}$	94.9

4.3.2 Modal Analysis

Table 4.3 shows the eigenvectors for the modes given earlier. This subsection examines the natural tendencies of the linearized system. To examine the natural modes of a system, the input is set to zero and the initial conditions are chosen to excite only one mode. To examine a mode s_i, we let the initial condition be any linear combination of the real and complex components of a right eigenvector of the mode [125]. Eigenvectors to excite individual modes of the linearized model are given in table 4.3.

Phugoid Mode. The long-period or phugoid mode represents an interchange of potential and kinetic energy about the equilibrium operating point at nearly constant AOA [126,

Table 4.3: Eigenvector Matrix at Mach 8, 85kft: Level Flight, Flexible Vehicle

State	Phugoid	Unstable short period	Stable Short Period
Velocity	-1.54e-2±-9.39e-2i	-1.95e-5	2.26e-5
AOA	-4.30e-3±2.61e-2i	-2.62e-1	-2.69e-1
Pitch Rate	-1.09e-3±5.72e-3i	-8.67e-1	8.61e-1
Pitch	9.95e-1	-2.71e-1	-2.61e-1
η_1	-4.96e-3±3.01e-2i	-9.69e-2	-1.00e-1
$\dot{\eta_1}$	-1.68e-4±6.16e-5i	-3.10e-1	3.30e-1
η_2	1.32e-4±8.02e-4i	9.93e-4	1.02e-3
$\dot{\eta_2}$	4.46e-6±1.64e-6i	3.18e-3	-3.36e-3
η_3	4.51e-5±2.74e-4i	-3.44e-4	-3.53e-4
$\dot{\eta_3}$	1.53e-6±5.61e-7i	-1.10e-3	1.17e-3
State	Flexible Mode 1	Flexible Mode 2	Flexible Mode 3
Velocity	-3.59e-6±1.32e-7i	-5.44e-7±2.22e-8i	-3.98e-7±1.61e-8i
AOA	-1.44e-4±5.05e-4i	-3.14e-5±1.94e-4i	-1.41e-5±9.50e-6i
Pitch Rate	1.13e-2±3.39e-4i	9.40e-3±3.68e-4i	9.51e-4±3.66e-5i
Pitch	-2.47e-5±5.08e-4i	-1.15e-5±1.95e-4i	-5.87e-7±1.00e-5i
η_1	-8.31e-4±4.51e-2i	-3.08e-5±6.79e-4i	-1.34e-5±2.56e-4i
$\dot{\eta_1}$	9.99e-1	3.27e-2±8.31e-4i	2.42e-2±7.83e-4i
η_2	-3.46e-6±1.36e-4i	-4.12e-4±2.08e-2i	1.26e-6±2.73e-5i
$\dot{\eta_2}$	3.00e-3±2.12e-5i	9.99e-1	-2.59e-3±6.77e-5i
η_3	-5.79e-7±1.61e-5i	2.68e-7±9.50e-6i	-2.11e-4±1.05e-2i
$\dot{\eta_3}$	3.57e-4±6.24e-6i	-4.57e-4±3.84e-6i	1.00

page 148, 152]. The mode is stable and lightly damped for our model. Low phugoid damping becomes objectionable for pilots flying under instrument flight rules [126, page 153]; automatic stabilization systems should be designed to provide adequate damping. Figure 33 shows variations in the velocity, FPA (equivalently altitude) when this mode is excited. Stability derivatives based approximations for this mode, and longitudinal flying qualities based on phugoid-damping, can be found in [126, page 153] (the phugoid mode may be approximated by a double integrator for our vehicle).

Short Period Mode. For conventional aircrafts, the short-period mode is typically heavily damped and has a short period of oscillation; the motion occurs at nearly constant speed [126, page 148]. High frequency and heavy damping are desirable for rapid response to elevator commands without undesirable overshoot [126, page 162]. For our model, the short

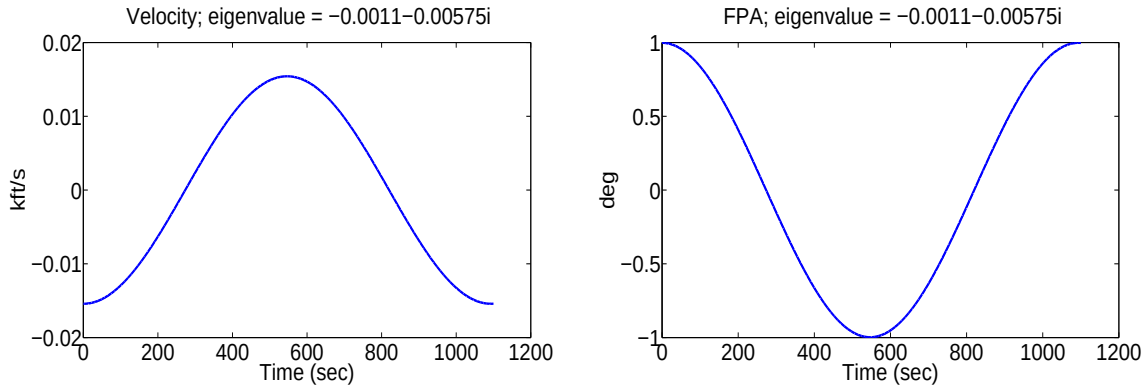

Figure 33: Phugoid mode excitation

period mode is not a complex conjugate pair; instead it is a stable and unstable pole pair. In section 4.4.1 the variations in the unstable mode are considered. Stability derivatives based approximations (see Appendix **??**, page **??**) and longitudinal flying qualities based on this mode can be found in [126, page 153].

Flexible Modes. The flexible modes of the HSV have very little impact on the outputs.

4.4 Dynamic Analysis - RHP Pole, Zero variations

4.4.1 Dynamic Analysis: RHP Pole

Figure 34 illustrates variations in the RHP pole with Mach, altitude and dynamic pressure.

- RHP pole fairly constant along constant dynamic pressure profiles;
  - increases with increasing dynamic pressure
  - Designing a minimum BW at the plant input for stabilization should be done at larger dynamic pressures to ensure sufficient control authority across the flight envelope
- RHP pole increases linearly with increasing mach
- RHP pole decreases monotonically with increasing altitude

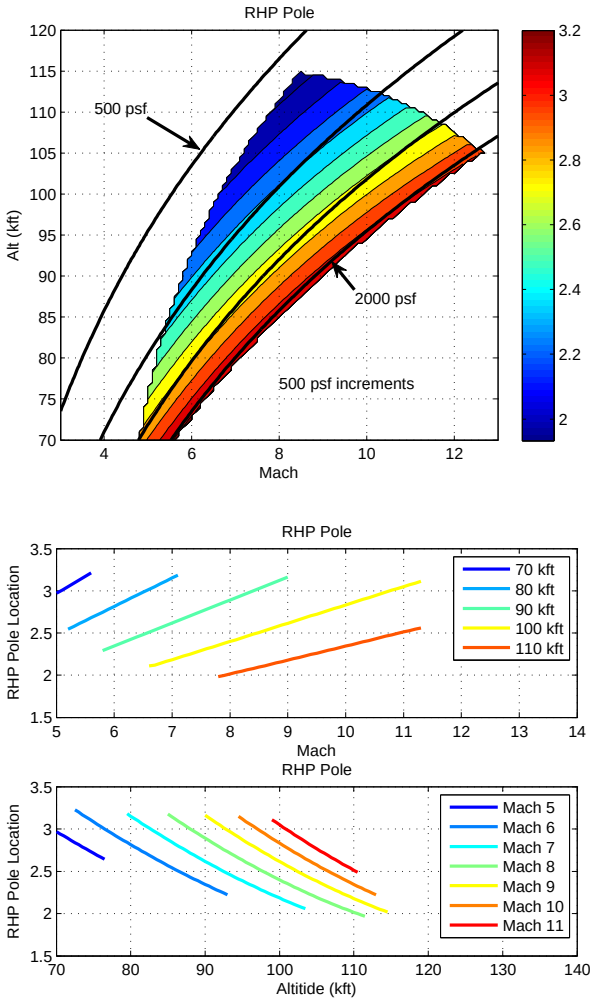

Figure 34: Right Half Plane Pole: Level Flight, Flexible Vehicle

4.4.2 Dynamic Analysis: RHP Zero

Figure 35 illustrates variations in the RHP zero with Mach, altitude and dynamic pressure.

- RHP zero decreases with decreases dynamic pressure
- RHP zero increases linearly with increasing mach
- RHP zero decreases monotonically with increasing altitude
  - RHP zero determines maximum BW at FPA (plant output/error)
  - $z_{min} = 4.8$, occurs at Mach 8.5, 115 kft, determines worst case maximum BW

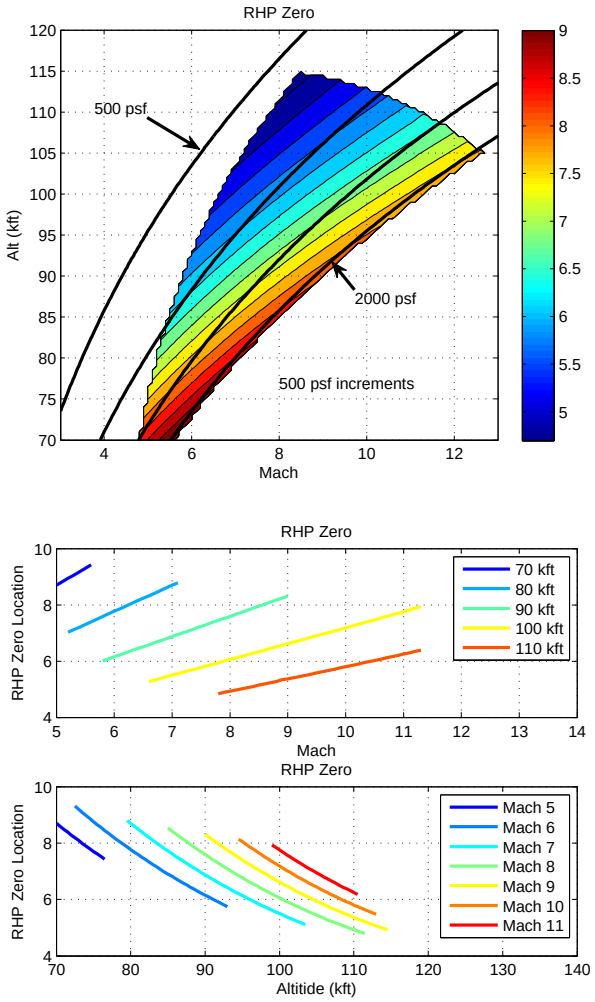

Figure 35: Right Half Plane Zero: Level Flight, Flexible Vehicle

4.4.3 Dynamic Analysis: RHP Zero-Pole ratio

Figure 36 illustrates variations in the RHP zero/pole ratio with Mach, altitude and dynamic pressure.

- Z-P ratio decreases with increasing altitude
- Worst ratio at altitude = 113 kft, Mach = 8.5

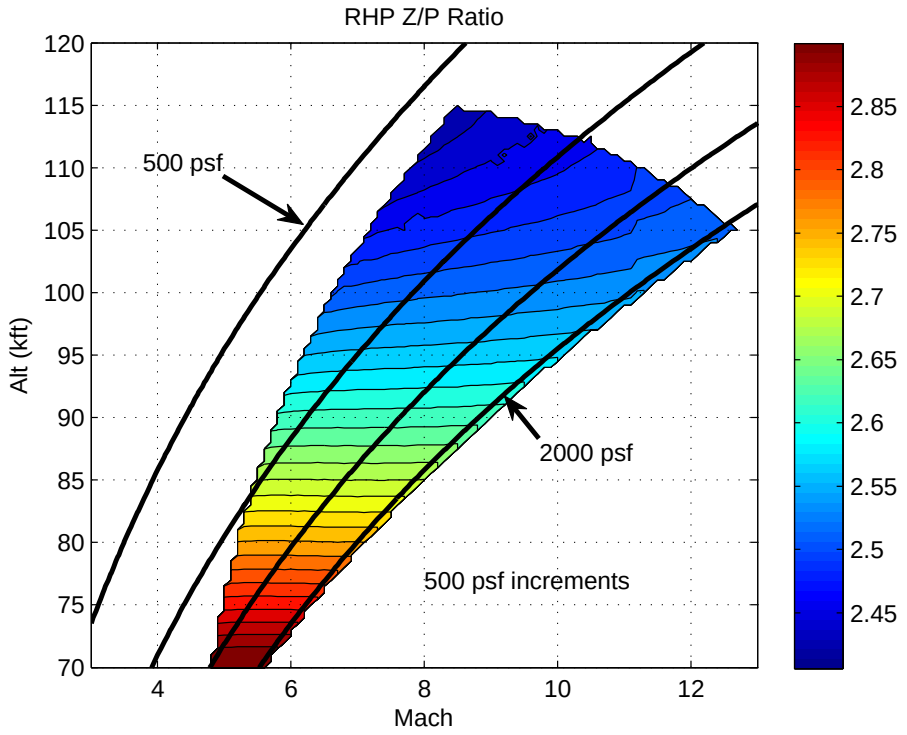

Figure 36: Right Half Plane Zero/Pole Ratio Contour: Level Flight, Flexible Vehicle

4.5 Dynamic Analysis - Frequency Responses

4.5.1 Dynamic Analysis - Bode Magnitude Response

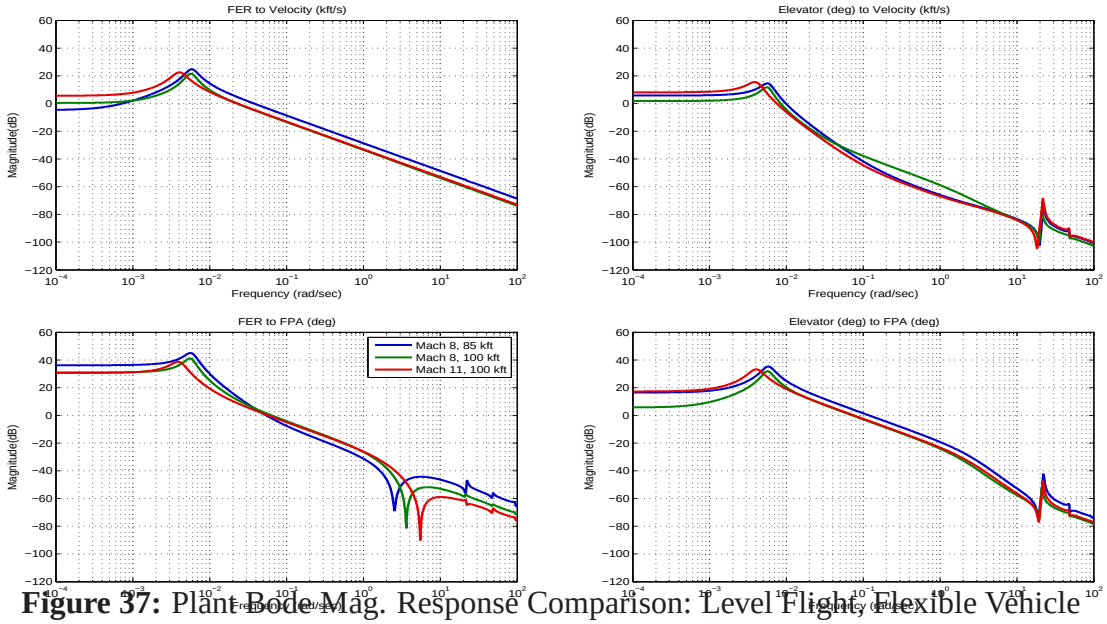

Figure 37: Plant Bode Mag. Response Comparison: Level Flight, Flexible Vehicle

4.5.2 Dynamic Analysis - Bode Phase Response

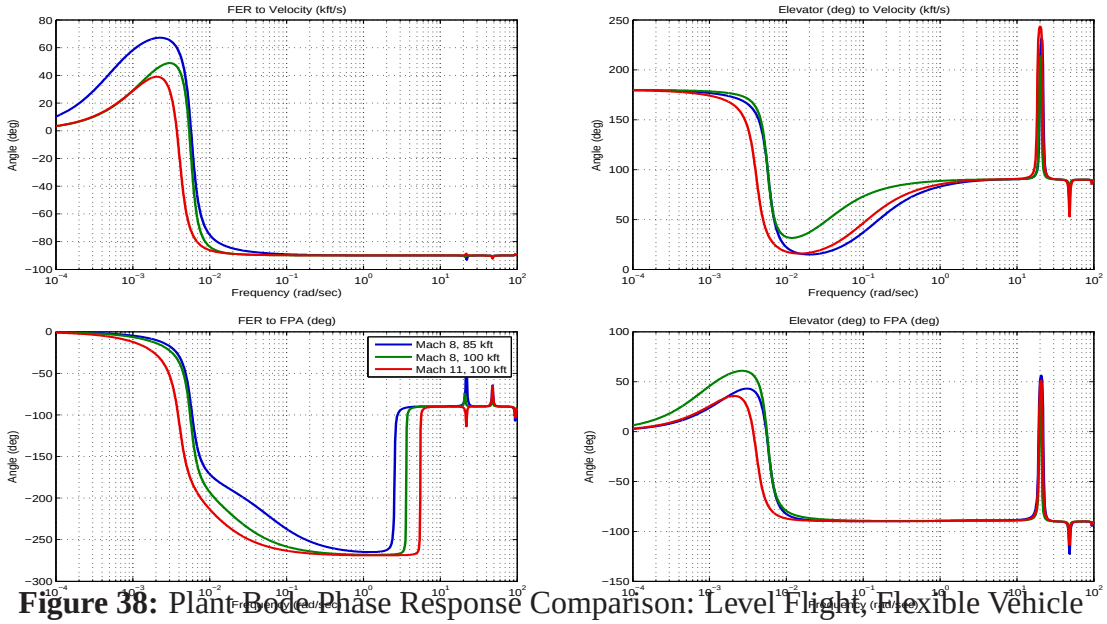

Figure 38: Plant Bode Phase Response Comparison: Level Flight, Flexible Vehicle

4.6 Dynamic Analysis - Singular Values

The figures 39 and 40 show the variation in the singular values with frequency, for the nominal plant.

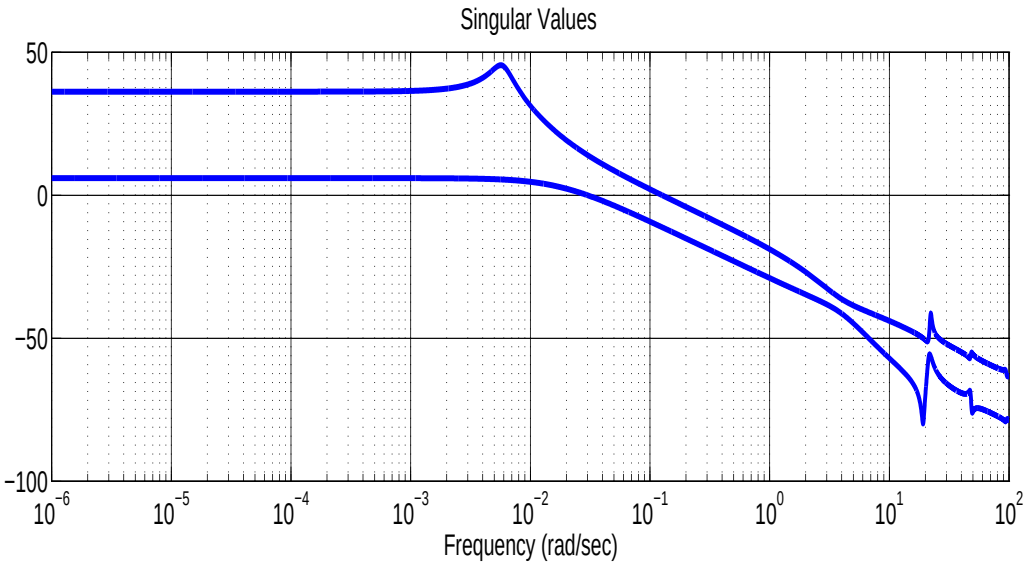

Figure 39: Singular Values: Level Flight, Flexible Vehicle, Mach 8, h=85 kft

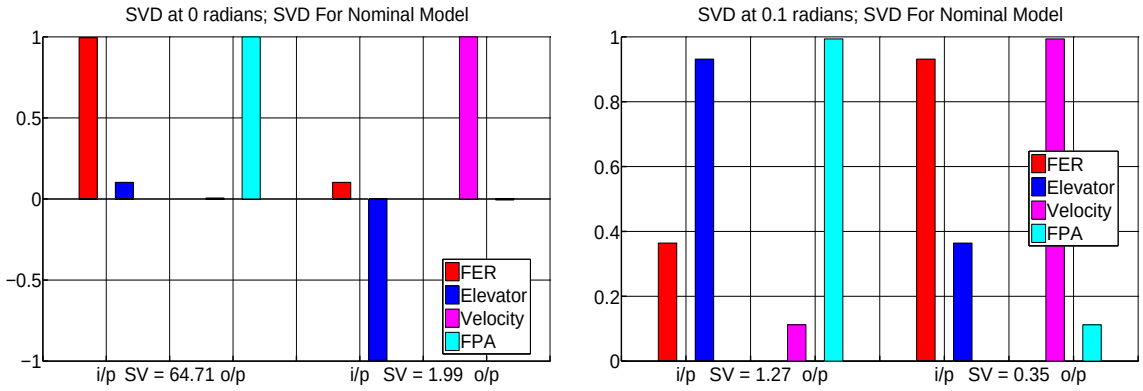

Figure 40: Singular Value Decomposition, Mach 8, h=85 kft

- At dc, FER (elevator) has greatest impact FPA (velocity).
- However, at low frequencies FER (elevator) should be used to command velocity (FPA).

4.7 FPA Control Via FER

The figure below shows the bode magnitude response for the nominal plant at Mach 8, 85kft (level flight).

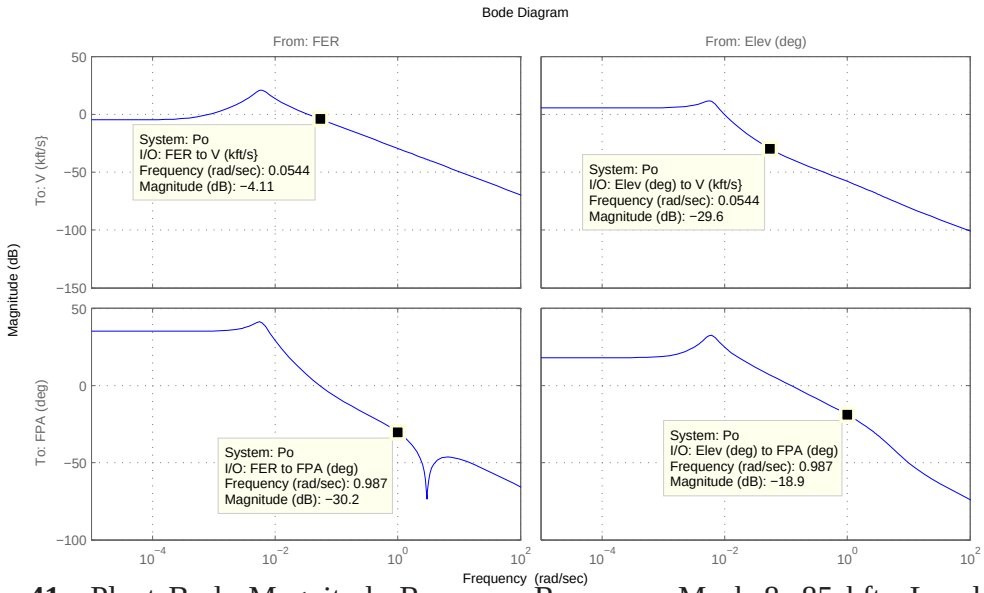

Figure 41: Plant Bode Magnitude Response Response, Mach 8, 85 kft: Level Flight, Flexible Vehicle

What is the feasibility of using FER to control FPA?

- At frequencies of 1 rad/sec (roughly corresponding to a 5 second settling time)
  - Each degree of FPA corresponds to 8.81 degrees (18.9 dB) of elevator
  - Each degree of FPA corresponds to an FER of 32.4 (30.2 dB)!!
- At frequencies of 0.05 rad/sec (roughly corresponding to a 100 second settling time)
  - Each degree of FPA corresponds to 0.5 degrees (-6.95 dB) of elevator
  - Each degree of FPA corresponds to an FER of 1 (0.05 dB)

4.8 Summary and Conclusions

In this chapter, the linearization algorithm and the dynamic properties of the nominal plant were presented. The vehicle is open loop unstable (due to cg rear of ac - long forebody

serves as a compression ramp). There exists a RHP zero associated with a tail-controller aircraft (unless a canard is used [123, 124]). The RHP pole and RHP zero increase with dynamic pressure. The RHP zero-pole ratio increases with altitude.

For classical controllers, the RHP zero limits the achievable bandwidth (i.e. there exists a finite upward gain margin); the RHP pole requires a minimum controller bandwidth (i.e. there is a positive downward gain margin). The lightly damped flexible modes present additional control challenges and limit the bandwidth (it is desirable to avoid exciting them). The dynamic properties at trim influence controller design and must be considered during the vehicle design process. In the following chapter, we shall consider how these properties change with different vehicle configurations.

5. Plume Modeling and Engine Design Considerations

5.1 Overview

The HSV model under consideration consists of an integrated airframe and engine [81]. The vehicle is open loop unstable [14]), and has a non-minimum RHP zero (unless a canard is present [14]). The model also has lightly damped flexible modes [9]. Due to the complexity of control, a multidisciplinary approach is required in the design of air-breathing hypersonic vehicles [127, 128]. The impact of parameters on control-relevant static properties (e.g. level-flight trimmable region, trim controls, AOA) and dynamic properties (e.g. instability and right half plane zero associated with flight path angle) must be considered at the design stage. In this chapter trade studies associated with vehicle/engine parameters are examined. Trade studies are broadly categorized as

- Effect of accurate plume calculation over vehicle properties
- Different method to compute vehicle plume
- Propulsion studies - Engine location, sizing

Fundamental Questions. The following fundamental questions are examined during trade studies

- What are the impacts of vehicle plume on static properties?
- What are the impacts of vehicle plume on the dynamic properties?

In section 5.2 (page 104), an engine analysis has been conducted based upon traditional as well as control-relevant metrics. A complete parametric study involving inlet capture area, diffuser area ratio, internal nozzle ratio, and nozzle exit area ratio is presented. In section 5.3 (page 109), plume calculation based on P_∞ are presented. Vehicle properties with plume calculation based on exact P_{shock} are discussed in 5.4 (page 119). Approximation to exact P_{shock} plume calculations is presented in 5.5 (page 123).

5.2 Engine Parameter Studies

This section examines the impact of varying the engine inlet height h_i and the diffuser area ratio A_d. The parametric trade studies were conducted at Mach 8, 85 kft, level flight. In what follows, h_e denotes the internal nozzle exit height and A_n denotes the internal nozzle area ratio.

Constraints for Engine Parameter Trade Studies (Mach 8, 85 kft, Level Flight). The above engines were obtained by conducting parametric trade studies at Mach 8, 85 kft, level flight. The following constraints were assumed in our studies:

- Flat base (internal nozzle exhaust height h_e equal to inlet height h_i); i.e. $h_e = h_i$ and $A_n = A_d^{-1}$;
- Inlet height h_i was varied between $\pm 50\%$ of nominal 3.25 ft;
- Engine mass m_{engine} was varied between $\pm 50\%$ of nominal 10 klbs;
- Diffuser area ratio A_d was varied between 0.1 and 0.35.

Impact of Engine Parameters on Static Properties (Mach 8, 85 kft, Level Flight)

Figure 42 shows the impact of varying (h_i, A_d) on FER, combustor temperature (assuming calorically perfect air), thrust, thrust margin at Mach 8, 85 kft, level flight.

Trim FER. From Figure 42 (upper left), one observes that the:

- trim FER decreases with decreasing A_d for a fixed h_i;
- trim FER decreases with increasing h_i when $h_i < 7$.

These suggests choosing A_d small (i.e. significant diffuser compression) and h_i large in order to achieve a small trim FER. The above, however, does not tell the full story since fuel consumption (trim fuel rate) - shown in Figure 42 (upper right) - increases with increasing h_i, and the thrust margin increases for $A_d < 0.125$.

Trim Combustor Temperature. From Figure 42 (lower left), one also observes that:

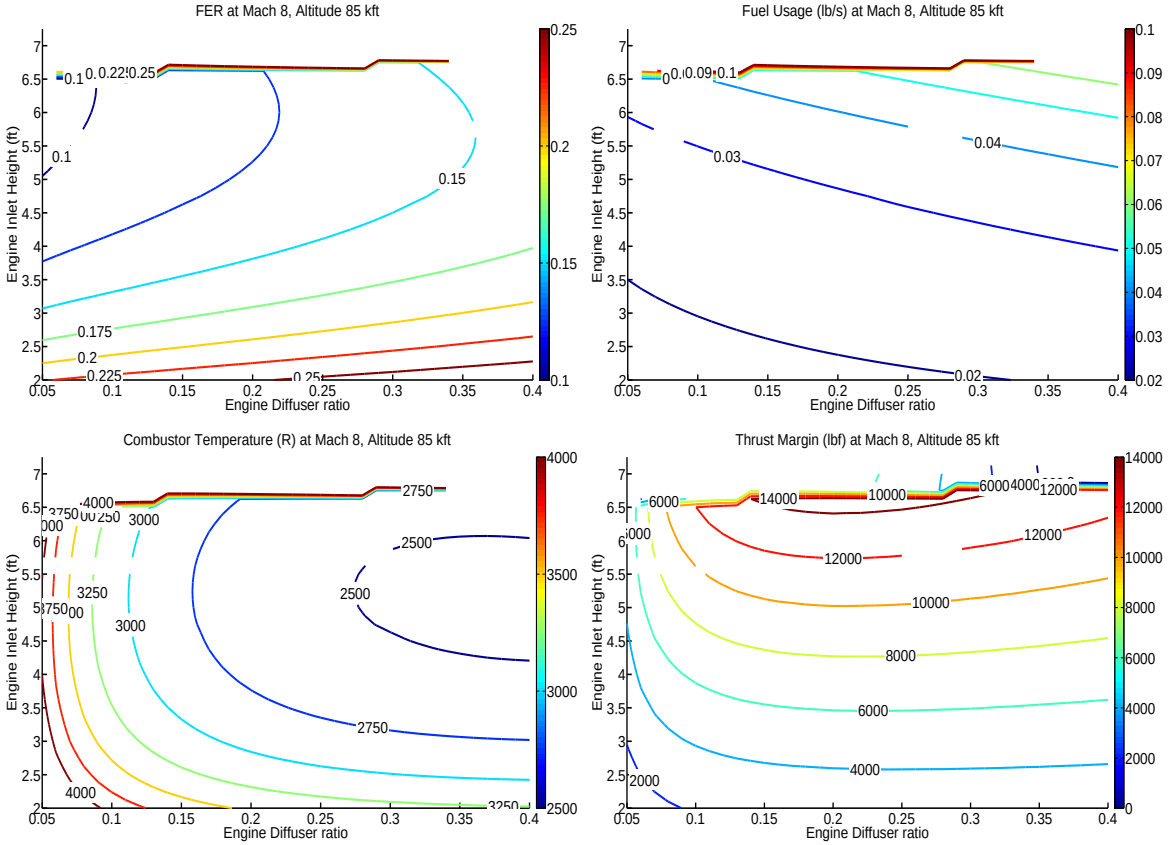

Figure 42: Trim FER, Combustor Temperature, Thrust, Thrust Margin: Dependence on h_i, A_d (Mach 8, 85 kft)

- Trim combustor temperature is a concave up function of (h_i, A_d) - minimized at $h_i \approx 5.5$, $A_d \approx 0.275$.
- Trim combustor temperature exhibits a steep gradient for $A_d > 0.125$

Since air is assumed to be calorically perfect, it follows that high temperature effects [129] are not captured within the model. As such, the combustor temperatures in Figure 42 (lower left) may be excessively large. High temperature gas effects within the combustor should be considered, since material temperature limits within the combustor are stated as $4500°R$ within [130].

Trim Thrust Margin. From Figure 42 (lower right), we also observe that

- Trim thrust margin is a concave down function of (h_i, A_d) - maximized at $h_i \approx 6$, $A_d \approx 0.125$.

Trim Elevator and AOA. Figure 43 shows how trim elevator and AOA depend on (h_i, A_d). From Figure 43, one observes that the:

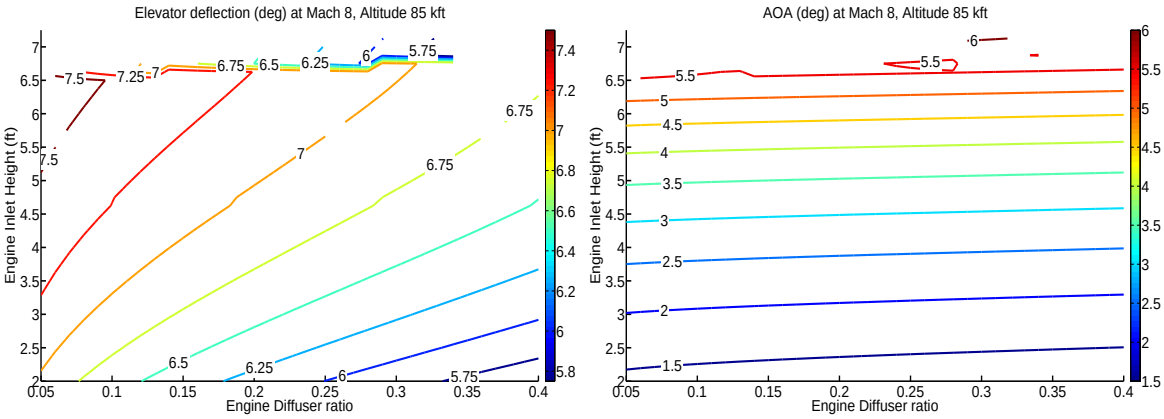

Figure 43: Trim Elevator Deflection and Trim AOA: Dependence on (h_i, A_d) - Mach 8, 85 kft, Level Flight

- Trim elevator increases with increasing h_i for a fixed A_d;
- Trim elevator increases with decreasing A_d for a fixed h_i;
- Trim AOA increases with increasing h_i for fixed A_d. Trim AOA decreases with increasing A_d for fixed h_i. (For h_i sufficiently large, trim AOA becomes nearly independent of A_d.)

Impact of Engine Parameters on Dynamic Properties (Mach 8, 85 kft, Level Flight)

The following figure shows the impact of h_i and A_d on the vehicle instability and RHP transmission zero associated with FPA.

From Figure 44, one observes that the:

- RHP pole increases with increasing A_d (for a fixed h_i) and decreasing h_i (for a fixed A_d);

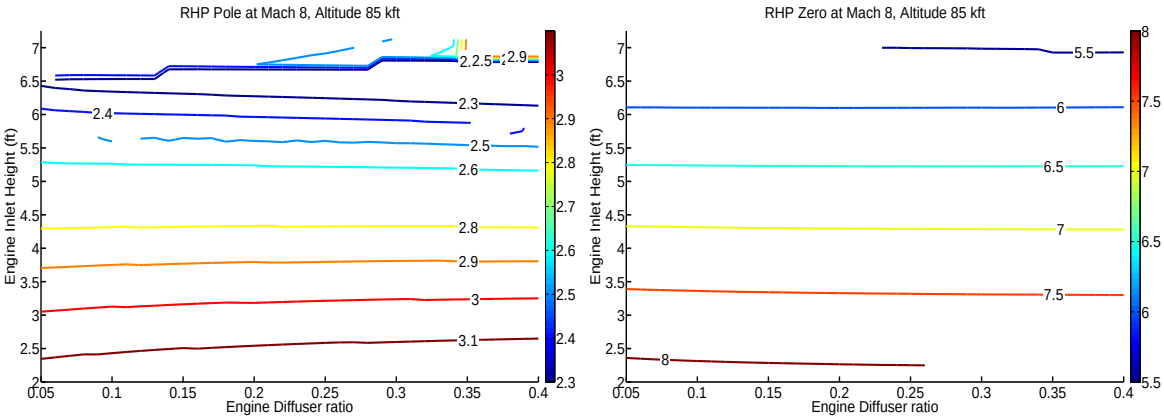

Figure 44: Right Half Plane Pole and Zero: Dependence on (h_i, A_d) - Mach 8, 85 kft, Level Flight

- RHP zero is constant with respect to A_d (for a fixed h_i); it decreases with increasing h_i (for a fixed A_d).

Comparison of Engine Designs (Mach 8, 85 kft, Level Flight)

In the previous sections, we considered the impact of increasing the engine height h_i and diffuser area ratio A_d. We consider $h_i \leq 6$ (bound chosen due to combustor temperature effects) and $A_d \geq 0.125$ (bound chosen due to thrust margin effects). Within this range, we observe the following trade-offs:

- Increasing h_i (fixed A_d)
  - PROS: Trim FER reduces, trim combustor temperature decreases (till $h_i \approx 5.5$ at $A_d = 0.125$), trim thrust margin increases, trim lift-to-drag increases (for $h_i > 4.0$ at $A_d = 0.125$, not shown),trim drag decreases (for $h_i > 4.0$ at $A_d = 0.125$, not shown), RHP pole reduces;
  - CONS: Trim fuel rate increases, trim elevator increases, trim AOA increases, RHP zero decreases, trim lift-to-drag decreases (for $h_i < 4.0$ at $A_d = 0.125$, not shown), trim drag increases (for $h_i < 4.0$ at $A_d = 0.125$, not shown);
- Decreasing A_d (fixed h_i)

- PROS: Trim FER decreases, trim fuel rate decreases, trim combustor temperature decreases, trim thrust margin increases, RHP pole decreases (marginally);
- CONS: Trim elevator increases, trim AOA increases (marginally), trim lift-to-drag decreases (not shown), trim drag increases (not shown).

Table 5.1 shows a comparison of the three engine designs described above. The first is the nominal engine design presented in [1–3, 5, 11, 13, 123, 131] As stated earlier, this configuration is geometrically unfeasible with respect to the implied flat base vehicle diagram shown in Figures 2 and 6. As can be seen from the table, it is generally "slow" with a small maximum acceleration capability. The second engine design will be used throughout the remainder of this thesis. It satisfies each of the constraints listed at the beginning of section 5.2 (page 104). The third configuration is a faster configuration that also obeys the constraints.

Table 5.1: Comparison of 3 Engine Designs (Mach 8, 85 kft, Level Flight)

Engine	h_i	A_d	A_n	h_e	Trim L/D	AOA	Trim Fuel Rate	FER
Nominal	3.25ft	1	6.35	5ft	2.17	1°	0.051 slugs/s	0.47
New	4.5ft	0.15	6.67	4.5ft	3.87	3.65°	0.1271 slugs/s	0.1756
Fast	6ft	0.12	8	6ft	4.52	3.90°	0.107 slugs/s	0.1286

Engine	Trim Temp.	Trim Thrust	Trim Elev.	Max Thrust	Max Acc.
Nominal	4500°R	1250 lbf	9.7°	2834 lbf	11.1 $\frac{ft}{s^2}$
New	2812.8°R	1693.5 lbf	7.07°	10029 lbf	44.65 $\frac{ft}{s^2}$
Fast	2982°R	1605 lbf	7.3686°	13350 lbf	62.11 $\frac{ft}{s^2}$

Engine	RHP Pole	RHP Zero	Z/P Ratio
Nominal	3.1	8.5	2.7
New	2.76	6.8	2.49
Fast	2.4	6.05	2.52

Table 5.1 shows that with respect to the nominal (slow or small) engine, the new (intermediately fast and sized) engine has the following associated PROS and CONS at Mach 8, 85 kft, level flight:

- PROS: smaller trim elevator, smaller trim FER, larger maximum thrust, larger thrust

margin, larger maximum acceleration, smaller RHP pole;

- CONS: larger engine, larger mass, larger trim thrust, larger trim combustor temperature, larger trim AOA, smaller RHP zero, smaller RHP zero-pole ratio.

For subsequent studies, following engine parameters were selected,

- $h_e = h_i = 4.5 \qquad A_d = 0.15 \qquad A_n = \frac{1}{A_d} = 6.67.$

This engine were feasible, large and fast, which makes the vehicle control problem more challenging. In further analysis, this engine is used.

5.3 Plume Calculation Based on P_∞

The aftbody pressure distribution is primarily due to the external expansion of the exhaust from the scramjet engine. The aftbody forms the upper portion of the nozzle. The lower portion of the exhaust plume (shear layer) forms the lower portion of the nozzle. In general, the determination of the shear layer involves an nonlinear iteration - equating the exhaust pressure with a suitable pressure (e.g. pressure across bow shock, or free stream pressure) upstream of the shear layer. This calculation can be very time consuming. To address this issue, the authors within [81, page 1315], [3] make a simplifying assumption - hereafter referred to as the "plume assumption" or simple approximation (simple approx for short). Which is given as,

$$P_2(s_2) \approx \frac{P_e}{1 + (\frac{s_2}{l_2})(\frac{P_e}{P_\infty} - 1)} \tag{5.1}$$

The forces across the aftbody are given as,

$$F_x = p_\infty l_2 \frac{p_e}{p_\infty} \frac{\ln \frac{p_e}{p_\infty}}{\frac{p_e}{p_\infty} - 1} tan(\tau_2 + \tau_{1,u}) \tag{5.2}$$

$$F_z = -p_\infty l_2 \frac{p_e}{p_\infty} \frac{\ln \frac{p_e}{p_\infty}}{\frac{p_e}{p_\infty} - 1} \tag{5.3}$$

where P_e is the pressure at the engine exit, P_∞ is the free stream pressure, l_2 is the length

of the vehicle's afterbody/nozzle surface, and s_2 is the distance from the vehicle's lower apex to the point of interest along the vehicle's afterbody/nozzle surface. This simplifying assumption significantly speeds up the calculation of the aft-body pressure distribution. The authors assume that,

- The free stream pressure p_∞ is the appropriate upstream pressure to determine the shear layer.
- External nozzle and plume shape do not change with respect to the vehicle's body axes. This implies that the plume shape is independent of the flight condition.

Based on further analysis it is observed that, these two assumptions are not valid. Free stream pressure, p_∞ is not the appropriate upstream pressure to determine the shear layer. At the same time, vehicle plume shape change with flight conditions.

Static Properties.

The some of the static properties of vehicle are described below,

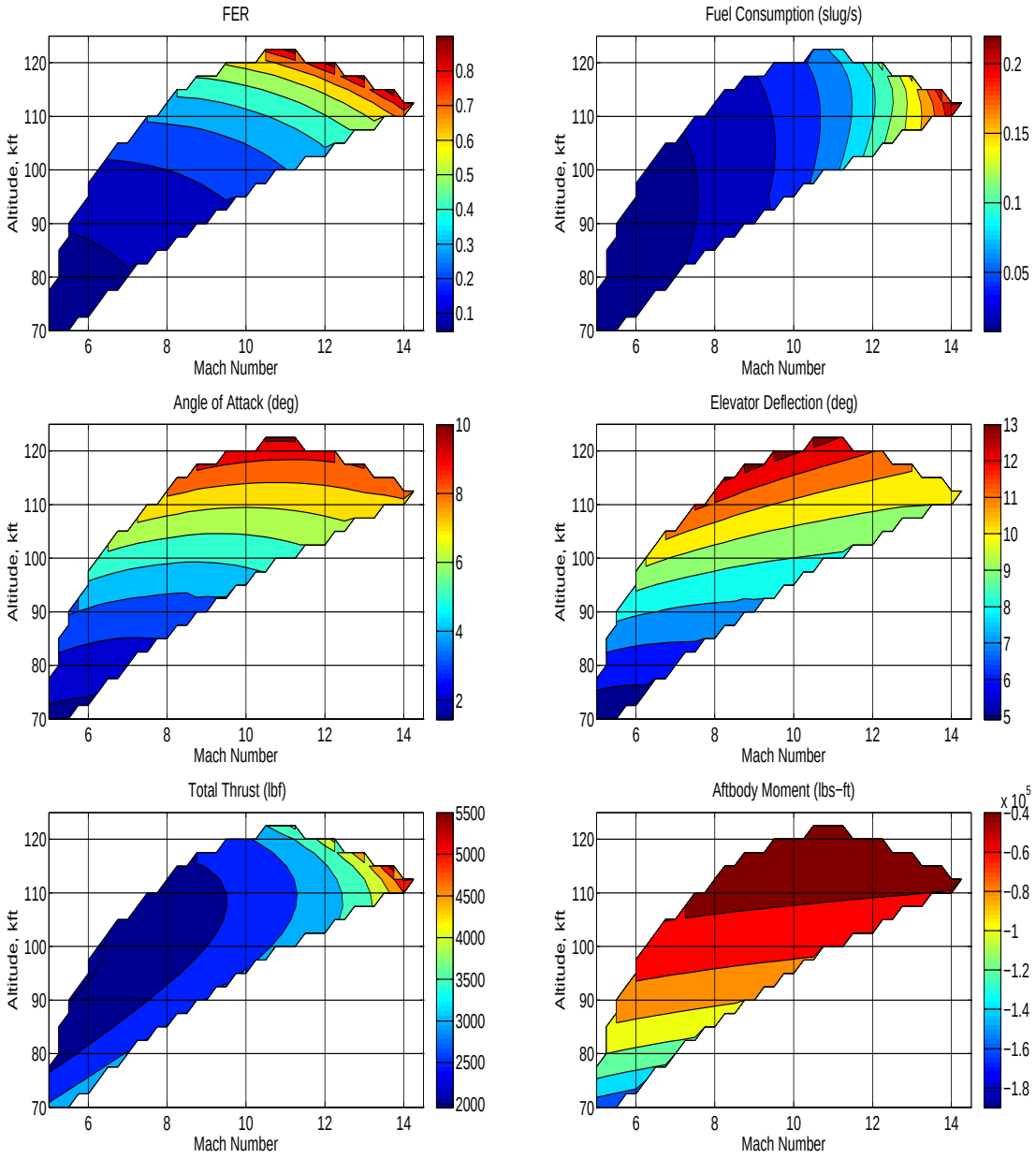

Figure 45: Trim FER, Fuel Consumption, Angle of Attack, Elevator, Total Thrust and Aftbody Moment with Simple Aprox Calculation

- FER and fuel consumption increases with altitude and Mach number
- AOA and elevator deflection increases with altitude and Mach number

- Total thrust increases with Mach number
- Aftbody moment increases with increase in altitude and Mach number

Dynamic Properties.

The dynamic properties of vehicle are described below,

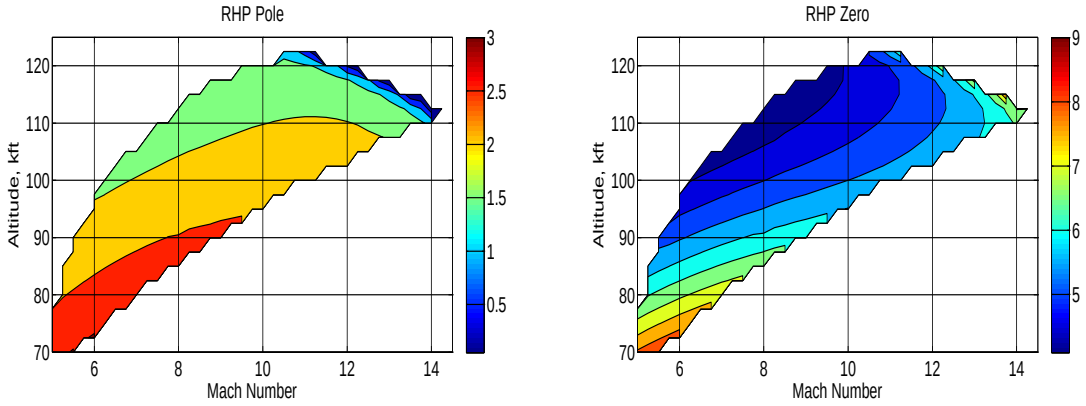

Figure 46: RHP Pole and RHP Zero Across Trimmable Region with Simple Approx Calculation

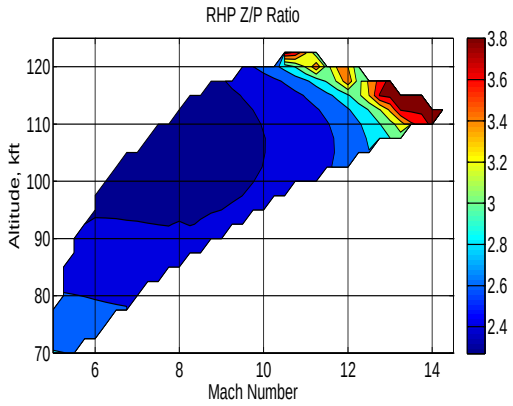

Figure 47: RHP Z-P Ratio Across Trimmable Region with Simple Approx Calculation

- RHP pole decreases with altitude
- RHP zero decreases with altitude
- Z-P ratio decreases with altitude and Mach number

5.3.1 Exact Plume Calculation Based on P_∞- (P_∞-Exact)

Within [132], a procedure for a more accurate plume calculation is described. To determine the location of the shear layer, an iterative (numerical) procedure is proposed. The method involves matching the downstream inner plume pressure is calculated from quasi 1D isentropic flow using engine exhaust properties, to the upstream outer plume pressure calculated from Newtonian impact theory. Quasi 1D isentropic flow properties are calculated as follows [82],

$$\frac{[1+\frac{1}{2}(\gamma-1)M_{s_2}^2]^{\frac{(\gamma+1)}{(\gamma-1)}}}{M_{s_2}^2} = (A_{s_2})^2\frac{[1+\frac{1}{2}(\gamma-1)M_e^2]^{\frac{(\gamma+1)}{(\gamma-1)}}}{M_e^2} \tag{5.4}$$

$$P_{s_2} = P_e[\frac{1+\frac{1}{2}(\gamma-1)M_e^2}{1+\frac{1}{2}(\gamma-1)M_{s_2}^2}]^{\frac{\gamma}{(\gamma-1)}} \tag{5.5}$$

$$A_{s_2} = \frac{he + s_2 sin(\tau_2+\tau_{1u}) + s_2 sin(\beta)}{he} \tag{5.6}$$

where M_{s_2} and P_{s_2} are flow properties at point s_2 and M_e and P_e are flow properties at internal nozzle exit. A_{s_2} is nozzle area ratio defined as the ratio of the external nozzle exit area to external nozzle inlet area and it is it is function of β. The pressure from Newtonian impact theory is calculated as [21],

$$\frac{P-P_\infty}{\frac{1}{2}\rho_\infty V_\infty^2} = 2\sin^2\beta \tag{5.7}$$

where P_∞, V_∞ and ρ_∞ are free stream properties, β is angle of shear layer and P is pressure exerted on shear layer. With the location of shear layer known, the aftbody/nozzle pressure distribution, forces, and moments can be determined. For the engine described in [3], the comparison of pressure distribution along the aftbody of vehicle with simple approximation and exact plume calculation based on P_∞ are shown in 48

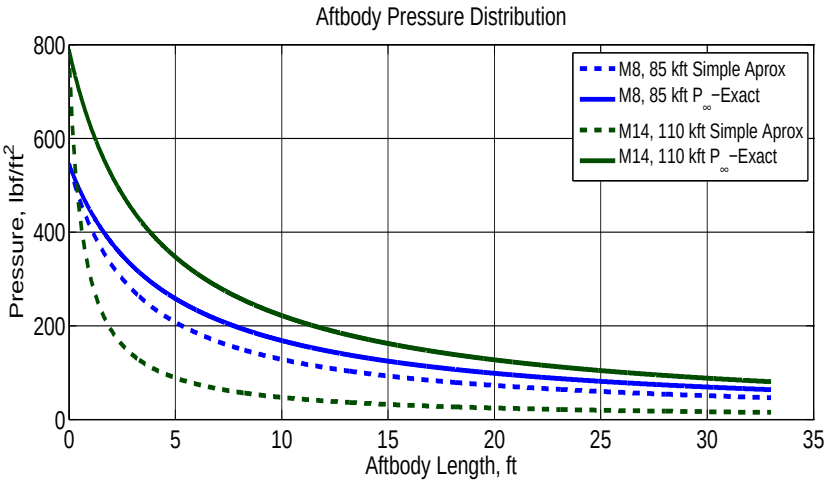

Figure 48: Plume Pressure Distribution Along Aftbody

From Figure 48 it is clear that,

- Simple approximation is inadequate to predict exact pressure distribution
- Error in determining aftbody pressure causes error in vehicle forces and moment calculations

The shape of shear layer below the engine base level is shown in Figure 49

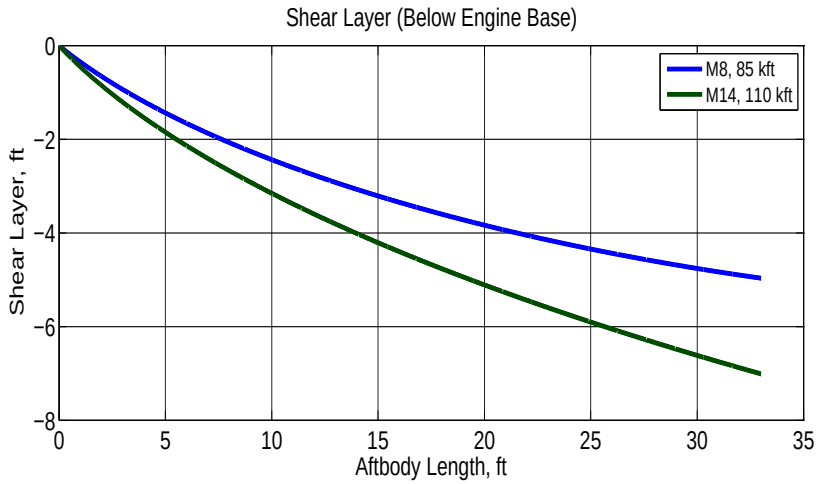

Figure 49: Shear Layer Below Engine Base

- Shear layer is not independent of flight condition
- The shear layer increases with increase in Mach number and altitude

The distribution of forces along the aftbody are shown in Figure 50

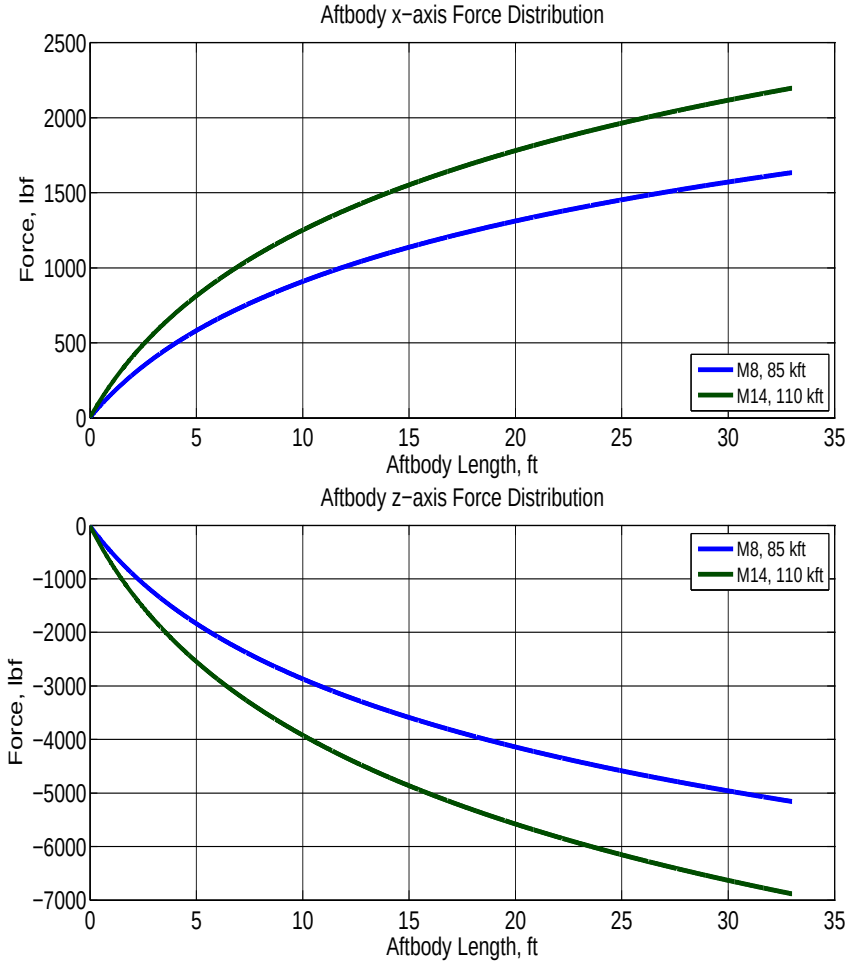

Figure 50: Force Distribution Along Aftbody

- The forces across the aftbody increases with increase in Mach number and altitude

Comparison of different pitching moments acting on vehicle body at Mach 8, 85 kft with simple approximation and P_∞-Exact calculations are given in Table 5.2

Moment	Simple Approx (lbs-ft)	P_∞-Exact (lbs-ft)
Lower Fore-body	269340	270060
Upper body	-22079	-22055
Vehicle Bottom	-4579.2	-4524
Aft-body	-94004	-119910
Engine Inlet	-43987	-44119
Elevator	-109900	-81464
Viscous Moment	-7248.4	-6800.1
Thrust Moment	12460	8811.6

Table 5.2: Moments acting on vehicle at Mach 8, 85 kft

From Table 5.2 it is clear that,

- With P_∞-Exact calculation aft-body moment increases
- With P_∞-Exact calculation thrust and elevator moment decreases

Static Properties.

The some of the static properties of vehicle are described below,

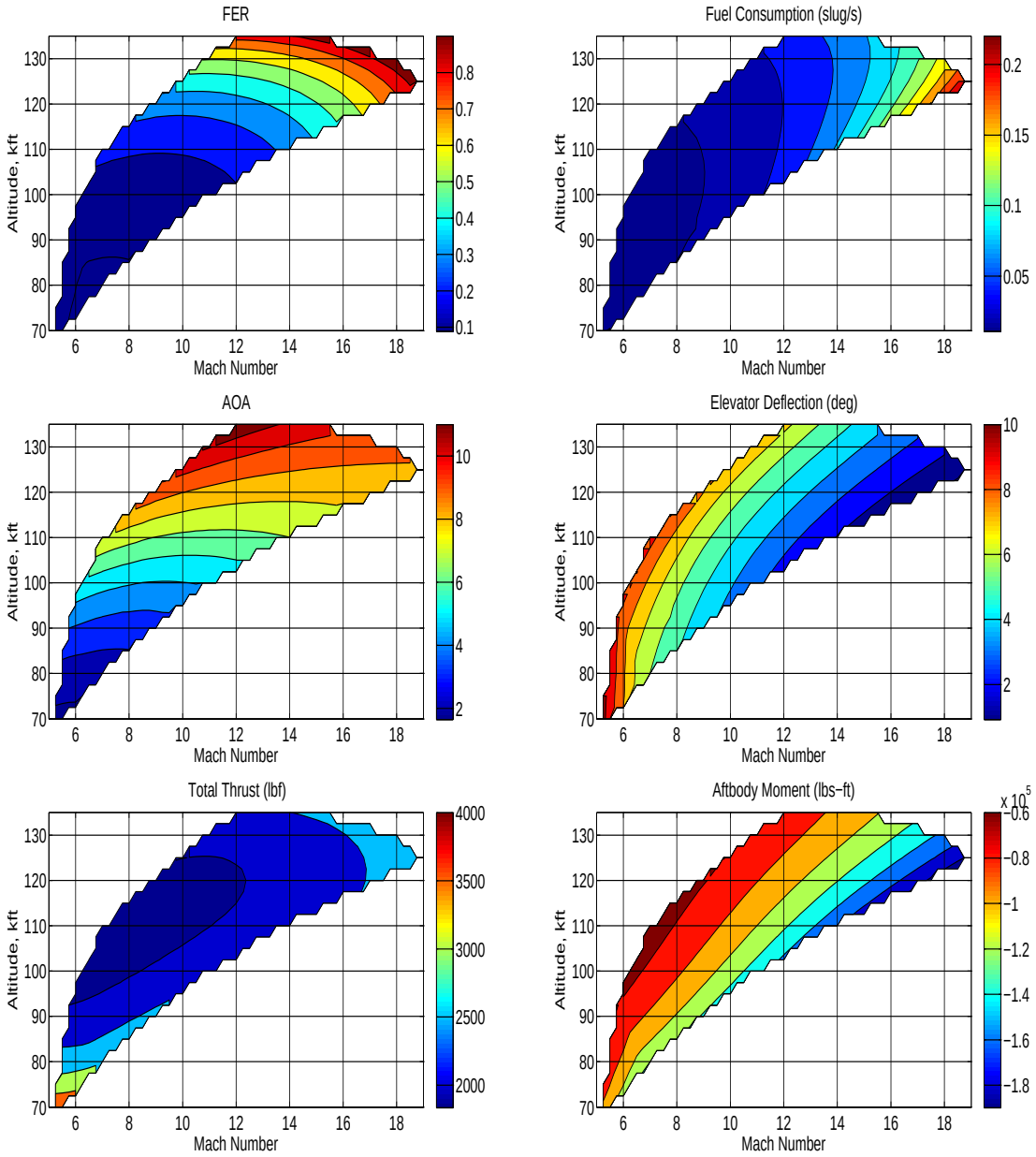

Figure 51: Trim FER, Fuel Consumption, Angle of Attack, Elevator, Total Thrust and Aftbody Moment with P_∞-Exact Calculation

- FER and fuel consumption increases with altitude and Mach number
- AOA and elevator deflection increases with altitude and Mach number

- Total thrust decreases with increase in altitude and Mach number

Dynamic Properties.

The dynamic properties of vehicle are described below,

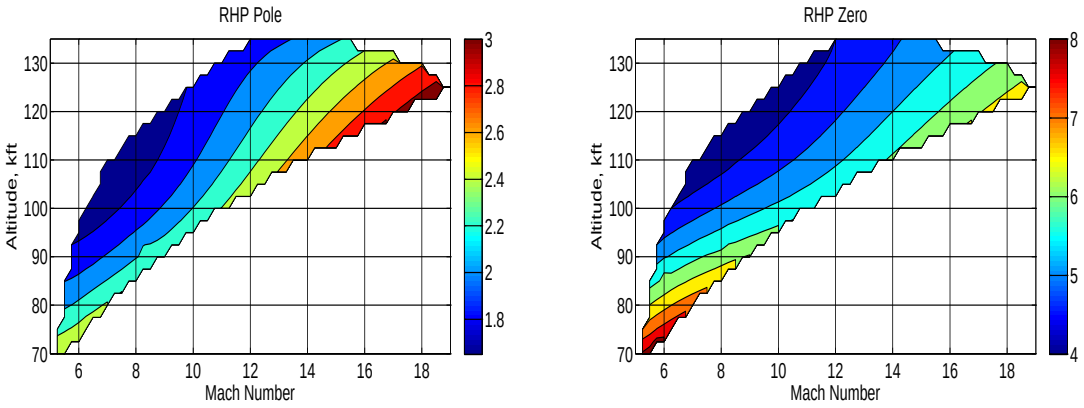

Figure 52: RHP Pole and RHP Zero Across Trimmable Region with P_∞-Exact Calculation

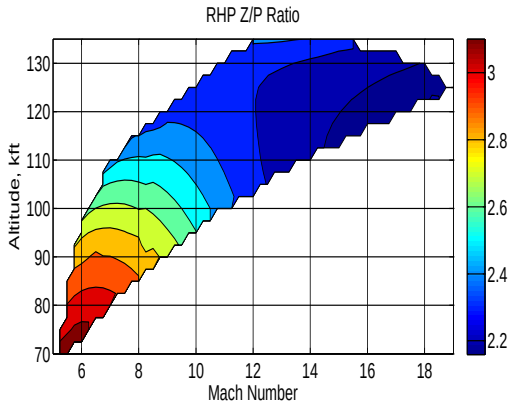

Figure 53: RHP Z-P Ratio Across Trimmable Region with P_∞-Exact Calculation

- RHP pole decreases with altitude
- RHP zero decreases with altitude
- Z-P ratio decreases with altitude and Mach number

Computational Time.

Determining the trimmable region with simple approximation takes near about 30 mins with a 2.66GHz processor. When the exact plume calculation based on P_∞ is conducted, the time increases to about 24 hrs.

5.4 Exact Plume Calculation Based on P_{shock}- (P_{shock}-Exact)

In [3, 81, 132], free stream (upstream) properties are used to determine the shear layer, but basic (preliminary) CFD analysis shows that the shear layer is far from the (upstream) free stream flow. It has been observed that for most level-flight conditions, P_{shock} flow properties should be used for more accurate plume calculations. In Figure 54, schematic of vehicles used by Chavez's[81] and Bolender[3] are presented.

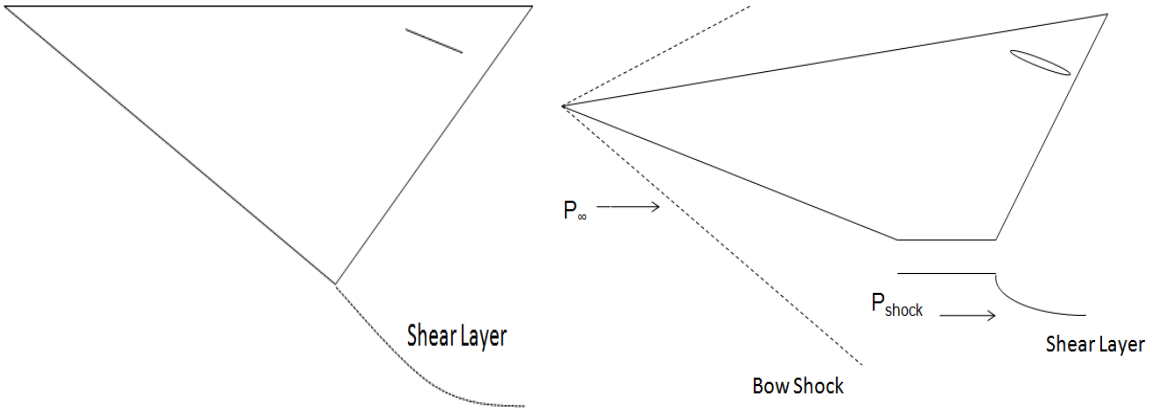

Chavez's Vehicle Bolender's Vehicle

Figure 54: Difference in Vehicle Geometry

From Figure 54 it is clear that,

- Use of P_∞ for plume calculation in terms of Chavez's[81] vehicle might be good approximation
- For Bolender[3] type vehicle P_∞ might be far way from shear layer location. In this case use of P_{shock} pressure for plume calculation is more appropriate.

It should be noted that, exact plume analysis requires high fidelity CFD (Computational Fluid Dynamics). Method presented here needs to be validated with detaile CFD calculations.

Below in Figure 55 - 57, static and dynamic properties of vehicle with Exact Plume Calculation Based on P_{shock} are presented.

Static Properties.

The some of the static properties of vehicle are described below,

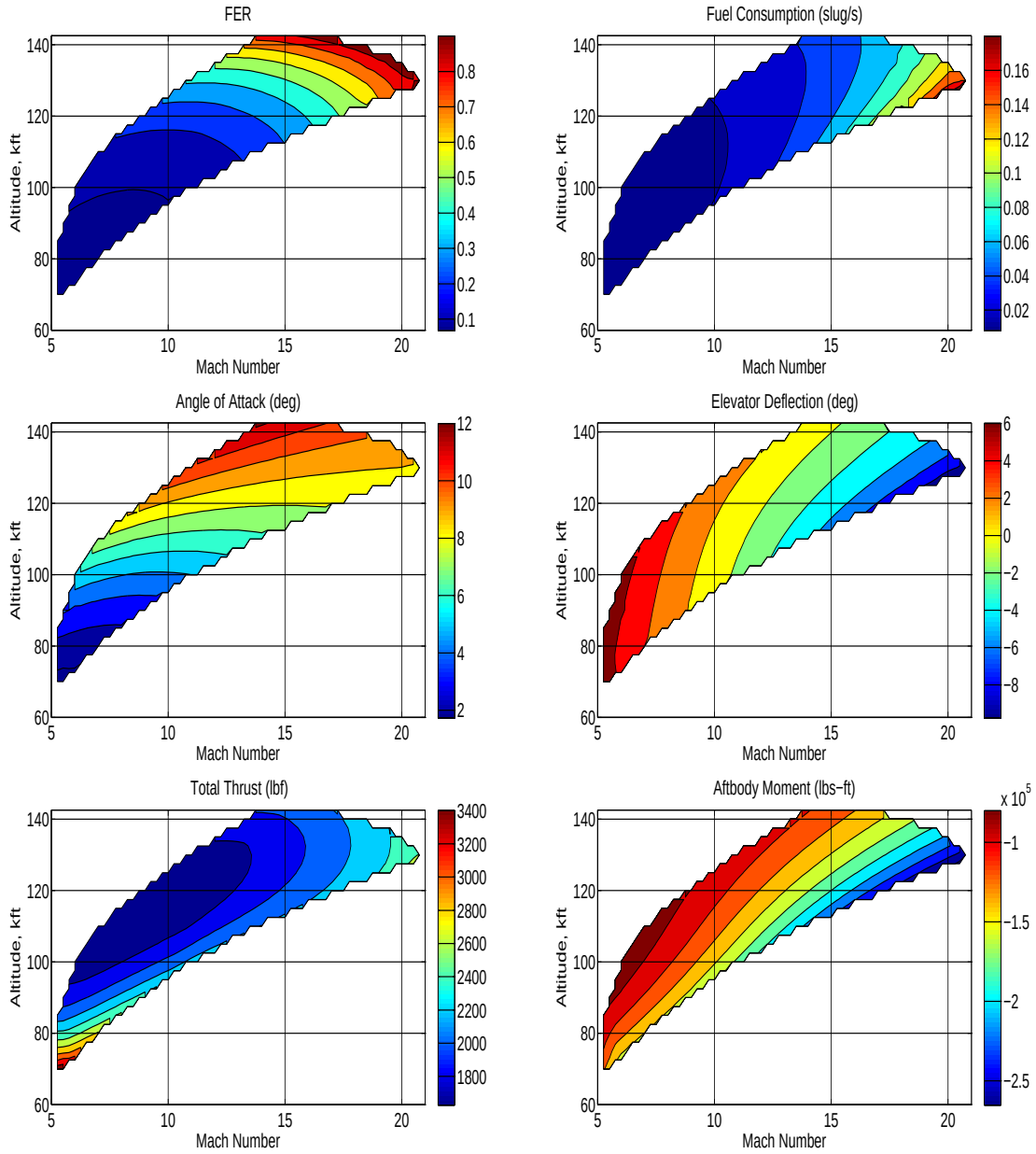

Figure 55: Trim FER, Fuel Consumption, Angle of Attack, Elevator, Total Thrust and Aftbody Moment with P_{shock}-Exact Calculation

- FER and fuel consumption increases with altitude and Mach number
- AOA increases with altitude and Mach number

- Elevator deflection decreases with increase in altitude and Mach number
- Total thrust decreases with increase in altitude and Mach number

Comparison of different pitching moments acting on vehicle body at Mach 8, 85 kft with P_∞-Exact and P_{shock}-Exact calculations are given in Table 5.3

Moment	P_∞-Exact (lbs-ft)	P_{shock}-Exact (lbs-ft)
Lower Fore-body	270060	270890
Upper body	-22055	-22015
Vehicle Bottom	-4524	-4476.1
Aft-body	-119910	-144990
Engine Inlet	-44119	-44275
Elevator	-81464	-54513
Viscous Moment	-6800.1	-6371.3
Thrust Moment	8811.6	5753.3

Table 5.3: Moments acting on vehicle at Mach 8, 85 kft

From Table 5.3 it is clear that,

- With P_∞-Exact calculation aft-body moment increases
- With P_∞-Exact calculation thrust and elevator moment decreases

Dynamic Properties.

The dynamic properties of vehicle are described below,

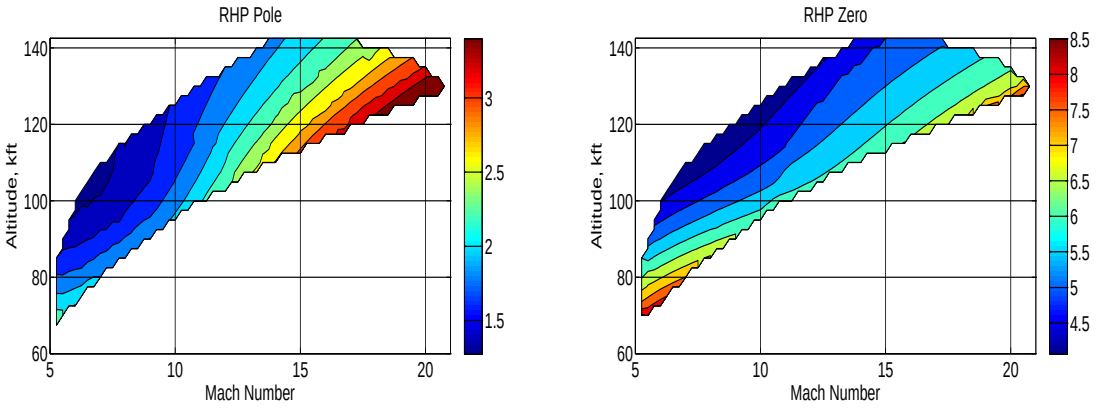

Figure 56: RHP Pole and RHP Zero Across Trimmable Region with P_{shock}-Exact Calculation

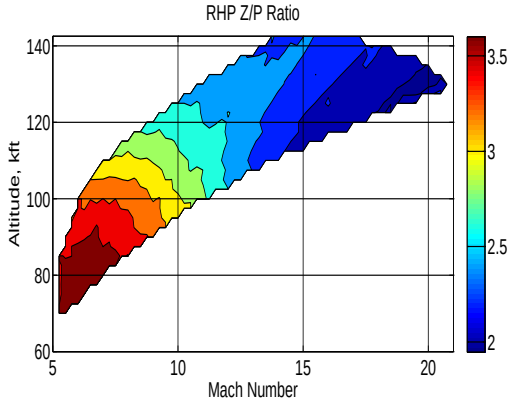

Figure 57: RHP Z-P Ratio Across Trimmable Region with P_{shock}-Exact Calculation

- RHP pole decreases with altitude
- RHP zero decreases with altitude
- Z-P ratio decreases with altitude and Mach number

Computational Time.

Determining the trimmable region with P_{shock}-Exact takes near about 1740 min (29 hrs) with a 2.66GHz processor.

5.5 New Plume Approximation Based on P_{shock}- (P_{shock}-Approx)

New plume approximation is required because of,

- Simple approx is inadequate to determine exact static and dynamic properties of vehicle
- Computational time for P_{shock}-Exact is very high

Careful analysis shows that the plume depends greatly on the following variables,

- Free stream Mach number, M_∞
- Altitude, h
- Engine exit pressure, P_e
- Engine exit temperature, T_e
- Engine exit Mach number, M_e
- Angle-of-Attack (AOA), α

New approximation were obtained by fitting second order regression model. The method of least squares were used to estimate the regression coefficients of linear regression model. In [133], detail method for parameter estimation of linear regression model is given. A regression model were obtained using the JMP package [134]. The aft-body forces (X_e and Z_e) and aft-body moment (M_e) for new plume approximation are as follows,

$$
\begin{aligned}
X_e \;=\;& -241.467549534425 - 73.9674954661361 * M_\infty \\
& +0.0050486001148475 * h + 3.64321295403527 * P_e \\
& -0.453367902206378 * T_e + 169.802464559742 * M_e \\
& -1313.43449446937 * \alpha + M_\infty * (h * 0.000109227890001644) \\
& +M_\infty * (P_e * -0.0132193986773645) + M_\infty * (T_e * -0.00296031950933322) \\
& +M_\infty * (M_e * 3.32246244913899) + M_\infty * (\alpha * 138.851291451297) \\
& +h * (P_e * -0.0000004043642374498) + h * (T_e * 0.0000016751460735802) \\
& +h * (M_e * -0.00147953867007122) + h * (\alpha * -0.0000203301797773823) \\
& +P_e * (T_e * 0.0000370706507825586) + P_e * (M_e * 0.0167514502946311) \\
& +P_e * (\alpha * 1.9413147667132) + T_e * (M_e * 0.052444946205965) \\
& +T_e * (\alpha * 0.124559951410295) + M_e * (\alpha * 164.887922907893)
\end{aligned}
$$

$$
\begin{aligned}
Z_e \;=\;& 1210.23837165371 + 302.013949420582 * M_\infty \\
& -0.0214734092779782 * h - 11.4135426935872 * P_e \\
& +1.42242624051143 * T_e + -657.342569110174 * M_e \\
& +3910.6283852511 * \alpha + M_\infty * (h * -0.000180012229403372) \\
& +M_\infty * (P_e * 0.0730031725579386) + M_\infty * (T_e * 0.00863269595650835) \\
& +M_\infty * (M_e * -17.6546289444599) + M_\infty * (\alpha * -672.989664118864) \\
& +h * (P_e * -0.0000152275594537216) + h * (T_e * -0.0000050232346090014) \\
& +h * (M_e * 0.00574994287507933) + h * (\alpha * 0.0108026616621795) \\
& +P_e * (T_e * -0.000104797065725379) + P_e * (M_e * 0.079527400680424) \\
& +P_e * (\alpha * -0.904242904899507) + T_e * (M_e * -0.174967571864974) \\
& +T_e * (\alpha * -0.404707658456752) + M_e * (\alpha * -664.231047476425)
\end{aligned}
$$

$$
\begin{aligned}
M_e \;=\;& 30504.7420718105 + 7526.15897905715 * M_\infty \\
& -0.522225567065132 * h - 284.414258611145 * P_e \\
& +33.3771913419737 * T_e - 17015.6160234134 * M_e \\
& +90128.9887738779 * \alpha + M_\infty * (h * -0.00746625216849673) \\
& +M_\infty * (P_e * 1.29089451008783) + M_\infty * (T_e * 0.174206012699645) \\
& +M_\infty * (M_e * -430.62129136583) + M_\infty * (\alpha * -16648.4352543596) \\
& +h * (P_e * -0.000229109170739594) + h * (T_e * -0.000112529918954213) \\
& +h * (M_e * 0.14714370350768) + h * (\alpha * 0.360727100868712) \\
& +P_e * (T_e * -0.00185491119434568) + P_e * (M_e * 2.26950322551427) \\
& +P_e * (\alpha * -59.5503942708982) + T_e * (M_e * -4.01635237528439) \\
& +T_e * (\alpha * -11.6411823510669) + M_e * (\alpha * -17057.4823975028)
\end{aligned}
$$

Comparison of different pitching moments acting on vehicle body at Mach 8, 85 kft with P_{shock}-Exact and P_{shock}-Approx calculations are given in Table 5.4

Moment	P_{shock}-Exact (lbs-ft)	P_{shock}-Approx (lbs-ft)
Lower Fore-body	270890	270890
Upper body	-22015	-22015
Vehicle Bottom	-4476.1	-4476.2
Aft-body	-144990	-145000
Engine Inlet	-44275	-44276
Elevator	-54513	-54506
Viscous Moment	-6371.3	-6371.2
Thrust Moment	5753.3	5752.1

Table 5.4: Moments acting on vehicle at Mach 8, 85 kft

From Table 5.4 it is clear that,

- Moments calculated from P_{shock}-Approx are close to moments calculated from P_{shock}-Exact.

Below in Figure 58 - 62, static and dynamic properties of vehicle with Exact Plume Calculation Based on P_{shock} are presented,

Static Properties.

The some of the static properties of vehicle are described below,

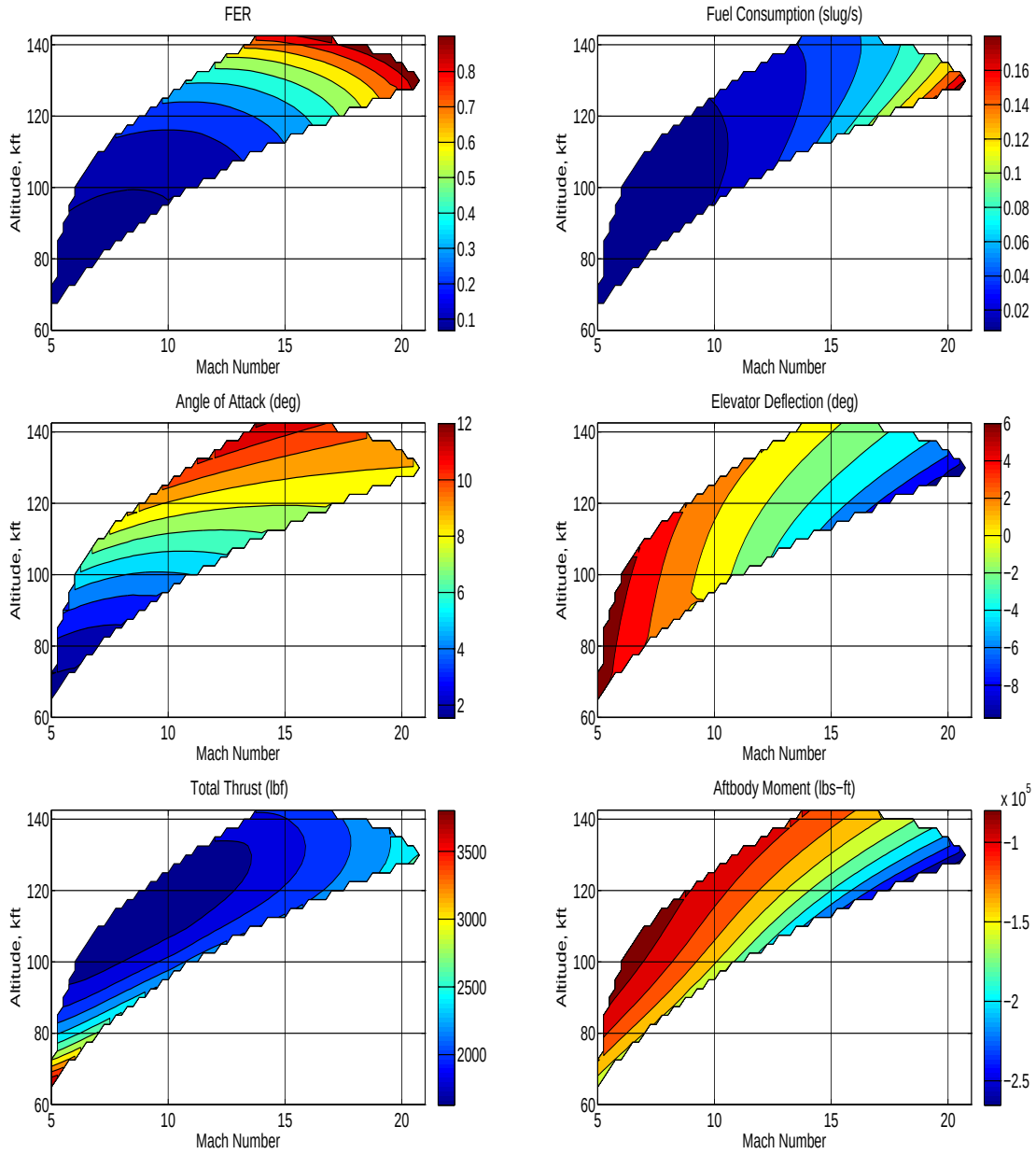

Figure 58: Trim FER, Fuel Consumption, Angle of Attack, Elevator, Total Thrust and Aftbody Moment with P_{shock}-Approx Calculation

- FER and fuel consumption increases with altitude and Mach number
- AOA increases with altitude and Mach number

- Elevator deflection decreases with increase in altitude and Mach number
- Total thrust decreases with increase in altitude and Mach number

Dynamic Properties.

The dynamic properties of vehicle are described below,

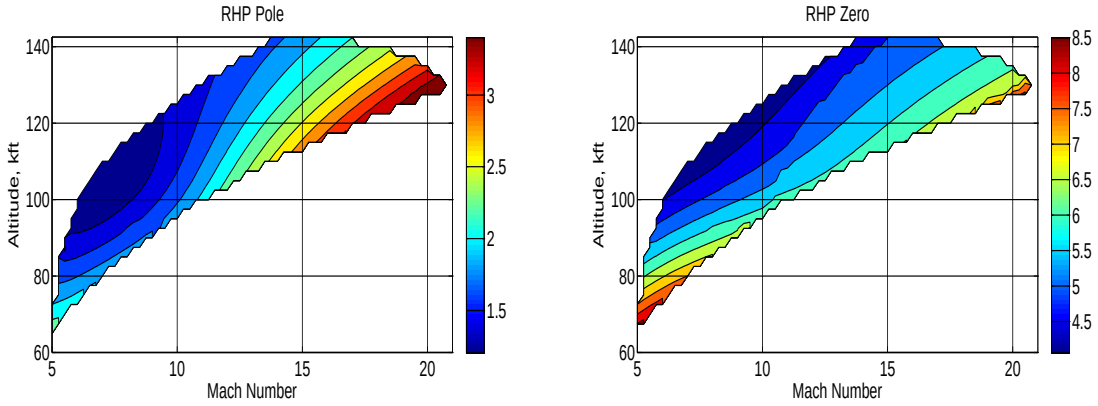

Figure 59: RHP Pole and RHP Zero Across Trimmable Region with P_{shock}-Approx Calculation

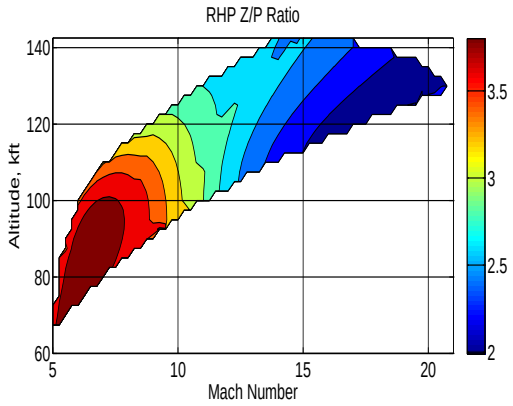

Figure 60: RHP Z-P Ratio Across Trimmable Region with P_{shock}-Approx Calculation

- RHP pole decreases with altitude
- RHP zero decreases with altitude
- Z-P ratio decreases with altitude and Mach number
- In terms of dynamic properties, P_{shock}-Approx is very close to P_{shock}-Exact

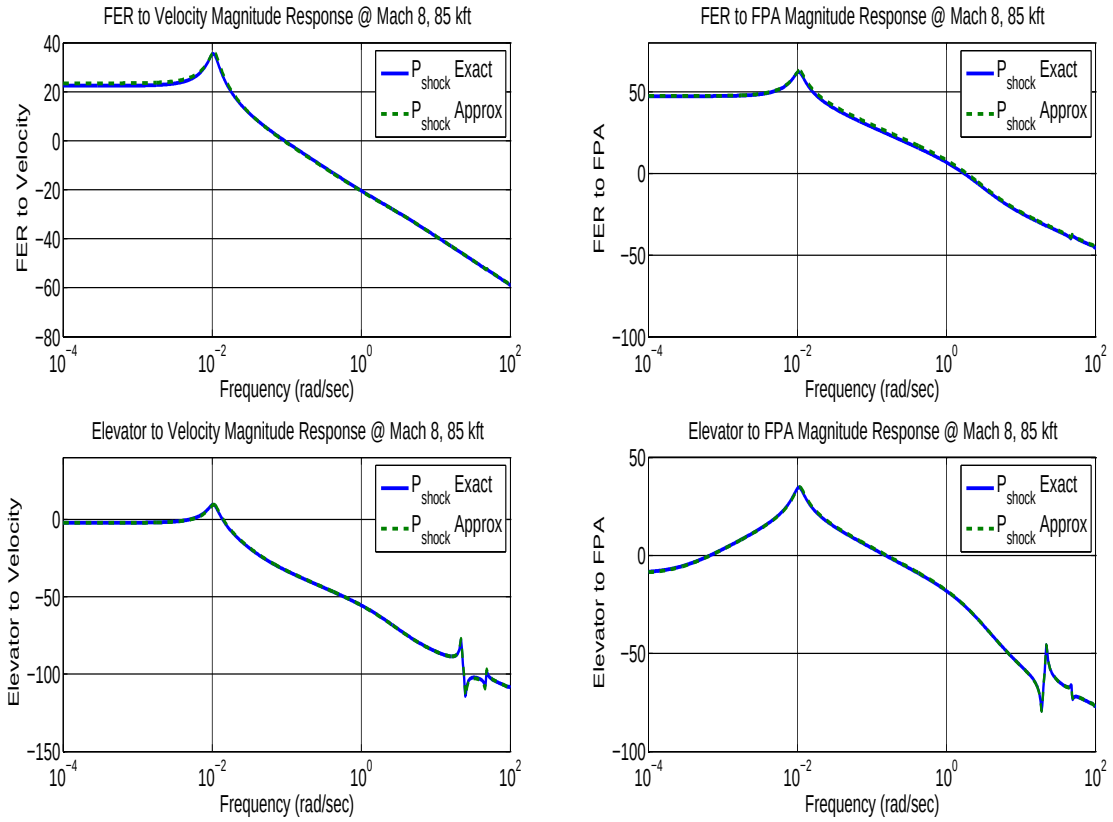

Figure 61: Comparison of Bode Magnitude plots with P_{shock}-Exact and P_{shock}-Approx at Mach 8, 85 kft

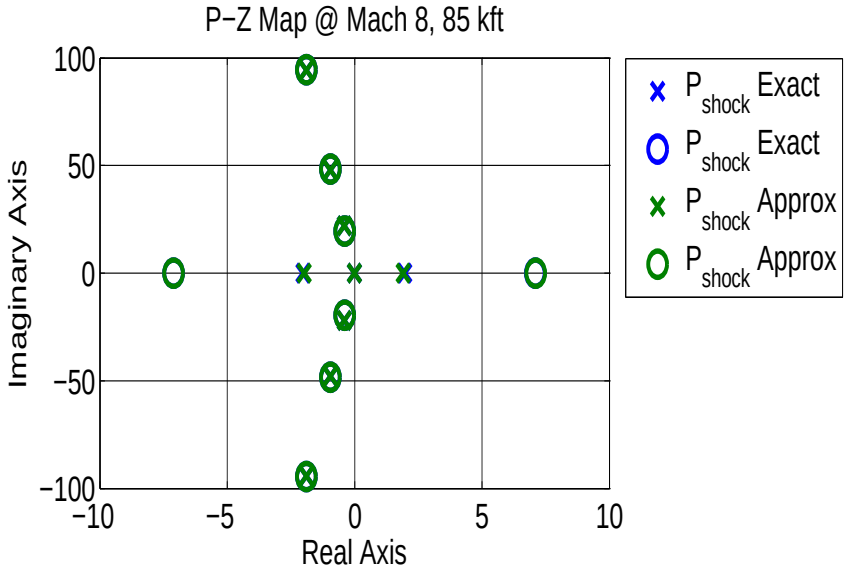

Figure 62: P-Z Map Comparison for P_{shock}-Exact and P_{shock}-Approx at Mach 8, 85 kft

Computational Time.

Determining the trimmable region with P_{shock}-Approx takes near about 40 min with a 2.66GHz processor.

5.6 Summary

In this chapter trade studies w.r.t the vehicle/engine parameters were considered. An engine analysis was conducted based upon traditional as well as control-relevant metrics. The effect of two different methods of plume calculations over vehicle static and dynamic was presented. Approximation to accurate plume calculation was obtained.

6. Control System Design

6.1 Overview

In this chapter, we consider the design of a control system for the nonlinear HSV model. We consider a two input model in this thesis (the FER and elevator are the two controls: see section 2.3 (page 30)), and we consider the FPA and velocity to be the two outputs. As seen in section 4.4 (page 95), the system is unstable and non-minimum phase. We consider some of the control challenges for the model, and present a simple control architecture to stabilize the linearized plant and track target velocity and FPA commands. We consider the changes in the controller and the trade-offs associated with different vehicle configurations.

Fundamental Questions. This chapter considers the following control-relevant questions:

- What are the control challenges for the model?
- What amount of controller complexity is needed?
- How can control be combined with vehicle design?

This chapter is organized as follows: section 6.2 (page 130) considers the control challenges associated with the model. In section 6.3 (page 136), controller design methodology and performance trade-offs associated with vehicle performance are discussed.

6.2 Control Challenges

In this section we present some of the challenges associated with the control of the HSV model. Some of the key challenges/limitations associated with the model are:

- Unstable and non-minimum phase plant with lightly damped flexible modes
- Varying Dynamic Characteristics
- Control Saturation Constraints
- Gap between the linearized plant
- Condition Number of plant

We discuss these issues in more detail below.

Linearized Plant Dynamics. In chapter 4, we considered a linearization procedure and the dynamics of the linearized model. Also, in chapter 5, we consider the dynamic properties for a vehicle with different methods of plume computation. From these studies, we see that the linearized model has the following properties:

- RHP Pole - The long lower forebody of typical hypersonic waveriders combined with a rearward shifted center-of-gravity (CG), results in a pitch-up instability. The linearized plant is hence unstable (unless the CG is shifted forward significantly). The instability requires a minimum BW for stability [97].
- RHP zero - The non-minimum phase (inverse response) behavior is associated with the elevator to flight-path-angle (FPA) map and is characteristic of tail-controlled vehicles, unless a canard is used [123, 124]. It is understood, of course, that any canard approach would face severe heating, structural, and reliability issues. The RHP zero limits the maximum achievable bandwidth [106–108].
- Lightly damped flexible modes - The flexible modes affect the rigid body dynamics through generalized forces (see section 2.1, page 22, or [9]). Exciting the flexible modes affects the outputs and controls - structural flexing impacts the bow shock. This, in turn impacts the scramjet's inlet properties, thrust generated, aft body forces, the associated pitching moments, and hence the vehicle's attitude. Given the tight altitude-Mach flight regime - within the air-breathing corridor [19] - that such vehicle must operate within, the concern is amplified. We see that there are significant aeroelastic-propulsive interactions. Flexible effects also impact the AOA seen by the elevator, and degrade the performance of a canard ganged to the elevator via a static gain [9]. In short, one must be careful that the control system BW and complexity are properly balanced so that these lightly damped flexible modes are not overly excited - the flexible modes limit the maximum achievable bandwidth [106–108].

Control Saturation Constraints Control saturation is of particular concern for unstable vehicles such as the one under consideration. State-dependent margins can limit the speed/size of the commands that may be followed. Two specific saturation nonlinearities are a concern for any control system implementation.

- *Maximum Elevator/Canard Deflection and Instability*. FPA is controlled via the elevator/canard combination [123]. Because these dynamics are inherently unstable, elevator saturation can result in instability [105]. Classical anti-windup methods may be inadequate to address the associated issues - particularly when the vehicle is open loop unstable. The constraint enforcement method within [105, 135] and generalized predictive control [106] have been used to address such issues. It should be noted that control surface/actuator rate limits must also be properly addressed by the control system in order to avoid instability.

- *Thermal Choking/Unity FER: State Dependent Constraint*. In section 2.7.5, we defined a instantaneous state dependent margin (FER margin) for the fuel equivalence ratio. The FER margin constraints impose BW and reference command size constraints. The FER constraint can be computed (on-line) based on the flight condition, and must be accounted for by the control law. Here, uncertainty is of great concern because of potential engine unstart issues (see section 2.7.5, page 48) - issues not captured within the model. Engineers, of course, would try to "build-in protection" so that this is avoided. As such, engineers are forced to tradeoff operational envelop for enhance unstart protection. In [106], the authors consider GPC-based constraint enforcement to address thermal choking, unity FER, and elevator saturation constraint issues in a systematic non-conservative manner. Other papers addressing saturation include: saturation prevention [7, 105, 136], and thermal choking prevention[104, 136].

Varying Dynamic Characteristics. Within [104], it is shown that the nonlinear model changes significantly as a function of the flight condition. Specifically, it is shown that the vehicle pitch-up instability and non-minimum phase zero vary significantly across the vehicle's trimmable region. In addition, the mass of the vehicle can be varied during a simulation in order to represent fuel consumption. Several methods have been presented in the literature to deal with the nonlinear nature of the model. Papers addressing modeling issues include: nonlinear modeling of longitudinal dynamics [13], heating effects and flexible dynamics [5, 9, 137], FPA dynamics [123], unsteady and viscous effects [1, 4], and high fidelity engine modeling [113, 138, 139]. Papers addressing nonlinear control issues include: control via classic inner-outer loop architecture[107], nonlinear robust/adaptive control [140], robust linear output feedback [131], control-oriented modeling [2], and linear parameter-varying control of flexible dynamics [141].

Gap between Linearized Plant The gap metric represents a system-theoretic measure that quantifies the "distance" between two dynamical systems and whether or not a common controller can be deployed for the systems under consideration [142]. Within [143], the gap between two LTI dynamical systems (P_1, P_2) is defined as follows:

$$g(P_1, P_2) \stackrel{\text{def}}{=} \max\{ \inf_{Q \in H_\infty} \| \left[\begin{smallmatrix} D_1 \\ N_1 \end{smallmatrix}\right] - \left[\begin{smallmatrix} D_2 \\ N_2 \end{smallmatrix}\right] Q \|_\infty, \quad \inf_{Q \in H_\infty} \| \left[\begin{smallmatrix} D_2 \\ N_2 \end{smallmatrix}\right] - \left[\begin{smallmatrix} D_1 \\ N_1 \end{smallmatrix}\right] Q \|_\infty \ \} \quad (6.1)$$

where $P_1 = N_1 D_1^{-1}$, $P_2 = N_2 D_2^{-1}$, and (N_i, D_i) denotes a normalized right coprime factorization for P_i $(i = 1, 2)$ in the sense of [144]. The gap metric (and the ν gap [145]) has often been considered from a robustness perspective in the stabilization of feedback systems [146]. Within [147], the authors relate the gap metric with traditional stability margins. The gap metric has also been considered for the design of controllers for space vehicles [148, 149]. In subsequent section, controller design ware presented. The controller were first designed on approximate plant and then implemented on exact plant. If the gap

between the two plants were big, the deviation of responses from approximate plant and exact plant were also big. The comparison between the different plant gaps at Mach 8, 85kft are shown below,

Models	Simple Approx	P_∞-Exact	P_{shock}-Exact	P_{shock}-Approx
Simple Approx	0	1	1	1
P_∞-Exact	1	0	0.28	0.32
P_{shock}-Exact	1	0.28	0	0.05
P_{shock}-Approx	1	0.32	0.05	0

Table 6.1: Gap between plants (Mach 8, 85kft)

Condition Number of plant Figure 63 show the condition number of the slow and fast engine for P_{shock}-Exact and P_{shock}-Approx calculations. We see that the fast engine has higher condition numbers in all cases. Ill conditioned plants can cause control problems [150, 151].

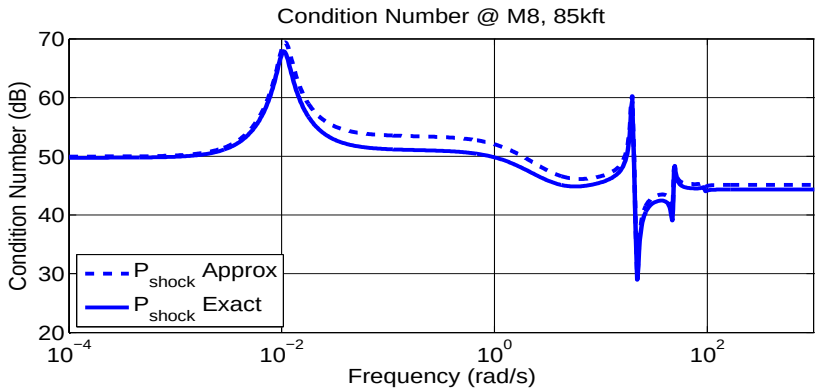

Figure 63: Condition Number at Mach 8, 85kft

The pick condition number for P_{shock}-Exact and P_{shock}-Approx calculations were shown in figure 64 and 65

- Condition number decreases with increase in altitude and Mach number

Engine size (aggressiveness, acceleration capability) and the associated vertical moment arm (distance thrust vector below vehicle center of gravity) are shown to be particularly significant. As the engine is made more aggressive and the associated vertical moment arm

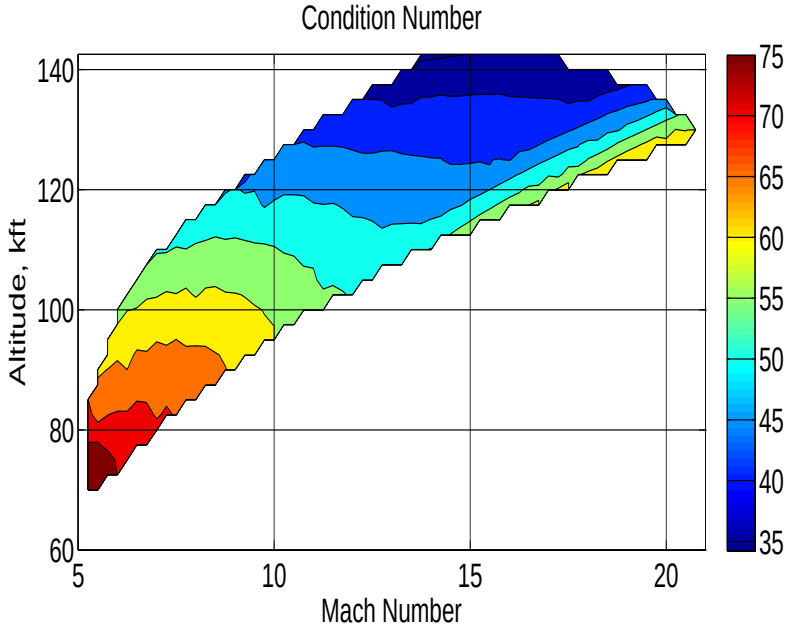

Figure 64: Condition Number for P_{shock}-Exact calculations

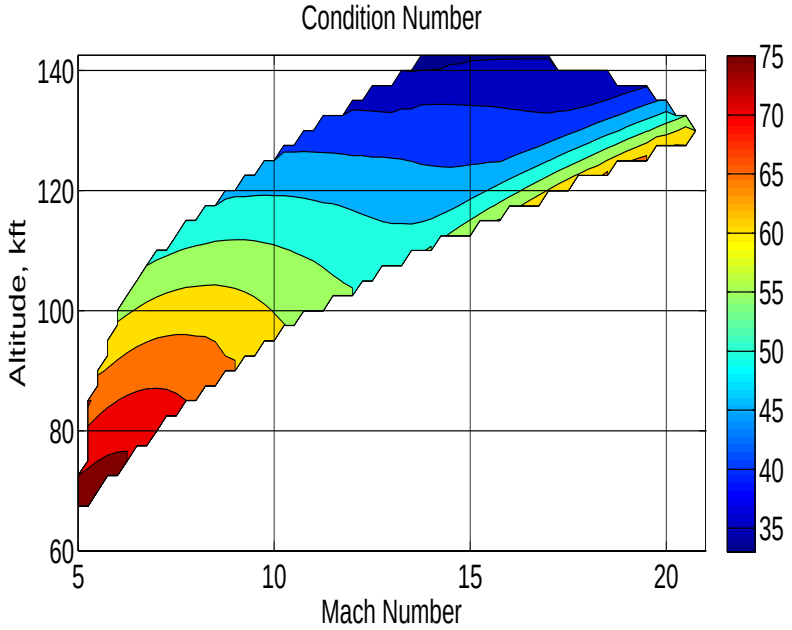

Figure 65: Condition Number for P_{shock}-Approx calculations

is increased, the coupling from FER to FPA increases. This increased coupling makes the control system design more challenging - requiring a multivariable controller under many likely mission scenarios (e.g. high acceleration, large payload/volumetric requirements).

6.3 Controller Design

For controller design $\mathcal{H}^\infty$ methodology were used. Figure 66 generalized feedback system were shown, where G represents generalized plant which contains actual plant and weighting functions. K represents controller.

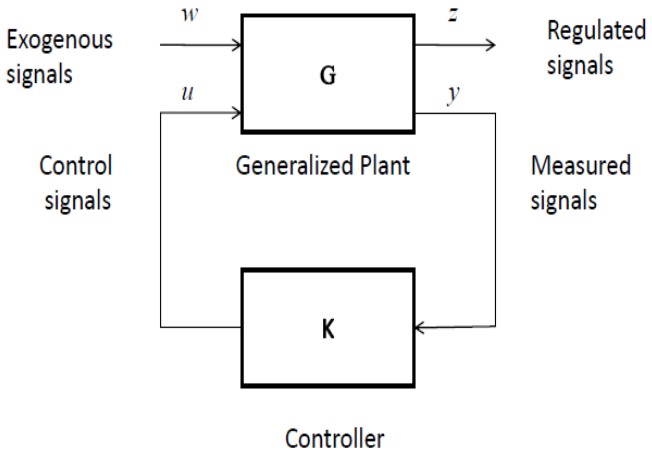

Figure 66: Generalized Feedback System

Problem Statement Find a real-rational (finite-dimensional) proper internally stabilizing controller K that satisfies,

$$\|T_{wz}\|_{\mathcal{H}^\infty} = \left\| \begin{bmatrix} W_1 S \\ W_2 K S \\ W_3 T \end{bmatrix} \right\|_{\mathcal{H}^\infty} < \gamma \tag{6.2}$$

where W_1, W_2 and W_3 are weighting functions and $\gamma > 0$ is a parameter to be minimized. General rules (guidelines) for selecting the weighting functions W_1, W_2 and W_3 are now developed [152]. The mixed-sensitivity problem is defined by weighting functions possess-

ing the following structure for each signal channel:

$$W_{1_i} = \frac{s/M_{e_i} + \omega_{e_i}}{s + \epsilon_1 \omega_{e_i}} \tag{6.3}$$

$$W_{2_j} = \frac{s^2 + \epsilon_{u_j} s + \omega_{u_j}}{s^2 + \epsilon_2 s + \omega_2} \tag{6.4}$$

$$W_{3_k} = \frac{s + \omega_{y_k}/M_{y_k}}{\epsilon_3 s + \omega_{y_k}} \tag{6.5}$$

where $(i = 1, 2, ..., n_y, j = 1, 2, ..., n_u, k = 1, 2, ..., n_y)$, and n_y, and n_u represent the number of measurements and the number of controls respectively. In this case three outputs were measured in the feedback loop, and two controls were used. The three measurements used were the speed (v), flight path angle (γ), and pitch (θ). Plant has two control inputs FER and elevator deflection.

Design Procedure

- $\mathcal{H}^\infty$ design methodology was used
- P_{shock}-Approx plants used (flight condition - Mach 8, 85kft)
- Controller design based on rigid plants
- Peak sensitivities at error maintained at less than 4 dB
- Attempted to minimize peak sensitivities at controls

Results

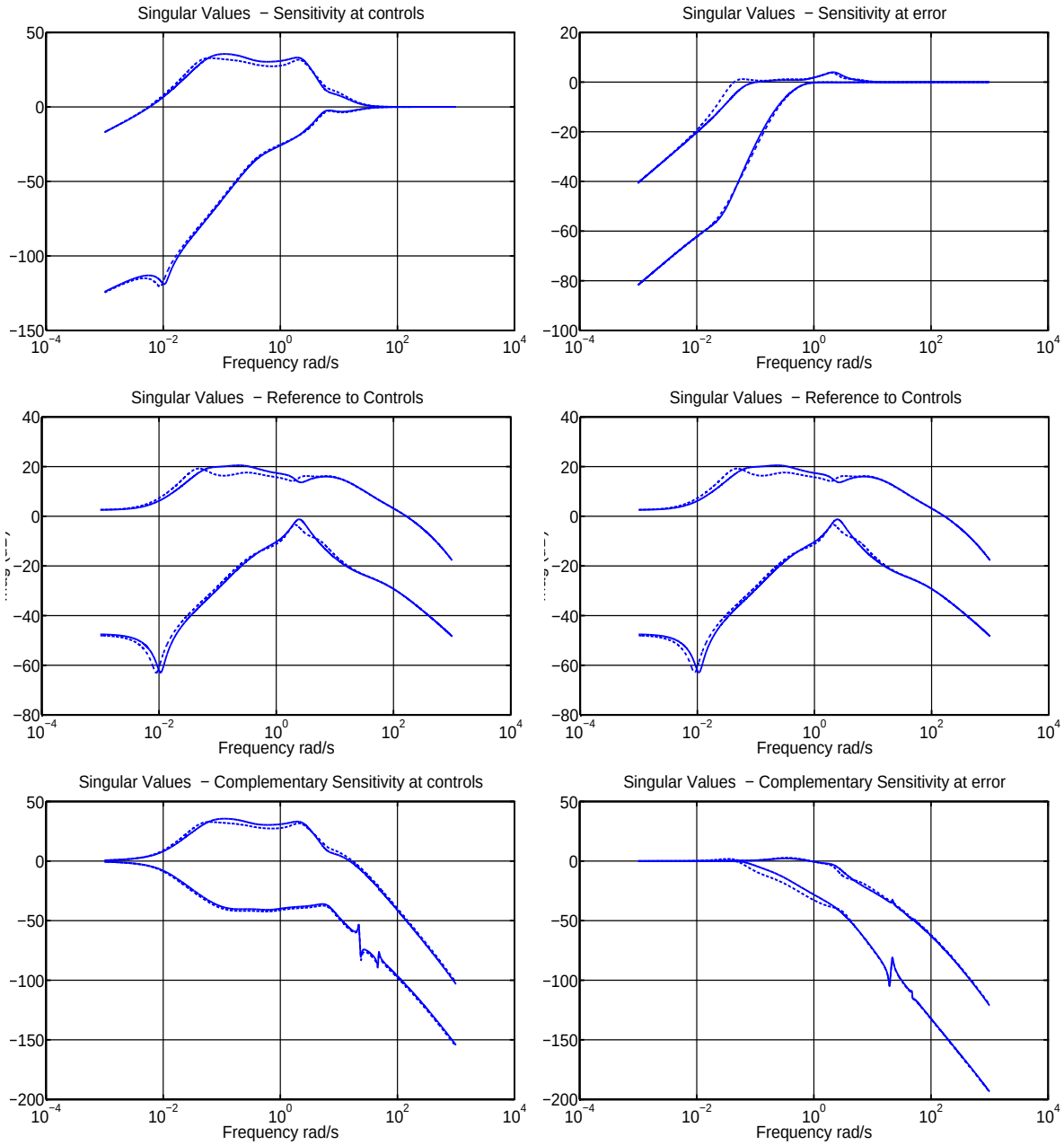

Figure 67: Singular Values for Ts= 10sec, when P_{shock}-Approx Controller Applied to P_{shock}-Approx(solid) and P_{shock}-Exact(dotted) at Mach 8, 85kft

- Singular values of P_{shock}-Approx and P_{shock}-Exact are close.

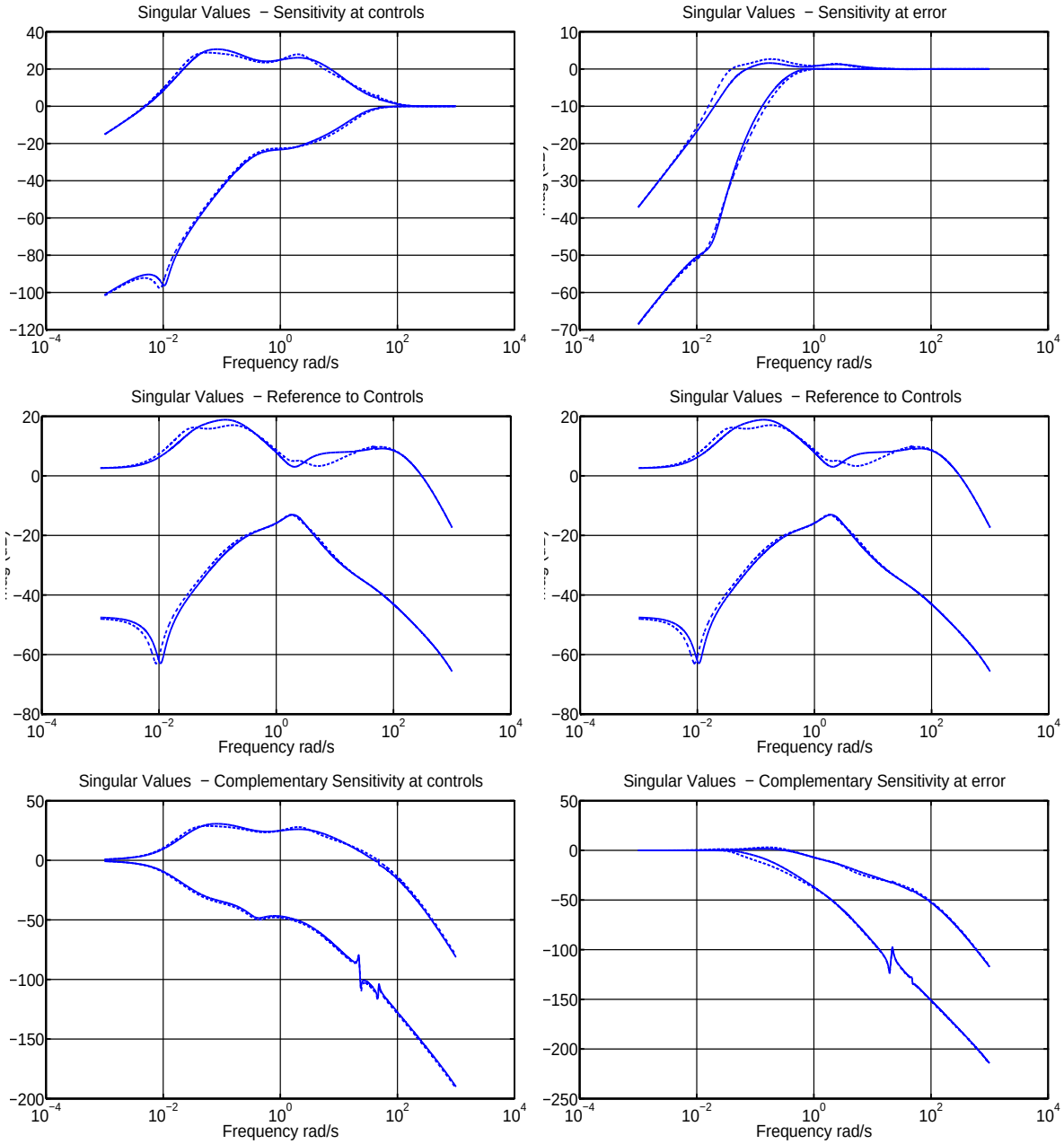

Figure 68: Singular Values for Ts= 25sec, when P_{shock}-Approx Controller Applied to P_{shock}-Approx(solid) and P_{shock}-Exact(dotted) at Mach 8, 85kft

- Singular values of P_{shock}-Approx and P_{shock}-Exact are close.

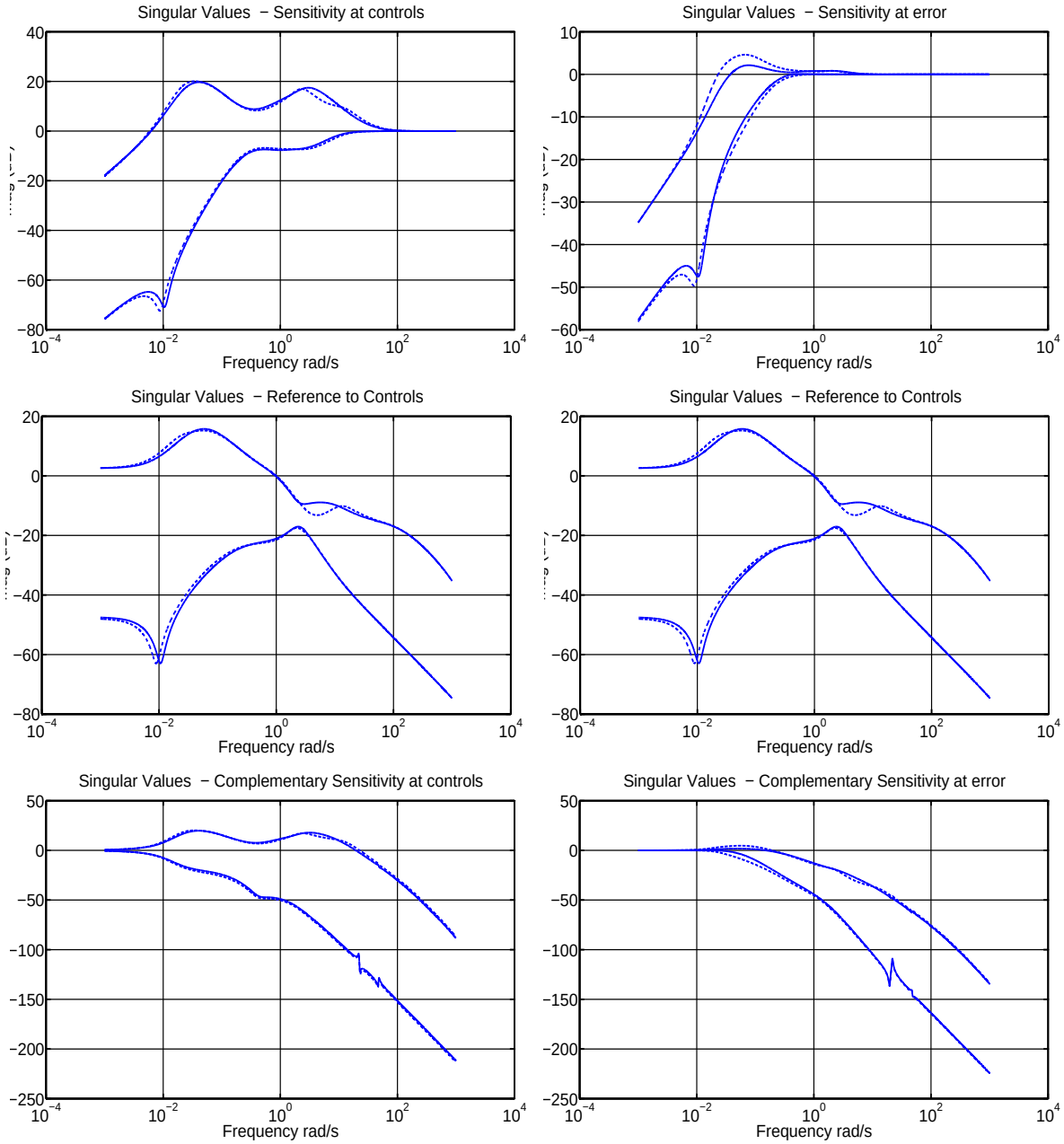

Figure 69: Singular Values for Ts= 50sec, when P_{shock}-Approx Controller Applied to P_{shock}-Approx(solid) and P_{shock}-Exact(dotted) at Mach 8, 85kft

- Singular values of P_{shock}-Approx and P_{shock}-Exact are close.

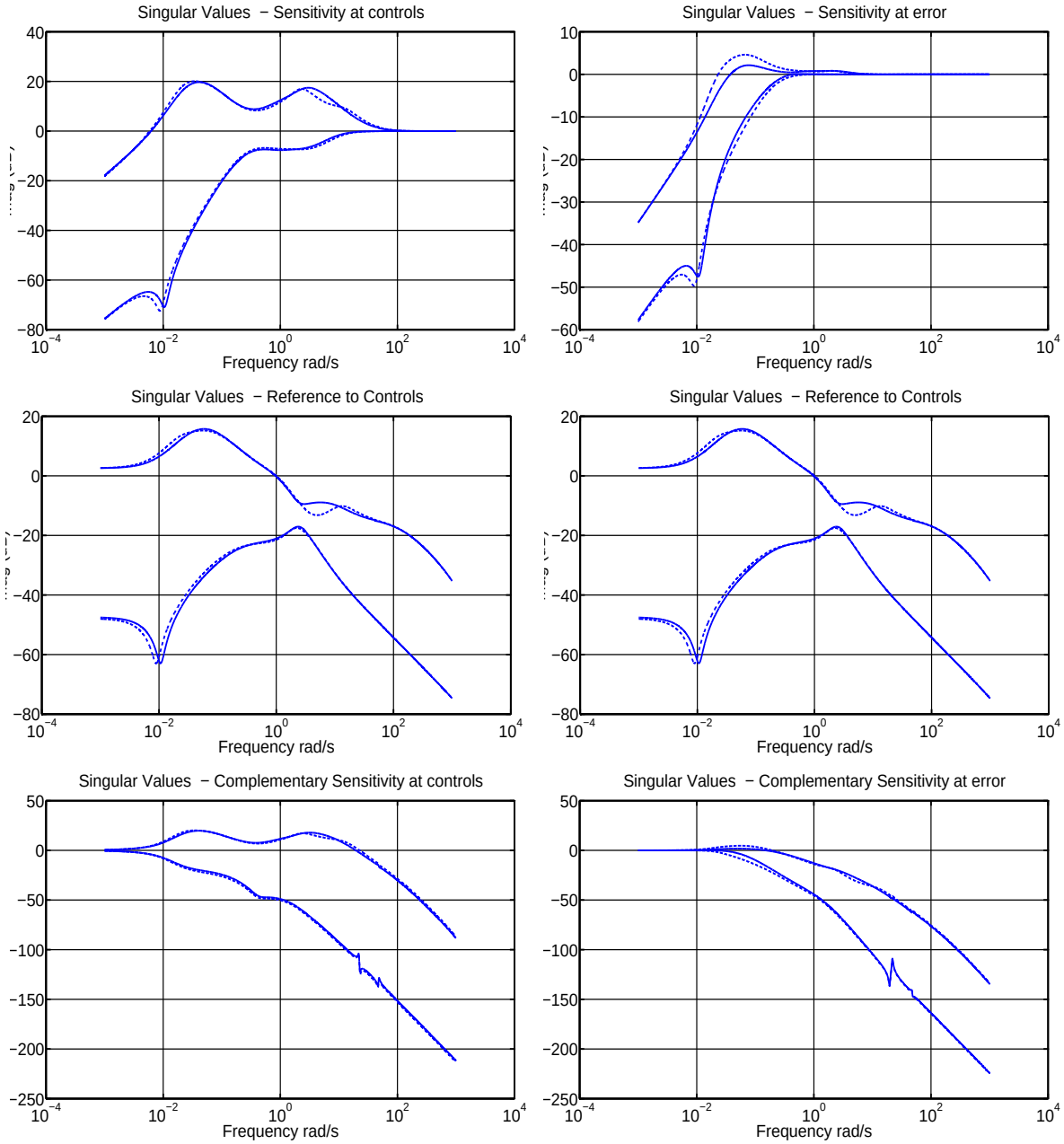

Figure 70: Singular Values for Ts= 50sec, when P_{shock}-Approx Controller Applied to P_{shock}-Approx(solid) and P_{shock}-Exact(dotted) at Mach 8, 85kft

- Singular values of P_{shock}-Approx and P_{shock}-Exact are close.

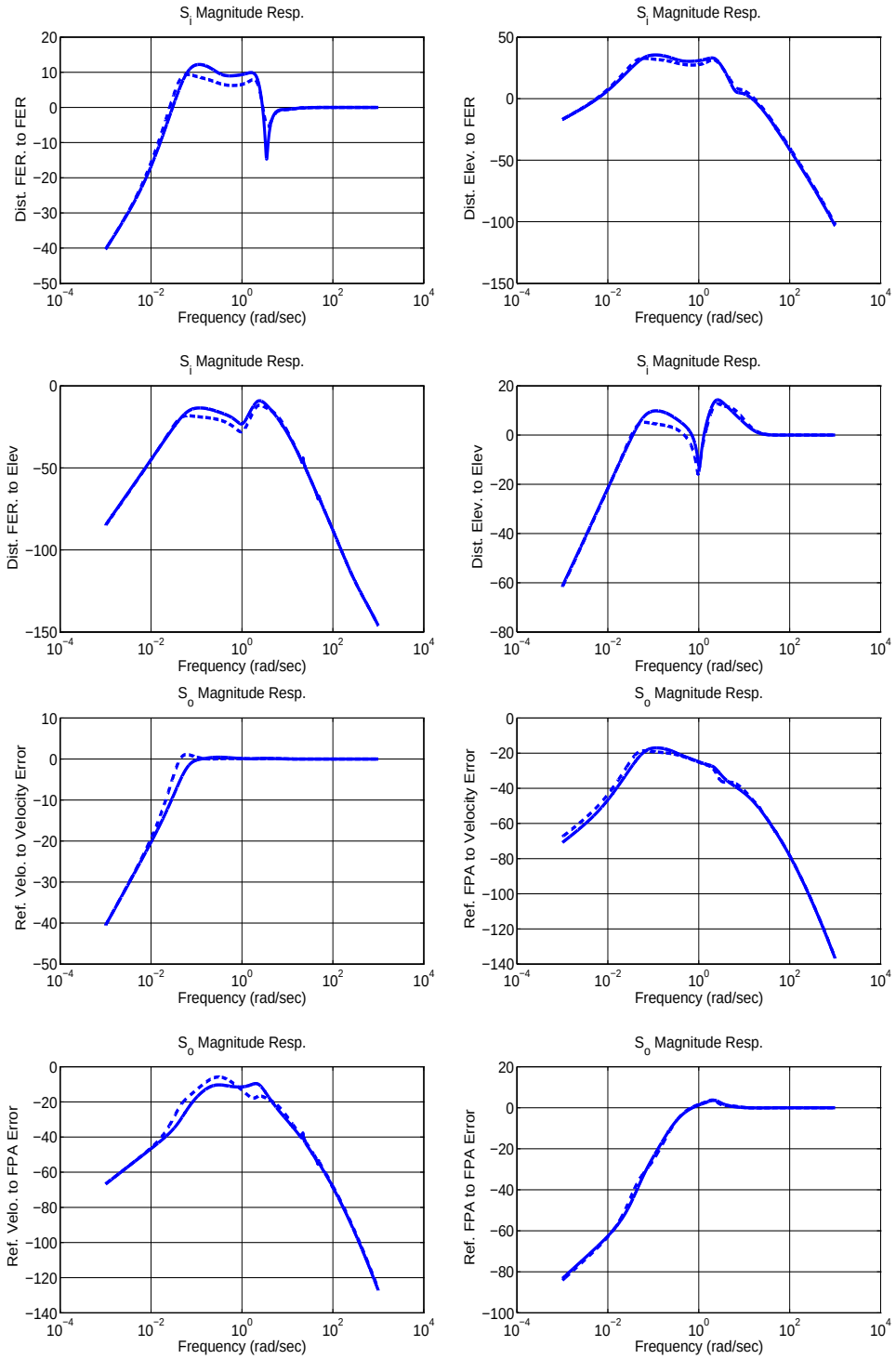

Figure 71: Bode Magnitude Plots for Ts= 10sec, when P_{shock}-Approx Controller Applied to P_{shock}-Approx(solid) and P_{shock}-Exact(dotted) at Mach 8, 85kft

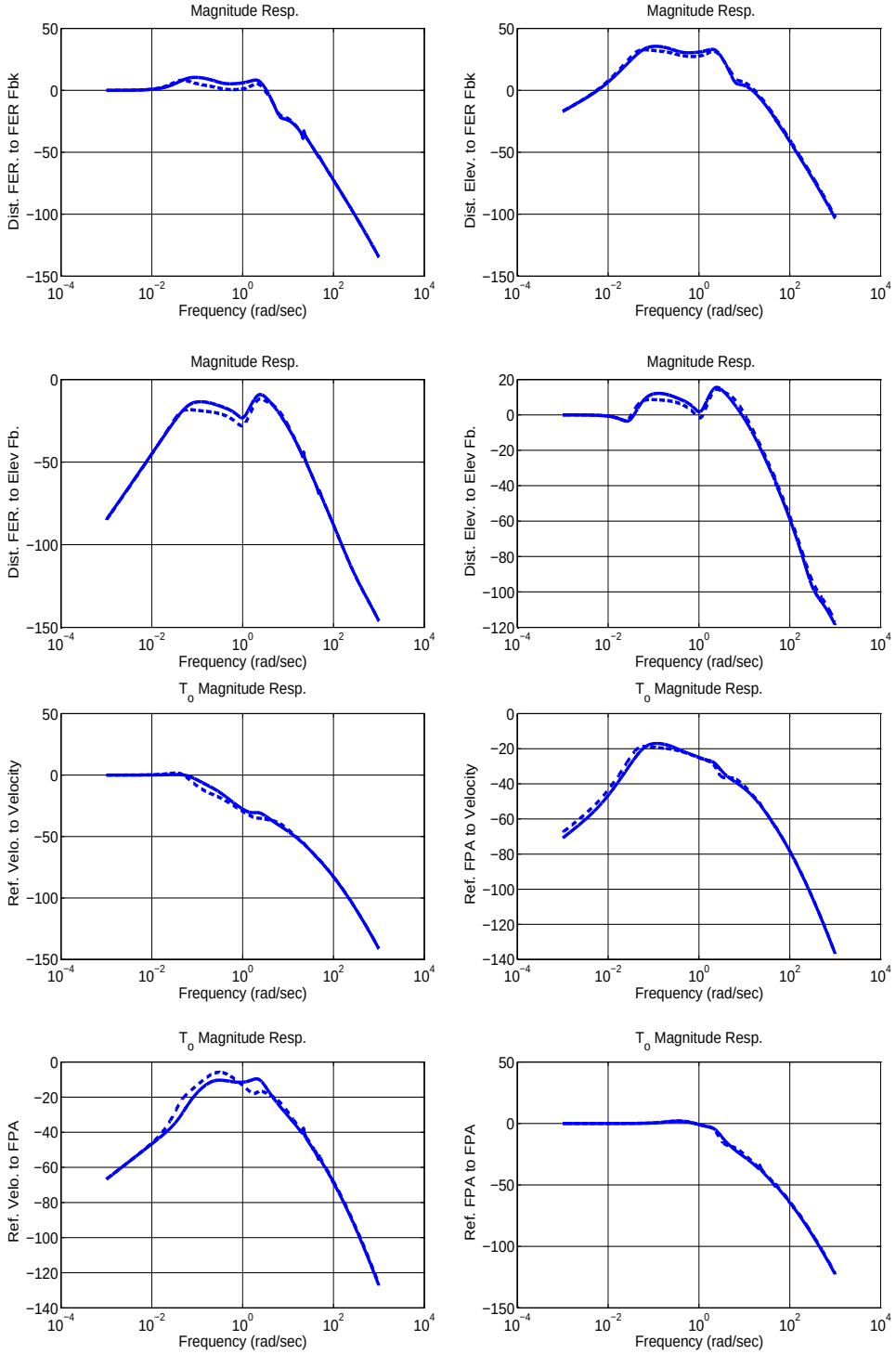

Figure 72: Bode Magnitude Plots for Ts= 10sec, when P_{shock}-Approx Controller Applied to P_{shock}-Approx(solid) and P_{shock}-Exact(dotted) at Mach 8, 85kft

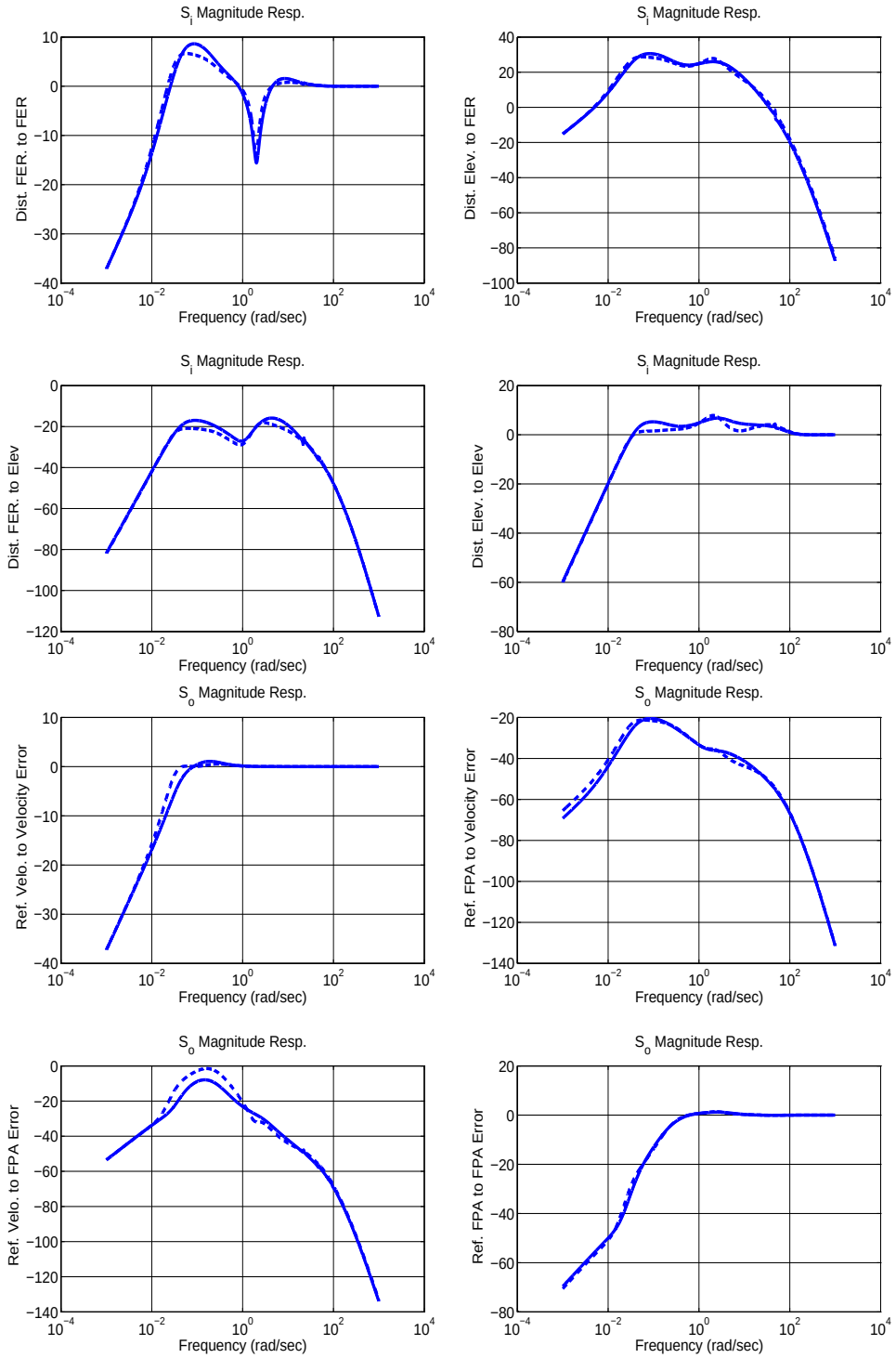

Figure 73: Bode Magnitude Plots for Ts= 25sec, when P_{shock}-Approx Controller Applied to P_{shock}-Approx(solid) and P_{shock}-Exact(dotted) at Mach 8, 85kft

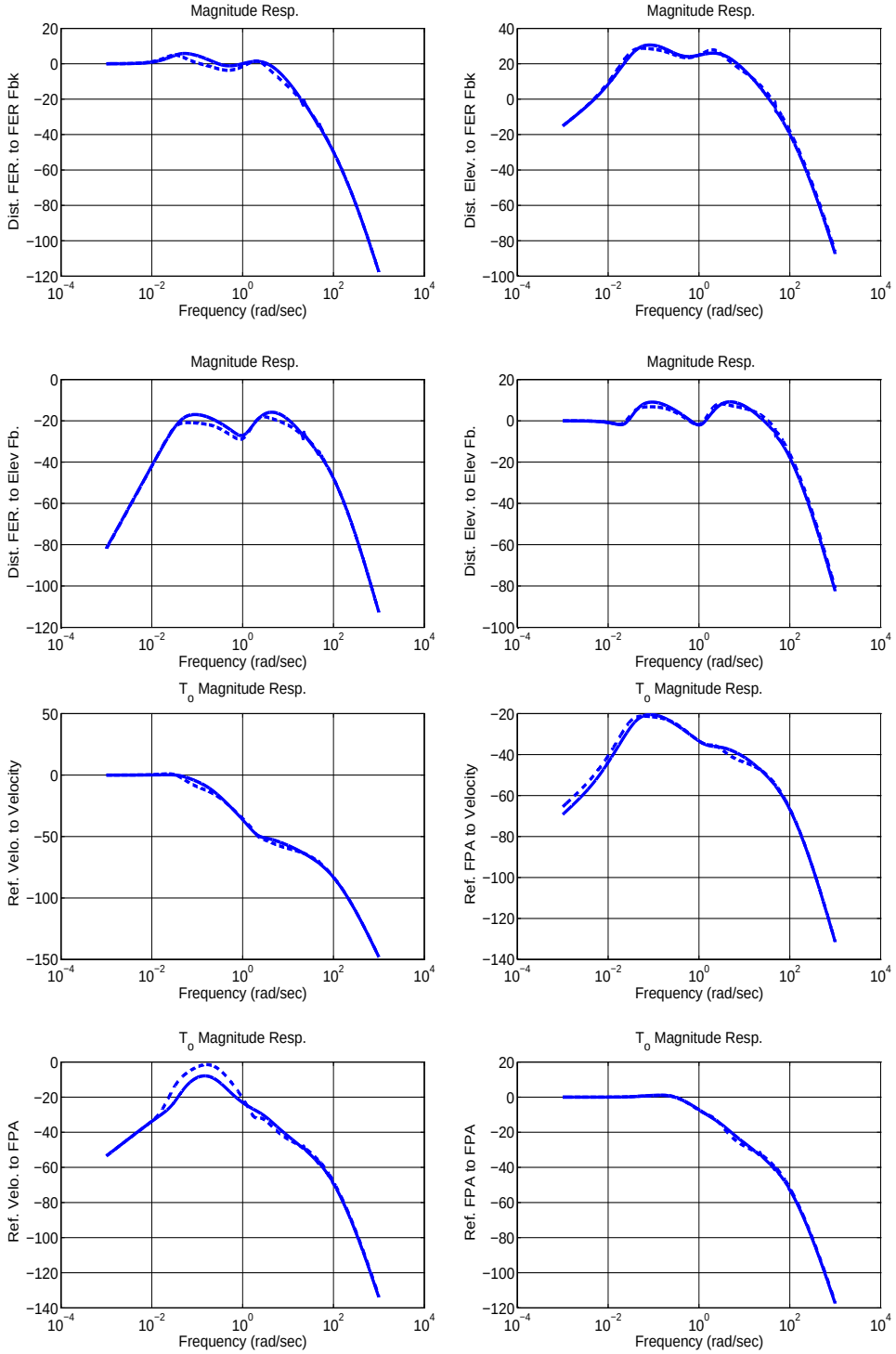

Figure 74: Bode Magnitude Plots for Ts= 25sec, when P_{shock}-Approx Controller Applied to P_{shock}-Approx(solid) and P_{shock}-Exact(dotted) at Mach 8, 85kft

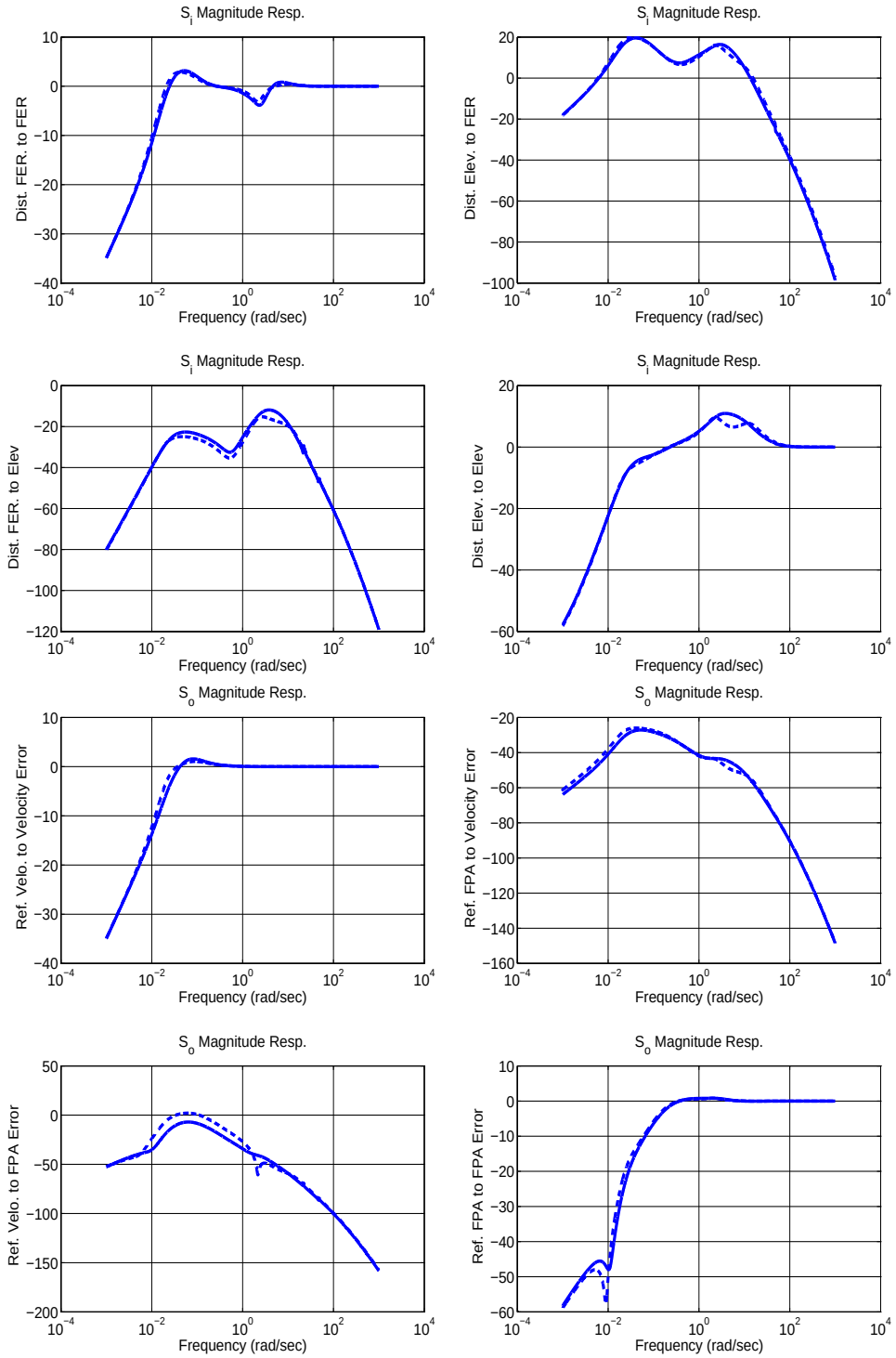

Figure 75: Bode Magnitude Plots for Ts= 50sec, when P_{shock}-Approx Controller Applied to P_{shock}-Approx(solid) and P_{shock}-Exact(dotted) at Mach 8, 85kft

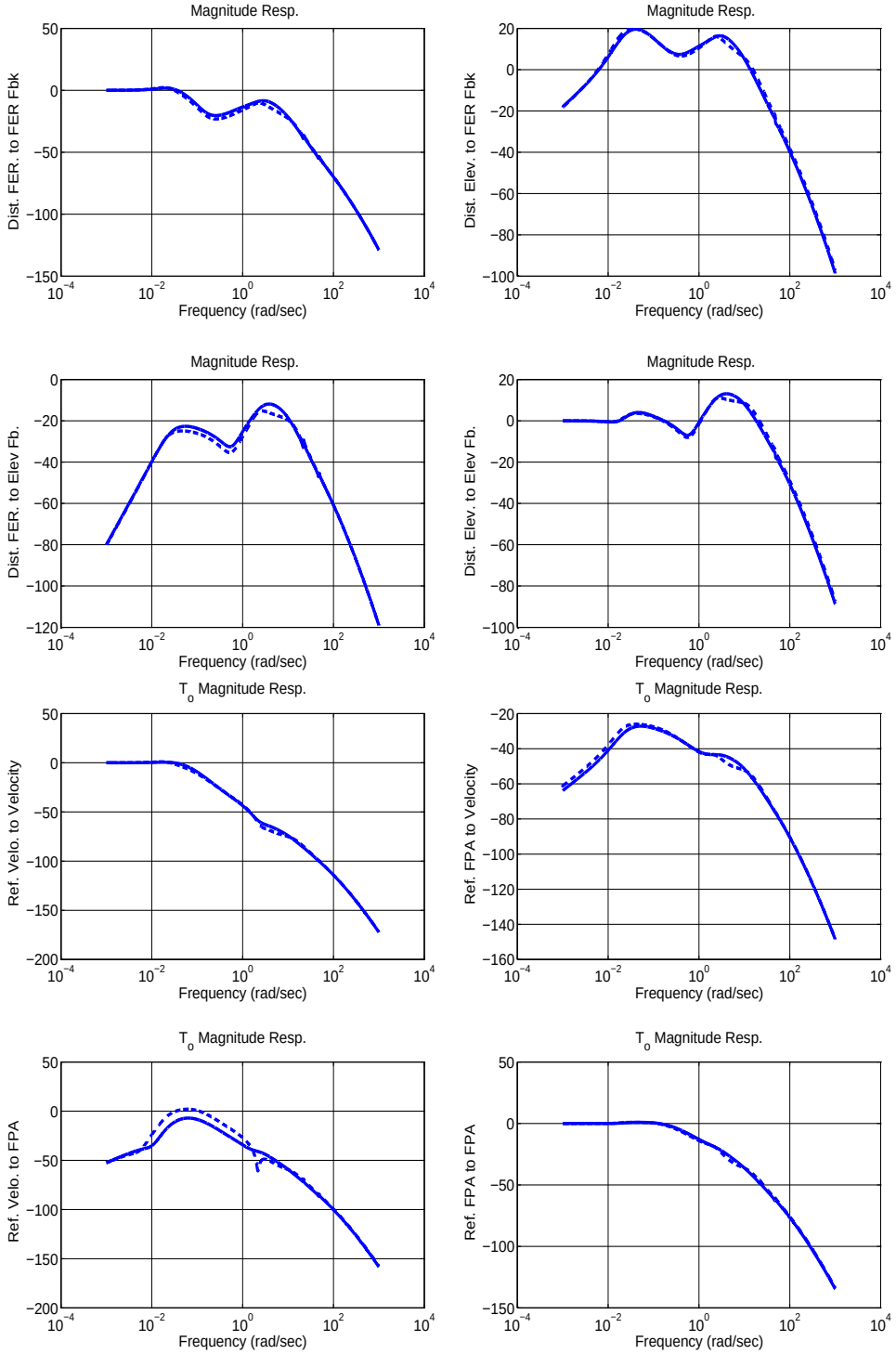

Figure 76: Bode Magnitude Plots for Ts= 50sec, when P_{shock}-Approx Controller Applied to P_{shock}-Approx(solid) and P_{shock}-Exact(dotted) at Mach 8, 85kft

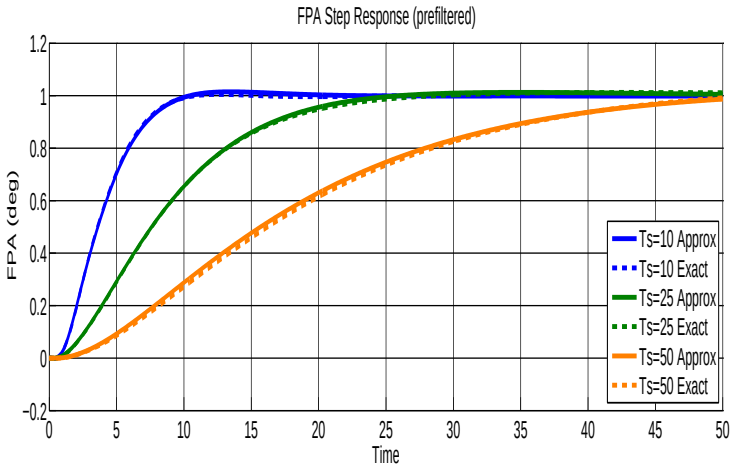

Figure 77: Step Response for Ts=10,25 and 50 sec

Table 6.2 illustrates tradeoffs in the peak singular value of the sensitivities as the settling time (for step FPA commands) is increased. All sensitivities given represent peak sensitivities measured in dB.

Time (s)	$\overline{S_o}$	$\overline{T_o}$	$\overline{S_i}$	$\overline{T_i}$	$\overline{KS}$	$\overline{S_iP}$
10	3.98	2.13	35.46	35.46	20.52	13.84
25	1.58	1.61	30.63	30.63	18.84	16.64
50	2.14	1.78	19.70	19.75	15.74	23.47

Table 6.2: Closed loop properties for different settling time

Note that as the settling time decreases, peaking properties at the plant input become worse. This is an expected tradeoff for a poorly conditioned plant such as ours. We apply the P_{shock}-Approx based designs to the P_{shock}-Exact model. The results are shown in Table 6.3.

Time (s)	$\overline{S_o}$	$\overline{T_o}$	$\overline{S_i}$	$\overline{T_i}$	$\overline{KS}$	$\overline{S_iP}$
10	3.80	2.79	32.76	32.76	19.23	13.45
25	2.67	3.03	28.74	28.74	17.01	15.61
50	4.62	4.68	20.08	20.12	15.19	23.11

Table 6.3: Closed loop properties (P_{shock}-Approx controller with P_{shock}-Exact Plant)

From Tables 6.2 and 6.3, we observe the following:

- $\overline{S_i}$, $\overline{T_i}$ and $\overline{KS}$ decrease with increasing settling time.
- $\overline{S_i P}$ increases with increasing settling time.
- Plants with higher condition numbers have more severe trade-offs.
- Closed loop properties of P_{shock}-Exact with P_{shock}-Approx based controller are close to each other.
- Large FPA settling time is needed in order to obtain reasonable (performance/robustness) properties at the plant input

6.4 Summary

In this chapter, $\mathcal{H}^\infty$ controller design for the hypersonic vehicle was presented. The nominal performance of the controller were presented. It is shown that, the peak frequency-dependent (singular value) conditioning of the two-input two-output plant (FER-elevator to speed-FPA) worsens. This forces the control designer to trade off desirable (performance/robustness) properties between the plant input and output. For the vehicle under consideration (with a very aggressive engine and significant coupling), it is shown that a large FPA settling time is needed in order to obtain reasonable (performance/robustness) properties at the plant input. The results in this section offer insight into control-relevant vehicle design.

7. Conclusions

7.1 Summary

This thesis examines modeling, analysis, vehicle design, and control system design issues for scramjet-powered hypersonic vehicles. A nonlinear 3DOF (degree of freedom) longitudinal model which includes aero-propulsion-elasticity effects is used for all analysis. The model is based upon classical compressible flow and Euler-Bernouli structural concepts. While higher fidelity CFD (computational fluid dynamics) and FE (finite element) methods are needed for more precise intermediate and final evaluations, the methods presented within the thesis are shown to be useful for guiding initial (control-relevant) design work. The model is used to examine the vehicle's static and dynamic characteristics over the vehicle's trimmable region. The vehicle is characterized by unstable non-minimum phase dynamics with significant (approximately lower triangular) longitudinal coupling between fuel equivalency ratio (FER) or fuel flow and flight path angle (FPA). Propulsion system design issues are given special consideration. The impact of engine characteristics (design) and plume modeling on control system design are shown to be very important.

Engine size (aggressiveness, acceleration capability) and the associated vertical moment arm (distance thrust vector below vehicle center of gravity) are shown to be particularly significant. As the engine is made more aggressive and the associated vertical moment arm is increased, the coupling from FER to FPA increases. This increased coupling makes the control system design more challenging - requiring a multivariable controller under many likely mission scenarios (e.g. high acceleration, large payload/volumetric requirements).

As the effective coupling from FER to FPA is increased, it is shown the peak frequency-dependent (singular value) conditioning of the two-input two-output plant (FER-elevator to velocity-FPA) worsens. This forces the control designer to trade off desirable (performance/robustness) properties between the plant input and output. For the vehicle under consideration (with a very aggressive engine and significant coupling), it is shown that a

large FPA settling time is needed in order to obtain reasonable (performance/robustness) properties at the plant input. Ideas for alleviating this fundamental tradeoff are highlighted.

Plume modeling is also shown to be particularly significant. It is specifically shown that the fidelity of the plume (shear-layer) model is critical for adequately predicting vehicle static properties, dynamic properties, and assessing the overall difficulty of the control system design. More precisely, if insufficient plume fidelity is used for the design plant model then an associated control system design may not work well with the higher fidelity plant.

7.2 Ideas for Future Research

The work presented in this thesis provides motivation for conducting comprehensive trade studies using higher fidelity vehicle models;i.e. 6DOF + flexibility [153]. As such, the work motivates the development of general 6DOF tools that adequately address control-relevant modeling, analysis, and design issues for hypersonic vehicles during the early vehicle conceptualization/design phases. One specific concern will be to assess when conclusions obtained from a 3DOF model may be misleading.

Future work will also involves comparing these analytical solutions with higher fidelity CFD (computational fluid dynamics) solutions.

REFERENCES

[1] M. A. Bolender, M. W. Oppenheimer, and D. B. Doman, "Effects of unsteady and viscous aerodynamics on the dynamics of a flexible air-breathing hypersonic vehicle," in *AIAA 2007-6397*, 2007.

[2] J. T. Parker, A. Serrani, S. Yurkovich, M. A. Bolender, and D. B. Doman, "Control-oriented modeling of an air-breathing hypersonic vehicle," *AIAA J. Guidance, Control, and Dynamics, Accepted for publication*, 2007.

[3] M. A. Bolender and D. B. Doman, "A Non-Linear Longitudinal Dynamical Model of an Air-Breathing Hypersonic Vehicle," *J. Spacecraft and Rockets*, vol. 44 no. 2, pp. 373 – 387, 2007.

[4] M. W. Oppenheimer, D. B. Doman, M. A. Bolender, and T. Skujins, "A flexible hypersonic vehicle model developed with piston theory," in *AIAA 2007-6396*, 2007.

[5] M. Bolender and D. Doman, "Modeling unsteady heating effects on the structural dynamics of a hypersonic vehicle," in *AIAA-2006-6646*, 2006.

[6] D. Doman, M. Oppenheimer, and M. Bolender, "Progress in guidance and control research for space access and hypersonic vehicles," Air Force Research Laboratory (AFRL), Wright Patterson Air Force Base, pp. 1 – 18, Tech. Rep., 2006.

[7] D. Sigthorsson, A. Serrani, S. Yurkovich, M. Bolender, and D. Doman, "Tracking control for an overactuated hypersonic air-breathing vehicle with steady state constraints," in *AIAA Guidance, Navigation and Control Conf., Paper No. AIAA-2006-6558,*, 2006.

[8] T. Adami, J. Zhu, M. Bolender, D. Doman, and M. Oppenheimer, "Flight control of hypersonic scramjet vehicles using a differential algebraic approach," in *AIAA*

Guidance, Navigation and Control Conf., Paper No. AIAA-2006-6559,, 2006.

[9] T. Williams, M. A. Bolender, D. Doman, and O. Mortaya, "An Aerothermal Flexible Mode Analysis of a Hypersonic Vehicle," Airforce Research Laboratory (AFRL), Wright Patterson Air Force Base, pp. 1 – 25,, Tech. Rep., 2006.

[10] J. T. Parker, A. Serrani, S. Yurkovich, M. Bolender, and D. Doman, "Approximate feedback linearization of an air-breathing hypersonic vehicle," Air Force Research Laboratory (AFRL), Wright Patterson Air Force Base, pp. 1 – 20, Tech. Rep., 2005.

[11] K. Groves, D. Sigthorsson, A. Serrani, S. Yurkovich, M. Bolender, and D. Doman, "Reference command tracking for a linearized model of an air-breathing hypersonic vehicle," in *AIAA Guidance, Navigation and Control Conf. and Exhibit, Paper No. AIAA-2005-6144*, 2005.

[12] K. P. Groves, A. Serrani, S. Yurkovich, M. Bolender, and D. Doman, "Anti-windup control for an air-breathing hypersonic vehicle model," Air Force Research Laboratory (AFRL), Wright Patterson Air Force Base, pp. 1 – 27, Tech. Rep., 2005.

[13] M. A. Bolender and D. B. Doman, "A Non-Linear Model for the Longitudinal Dynamics of a Hypersonic Air-Breathing Vehicle," in *Proceedings of the 2005 Guidance, Navigation and Control Conf., Paper No. 2005-6255*, 2005.

[14] ——, "Flight Path Angle Dynamics of Air-Breathing Hypersonic Vehicles," Airforce Research Laboratory (AFRL), Wright Patterson Air Force Base, pp. 1 – 37, Tech. Rep., 2005.

[15] E. Baumann, C. Bahm, B. Strovers, R. Beck, and M. Richard, "The X-43A Six Degree of Freedom Monte Carlo Analysis," in 46^{th} *AIAA Aerospace Sciences Meeting and Exhibit, Paper No. 2008-203*, 2008.

[16] C. Peebles, *Road to Mach 10: Lessons Learned from the X-43A Flight Research Program*. AIAA, 2008.

[17] C. R. McClinton, "X-43 Scramjet Power Breaks the Hypersonic Barrier Dryden Lectureship in Research for 2006," 44^{th}*AIAA Aerospace Sciences Meeting and Exhibit, Paper No. 2006-1*, 2007.

[18] V. L. Rausch, C. R. McClinton, and J. L. Crawford, "Hyper-X Flight Validation of Hypersonic Airbreathing Technology," Technical Report, NASA Hyper-X Program Office, pp. 1 – 7, 1997.

[19] W. H. Heiser, D. T. Pratt, D. Daley, and U. Mehta, *Hypersonic Airbreathing Propulsion*. AIAA, 1994.

[20] M. Davis and J. White, "X-43A Flight-Test-Determined Aerodynamic Force and Moment Characteristics at Mach 7.0 ," *J. of Spacecraft and Rockets*, vol. 45, no. 3, pp. 472–484, 2008.

[21] J. Anderson, *Hypersonic and High-Temperature Gas Dynamics*. Second Edition. AIAA, 2006.

[22] E. A. Morelli, S. D. Derry, and M. S. Smith, "Aerodynamic Parameter Estimation for Flight 2 of the X-43A," *Joint Army Navy NASA Air Force JANNAF Conf.*, 2005.

[23] S. D. Holland, W. C. Woods, and W. C. Engelund, "Hyper-X Research Vehicle Experimental Aerodynamics Test Program Overview," *J. Spacecraft and Rockets*, vol. 38, no. 6, pp. 828–835, 2001.

[24] Q. Wang and R. F. Stengel, "Robust nonlinear control of a hypersonic vehicle," *J. Guidance, Control, and Dynamics*, pp. 577 – 585, 2000.

[25] B. Cobleigh, "Development of the X-33 Aerodynamic Uncertainty Model," NASA/TP-1998-206544, April 1998.

[26] H. Buschek and A. J. Calise, "Uncertainty Modeling and Fixed-Order Controller Design for a Hypersonic Vehicle Model," *J. Guidance, Control and Dynamics*, pp.

42 – 48, 1997.

[27] J. J. Bertin, *Hypersonic Aerothermodynamics*. AIAA Education Series, 1994.

[28] H. Buschek and A. J. Calise, "Robust control of hypersonic vehicles considering propulsive and aeroelastic effects," *Paper No. AIAA-1993-3762*, pp. 1 – 11, 1993.

[29] J. J. Bertin, J. Periaux, and J. Ballmann, *Advances in Hypersonics: Defining the Hypersonic Environment, Volume 1*. Birkhauser Boston, 1992.

[30] ——, *Advances in Hypersonics: Modeling Hypersonic Flows, Volume 2*. Birkhauser Boston, 1992.

[31] ——, *Advances in Hypersonics: Computing Hypersonic Flows, Volume 3*. Birkhauser Boston, 1992.

[32] J. Young and J. Underwood, "Development of Aerodynamic Uncertainties for the Space Shuttle Orbiter ," *J. of Spacecraft and Rockets*, vol. 20, no. 6, pp. 513–517, 1983.

[33] J. Heeg, T. A. Zieler, A. S. Potozky, C. V. Spain, and W. C.Englend, "Aerothermoelastic Analysis of a NASP Demonstrator Model, Report No. NAS 1.15109007," NASA, Tech. Rep., 1993.

[34] D. Johnson, C. Hill, S. Brown, and G. Batts, "Natural Environment Application for NASP-X-30 design and mission planning ," in 31^{st} *Aerospace Sciences Meeting and Exhibit, Paper No. 1993-851*, 1993.

[35] D. Johnson, "Beyond the X-30 - Incorporating mission capability ," in 3^{rd} *Int. Aerospace Planes Conf., Paper No. 1991-5078*, 1991.

[36] J. D. Shaughnessy, S. Z. Pinckney, J. D. McMinn, C. I. Cruz, and M. L. Kelley, "Hypersonic Vehicle Simulation Model: Winged-Cone Configuration, No. 102610,"

NASA, Tech. Rep., 1990.

[37] J. J. McNamara and P. P. Friedmann, "Aeroelastic and Aerothermoelastic Analysis of Hypersonic Vehicles: Current Status and Future Trends," 48^{th} *AIAA/ASME/ASCE/AHS/ASC Structures, Structural Dynamics, and Materials Conference, Paper No. 2007-2013*, 2007.

[38] P. P. Friedmann, J. J. McNamara, B. Thuruthimattam, and I. Nydick, "Aeroelastic Analysis of Hypersonic Vehicles," *J. Fluids and Structures*, pp. 681 – 712, 2004.

[39] J. McNamara, P. Friedmann, K. Powell, B. Thuruthimattam, and R. Bartels, "Aeroelastic and Aerothermoelastic Vehicle Behavior in Hypersonic Flow ," in *AIAA/CIRA* 13^{th} *International Space Planes and Hypersonics Systems and Tech. Conf., Paper No. AIAA-2005-3305*, 2005.

[40] B. Pamadi, G. Brauckmann, M. Ruth, and H. Fuhrmann, "Aerodynamic Characteristics, Database Development, and Flight Simulation of the X-34 Vehicle," *J. of Spacecraft and Rockets*, vol. 38, pp. 334–344, 2001.

[41] C. Bahm, E. Baumann, J. Martin, D. Bose, R. E. Beck, and B. Strovers, "The X-43A Hyper-X Mach 7 Flight 2 Guidance, Navigation, and Control Overview and Flight Test Results," in *AIAA/CIRA International Space Planes and Hypersonic Systems and Technologies Conference*, 2005, pp. 682 – 704.

[42] J. Hank, J. Murphy, and R. Mutzman, "The X-51A Scramjet Engine Flight Demonstration Program ," in 15^{th} *AIAA International Space Planes and Hypersonic Systems and Technologies Conf, Paper No. AIAA-2008-2540*, 2008.

[43] S. Walker, M. Tang, S. Morris, and C. Mamplata, "Falcon HTV-3X - A Reusable Hypersonic Test Bed," in 15^{th} *AIAA International Space Planes and Hypersonic Systems and Tech. Conf., Paper No. AIAA-2008-2544*, 2008.

[44] S. Walker, J. Sherk, D. Shell, R. Schena, J. Bergmann, and J. Gladbach, "The DARPA/AF Falcon Program: The Hypersonic Technology Vehicle 2 (HTV-2) Flight Demonstration Phase," in 15^{th} *AIAA International Space Planes and Hypersonic*

Systems and Technologies Conf., Paper No. 2008-2539, 2008.

[45] S. H. Walker and F. Rodgers, "Falcon Hypersonic Technology Overview," *AIAA/CIRA* 13^{th} *International Space Planes and Hypersonics Systems and Technologies, Paper No. 2005-3253*, 2005.

[46] B. Fidan, M. Mirmirani, and P. Ioannou, "Flight Dynamics and Control of Air-Breathing Hypersonic Vehicles: Review and New Directions," in 12^{th} *AIAA/AHI Space Planes and Hypersonic Systems and Technologies Conf. Paper No. 2003-7081*, 2003.

[47] R. T. Voland, L. D. Huebner, and C. R. McClinton, "X-43A Hypersonic Vehicle Technology Development," Technical Report, NASA Langley Research Center, Hampton, VA, Report No. IAC-05-D2.6.01, 2005.

[48] A. Kumar, J. P. Drummond, C. R. McClinton, and J. L. Hunt, "Research in Hypersonic Airbreathing Propulsion at the NASA Langley Research Center," National Aeronautics and Space Administration (NASA), Report No. ISABE-2001-4, Tech. Rep., 2001.

[49] J. Heeg, M. G. Gilbert, and A. S. Pototzky, "Active control of aerothermoelastic effects for a conceptual hypersonic aircraft," *J. of Aircraft*, pp. 453 – 458, 1993.

[50] M. G. Gilbert, J. Heeg, A. S. Potozky, C. V. Spain, D. L. Scistmann, and H. J. Dunn, "The Application of Active Controls Technology to a Generic Aircraft Configuration," National Aeronautics and Space Administration (NASA), Report No. NAS 1.15101689, Tech. Rep., 1990.

[51] J. Heeg, M. G. Gilbert, and A. S. Pototzky, "Active control of aerothermoelastic effects for a conceptual hypersonic vehicle," in *AIAA Guidance, Navigation and Control Conf., Paper No. AIAA-1990-3337, pp. 200 – 208*, 1990.

[52] A. S. Potozky, C. V. Spain, D. L. Spain, and T. E. Noll, "Application of Unsteady Aeroelastic Analysis Techniques on the National Aerospace Plane," National Aeronautics and Space Administration (NASA), Report No. NAS 1.15100648, Tech.

Rep., 1988.

[53] D. Glass, “Ceramic Matrix Composite (CMC) Thermal Protection Systems (TPS) and Hot Structures for Hypersonic Vehicles ,” in 15^{th} *AIAA International Space Planes and Hypersonic Systems and Technologies Conf/*, 2008.

[54] [Online]. Available: http://www.uq.edu.au/hypersonics/index.html?page=19501

[55] M. Smart, N. Hass, and A. Paull, “Flight Data Analysis of the HyShot 2 Scramjet Flight Experiment,” *AIAA Journal*, vol. 44, Issue 10, pp. 2366–2375, 2006.

[56] S. Walker, F. Rodgers, A. Paull, and D. V. Wie, “HyCAUSE Flight Test Program,” in 15^{th} *AIAA International Space Planes and Hypersonic Systems and Technologies Conf., Paper No. 2008-2580*, 2008.

[57] X-43A Mishap Investigation Board, “Report of Findings: X-43A Mishap,” Technical Report, pp. 1 – 33, 2003.

[58] D. E. Reubush, L. T. Nguyen, , and V. L. Rausch, “Review of X-43A Return to Flight Activities and Current Status,” *12th AIAA International Space Planes and Hypersonic Systems and Technologies, Paper No. 2003-7085*, 2003.

[59] L. Marshall, G. Corpening, and R. Sherrill, “A Chief Engineer’s View of the NASA X-43A Scramjet Flight Test,” in *AIAA/CIRA* 13^{th} *International Space Planes and Hypersonics Systems and Tech. Conf., Paper No. AIAA-2005-3332* , 2005.

[60] C. Bahm, E. Baumann, J. Martin, D. Bose, R. Beck, and B. Strovers, “The X-43A Hyper-X Mach 7 Flight 2 Guidance, Navigation, and Control Overview and Flight Test Results,” in *AIAA/CIRA* 13^{th} *International Space Planes and Hypersonics Systems and Technologies Conf., Paper No. AIAA-2005-3275*, 2005.

[61] S. M. Ferlemann, C. R. McClinton, K. E. Rock, and R. T. Voland, “Hyper-X Mach 7 Scramjet Design, Ground Test and Flight Results,” Technical Report, NASA Langley

Research Center, Hampton, VA, pp. 1 – 9, 1999.

[62] C. E. Cockrell, W. C. Englelund, R. D. Bittner, T. N. Jentink, A. D. Dilley, and A. Frendi, "Integrated Aeropropulsive Computational Fluid Dynamics Methodology for the Hyper-X Flight Experiment," *J. of Spacecraft and Rockets*, pp. 836 – 843, 2001.

[63] L. Marshall, C. Bahm, G. Corpening, and R. Sherril, "Overview With Results and Lessons Learned of the X-43A Mach 10 Flight," in *AIAA/CIRA* 13^{th} *International Space Planes and Hypersonics Systems and Technologies Conf., 2005-3336*.

[64] R. C. Rogers, A. T. Shih, and N. E. Hass, "Scramjet Engine Flowpath Development for the Hyper-X Mach 10 Flight Test," National Aeronautics and Space Administration (NASA), Report No. ISABE-2005-1025, Tech. Rep., 2005.

[65] J. Davidson, F. Lallman, J. D. McMinn, J. Martin, J. Pahle, M. Stephenson, and J. Selmon, "Flight Control Laws for NASA's Hyper-X Research Vehicle," *AIAA Guidance, Navigation, and Control Conference and Exhibit, Paper No. 1999-4124*, 1999.

[66] E. Morelli, S. Derry, and M. Smith, "Aerodynamic Parameter Estimation for the X-43A (Hyper-X) from Flight Data," in *AIAA Atmospheric Flight Mechanics Conf. and Exhibit, Paper No. AIAA-2005-5921*, 2005.

[67] D. Dolvin, "Hypersonic International Flight Research and Experimentation (HIFiRE) Fundamental Science and Technology Development Strategy ," in 15^{th} *AIAA International Space Planes and Hypersonic Systems and Technologies Conf., Paper No. 2008-2582*, 2008.

[68] B. H. M. Tang and R. Chase, "The Quest for Hypersonic Flight with Air-Breathing Propulsion," in 15^{th} *AIAA International Space Planes and Hypersonic Systems and Technologies Conf., Paper No. 2008-2546*, 2008.

[69] "Blackswift Program Solicitation," Defense Advanced Research Projects Agency,

Tech. Rep., February, 2008.

[70] M. D. Salas, "DIGITAL FLIGHT: the last CFD aeronautical grand challenge," *J. Scientific Computing*, pp. 1 – 63, 2004.

[71] J. J. McNamara, "Aeroelastic and Aerothermoelastic Behavior of Two and Three Dimensional Lifting Surfaces in Hypersonic Flow," Ph.D. dissertation, University of Michigan, 2005.

[72] M. Maughmer, L. Ozoroski, D. Straussfogel, and L. Long, "Validation of Engineering Methods for Predicting Hypersonic Vehicle Control Forces and Moments," *J. of Guidance, Control and Dynamics*, vol. 16, pp. 762–769, 1993.

[73] S. Keshmirir, "Nonlinear and Linear Longitudinal and Lateral-Directional Dynamical Model of Air-Breathing Hypersonic Vehicle," in 15^{th} *AIAA International Space Planes and Hypersonic Systems and Technologies Conf.*, 2008.

[74] S. Keshmiri, "Modeling and Simulation of a Generic Hypersonic Vehicle," Ph.D. dissertation, University of Kansas, 2007.

[75] S. Keshmiri, R. Colgren, and M. Mirmirani, "Modeling and Simulation of a Generic Hypersonic Vehicle using Merged Aerodynamic Models," in 14^{th} *AIAA/AHI Space Planes and Hypersonic Systems and Technologies Conf., Paper No. 2006-8087*, 2006.

[76] ——, "Six-DOF Modeling and Simulation of a Generic Hypersonic Vehicle for Control and Navigation Purposes," in *AIAA Guidance, Navigation and Control Conf., Paper No. 2006-6694*, 2006.

[77] S. Keshmiri, R. Colgren, S. Farokhi, and M. Mirmirani, "Ramjet and Scramjet Engine Cycle Analysis for a Generic Hypersonic Vehicle," in 14^{th} *AIAA/AHI Space Planes and Hypersonic Systems and Technologies Conf., Paper No. 2006-8158*, 2006.

[78] S. Keshmiri, R. Colgren, and M. Mirmirani, "Development of an Aerodynamic Database for a Generic Hypersonic Air Vehicle," in *AIAA Guidance, Navigation and Control Conf., Paper No. 2006-6257*, 2005.

[79] ——, "Six-DOF Modeling and Simulation of a Generic Hypersonic Vehicle for Conceptual Design Studies," in *AIAA Modeling and Simulation Technologies Conf., Paper No. 2004-4805*, 2004.

[80] P. Lohsoonthorn, E. Jonckheere, and S. Dalzell, "Eigenstructure vs constrained $\mathcal{H}^\infty$ design for hypersonic winged cone," *J. Guidance, Control and Dynamics*, pp. 648 – 658, 2001.

[81] F. R. Chavez and D. K. Schmidt, "Analytical Aeropropulsive/Aeroelastic Hypersonic-Vehicle Model with Dynamic Analysis," *J. Guidance, Control and Dynamics*, pp. 1308 – 1319, 1994.

[82] J. D. Anderson, *Modern Compressible Flow, 3^{rd} Edition*. McGraw-Hill, 2002.

[83] A. Clark, C. Wu, M. Mirmirani, and S. Choi, "Development of an Airframe Integrated Generic Hypersonic Vehicle Model," in *AIAA Aerospace Conference and Exhibit,Paper No. 2006-6560*, 2006.

[84] A. Clark, M. Mirmirani, S.Choi, C. Wu, and K. Mathew, "An Aero-Propulsion Integrated Elastic Model of a Generic Airbreathing Hypersonic Vehicle," in *AIAA Guidance, Navigation, and Control Conf., Paper No. 2006-6560*, 2006.

[85] R. Starkey and M. Lewis, "A Simple Analytical Model for Parametric Studies of Hypersonic Waveriders ," in 8^{th} *AIAA International Space Planes and Hypersonic Systems and Technologies Conf. Paper No. 1998-1616*, 1998.

[86] I. Blankson, "Airbreathing Hypersonic Cruise: Prospects for Mach 4-7 Waverider Aircraft," in *ASME Int. Gas Turbine and Aerospace Congress and Exposition, Paper No. 92-GT-437*, June 1992.

[87] D. Capriotti, K. Bowcutt, and J. Anderson, "Viscous Optimized Hypersonic Waveriders," in *AIAA 25^{th} Aerospace Sciences Meeting, Paper No. 1987-272*, 1987.

[88] T. Nonwiler, "Aerodynamic Problems of Manned Space Vehicles," *J. of the Royal Aeronautical Society*, vol. 63, pp. 521–528, 1959.

[89] R. Starkey, D. Liu, R. Chang, and P. Chem, "Rapid Conceptual Design and Analysis of a Hypersonic Air-Breathing Missile ," in *15^{th} AIAA International Space Planes and Hypersonic Systems and Technologies Conf., 2008-2590*, 2008.

[90] K. Bowcutt, G. Kuruvila, T. Grandine, and E. Cramer, "Advancements in Multidisciplinary Design Optimization Applied to Hypersonic Vehicles to Achieve Performance Closure," in *15^{th} AIAA International Space Planes and Hypersonic Systems and Technologies Conf, Paper No. AIAA-2008-2591*, 2008.

[91] P. Moses, K. Bouchard, R. Vause, S. Pinckney, S. Ferlemann, C. Leonard, L. Taylor, J. Robinson, J. Martin, D.H.Petley, and J. Hunt, "An airbreathing launch vehicle design with trubine-based low-speed propulsion and dual mode scramject high-speed propulsion," in *21^{st} International Space Planes and Hypersonic Systems and Technologies Conference*, 1999.

[92] J. Robinson, J. Martin, J. Bowles, U. Mehta, and C. Snyder, "An overview of the role of systems analysis in nasa's hypersonics project," in *14^{th} AIAA/AHI Space Planes and Hypersonic Systems and Technologies Conf. Paper No. AIAA-2006-8013*, 2006.

[93] J. Pittman and P. A. Bartolotta, "Fundamental aeronautics hypersonics project reference document," National Aeronautics and Space Administration (NASA), Tech. Rep., 2006.

[94] C. McClinton, "High Speed Hypersonic Aircraft Propulsion Technology Development," NASA Hypersonics GNC Kickoff Workshop Presentation, NASA Glenn, 84 slides, April 2007.

[95] D. McRuer, "Design and Modeling Issues for Integrated Airframe/Propulsion Con-

trol of Hypersonic Flight Vehicles," in *American Control Conf., pp. 729 – 734*, 1991.

[96] J. C. E. Cockrell, A. H. Auslender, R. W. Guy, C. R. McClinton, and S. S. Welch, "Technology Roadmap for Dual-Mode Scramjet Propulsion to Support Space-Access Vision Vehicle Development," in *AIAA/AAAF International Space Planes and Hypersonic Systems and Technologies Conf., pp. 1 – 14*, 2002.

[97] G. Stien, "Respect the unstable," IEEE Control Systems Magazine, August 2003, pp. 12 - 25.

[98] A. A. Rodriguez, *Analysis and Design of Multivariable Feedback Control Systems*, Control3D, Ed. Control3D, LLC, 2004.

[99] R. Lind, "Linear parameter-varying modeling and control of structural dynamics with aerothermoelastic effects," *J. Guidance, Control, and Dynamics*, pp. 733 – 739, 2002.

[100] M. W. Oppenheimer and D. B. Doman, "Control of unstable, nonminumum phase hypersonic vehicle," in *IEEE Aerospace Conf., pp. 5782 – 5787*, 2006.

[101] J. Khatri, "Modeling, analysis, and control of a hypersonic vehicle with significant aero-thermo-elastic-propulsion interactions and thermo-elastic uncertainty," Master's thesis, Arizona State University, 2010.

[102] M. W. Oppenheimer and D. B. Doman, "A hypersonic vehicle model using developed with piston theory," in *AIAA 2006-6637*, 2006.

[103] M. Oppenheimer and D. Doman, "A Hypersonic Vehicle Model Developed with Piston Theory," Airforce Research Laboratory (AFRL), Wright Patterson Air Force Base, pp. 1 – 26, Tech. Rep., 2006.

[104] A. Rodriguez, J. Dickeson, R. McCullen, A. Kelkar, and J. Vogel, "Control System Tradeoffs for a Scramjet-Powered Hypersonic Vehicle," in *to be submitted to 2008*

GNC, 2008.

[105] K. Groves, A. Serrani, S. Yurkovich, M. Bolender, and D. Doman, "Anti-Windup Control for an Air-Breathing Hypersonic Vehicle Model," in *AIAA Guidance, Navigation, and Control Conf. and Exhibit, Paper No. AIAA 2006-6557*, 2006.

[106] D. Soloway, A. Rodriguez, J. Dickeson, O. Cifdaloz, J. Benavides, S. Sridharan, A. Kelkar, and J. Vogel, "Constraint Enforcement for Scramjet-Powered Hypersonic Vehicles with Significant Aero-Elastic-Propulsion Interactions," in *2009 American Control Conference, Accepted for Publication*, 2009.

[107] J. Dickeson, A. Rodriguez, S. Sridharan, J. Benavides, D. Soloway, A. Kelkar, and J. Vogel, "Decentralized control of an airbreathing scramjet-powered hypersonic vehicle," in *AIAA Conf. on Guidance, Navigation and Control, AIAA-2009-6281*, 2009.

[108] A. A. Rodriguez, J. J. Dickeson, S. Sridharan, A. Khorad, J. Khatri, J. Benavides, D. Soloway, A. Kelkar, and J. M. Vogel, "Control-Relevant Modeling, Analysis, and Design for Scramjet-Powered Hypersonic Vehicles," in *16th AIAA/DLR/DGLR International Space Planes and Hypersonic Systems and Technologies Conference*, 2009.

[109] C. Breitsamter, T. Cvrlje, B. Laschka, M. Heller, and G. Sachs, "Lateral–Directional Coupling and Unsteady Aerodynamic Effects of Hypersonic Vehicles," *J. Spacecraft and Rockets*, pp. 159 – 167, 2001.

[110] M. E. Tauber and G. P. Menees, "Aerothermodynamics of transatmospheric vehicles," *Journal of Aircraft*, vol. 24, No. 9, pp. 594 – 602, 1986.

[111] S. Berry, K. Daryabeigi, K. Wurster, and R. Bittner, "Boundary Layer Transition on X-43A ," in 38^{th} *Fluid Dynamics Conf. and Exhibit, Paper No. 2008-3736*, 2008.

[112] S. A. Berry, A. H. Auslender, A. D. Diller, and J. F. Calleja, "Hypersonic Boundary-Layer Trip Development for Hyper-X," *J. Spacecraft and Rockets*, pp. 853 – 864,

2001.

[113] S. Torrez, N. Scholten, J. Driscoll, M. Bolender, M. Oppenheimer, and D. D. Doman, "A Scramjet Engine Model Including Effects of Precomubstions Shocks and Dissociation," in 44^{th} *AIAA/ASME/SAE/ASEE Joint Propulsion Conference and Exhibit, Paper No. 2008-6386*, 2008.

[114] D. H. Baldelli, R. Lind, and M. Brenner, "Nonlinear Aeroelastic/Aeroservoelastic Modeling by Block-Oriented Identification," *J. Guidance, Control and Dynamics*, pp. 1056 – 1064, 2005.

[115] R. Lind and M. Brenner, *Robust Aeroservoelastic Atability Analysis: Flight Test Applications*. Springer, 1999.

[116] "Aiaa guide to reference and standard atmosphere models (g-003b-2004)," 2004.

[117] D. L. Johnson, B. C. Roberts, and W. W. Vaughan, "Reference and Standard Atmosphere Models," in *10th Conference on Aviation, Range, and Aerospace Meteorology*, 2002.

[118] M. W. Oppenheimer and D. B. D. B. Doman, "Viscous effects for a hypersonic vehicle model," in *In preperation for submittal to the 2008 AIAA Atmospheric Flight Mechanics Conference*, 2008.

[119] C. R. McClinton, J. L. Hunt, R. H. Ricketts, P. Reukau, and C. L. Peddie, "Airbreathing Hypersonic Technology Vision Vehicles and Development Dreams," in *AIAA International Space Planes and Hypersonic Systems and Technologies Conf., Paper No. 1999-4978*, 1999.

[120] A. Khorad, "Modeling, analysis, and control of a hypersonic vehicle with significant aero-thermo-elastic-propulsion interactions and propulsion uncertainty," Master's thesis, Arizona State University, 2010.

[121] D. K. Schmidt, "Dynamics and Control of Hypersonic Vehicles- The integration

Challenge for the 1990's," in rd *Intl. Aerospace Planes Conf., Paper No.1991-5057*, 1991.

[122] W. J. S. J. P. Weidner and J. A. Penland, "Scramjet Integration on Hypersonic Research Airplane Concepts," *J. Aircraft*, vol. 14, no. 5, pp. 460–466, May 1977.

[123] M. Bolender and D. Doman, "Flight Path Angle Dynamics of Air-Breathing Hypersonic Vehicles," AIAA Guidance Navigation and Control Conf and Exhibit, Paper No. 2006-6692, Tech. Rep., 2006.

[124] R. J. McCullen, "Modeling and control of scramjet-powered-hypersonic vehicles with aero-thermo-elastic-propulsive effects." Master's thesis, Arizona State University, 2008.

[125] A. A. Rodriguez, *Linear Systems, Analysis and Design*, Control3D, Ed. Control3D, LLC, 2004.

[126] R. C. Nelson, *Flight Stability and Automatic Control*, Second, Ed. McGraw Hill, 1998.

[127] K. G. Bowcutt, "A perspective on the future of aerospace vehicle design," in *12th AIAA International Space Planes and Hypersonic Systems and Technologies, Paper No. AIAA 2003-6957*, 2003.

[128] ——, "Multidisciplinary optimization of airbreathing hypersonic vehicles," *Journal of Propulsion and Power*, vol. Vol. 17, No. 6, pp. 1184–1190, 2001.

[129] J. c. T. S. Srinivasan and K. J. Weilmuenster, "Simplified Curve Fits for the Thermodynamic Properties of Equilibrium Air, NASA Reference Publication 1181," NASA, Tech. Rep., 1987.

[130] R. Starkey and M. Lewis, "Critical design issues for airbreathing hypersonic wa-

verider missles," *J. of Spacecraft and Rockets*, vol. 38, 2001.

[131] D. Sigthorsson, P. Jankovsky, A. Serrani, S. Yurkovich, M. Bolender, and D. Doman, "Robust Linear Output Feedback Control of an Airbreathign Hypersonic Vehicle," *J. of Guidnace, Control and Dynamics*, vol. 31, pp. 1–15, 2008.

[132] F. R. Chavez and D. K. Schmidt, "An Integrated Analytical Aeropropulsive/Aeroelastic Model for the Dynamic Analysis of Hypersonic Vehicle, NASA ARC92-2," NASA, Tech. Rep., June 1992.

[133] D. C. Montgomery, *Design and Analysis of Experiments*, 7, Ed. John Wiley and Sons, 2008.

[134] *JMP, Version 7*. SAS Institute Inc., Cary, NC, 1989-2007.

[135] A. Teel and N. Kapoor, "The $\mathcal{L}_2$ anti-windup problem: Its definition and solution." in *Proc. of the European Control Conf.*, 1997.

[136] A. Zinnecker, A. Serrani, M. Bolender, and D. Doman, "Combined reference governor and anti-windup design for constrained hypersonic vehicles models," in *AIAA Guidance, Navigation, and Control Conference 2009, Paper No. 2009-6283*, 2009.

[137] A. Culler, T. Williams, and M. Bolender, "Aerothermal modeling and dynamic analysis of a hypersonic vehicle," in *AIAA Atmospheric Flight Mechanics Conference and Exhibit 2007 Paper. No. 2007-6395*, 2007.

[138] S. Torrez, J. Driscoll, M. Bolender, M. Oppenheimer, and D. Doman, "Effects of Improved Propulsion Modeling on the Flight Dynamic of Hypersonic Vehicles," in *AIAA Atmospheric Flight Mechanics Conf. and Exhibit, Paper No. 2008-6386*, 2008.

[139] S. Torrez, J. Driscoll, D. Dalle, M. Bolender, and D. Doman, "Hypersonic vehicle thrust sensitivity to angle of attack and mach number," in *AIAA Atmospheric Flight*

Mechanics Conference 2009, Paper No. 2009-6152, 2009.

[140] L. Fiorentini, A. Serrani, M. Bolender, and D. Doman, "Nonlinear Robust/Adaptive Controller Design for an Air-breathing Hypersonic Vehicle Model," in *AIAA Guidnace Navigation and Control Conf. and Exhibit, Paper No. 2007-6329,* 2007.

[141] S. Bhat and R. Lind, "Control-oriented analysis of thermal gradients for a hypersonic vehicle," in *Proc. ACC '09. American Control Conference*, 10–12 June 2009, pp. 2513–2518.

[142] K. Glover, G. Vinnicombe, and G. Papageorgiou, "Guaranteed multi-loop stability margins and the gap metric," in *Proceedings of the 39th IEEE Conference on Decision and Control*, 2000.

[143] T. T. Georgiou, "On the computation of the gap metric," in *Proceedings of the 27th Conference on Decision and Control*, 1988.

[144] M. Vidyasagar, "The graph metric for unstable plants and robustness estimates for feedback stability," *IEEE Transactions On Automatic Control,* vol. Vol. 29, pp. 403–418, 1984.

[145] G. Vinnicombe, "Structured uncertainty and the graph topology," in *Proceedings of the 30th Conference on Decision and Control*, 1991.

[146] K. E. Ahmed, "The gap metric: Robustness of stabilization of feedback systems," *IEEE Transactions On Automatic Control*, vol. Vol. 30, No. 3, pp. 240 – 247, 1985.

[147] K. Glover, G. Vinnicombe, and G. Papageorgiou, "Guaranteed multi-loop stability margins and the gap metric," in *Proceedings of the 39th IEEE Conference on Decision and Control*, 2000.

[148] A. Fujimori, F. Terui, and P. N. Nikiforuk, "Flight control designs using v-gap metric and local multi-objective gain-scheduling," in *AIAA Guidance, Navigation, and*

Control Conference and Exhibit, AIAA 2003-5414, 2003.

[149] ——, "Flight control design of an unmanned space vehicle using gain scheduling," *Journal of Guidance, Control and Dynamics*, vol. Vol. 28, No. 1, pp. 96 – 105, 2005.

[150] S. Skogestad, M. Morari, and J. C. Doyl, "Robust control of ill-conditioned plants: High-purity distillation," *IEEE Transactions on Automatic Control*, vol. Vol 33, No. 12, pp. 1092 – 1105, 1988.

[151] J. S. Freudenberg and D. P. Looze, "Relations between properties of multivariable feedback systems at different loop-breaking points: Part ii," in *American Control Conference*, 1986.

[152] K. Zhou and J. C. Doyle, "Essentials of robust control," Prentice Hall, 1998.

[153] V. J. W. C. S. A. Kelkar, A. and A. Rodriguez, "Modeling and Analysis Framework for Early Stage Studies in Scramjet-Powered Hypersonic Vehicles," in 16^{th} *AIAA/DLR/DGLR International Space Planes and Hypersonic Systems and Technologies Conf., Paper No. 2009-7325*, 2009.

APPENDIX A

CODE

Macro: atmosphere4.m

```
function [temp,press,rho,Hgeopvector]=atmosphere4(Hvector,GeometricFlag)
%function [temp,press,rho,Hgeopvector]=atmosphere4(Hvector,GeometricFlag)
% Standard Atmospheric data based on the 1976 NASA Standard Atmoshere.
% Hvector is a vector of altitudes.
% If Hvector is Geometric altitude set GeometricFlag=1.
% If Hvector is Geopotential altitude set GeometricFlag=0.
% Temp, press, and rho are temperature, pressure and density
% output vectors the same size as Hgeomvector.
% Output vector Hgeopvector is a vector of corresponding geopotential altitudes (ft).
% This atmospheric model is good for altitudes up to 295,000 geopotential ft.
% Ref: Intoduction to Flight Test Engineering by Donald T. Ward and Thomas W. Strganac
% index   Lapse rate   Base Temp     Base Geopo Alt        Base Pressure            Base Density
%   i     Ki(degR/ft)  Ti(degR)        Hi(ft)              P, lbf/ftˆ2           RHO, slug/ftˆ3
format long g
D= [1     -.00356616    518.67              0                   2116.22       0.00237691267925741
    2        0          389.97        36089.239          472.675801650081      0.000706115448911997
    3      .00054864    389.97        65616.798          114.343050672041      0.000170813471460564
    4      .00153619    411.57       104986.878          18.1283133205764      2.56600341257735e-05
    5        0          487.17       154199.475          2.31620845720195      2.76975106424479e-06
    6     -.00109728    487.17       170603.675          1.23219156244977      1.47347009326248e-06
    7     -.00219456    454.17       200131.234          0.38030066501701      4.87168173794687e-07
    8        0          325.17       259186.352        0.0215739175227548      3.86714900013768e-08];
format short
R=1716.55;        %ftˆ2/(secˆ2degR)
gamma=1.4; g0=32.17405;        RE=20926476; K=D(:,2); T=D(:,3); H=D(:,4); P=D(:,5); RHO=D(:,6);
temp=zeros(size(Hvector)); press=zeros(size(Hvector)); rho=zeros(size(Hvector));
Hgeopvector=zeros(size(Hvector));

% Convert from geometric altitude to geopotental altitude, if necessary.
if GeometricFlag
        Hgeopvector=(RE*Hvector)./(RE+Hvector);
else
   Hgeopvector=Hvector;
end
ih=length(Hgeopvector);  n1=find(Hgeopvector<=H(2));
n2=find(Hgeopvector<=H(3) & Hgeopvector>H(2));
n3=find(Hgeopvector<=H(4) & Hgeopvector>H(3));
n4=find(Hgeopvector<=H(5) & Hgeopvector>H(4));
n5=find(Hgeopvector<=H(6) & Hgeopvector>H(5));
n6=find(Hgeopvector<=H(7) & Hgeopvector>H(6));
n7=find(Hgeopvector<=H(8) & Hgeopvector>H(7));
n8=find(Hgeopvector<=295000 & Hgeopvector>H(8));
icorrect=length(n1)+length(n2)+length(n3)+length(n4)+length(n5)+length(n6)+length(n7)+length(n8);
if icorrect<ih
        disp('One or more altitutes is above the maximum for this atmospheric model')
        icorrect
        ih
end
% Index 1, Troposphere, K1= -.00356616
if length(n1)>0
        i=1;
        h=Hgeopvector(n1);
```

```
        TonTi=1+K(i)*(h-H(i))/T(i);
        temp(n1)=TonTi*T(i);
        PonPi=TonTi.^(-g0/(K(i)*R));
        press(n1)=P(i)*PonPi;
        RonRi=TonTi.^(-g0/(K(i)*R)-1);
        rho(n1)=RHO(i)*RonRi;
end
% Index 2,  K2= 0
if length(n2)>0
        i=2;
        h=Hgeopvector(n2);
        temp(n2)=T(i);
        PonPi=exp(-g0*(h-H(i))/(T(i)*R));
        press(n2)=P(i)*PonPi;
        RonRi=PonPi;
        rho(n2)=RHO(i)*RonRi;
end
% Index 3,  K3= .00054864
if length(n3)>0
        i=3;
        h=Hgeopvector(n3);
        TonTi=1+K(i)*(h-H(i))/T(i);
        temp(n3)=TonTi*T(i);
        PonPi=TonTi.^(-g0/(K(i)*R));
        press(n3)=P(i)*PonPi;
        RonRi=TonTi.^(-g0/(K(i)*R)-1);
        rho(n3)=RHO(i)*RonRi;
end
% Index 4,  K4= .00153619
if length(n4)>0
        i=4;
        h=Hgeopvector(n4);
        TonTi=1+K(i)*(h-H(i))/T(i);
        temp(n4)=TonTi*T(i);
        PonPi=TonTi.^(-g0/(K(i)*R));
        press(n4)=P(i)*PonPi;
        RonRi=TonTi.^(-g0/(K(i)*R)-1);
        rho(n4)=RHO(i)*RonRi;
end
% Index 5,  K5= 0
if length(n5)>0
        i=5;
        h=Hgeopvector(n5);
        temp(n5)=T(i);
        PonPi=exp(-g0*(h-H(i))/(T(i)*R));
        press(n5)=P(i)*PonPi;
        RonRi=PonPi;
        rho(n5)=RHO(i)*RonRi;
end
% Index 6,  K6= -.00109728
if length(n6)>0
        i=6;
        h=Hgeopvector(n6);
```

```
106         TonTi=1+K(i)*(h-H(i))/T(i);
107         temp(n6)=TonTi*T(i);
108         PonPi=TonTi.^(-g0/(K(i)*R));
109         press(n6)=P(i)*PonPi;
110         RonRi=TonTi.^(-g0/(K(i)*R)-1);
111         rho(n6)=RHO(i)*RonRi;
112 end
113 % Index 7,  K7= -.00219456
114 if length(n7)>0
115         i=7;
116         h=Hgeopvector(n7);
117         TonTi=1+K(i)*(h-H(i))/T(i);
118         temp(n7)=TonTi*T(i);
119         PonPi=TonTi.^(-g0/(K(i)*R));
120         press(n7)=P(i)*PonPi;
121         RonRi=TonTi.^(-g0/(K(i)*R)-1);
122         rho(n7)=RHO(i)*RonRi;
123 end
124 % Index 8,  K8= 0
125 if length(n8)>0
126         i=8;
127         h=Hgeopvector(n8);
128         temp(n8)=T(i);
129         PonPi=exp(-g0*(h-H(i))/(T(i)*R));
130         press(n8)=P(i)*PonPi;
131         RonRi=PonPi;
132         rho(n8)=RHO(i)*RonRi;
133 end
```

Macro: hsv_param.m

```
1  function p=hsv_param(model_opts)
2  % This is an input file that holds the vehicle geometry and inserts the data
3  % into a vector that is then passed to the aero code for analysis.
4  %The origin is located at the nose of the vehicle with x positive out the nose,
5  %z is positive down, and the pitching moment, M, is positive up.
6  %options check
7  for i_check = [2 3 4 7 8]
8      if (model_opts(i_check) < 0) || ~isreal(model_opts(i_check))
9          error([’model_opts(’ num2str(i_check) ’) must be positive scalar’])
10     end
11 end
12 for i_check = [1 5 6 9]
13     if ~((model_opts(i_check) == 0) || (model_opts(i_check) == 1))
14         error([’model_opts(’ num2str(i_check) ’) must be 0 or 1’])
15     end
16 end
17 for i_check = [2 7]
18     if (model_opts(i_check) == 0)
19         error([’model_opts(’ num2str(i_check) ’) must be strictly positive scalar’])
20     end
```

```
end
k_Can = model_opts(3);
k_Elev = model_opts(4);
k_Mass = model_opts(7);
k_CG = model_opts(8);
%Fuselage Length:
p.L=100;
%Forebody length:
p.L_1=47;
%Engine Length
p.Le=20;
%Aftbody length
p.L_2=p.L-p.L_1-p.Le;
%Define tau_11, the upper surface angle measured wrt the x axis
 p.tau_1U=3*pi/180; %in radians
%Define tau_12, the lower forebody wedge angle measured wrt the x axis
p.tau_1L=6.2*pi/180; %in radians
%Vehicle height at the end of the forebody is determined from the front "wedge" angles tau_11 and tau_12
h11=p.L_1*tan(p.tau_1U); h12=p.L_1*tan(p.tau_1L); h1=h11+h12;
%Height of top surface at the station where the engine stops
h21=(p.L_1+p.Le)*tan(p.tau_1U); h2=h21+h12;
%Aftbody wedge angle: (angle between top surface and aft body)
l2=sqrt((p.L_2/cos(p.tau_1U))^2+h2^2-2*h2*p.L_2*cos(p.tau_1U+pi/2)/cos(p.tau_1U));
p.tau_2=asin(h2/l2*sin(p.tau_1L+pi/2)); p.h=(h1+h2)/2;
%Mass properties (we will always assume the vertical position of the cg to
%be even with the nose of the vehicle
zbar=0;
%Control Surface positions
p.rel=[-85 -3.5];  %elevator location
p.rcan=[-5 0];   %canard location
%Control surface areas
p.Se=17*k_Elev; p.Sc=10*k_Can;
%Now, get the frequencies, modeshapes, EI, mass, and Iyy from the assumed
%modes code.
%Engine geometry (may not match up physically...)
p.An=6.35;    %internal nozzle area ratio
p.Ae_on_b=5;  %engine nozzle exit area per unit width
p.hi=3.25; %assume this is the height of the engine inlet (ft)
%do the assumed modes stuff
SCRAMFlag=1; %1 = scramjet, 0 = rocket
PhaseFraction_1=0.0; %0=beginning of phase; 1=end of phase
PhaseFraction_2=0.1;
PhaseFraction_3=1.0;
%These three temp distributions are pre-calculated for point design
%considerations
Tempdist_1=[100,100,100,100,100,100,100,100,100,100,100];%t=0
Tempdist_2=[543,498,486,480,475,472,469,467,465,463,461];%t=3600 sec
Tempdist_3=[907,825,803,791,783,777,772,768,764,761,758];%t=7200 sec
[wn,phi_n,Iyy,mass,EI,xcg]=hsv_modes(SCRAMFlag, PhaseFraction_2, Tempdist_2,model_opts);
wn=wn(3:5); phi_n=phi_n(:,3:5); p.Iyy=Iyy*k_Mass; p.mass=k_Mass*mass;
p.EI=EI; p.cg=[-xcg+k_CG  zbar]; p.wn=wn; p.phi_n=phi_n;
%Misc definitions
p.Sref = p.L^2; p.cbar = p.L; p.xa=abs(p.L+p.cg(1)); p.xf=abs(p.cg(1)); p.model_opts = model_opts;
```

Macro: hsv_modes.m

```
function [wn,phi_n,Iyy,mass,EIbar,x_cg]=hsv_modes_2(SCRAMFlag,PhaseFraction,TempDist,model_opts);
%Define constants, etc (all English units)
% model_opts(1) = 1: Flexible
%                 0: Rigid
% model_opts(2) = k_EI: scalar to multiply elasticity Modulus by
% model_opts(3) = k_Can: scalar to multipy canard area by
%                       k_Can = 0; no canard
%                       k_Can = 1; use Bolender's  default size
% model_opts(4) = k_Elev: scalar to multipy eleveator area by
%                       k_Elev = 0; no elevator (not recommended)
%                       k_Elev = 1; use Bolender's  default size
% model_opts(5) = 1: Included viscous effects
%                 0: No viscous effects
% model_opts(6) = 1: Included unsteady effects
%                 0: No unsteady effects
% model_opts(7) = 1: Included 2nd piggy back vehicle geometry
%                 0: Single vehicle
%
k_EI = model_opts(2);
if ~model_opts(1)   %if Rigid, set k_EI very large
    k_EI = 5000;
end
nmodes=8;
nmodesout=5; %because first two are rigid body modes...
kpts=1001;
Lbeam=100;
Ixx=1/12*.8^3;%1/12*2.93^3*1; %1/12*3.78^3*1;  %ft^4
Mass_uniform_beam=75000; %lbs
g=32.17; z=[]; zdp=[]; M=[]; K=[];
%position along beam
x=linspace(0,Lbeam,kpts);
dx=x(2)-x(1);

foresystem=5000;  %lbs
foresystem_x=10;
foresystem_dist_range=4;
foreH2=114000;%lbs
foreH2_x=40;
foreH2_dist_range=20;
foreH2_half_through_climb=99000; %lbs
payload=2500;%lbs
payload_x=55;
payload_dist_range=10;
LO2=155000;%lbs
LO2_x=55;
LO2_dist_range=14;
engine_lbs=10000;%lbs
engine_x=60;
engine_dist_range=14;
aftH2=86000;%lbs
aftH2_x=75;
aftH2_dist_range=15;
```

```
aft_sys=7500;%lbs
aft_sys_x=90;
aft_sys_dist_range=4;
struct_pt_mass_at_cg=50000;%lbs
struct_pt_mass_at_cg_x=55;
struct_pt_mass_at_cg_range=30;
nT=length(TempDist);
Temp_profile=interp1(linspace(0,100,nT),TempDist,linspace(0,100,1001));
%Young's Modulus Ti as a function of temperature
Tdata=[83,210,300,400,480,600,700,800,895]; %deg F
Edata=10^6*[16.09,15.33,15.0,14.5,14.06, 13.53, 12.98, 12.43,11.91]*144;
Efit=polyfit(Tdata,Edata,1);
E_of_x=polyval(Efit,Temp_profile);
EI=k_EI*E_of_x*Ixx;
EIbar=mean(EI);
%now set the mass distribution based on where you are in the trajectory:
if SCRAMFlag == 0,
    LO2fuelratio = 1 - PhaseFraction;
    foreHydfuelratio = 1 - PhaseFraction*(1 - foreH2_half_through_climb/foreH2);
    aftHydfuelratio=foreHydfuelratio;
elseif SCRAMFlag==1
    LO2fuelratio = 0;
    foreHydfuelratio = foreH2_half_through_climb/foreH2 -PhaseFraction*foreH2_half_through_climb/foreH2;
    aftHydfuelratio = foreHydfuelratio;
end
distFuelm = [foresystem  foreHydfuelratio*foreH2 payload LO2fuelratio*LO2 engine_lbs aftHydfuelratio*aftH2...
    aft_sys struct_pt_mass_at_cg];
distFuelloca = [foresystem_x foreH2_x payload_x LO2_x engine_x aftH2_x aft_sys_x struct_pt_mass_at_cg_x];
distFuelRange = [foresystem_dist_range foreH2_dist_range payload_dist_range LO2_dist_range engine_dist_range...
    aftH2_dist_range aft_sys_dist_range struct_pt_mass_at_cg_range];
distFuelMasses = [distFuelm; distFuelloca; distFuelRange];
%Now get the frequencies for a free-free beam of length Lbeam
iguess=[1.5*pi 2.5*pi (2*(4:nmodes+2)-1)*pi/2];
    %errors on higher frequencies due to the cosh(beta*L) term growing rather large
for icount=1:nmodes
    beta(icount)=fzero(@free_free_beam,iguess(icount)/Lbeam,[],Lbeam);
end
%Now get the mode shapes and put them into a matrix
z=zeros(kpts,nmodes);
for icount=1:nmodes
    z(:,icount)=mode_shape(x,beta(icount),Lbeam).';
    zdp(:,icount)=mode_shaped2(x,beta(icount),Lbeam).';  %second derivative (spatial) of the mode shape
end
%Compute the mass distribution function (ie mass per unit length)
for i=1:length(x)
    m_of_x(i)=mass_distribution(x(i),distFuelMasses,Mass_uniform_beam,Lbeam)/g/50;
    %convert lbm to slugs to get the correct units %divided by assumed width=50ft
end
%Compute the total mass:
Mass_total=m_of_x*ones(length(x),1)*dx;
%Compute the cg:
x_cg=1/Mass_total*m_of_x*x.'*dx;
%Append the rigid body modes to the flex mode shapes
```

```
z=[ones(kpts,1) x.'-x_cg z];
zdp=[zeros(kpts,2) zdp];
%Start the computation of the "assumed modes" part
%1) compute the mass matrix
M=z.'*diag(m_of_x)*z*dx;
%2) compute the stiffness matrix
K=zdp.'*diag(EI)*zdp*dx;
%Solve the eigenvalue problem
[V,wnsq]=eig(inv(M)*K);
wnsq=diag(wnsq);
wn=sqrt(wnsq);
%order the frequencies from lowest to highest
[ans,jj]=sort(wn);
wn=wn(jj);
%reorder the eigenvectors
V=V(:,jj);
%Compute the modeshapes..
for i=1:nmodesout
    phi(:,i)=(V(:,i).'*z.');
    if phi(1,i) < 0
        phi(:,i)=-phi(:,i);
    end
end
disp(['The first ',num2str(nmodesout),' frequencies are:'])
disp(num2str(wn(1:nmodesout)))
%Perform the mass normalization
Mnew=phi.'*diag(m_of_x)*phi*dx;
for i=1:nmodesout
    phi_n(:,i)=phi(:,i)/sqrt(Mnew(i,i));
end
mass=Mnew(1,1);
Iyy=Mnew(2,2);
if ~model_opts(1)
    EIbar = inf;
end
```

Macro: mass_distribution.m

```
function m_of_x= mass_distribution(x,distFuelMasses,mass_uniform_beam,Lbeam)
%Evaluate the mass distribution at point x
[m,n]=size(distFuelMasses);
mx0=mass_uniform_beam/Lbeam;
if x<=0 | x>=Lbeam
    m_of_x=0;
else
    m_of_x=mx0;
    for i=1:n
        if x >= distFuelMasses(2,i)-distFuelMasses(3,i)/2 & x <= distFuelMasses(2,i)+distFuelMasses(3,i)/2
            m_of_x=m_of_x+distFuelMasses(1,i)/distFuelMasses(3,i);
        end
    end
```

```
end
```

Macro: mode_shape.m

```
function y= mode_shape(x, beta, L);
%Evaluate the mode shape at x for a given beta and L
y=(cos(beta.*L)-cosh(beta.*L)).*(sin(beta.*x)+sinh(beta.*x))-(sin(beta.*L)-...
    sinh(beta.*L)).*(cos(beta.*x)+cosh(beta.*x));
```

Macro: mode_shape2.m

```
function ydp= mode_shaped2(x, beta, L);
%Evaluate the second derivative of the mode shape at x for a given beta and L
ydp=beta.^2.*(cos(beta.*L)-cosh(beta.*L)).*(-sin(beta.*x)+sinh(beta.*x))-...
    beta.^2.*(sin(beta.*L)-sinh(beta.*L)).*(-cos(beta.*x)+cosh(beta.*x));
```

Macro: eqns_of_motion.m

```
function [xdot,Data]=eqns_of_motion(t,x,u,p,varargin)
%States
Vt=x(1); alpha=x(2); Q=x(3); h=x(4); theta=x(5); eta1=x(6);
eta1dot=x(7); eta2=x(8); eta2dot=x(9); eta3=x(10); eta3dot=x(11);
%Control inputs
delta_e=u(1); delta_c=u(2); phi=u(3);
%Compute Mach, after first calling the std atmosphere
[temp,press,rho]=atmosphere4(h,1);
Mach=Vt/sqrt(1.4*1716*temp);
%Misc parameters
zeta=0.02; %(assumed for the structure)
g0=32.17;
Re = 2.092567257e7;  %mean radius of earth, ft
r=Re+h;
g=g0*(Re/r)^2;
%Define the perturbations for the piston theory increments
Xold=x;
if(~isempty(varargin))
    Xold=varargin{1,1};
end
%Call to get the forces
[Lift,Drag,Thrust,Moment,N,Data]=aeroforces(p,x,u,Xold);
%Equations of motion
Vdot=(Thrust*cos(alpha)-Drag)/p.mass-g*sin(theta-alpha);
alpha_dot=(-Thrust*sin(alpha)-Lift)/(p.mass*Vt)+Q+(g/Vt-Vt/r)*cos(theta-alpha);
Qdot=Moment/p.Iyy;
hdot=Vt*sin(theta-alpha);
theta_dot=Q;
eta1ddot=-2*zeta*p.wn(1)*eta1dot-p.wn(1)^2*eta1+N(1);
eta2ddot=-2*zeta*p.wn(2)*eta2dot-p.wn(2)^2*eta2+N(2);
```

```
eta3ddot=-2*zeta*p.wn(3)*eta3dot-p.wn(3)^2*eta3+N(3);
Zeq = Lift-g*p.mass;
Xeq = Thrust-Drag;
xdot=[Vdot;alpha_dot;Qdot;hdot;theta_dot;eta1dot;eta1ddot;eta2dot;eta2ddot;eta3dot;eta3ddot];
Data.States = [Vt alpha Q h theta eta1 eta1dot eta2 eta2dot eta3 eta3dot]';
Data.Controls = [delta_e delta_c phi]';
Data.State_Derivatives = xdot;
Data.Forces.Zeq = Zeq;
Data.Forces.Xeq = Xeq;
```

Macro: oblique_shock.m

```
function [M2,p2,T2,theta]=oblique_shock(M1,p1,T1,delta)
%Given M1, P1, T1, and the turning angle (in radians), compute
%the Mach number, pressure (static) and temperature behind
%the oblique shock and the angle of the shock (in deg)
%M Bolender 20 Jan 2004
if M1<=1
 error('Initial Mach must be supersonic!!!!')
end
gam=1.4;
%From page 143 of Anderson, Modern Compressible Flow with Historical
%Perspective
lambda=sqrt((M1^2-1)^2-3*(1+(gam-1)/2*M1^2)*(1+(gam+1)/2*M1^2)*tan(delta)^2);
chi=((M1^2-1)^3-9*(1+(gam-1)/2*M1^2)*(1+(gam-1)/2*M1^2+(gam+1)/4*M1^4)*tan(delta)^2)/lambda^3;
num=M1^2-1+2*lambda*cos((4*pi+acos(chi))/3);
den=3*tan(delta)*(1+(gam-1)/2*M1^2);
theta=atan(num/den);
M1n=M1*sin(theta);
M1t=M1*cos(theta);
M2n= sqrt((M1n^2+2/(gam-1))/(2*gam/(gam-1)*M1n^2-1));
p2p1=(2*gam*M1n^2-gam+1)/(gam+1);
T2T1=(1+(gam-1)/2*M1n^2)*(2*gam/(gam-1)*M1n^2-1)/(M1n^2*(2*gam/(gam-1)+(gam-1)/2));
M2t= M1t*sqrt(1/T2T1);
M2=sqrt(M2t^2+M2n^2);
p2=p2p1*p1;
T2=T2T1*T1;
theta=theta*180/pi;
```

Macro: expansion_fan.m

```
function [M2,p2,T2,error,nu2]=expansion_fan(M1,p1,T1,delta,error)
%Given the flow conditions before a corner, calculate the
%flow after the expansion fan and return the conditions.
%Note that delta must be given in radians. nu will be returned
%in degrees.
%M Bolender 20 Jan 2004
%Revised: 18 July 05:  better inital guess!!!!
gam=1.4; %ratio of specific heats for air
nu=sqrt((gam+1)/(gam-1))*atan(sqrt((gam-1)/(gam+1)*(M1^2-1)))-atan(sqrt(M1^2-1));
```

```
%now that we have nu, we have to do some root finding in order to get the
%Mach number of the flow after the expansion
nu2=nu+delta;
if nu2 >=130.4*pi/180
    nu2=130.4*pi/180;  % this keeps the sim from dying due to an infeasible soln
    disp('Maximum expansion angle exceeded')
    error = 4;
end
a=1.98350571881355;
b=0.391856059187111;
c=-0.837922863389792;
M2=tan((nu2-c)/a)/b;
Mguess=tan((nu2-c)/a)/b;
[M2,FVAL,EXITFLAG,OUTPUT]=fzero(@f,Mguess,[],gam,nu2);
T2=T1*(1+(gam-1)/2*M1^2)/(1+(gam-1)/2*M2^2);
p2=p1*(T2/T1)^(gam/(gam-1));
nu=nu*180/pi;
%*************************************************************************
%  define a function that gives the nu-nu_des so we can do root finding for the  *
%  Mach number after the expansion fan                                            *
%                                                                                 *
%*************************************************************************
function y=f(M,gam,nu2)
y=sqrt((gam+1)/(gam-1))*atan(sqrt((gam-1)/(gam+1)*(M^2-1)))-atan(sqrt(M^2-1))-nu2;
```

Macro: scjet.m

```
function [M3,p3,T3]=scjet(M2,p2,T2,phi)
gam=1.4;  %ratio of specific heats
eta_c=0.9;    %combustion efficiency
lambda=6/206;  %Stoichiometric (mass) fuel-to-air ratio
Hf=51500;  %Lower heating value of H2
cp=0.24;   %BTU/(lbm deg R), specific heat at constant pressure for air
Tt2=T2*(1+(gam-1)/2*M2^2);  %total temperature
Tt3Tt2=(1+Hf*eta_c*lambda*phi/(cp*Tt2))/(1+lambda*phi);
Tt3=Tt3Tt2*Tt2;
Delta_T_0=Tt3-Tt2;
%For the change in total temperature, determine Mach at combustor exit
rhs=M2^2*(1+.5*(gam-1)*M2^2)/(gam*M2^2+1)^2+M2^2/(gam*M2^2+1)^2*Delta_T_0/T2;
M3=sqrt((25/2).*((-5) + 49.*rhs).^(-1) + (5/2).*sqrt(5).*sqrt(5 + (-24).*rhs) ...
  .*((-5) + 49.*rhs).^(-1) + (-35).*rhs.*((-5) + 49.*rhs).^(-1));
p3=p2*(1+gam*M2^2)/(1+gam*M3^2);
T3=T2*((1+gam*M2^2)/(1+gam*M3^2)*M3/M2)^2;
```

Macro: aeroforces.m

```
function [Lift,Drag,Thrust,M,N,Data]=aeroforces(p, X, u, Xold)
%p = a vector a parameters that defines the aircraft's outer mold line &
%mass properties
%X = aircraft's current state
```

```
%u = aircraft's control input
%Xold = state of the aircraft at the last time step
%This function calculates the forces acting on a generic hypersonic airbreathing vehicle
%Use the gas dynamic relationships found in John, "Gas Dynamics" Second Edition,
%Allyn and Bacon, 1984.
%Mike Bolender
%AFRL/VACA
%3 Feb 2004  Initial code
%rev 23 Feb 2004 to change the CG location
%rev 24 Feb 2004 to clean up some of the moment arms
%rev 25 Feb 2004 to remove dependence on hardwired aircraft geometry
%rev 26 Feb 2004 to accommodate a new vehicle geometry that includes a top surface that is
% inclined at an angle tau_1U
%rev 09 Mar 2004 to include the aeroelastic effects.
%rev 10 May 2005  change control input from DT0 to phi and a fixed Ad.
%rev 14 Sept 2005  Change to the new vibe model (free-free beam).
%rev 13 Mar 2006 Add canard and remove the cowl door as an input.
%rev 4-5 Sept 2007 Initial re-write to use a data structure for the aircraft
%outer mold line geometry and general clean-up of the code
% Jeff Dickeson
% Arizona State University
% rev Jan 20 2007, add model options to p
% model_opts(1) = 1: Flexible
%                 0: Rigid
% model_opts(2) = k_EI: scalar to multiply elasticity Modulus by
% model_opts(3) = k_Can: scalar to multipy canard area by
%                       k_Can = 0; no canard
%                       k_Can = 1; use Bolender's  default size
% model_opts(4) = k_Elev: scalar to multipy eleveator area by
%                       k_Elev = 0; no elevator (not recommended)
%                       k_Elev = 1; use Bolender's  default size
% model_opts(5) = 1: Included viscous effects
%                 0: No viscous effects
% model_opts(6) = 1: Included unsteady effects
%                 0: No unsteady effects
% model_opts(7) = 1: Included 2nd piggy back vehicle geometry
%                 0: Single vehicle
%
%%%
```

```
nn=length(p.phi_n(:,1));
dx=p.L/(nn-1);
dphi1_dx0=(p.phi_n(2,1)-p.phi_n(1,1))/dx; dphi1_dxL=(p.phi_n(end,1)-p.phi_n(end-1,1))/dx;
dphi2_dx0=(p.phi_n(2,2)-p.phi_n(1,2))/dx; dphi2_dxL=(p.phi_n(end,2)-p.phi_n(end-1,2))/dx;
dphi3_dx0=(p.phi_n(2,3)-p.phi_n(1,3))/dx; dphi3_dxL=(p.phi_n(end,3)-p.phi_n(end-1,3))/dx;
DPHI0=[dphi1_dx0 dphi2_dx0 dphi3_dx0]; DPHIL=[dphi1_dxL dphi2_dxL dphi3_dxL];
Delta_tau_1=DPHI0*eta; Delta_tau_2=DPHIL*eta;
if ~p.model_opts(1)   %if Rigid, set Delta_tau = 4;
    Delta_tau_1 = 0;
    Delta_tau_2 = 0;
end
%Physical Constants:
R=1716;  gam=1.4;
%Compute wedge angles given the displacement of the fuselage due to
%flexibility
tau_1U=p.tau_1U-Delta_tau_1; tau_1L=p.tau_1L+Delta_tau_1;  tau_2=p.tau_2-Delta_tau_2;
rcg=[p.cg(1) p.cg(2)];  %position vector of the cg
rcs=p.rel-rcg; rin=[-p.L_1 p.L_1*tan(tau_1L)]-rcg;
rfb=[-p.L_1/2 p.L_1/2*tan(tau_1L)]-rcg; rc=[p.rcan(1) p.rcan(2)]-rcg;
%Calculate atmosphere properties
[Tinf,pinf,rhoinf]=atmosphere4(h,1);
asonic=sqrt(gam*R*Tinf); %speed of sound at the flight altitude in ft/sec
Minf=V/asonic;
%%%%%%%%%%%%%%%%%%%%%%%%%%%%%%%%%%%%%%%%%%%%%%%%%%%%%%%%%%%%%%%%%%%%%%%%%%%%%%%
%Get flow parameters after the bow shock on the lower forebody
if tau_1L+alpha > 0
    [M1,p1,T1,theta]=oblique_shock(Minf,pinf,Tinf,tau_1L+alpha);
    theta_r=theta*pi/180;
    theta_sol=atan((p.L_1*tan(tau_1L)+p.hi)/p.L_1);
    %angle that the shock needs to make to impinge on the engine lip
elseif tau_1L+alpha < 0
    [M1,p1,T1,ErrorFlag]=expansion_fan(Minf,pinf,Tinf,abs(tau_1L+alpha),ErrorFlag);
    theta_r=0;     theta=0;    theta_sol=0;
elseif tau_1L+alpha==0
    M1=Minf;    p1=pinf;    T1=Tinf;    theta_r=0; theta=0;
    theta_sol=atan((p.L_1*tan(tau_1L)+p.hi)/p.L_1);
    %angle that the shock needs to make to impinge on the engine lip
end
%Compute the forces on the lower forebody in the x and z dir
Xf=-p1*tan(tau_1L)*p.L_1;Zf=-p1*p.L_1; Mf=rfb(2)*Xf-rfb(1)*Zf;
%%%%%%%%%%%%%%%%%%%%%%%%%%%%%%%%%%%%%%%%%%%%%%%%%%%%%%%%%%%%%%%%%%%%%%%%%%%%%%%
%We assume the top surface of the vehicle is a ramp with angle tau_1U. This calculates the pressure over top of
%the vehicle
if abs(tau_1U-alpha) < 1e-6
    Mu=Minf; Tu=Tinf; pu=pinf;
elseif abs(tau_1U-alpha) > 1e-6 && sign(tau_1U-alpha) == 1
    [Mu,pu,Tu]=oblique_shock(Minf,pinf,Tinf,tau_1U-alpha);
elseif abs(tau_1U-alpha) > 1e-6 && sign(tau_1U-alpha) ==-1
    [Mu,pu,Tu,ErrorFlag]=expansion_fan(Minf,pinf,Tinf,abs(tau_1U-alpha),ErrorFlag);
end
%Compute the forces on the upper forebody
Xu=-pu*tan(tau_1U)*p.L; Zu=pu*p.L;
ru=[-p.L/2 -p.L/2*tan(tau_1U)]-rcg; M_u=ru(2)*Xu-ru(1)*Zu;
```

```
%%%%%%%%%%%%%%%%%%%%%%%%%%%%%%%%%%%%%%%%%%%%%%%%%%%%%%%%%%%%%%%%%%%%%%%%%%%%%%%%
%Now get the pressure on the bottom of the vehicle
    if abs(theta-alpha*180/pi-theta_sol*180/pi)>1e-6 && theta-alpha*180/pi>theta_sol*180/pi
        [Mb,pb,Tb,ErrorFlag,nu]=expansion_fan(M1,p1,T1,tau_1L,ErrorFlag);
        Zb=-pb*(p.Le);
    elseif abs(theta-alpha*180/pi-theta_sol*180/pi)>1e-6 && theta-alpha*180/pi<theta_sol*180/pi
        %no spillage, an oblique shock is present off the bottom of the vehicle
        [Mb,pb,Tb,tb]=oblique_shock(Minf,pinf,Tinf,alpha);
        Zb=-pb*(p.Le);
    elseif abs(theta-alpha*180/pi-theta_sol*180/pi)<1e-6
        Zb=-pinf*(p.Le);
    end
M_b=-Zb*(rin(1)+0.5*(-p.Le));  %moment due to pressure on the bottom of the aircraft
%%%%%%%%%%%%%%%%%%%%%%%%%%%%%%%%%%%%%%%%%%%%%%%%%%%%%%%%%%%%%%%%%%%%%%%%%%%%%%%%
%Turn the forebody flow through an angle tau_1L to get the boundary conditions at
%the engine inlet
[M1a,p1a,T1a]=oblique_shock(M1,p1,T1,tau_1L);
%%%%%%%%%%%%%%%%%%%%%%%%%%%%%%%%%%%%%%%%%%%%%%%%%%%%%%%%%%%%%%%%%%%%%%%%%%%%%%%%
%We use the flow properties from behind the bow shock as the boundary conditions
%on the engine diffuser inlet.
polyM2=[1/15625 0 6/3125 0 3/125 0 4/25 0 3/5 0 (6/5-(Ad/M1a)^2*(1+.2*M1a^2)^6) 0 1];
roots_polyM2=roots(polyM2);
im2=find(imag(roots_polyM2)==0);
if ~isempty(im2)
 M2=max(roots_polyM2(im2));
 p2=p1a*( (1+(gam-1)/2*M1a^2)/(1+(gam-1)/2*M2^2))^(gam/(gam-1));
 T2=T1a*(1+(gam-1)/2*M1a^2)/(1+(gam-1)/2*M2^2);
elseif isempty(im2)
 %error('M2: Not a physical situation')
 disp('M2: Not a physical situation')
 ErrorFlag = 1;
end
%%%%%%%%%%%%%%%%%%%%%%%%%%%%%%%%%%%%%%%%%%%%%%%%%%%%%%%%%%%%%%%%%%%%%%%%%%%%%%%%
%Compute combustor exit properties given the diffuser exit/combustor inlet properties
[M3,p3,T3]=scjet(M2,p2,T2,phi);
if ~isreal(M3)
    M3 = real(M3);
    p3 = real(p3);
    T3 = real(T3);
    ErrorFlag = 2;
end
%%%%%%%%%%%%%%%%%%%%%%%%%%%%%%%%%%%%%%%%%%%%%%%%%%%%%%%%%%%%%%%%%%%%%%%%%%%%%%%%
%The next step is to consider the exit nozzle for the scramjet
polyM4=[1/15625 0 6/3125 0 3/125 0 4/25 0 3/5 0 (6/5-p.An^2*(1+.2*M3^2)^6/M3^2) 0 1];
roots_polyM4=roots(polyM4);
im4=find(imag(roots_polyM4)==0);
if ~isempty(im4)
    Me=max(roots_polyM4(im4));
    pe=p3*( (1+(gam-1)/2*M3^2)/(1+(gam-1)/2*Me^2))^(gam/(gam-1));
    Te=T3*(1+(gam-1)/2*M3^2)/(1+(gam-1)/2*Me^2);
elseif isempty(im4)
    disp('Me: Not a physical situation')
    ErrorFlag = 3;
```

```
end
if(pe<pinf)
        ErrorFlag=5;
end
%%%
```

```
    Fnormal=0;
    Xcs=0;
    Zcs=0;
    Mel=Minf;Meu=Minf; pel=pinf; peu=pinf; Tel=Tinf; Teu=Tinf;
end%Compute the moment
M_cs=rcs(2)*Xcs-rcs(1)*Zcs;
%%%%%%%%%%%%%%%%%%%%%%%%%%%%%%%%%%%%%%%%%%%%%%%%%%%%%%%%%%%%%%%%%%%%%%%%%%%%%%%
%Canard
if (delta_c+alpha-Delta_tau_1)>tol
    [Mc_o,pc_o,Tc_o]=oblique_shock(Minf,pinf,Tinf,abs(alpha+delta_c-Delta_tau_1));
    [Mc_e,pc_e,Tc_e,ErrorFlag]=expansion_fan(Minf,pinf,Tinf,abs(delta_c+alpha-Delta_tau_1),ErrorFlag);
    pcl=pc_o; Tcl=Tc_o; Mcl=Mc_o;
    pcu=pc_e; Tcu=Tc_e; Mcu=Mc_e;
    Fnormal=-(pcl-pcu)*p.Sc;
    if delta_c-Delta_tau_1 >= 0
        Xc=Fnormal*sin(delta_c-Delta_tau_1);
        Zc=Fnormal*cos(delta_c-Delta_tau_1);
    elseif delta_c-Delta_tau_1 < 0
        Xc=-Fnormal*sin(delta_c-Delta_tau_1);
        Zc=Fnormal*cos(delta_c-Delta_tau_1);
    end
elseif (delta_c+alpha-Delta_tau_1) < -tol
    [Mc_o,pc_o,Tc_o]=oblique_shock(Minf,pinf,Tinf,abs(alpha+delta_c-Delta_tau_1));
    [Mc_e,pc_e,Tc_e,ErrorFlag]=expansion_fan(Minf,pinf,Tinf,abs(delta_c+alpha-Delta_tau_1),ErrorFlag);
    pcl=pc_e; Tcl=Tc_e; Mcl=Mc_e;
    pcu=pc_o; Tcu=Tc_o; Mcu=Mc_o;
    Fnormal=-(pcl-pcu)*p.Sc;
    if delta_c-Delta_tau_1> 0
        Xc=-Fnormal*sin(delta_c-Delta_tau_1);
        Zc=Fnormal*cos(delta_c-Delta_tau_1);
    elseif delta_c-Delta_tau_1<= 0
        Xc=Fnormal*sin(delta_c-Delta_tau_1);
        Zc=Fnormal*cos(delta_c-Delta_tau_1);
    end
else
    Fnormal=0;
    Xc=0;
    Zc=0;
    Tcl=Tinf; pcl=pinf; Mcl=Minf;
    Tcu=Tinf; pcu=pinf; Mcu=Minf;
end
%Compute the moment
M_c=rc(2)*Xc-rc(1)*Zc;
%%%%%%%%%%%%%%%%%%%%%%%%%%%%%%%%%%%%%%%%%%%%%%%%%%%%%%%%%%%%%%%%%%%%%%%%%%%%%%%
%Compute the unsteady forces and moment
u_unsteady=[Minf pinf rhoinf asonic Mu pu pu/(R*Tu) sqrt(1.4*1716*Tu) M1 p1 p1/(R*T1) sqrt(1.4*1716*T1)...
    Mb pb pb/(1716*Tb) sqrt(1.4*1716*Tb) Mel pel pel/(1716*Tel) sqrt(1.4*1716*Tel) Meu peu peu/(1716*Teu)...
    sqrt(1.4*1716*Teu) pe/(1716*Te) sqrt(1.4*1716*Te) alpha Q Xold(2) Xold(3) etadot(1) Xold(7) delta_e].';
%These will be increments
[X_unsteady, Z_unsteady, Moment_unsteady]=force_moment_increments(u_unsteady,p);
if ~p.model_opts(6)
    X_unsteady = 0;
    Z_unsteady = 0;
```

```
    Moment_unsteady = 0;
end
%%%%%%%%%%%%%%%%%%%%%%%%%%%%%%%%%%%%%%%%%%%%%%%%%%%%%%%%%%%%%%%%%%%%%%%%%%%%%%%%
%Compute the viscous flow effects
%Hardwire the temperatures for the time being (2500 deg R)
Tw_upper=2500; Tw_lower_fore=2500; Tw_engine_nacelle=2500; Tw_rearramp=2500;
Tw_elevator_top=2500; Tw_elevator_bottom=2500; Tw_canard_top=2500; Tw_canard_bottom=2500;
u_viscous=[Tw_upper Tw_lower_fore Tw_engine_nacelle Tw_rearramp Tw_elevator_top...
    Tw_elevator_bottom Tw_canard_top Tw_canard_bottom...
    alpha delta_e delta_c Mu pu Tu sqrt(1.4*1716*Tu) M1 p1 T1 sqrt(1.4*1716*T1) ...
    Mb pb Tb sqrt(1.4*1716*Tb) Mel pel Tel sqrt(1.4*1716*Tel) Meu peu Teu sqrt(1.4*1716*Teu)...
Mcu pcu Tcu sqrt(1.4*1716*Tcu) Mcl pcl Tcl sqrt(1.4*1716*Tcl) Minf pinf Tinf asonic Me pe Te sqrt(1.4*1716*Te)];
[Lift_viscous,Drag_viscous,Moment_viscous]=viscous_effects(u_viscous,p);
if ~p.model_opts(5)
    Lift_viscous = 0;
    Drag_viscous = 0;
    Moment_viscous = 0;
end
%%%%%%%%%%%%%%%%%%%%%%%%%%%%%%%%%%%%%%%%%%%%%%%%%%%%%%%%%%%%%%%%%%%%%%%%%%%%%%%%
%Resolve the forces on each surface of the vehicle
%Now sum the forces
X=Xf+Xe+Fx_inlet+Xcs+Xu+Xc+X_unsteady;
Z=Zf+Zu+Zb+Ze+Fz_inlet+Zcs+Zc+Z_unsteady;
%compute lift and drag
Lift=X*sin(alpha)-Z*cos(alpha)+Lift_viscous;
Drag=-(X*cos(alpha)+Z*sin(alpha))+Drag_viscous;
%%%%%%%%%%%%%%%%%%%%%%%%%%%%%%%%%%%%%%%%%%%%%%%%%%%%%%%%%%%%%%%%%%%%%%%%%%%%%%%%
%Now we calculate the amount of spill due to the extension of the door.  The difference between mdot_spill and
%mdot_door_spill  is the extra airflow that is sent through the engine.
if theta_r~=0
    mdot_engine=pinf*Minf*sqrt(gam/(R*Tinf))*p.hi*sin(theta_r)*cos(p.tau_1L)/sin(theta_r-p.tau_1L-alpha);
    if(theta_r<theta_sol)
     mdot_engine=pinf*Minf*sqrt(gam/(R*Tinf))*((p.L_1/tan(p.tau_1L))*sin(p.tau_1L - alpha)+p.hi*cos(alpha));
    end
else
    mdot_engine=pinf*Minf*sqrt(gam/(R*Tinf))*p.hi*cos(p.tau_1L);
end
Ve=Me*sqrt(gam*R*Te);
Vinf=Minf*sqrt(gam*R*Tinf);
Thrust=mdot_engine*(Ve-Vinf)+(pe-pinf)*Ae_on_b;
%%%%%%%%%%%%%%%%%%%%%%%%%%%%%%%%%%%%%%%%%%%%%%%%%%%%%%%%%%%%%%%%%%%%%%%%%%%%%%%%
%Compute the total moment acting on the vehicle
M=Mf+M_e+M_inlet+M_cs+(p.L_1*tan(p.tau_1L)+p.hi/2-p.cg(2))*Thrust+M_u+M_b+M_c+Moment_unsteady+Moment_viscous;
%%%%%%%%%%%%%%%%%%%%%%%%%%%%%%%%%%%%%%%%%%%%%%%%%%%%%%%%%%%%%%%%%%%%%%%%%%%%%%%%
%Compute the generalized force
pvec=[p1 pb pu pe pinf Zcs Zc];
N=gen_force(p,pvec);
Data.Misc.Engine_mass_flow = mdot_engine;
Data.Error.Code = ErrorFlag;
if ErrorFlag == 0
    Data.Error.Type = 'No Errors';
elseif ErrorFlag == 1
    Data.Error.Type = 'M2: Not a physical situation';
```

```
elseif ErrorFlag == 2
    Data.Error.Type = 'M3: Not a physical situation';
elseif ErrorFlag ==3
    Data.Error.Type = 'Me: Not a physical situation';
elseif ErrorFlag ==5
    Data.Error.Type = 'pe: Less than pinf';
end
```

Macro: viscous_effects.m

```
function [L_viscous, D_viscous, Moment_viscous]=viscous_effects(u,p);
Tw_upper=u(1);  Tw_lower_fore=u(2); Tw_engine_nacelle=u(3); Tw_rearramp = u(4); Tw_elevator_top=u(5);
Tw_elevator_bottom=u(6); Tw_canard_top=u(7); Tw_canard_bottom=u(8); Alpha=u(9); de=u(10);
dc=u(11); M_upper = u(12); P_upper = u(13); T_upper = u(14); a_upper = u(15); M_lower_fore = u(16);
P_lower_fore = u(17); T_lower_fore = u(18); a_lower_fore = u(19);M_engine_nacelle = u(20);
P_engine_nacelle = u(21); T_engine_nacelle = u(22); a_engine_nacelle = u(23); M_elev_top=u(28);
P_elev_top=u(29); T_elev_top=u(30); a_elev_top= u(31); M_elev_bottom=u(24); P_elev_bottom=u(25);
T_elev_bottom=u(26); a_elev_bottom = u(27); M_canard_top=u(32); P_canard_top=u(33);
T_canard_top=u(34); a_canard_top=u(35); M_canard_bottom=u(36); P_canard_bottom=u(37);
T_canard_bottom=u(38); a_canard_bottom=u(39); Minf=u(40);  Pinf=u(41);
Tinf=u(42); ainf=u(43); Mengine_out=u(44); Pengine_out=u(45); Tengine_out=u(46); aengine_out=u(47);

mu_sl = 3.747e-7; T_sl = 518.67; R=1716;
%Flow properties
Vinf=Minf*sqrt(1.4*R*Tinf); rhoinf=Pinf/(R*Tinf);
%-------------------------------------------------------------------------------
% Upper Surface
V_upper = M_upper*a_upper; % Flow velocity at upper surface in ft/sec
T_upperstar = T_upper*(1+.032*M_upper^2+.58*(Tw_upper/T_upper - 1));
rho_upperstar = P_upper/(R*T_upperstar); % Density in slug/ft^3
mu_upperstar = mu_sl * (T_upperstar/T_sl)^(3/2)*((T_sl+198.6)/(T_upperstar+198.6)); %
Re_upper=rho_upperstar*V_upper*p.L/cos(p.tau_1U)/mu_upperstar;
N_upper = (5/4)*(.0592/2)*rhoinf*Vinf^2*(mu_upperstar/(rho_upperstar*V_upper))^(1/5)...
    (p.L/cos(p.tau_1U))^(4/5)*sin(p.tau_1U);
A_upper = (5/4)*(.0592/2)*rhoinf*Vinf^2*(mu_upperstar/(rho_upperstar*V_upper))^(1/5)...
    *(p.L/cos(p.tau_1U))^(4/5)*cos(p.tau_1U);
M_upper = (5/4)*(.0592/2)*rhoinf*Vinf^2*(mu_upperstar/(rho_upperstar*V_upper))^(1/5)...
    *(p.L/cos(p.tau_1U))^(4/5)*sin(p.tau_1U)*p.xf;
L_upper = N_upper*cos(Alpha)-A_upper*sin(Alpha); % Pounds
D_upper = (N_upper*sin(Alpha)+A_upper*cos(Alpha)); % Pounds
%-------------------------------------------------------------------------------
% Lower Forebody
V_lower_fore = M_lower_fore*a_lower_fore; % Flow velocity at lower forebody in ft/sec
T_lower_forestar = T_lower_fore*(1+.032*M_lower_fore^2+.58*(Tw_lower_fore/T_lower_fore - 1));
rho_lower_forestar = P_lower_fore/(R*T_lower_forestar); % Density in slug/ft^3
mu_lower_forestar = mu_sl * (T_lower_forestar/T_sl)^(3/2)*((T_sl+198.6)/(T_lower_forestar+198.6));
N_lower_fore = -(5/4)*(.0592/2)*rhoinf*Vinf^2*(mu_lower_forestar/...
    (rho_lower_forestar*V_lower_fore))^(1/5)*(p.L_1/cos(p.tau_1L))^(4/5)*sin(p.tau_1L);
A_lower_fore = (5/4)*(.0592/2)*rhoinf*Vinf^2*(mu_lower_forestar/...
    (rho_lower_forestar*V_lower_fore))^(1/5)*(p.L_1/cos(p.tau_1L))^(4/5)*cos(p.tau_1L);
M_lower_fore = -(5/4)*(.0592/2)*rhoinf*Vinf^2*(mu_lower_forestar/...
```

```
    (rho_lower_forestar*V_lower_fore))^(1/5)*(p.L_1/cos(p.tau_1L))^(4/5)*sin(p.tau_1L)*p.xf;
L_lower_fore = N_lower_fore*cos(Alpha)-A_lower_fore*sin(Alpha); % Pounds
D_lower_fore = N_lower_fore*sin(Alpha)+A_lower_fore*cos(Alpha); % Pounds
%-------------------------------------------------------------------------------------
% Engine Nacelle
V_engine_nacelle = M_engine_nacelle*a_engine_nacelle; % Flow velocity at station 3 (engine nacelle) in ft/sec
T_engine_nacellestar = T_engine_nacelle*(1+.032*M_engine_nacelle^2+.58*(Tw_engine_nacelle/T_engine_nacelle-1));
rho_engine_nacellestar = P_engine_nacelle/(R*T_engine_nacellestar); % Density in slug/ft^3
mu_engine_nacellestar = mu_sl * (T_engine_nacellestar/T_sl)^(3/2)*((T_sl+198.6)/(T_engine_nacellestar+198.6));
N_engine_nacelle = 0; % Pounds
A_engine_nacelle = (.0592/2)*(5/4)*rhoinf*Vinf^2*(mu_engine_nacellestar/...
    (rho_engine_nacellestar*V_engine_nacelle))^(1/5)*(p.Le)^(4/5);
M_engine_nacelle = -(.0592/2)*(5/4)*rhoinf*Vinf^2*(mu_engine_nacellestar/...
    (rho_engine_nacellestar*V_engine_nacelle))^(1/5)*(p.Le)^(4/5)*(p.L_1*tan(p.tau_1L)+p.hi);
L_engine_nacelle = N_engine_nacelle*cos(Alpha)-A_engine_nacelle*sin(Alpha); % Pounds
D_engine_nacelle = N_engine_nacelle*sin(Alpha)+A_engine_nacelle*cos(Alpha); % Pounds
%-------------------------------------------------------------------------------------
% Rear ramp
T_rearramp_avg = (Tengine_out + Tinf)/2;
M_rearramp_avg = (Mengine_out+Minf)/2; % Average Mach number
a_rearramp_avg = (aengine_out+ainf)/2; % Average speed of sound
V_rearramp_avg = M_rearramp_avg*a_rearramp_avg; % Average flow velocity on rear ramp
P_rearramp_avg = (Pengine_out+Pinf)/2; % Average flow pressure on rear ramp
T_rearramp_avgstar = T_rearramp_avg*(1+.032*M_rearramp_avg^2+.58*(Tw_rearramp/T_rearramp_avg - 1));
rho_rearramp_avgstar = P_rearramp_avg/(R*T_rearramp_avgstar); % Density in slug/ft^3
mu_rearramp_avgstar = mu_sl * (T_rearramp_avgstar/T_sl)^(3/2)*((T_sl+198.6)/(T_rearramp_avgstar+198.6));
N_rearramp = (5/4)*(.0592/2)*rhoinf*Vinf^2*(mu_rearramp_avgstar/(rho_rearramp_avgstar*V_rearramp_avg))^(1/5)...
    *(p.L_2/cos(p.tau_1U+p.tau_2))^(4/5)*sin(p.tau_1U+p.tau_2);
A_rearramp = (5/4)*(.0592/2)*rhoinf*Vinf^2*(mu_rearramp_avgstar/(rho_rearramp_avgstar*V_rearramp_avg))^(1/5)...
    *(p.L_2/cos(p.tau_1U+p.tau_2))^(4/5)*cos(p.tau_1U+p.tau_2);
M_rearramp = -(5/4)*(.0592/2)*rhoinf*Vinf^2*(mu_rearramp_avgstar/(rho_rearramp_avgstar*V_rearramp_avg))^(1/5)...
    *(p.L_2/cos(p.tau_1U+p.tau_2))^(4/5)*(p.L_1*tan(p.tau_1L)*cos(p.tau_1U+p.tau_2)+(p.xa-p.L_2)*sin(p.tau_1U...
    +p.tau_2));
L_rearramp = N_rearramp*cos(Alpha)-A_rearramp*sin(Alpha);
D_rearramp = N_rearramp*sin(Alpha)+A_rearramp*cos(Alpha);
%-------------------------------------------------------------------------------------
% Elevator
r_el=p.rel-p.cg;
xcs=r_el(1);
zcs=r_el(2);
V_elev_bottom = M_elev_bottom*a_elev_bottom; % Flow velocity on bottom of elevator in ft/sec
V_elev_top = M_elev_top*a_elev_top; % Flow velocity on top of elevator in ft/sec
T_elev_bottomstar = T_elev_bottom*(1+.032*M_elev_bottom^2+.58*(Tw_elevator_bottom/T_elev_bottom - 1));
rho_elev_bottomstar = P_elev_bottom/(R*T_elev_bottomstar); % Density in slug/ft^3
mu_elev_bottomstar = mu_sl * (T_elev_bottomstar/T_sl)^(3/2)*((T_sl+198.6)/(T_elev_bottomstar+198.6));
Re_elev_bottomstar= (rho_elev_bottomstar*V_elev_bottom*p.Se/mu_elev_bottomstar);

T_elev_topstar = T_elev_top*(1+.032*M_elev_top^2+.58*(Tw_elevator_top/T_elev_top - 1));
rho_elev_topstar = P_elev_top/(R*T_elev_topstar); % Density in slug/ft^3
mu_elev_topstar = mu_sl * (T_elev_topstar/T_sl)^(3/2)*((T_sl+198.6)/(T_elev_topstar+198.6));
Re_elev_topstar=rho_elev_topstar*V_elev_top*p.Se/mu_elev_topstar;

N_elevator_bottom = -(.0592/2)*(5/4)*rhoinf*Vinf^2*(mu_elev_bottomstar/(rho_elev_bottomstar*V_elev_bottom))^...
```

```
    (1/5)*p.Se^(4/5)*sin(de); % Pounds
A_elevator_bottom = (.0592/2)*(5/4)*rhoinf*Vinf^2*(mu_elev_bottomstar/(rho_elev_bottomstar*V_elev_bottom))^...
    (1/5)*p.Se^(4/5)*cos(de); % Pounds
M_elevator_bottom = (.0592/2)*(5/4)*rhoinf*Vinf^2*(mu_elev_bottomstar/(rho_elev_bottomstar*V_elev_bottom))...
    ^(1/5)*p.Se^(4/5)*(zcs*cos(de)+sin(de)*xcs); % Foot-Pounds
N_elevator_top = -(.0592/2)*(5/4)*rhoinf*Vinf^2*(mu_elev_topstar/(rho_elev_topstar*V_elev_top))^(1/5)...
    *p.Se^(4/5)*sin(de); % Pounds
A_elevator_top = (.0592/2)*(5/4)*rhoinf*Vinf^2*(mu_elev_topstar/(rho_elev_topstar*V_elev_top))^(1/5)...
    *p.Se^(4/5)*cos(de); % Pounds
M_elevator_top = (.0592/2)*(5/4)*rhoinf*Vinf^2*(mu_elev_topstar/(rho_elev_topstar*V_elev_top))^(1/5)...
    *p.Se^(4/5)...
    *(zcs*cos(de)+sin(de)*xcs); % Foot-Pounds

L_elevator_bottom = N_elevator_bottom*cos(Alpha) - A_elevator_bottom*sin(Alpha); % Pounds
D_elevator_bottom = N_elevator_bottom*sin(Alpha) + A_elevator_bottom*cos(Alpha); % Pounds
L_elevator_top = N_elevator_top*cos(Alpha) - A_elevator_top*sin(Alpha); % Pounds
D_elevator_top = N_elevator_top*sin(Alpha) + A_elevator_top*cos(Alpha); % Pounds
%-------------------------------------------------------------------------------
% Total Viscous Forces
L_viscous = L_upper+L_lower_fore+L_engine_nacelle+L_rearramp+L_elevator_bottom+L_elevator_top;
D_viscous = D_upper+D_lower_fore+D_engine_nacelle+D_rearramp+D_elevator_bottom+D_elevator_top;

N_viscous = N_upper+N_lower_fore+N_engine_nacelle+N_rearramp+N_elevator_bottom+N_elevator_top;
A_viscous = A_upper+A_lower_fore+A_engine_nacelle+A_rearramp+A_elevator_bottom+A_elevator_top;
Moment_viscous = M_upper+M_lower_fore+M_engine_nacelle+M_rearramp+M_elevator_bottom+M_elevator_top;
```

Macro: Flex_PistonTheory.m

```
function [X_unsteady,Z_unsteady,M_unsteady]=Flex_PistonTheoryIncrements_AssumedModes(u,p)

% Program to compute piston theory increments for the HSV vehicle.
%
% Mike Oppenheimer, AFRL/VACA, 7 Dec. 2005
%
% Calculations performed using first-order piston theory
%
% There are four standard parameters and five user defined parameters in
% the
% input, they are as follows:
%                           Standard: t,x,u,flag
%                           User Defined: p (structure defined in Aressim.m)
%-------------------------------------------------------------------------------
Minf=u(1); Pinf=u(2); rhoinf=u(3); ainf=u(4); M1=u(5); P1=u(6); rho1=u(7); a1=u(8);
Mach2=u(9); P2=u(10); rho2=u(11); a2=u(12); M3=u(13); P3=u(14); rho3=u(15); a3=u(16);
M4=u(17); P4=u(18); rho4=u(19); a4=u(20); M5=u(21); P5=u(22); rho5=u(23); a5=u(24);
rhoe=u(25); ae=u(26); Alpha=u(27); Q=u(28); Alpha_linearize=u(29); Q_linearize=u(30);
Etadot_linearize=u(31); Etadot=u(32); de=u(33);
xx=linspace(0,100,1001).';
pflex=polyfit(xx,p.phi_n(:,1),4);%4th order polynomial seems to be accurate enough
%assign the coefficients
a=pflex(1);b=pflex(2);c=pflex(3);d=pflex(4);e=pflex(5);
```

```
Vinf = Minf*ainf;
Delta_Eta_dot = Etadot;
% Flexible Stability Derivatives
%%%%%%%%%%%%%%%%%%%%%%%%%%%%%%%%%%%%%%%%%%%%%%%%%%%%%%%%%%%%%%%%%%%%%%%%%%%%%%%%
cosu = cos(p.tau_1U);
cosl = cos(p.tau_1L);
cos12 = cos(p.tau_1L + p.tau_2);
A1 = (rhoinf - rhoe)/(-p.L_2);
Lax = p.L_2 - p.xa;
A3 = (ainf - ae)/(-p.L_2);
xfl = p.xf - p.L_1;
xfn = p.xf - p.L_1 - p.Le;
% Z_etadot Pieces
Czp1 = -rho1*a1*cosu*((a/5*p.xf^5+b/4*p.xf^4+c/3*p.xf^3+d/2*p.xf^2+e*p.xf)-...
    (-a/5*p.xa^5+b/4*p.xa^4-c/3*p.xa^3+d/2*p.xa^2-e*p.xa));
Czp2 = -rho2*a2*cosl*((a/5*p.xf^5+b/4*p.xf^4+c/3*p.xf^3+d/2*p.xf^2+e*p.xf)-...
    (a/5*xfl^5+b/4*xfl^4+c/3*xfl^3+d/2*xfl^2+e*xfl));
Czp3 = -rho3*a3*((a/5*xfl^5+b/4*xfl^4+c/3*xfl^3+d/2*xfl^2+e*xfl)-(a/5*xfn^5+b/4*xfn^4+...
    c/3*xfn^3+d/2*xfn^2+e*xfn));
Czp41 = -cos12*(a*A1*A3/7*Lax^7+((b-2*A1*a)*A1*A3+(A1*ae+A3*rhoe)*a)/6*Lax^6);
Czp42 = -cos12*(((c-2*Lax*b+Lax^2*a)*A1*A3+(A1*ae+A3*rhoe)*(b-Lax*a)+rhoe*ae*a)/5*Lax^5);
Czp43 = -cos12*(((d-2*Lax*c+Lax^2*b)*A1*A3+(A1*ae+A3*rhoe)*(c-Lax*b)+rhoe*ae*b)/4*Lax^4);
Czp44 = -cos12*(((e-2*Lax*d+Lax^2*c)*A1*A3+(A1*ae+A3*rhoe)*(d-Lax*c)+rhoe*ae*c)/3*Lax^3);
Czp45 = -cos12*(((-2*Lax*e+Lax^2*d)*A1*A3+(A1*ae+A3*rhoe)*(e-Lax*d)+rhoe*ae*d)/2*Lax^2);
Czp46 = -cos12*((A1*A3*Lax^2*e+(A1*ae+A3*rhoe)*(-Lax*e)+rhoe*ae*e)*Lax);
Czp47 = cos12*(a*A1*A3/7*(-p.xa)^7+((b-2*A1*a)*A1*A3+(A1*ae+A3*rhoe)*a)/6*(-p.xa)^6);
Czp48 = cos12*(((c-2*Lax*b+Lax^2*a)*A1*A3+(A1*ae+A3*rhoe)*(b-Lax*a)+rhoe*ae*a)/5*(-p.xa)^5);
Czp49 = cos12*(((d-2*Lax*c+Lax^2*b)*A1*A3+(A1*ae+A3*rhoe)*(c-Lax*b)+rhoe*ae*b)/4*(-p.xa)^4);
Czp410 = cos12*(((e-2*Lax*d+Lax^2*c)*A1*A3+(A1*ae+A3*rhoe)*(d-Lax*c)+rhoe*ae*c)/3*(-p.xa)^3);
Czp411 = cos12*(((-2*Lax*e+Lax^2*d)*A1*A3+(A1*ae+A3*rhoe)*(e-Lax*d)+rhoe*ae*d)/2*(-p.xa)^2);
Czp412 = cos12*((A1*A3*Lax^2*e+(A1*ae+A3*rhoe)*(-Lax*e)+rhoe*ae*e)*(-p.xa));
Z_etadot = Delta_Eta_dot*(Czp1+Czp2+Czp3+Czp41+Czp42+Czp43+Czp44+Czp45+Czp46+Czp47+Czp48+...
    Czp49+Czp410+Czp411+Czp412);
sinu = sin(p.tau_1U);
tanu = tan(p.tau_1U);
sin12 = sin(p.tau_1U+p.tau_2);
tan12 = tan(p.tau_1U+p.tau_2);
sinl = sin(p.tau_1L);
tanl = tan(p.tau_1L);
L = p.xa+p.xf;                                      %verify
q = A1*A3*Lax^2-(A3*rhoe+A1*ae)*Lax+rhoe*ae;          %capital Q used previously as variable
xf = p.xf;
xa = p.xa;
A123 = A1*ae+A3*rhoe-2*A1*Lax*A3;
xtan = xa*tan12-L*tanu;
Aa = A1*ae+A3*rhoe;
% M_etadot Pieces
Cm1 = rho1*a1*sinu*tanu*(a/6*(xf^6-xa^6)+1/5*(b-a*xf)*(xf^5+xa^5)+1/4*(c-b*xf)*(xf^4-xa^4)...
    +1/3*(d-c*xf)*(xf^3+xa^3)+1/2*(e-d*xf)*(xf^2-xa^2)-e*xf*(xf+xa));
Cm2 = -rho2*a2*sinu*tanu*(a/6*(xf^6-xfl^6)+1/5*(b-a*xf)*(xf^5+xfl^5)+1/4*(c-b*xf)*(xf^4-xfl^4)...
    +1/3*(d-c*xf)*(xf^3+xfl^3)+1/2*(e-d*xf)*(xf^2-xfl^2)-e*xf*p.L_1);
Cm41 = sin12*1/8*A1*A3*a*tan12*(Lax^8-xa^8);
Cm42 = sin12*1/7*((A1*A3*b+A123*a)*tan12+A1*A3*a*xtan)*(Lax^7+xa^7);
```

```
Cm43 = sin12*1/6*((A1*A3*c+A123*b+q*a)*tan12+(A1*A3*b+A123*a)*xtan)*(Lax^6-xa^6);
Cm44 = sin12*1/5*((A1*A3*d+A123*c+q*b)*tan12+(A1*A3*c+A123*b+q*a)*xtan)*(Lax^5+xa^5);
Cm45 = sin12*1/4*((A1*A3*e+A123*d+q*c)*tan12+(A1*A3*d+A123*c+q*b)*xtan)*(Lax^4-xa^4);
Cm46 = sin12*1/3*((A123*e+q*d)*tan12+(A1*A3*e+A123*d+q*c)*xtan)*(Lax^3+xa^3);
Cm47 = sin12*1/2*(q*e*tan12+(A123*e+q*d)*xtan)*(Lax^2-xa^2);
Cm48 = sin12*q*e*xtan*p.L_2;
Cm5 = rho1*a1*cosu*(a/6*(xf^6-xa^6)+b/5*(xf^5+xa^5)+c/4*(xf^4-xa^4)+d/3*(xf^3+xa^3)+e/2*(xf^2-xa^2));
Cm6 = rho2*a2*cosl*(a/6*(xf^6-xfl^6)+b/5*(xf^5-xfl^5)+c/4*(xf^4-xfl^4)+d/3*(xf^3-xfl^3)+e/2*(xf^2-xfl^2));
Cm7 = rho3*a3*(a/6*(xfl^6-xfn^6)+b/5*(xfl^5-xfn^5)+c/4*(xfl^4-xfn^4)+d/3*(xfl^3-xfn^3)+e/2*(xfl^2-xfn^2));
Cm81 = cosu*1/8*a*A1*A3*(Lax^8-(-xa)^8);
Cm82 = cosu*1/7*((b-2*Lax*a)*A1*A3+Aa*a)*(Lax^7-(-xa)^7);
Cm83 = cosu*1/6*((c-2*Lax*b+Lax^2*a)*A1*A3+Aa*(b-Lax*a)+rhoe*ae*a)*((Lax^6-(-xa)^6));
Cm84 = cosu*1/5*((d-2*Lax*c+Lax^2*b)*A1*A3+Aa*(c-Lax*b)+rhoe*ae*b)*((Lax^5-(-xa)^5));
Cm85 = cosu*1/4*((e-2*Lax*d+Lax^2*c)*A1*A3+Aa*(d-Lax*c)+rhoe*ae*c)*((Lax^4-(-xa)^4));
Cm86 = cosu*1/3*((-2*Lax*e+Lax^2*d)*A1*A3+Aa*(e-Lax*d)+rhoe*ae*d)*((Lax^3-(-xa)^3));
Cm87 = cosu*1/2*(Lax^2*e*A1*A3+Aa*(-Lax*e)+rhoe*ae*e)*((Lax^2-(-xa)^2));
M_etadot = Delta_Eta_dot*(Cm1+Cm2+Cm41+Cm42+Cm43+Cm44+Cm45+Cm46+Cm47+Cm48+Cm5+...
    Cm6+Cm7+Cm81+Cm82+Cm83+Cm84+Cm85+Cm86+Cm87);
M_unsteady = M_etadot;
X_unsteady = 0;
Z_unsteady = Z_etadot;
```